COLLOIDAL GOLD NANORODS, IRIDESCENT BEETLES AND BREATH FIGURE TEMPLATED ASSEMBLY OF ORDERED ARRAY OF PORES IN POLYMER FILMS

A Dissertation
Presented to
The Academic Faculty

by

Vivek Sharma

In Partial Fulfillment
of the Requirements for the Degree
Doctor of Philosophy in the
School of Polymer, Textile and Fiber Engineering

Georgia Institute of Technology
December, 2008

COLLOIDAL GOLD NANORODS, IRIDESCENT BEETLES AND BREATH FIGURE TEMPLATED ASSEMBLY OF ORDERED ARRAY OF PORES IN POLYMER FILMS

Approved by:

Dr. Mohan Srinivasarao, Advisor
School of Polymer, Textile and Fiber Engineering
Georgia Institute of Technology

Dr. Michael F. Schatz
School of Physics
Georgia Institute of Technology

Dr. David Bucknall
School of Polymer, Textile and Fiber Engineeing
Georgia Institute of Technology

Dr. William Koros
School of Chemical and Biomolecular Engineering
Georgia Institute of Technology

Dr. Jung Ok Park
School of Polymer, Textile and Fiber Engineering
Georgia Institute of Technology

Dr. Paul Neitzel
School of Mechanical Engineering
Georgia Institute of Technology

Date Approved: [Sept. 02, 2008]

[**To my parents**]

आदमी का स्वपन, है वह बुलबुला जल का/ आज बनता और कल फ़िर टूट जाता है/
फ़िर भी ठहरा धन्य आदमी हो तो,/ बुलबुलों से खेलता, कविता बनाता है।
(चाँद और कवि, रामधारी सिंह 'दिनकर' [1])

"*A man's dream, is but a bubble over water/ it forms today, and bursts again tomorrow/ Yet, it only the man's who is blessed/ plays with bubbles, creates poetry*"
(Translated by Vivek as "*The Moon and The Poet*" by Ramdhari Singh 'Dinkar')

What though Dreams be wandering fancies,/ By some lawless force entwined,/
Empty bubbles and floating upwards/ Through the current of the mind,
There are powers and thoughts within us (…)
(James Clarke Maxwell, [2])

ACKNOWLEDGEMENTS

An old Indian adage says, “There is no knowledge without the Guru”. I am deeply grateful to my advisor, Prof. Mohan Srinivasrao for providing me the challenge, freedom and direction to learn about a wide range of topics. In five years, I have evolved both as a person and as a researcher under his tutelage. I was priviliged to be trained under his supervision, and I know I will ever thank him for education I received here.

Thereafter I wish to thank Dr. J. O. Park for paintstakingly reading my dissertation and offering me her help and advice at every stage of my doctoral work.

I was fortunate to have the opportunity of working on chaotic mixing with Prof. Mike Schatz and Prof. Roman Grigoriev in Physics for two years. I thank Prof. Schatz for supporting me for five semesters, and for providing me encouragement and education both as a mentor and later as my committee member. I am indebted to Prof. Grigoriev for teaching me nonlinear dynamics. I will also like to thank all the members of their groups: Kapil, Denis, Ed, Kyoko, Jennifer, Dany, Daniel and Andreas. I owe special thanks to Kapil for endless mentor-ship over the years and to Ed who contributed to both my understanding of chaotic mixing and for proofreading my dissertation.

I believe that this dissertation is an example of how concepts learned in various courses can be applied in research. In this context, I had the opportunity of learning Mass Transfer from Prof. Koros, and several ideas pertinent to the theoretical framework developed in this thesis emerged from what I learned in his class. Likewise, I had the opportunity of learning key concepts of fluid mechanics under Prof. Neitzel. I wish thank Prof. Bucknall for giving me helpful corrections for my thesis. I also wish to express my gratitude to them profusely for serving on my dissertation committee.

I wish to thank all the professors I had the opportunity to learn from in Chemical Engineering and Physics at Georgia Institute of Technology; Department of Polymer Science in University of Akron, Ohio; and in Indian Institute of Technology, Delhi. I owe special gratitude to Prof. Ali Dhinojwala at Akron for insightful discussions and encouragement he has always offered me. Similarly, I wish to thank Prof. Ashok Misra and Prof. A. K. Ghosh (IIT Delhi) for mentoring me from my undergraduate days. I was privileged to work with (late) Prof. Pushpa Bajaj as her last student, and I hope I was able to put her instruction into practice. I am deeply indebted to her for showing me the importance of patience and perseverance in research.

My dissertation research benefited from the discussions I have had with every student in Prof. Mohan Srinivasarao's group. I must thank Dr. Lulu Song for leaving a wealth of data on breath-figure-templated assembly and Dr. Kyoungweon Park for arousing my interest in gold nanorods. I am grateful to Dr. Jian Zhou, Dr. J. S. Park, Haixia, Sai, Min Sang, Beom-Jim, Xuxia, Minsu and most significantly, Matija Crne for involving me in interesting discussions about a range of topics.

Matija Crne deserves my special acknowledgements, for being a friend and peer, always there across the table: for ping-pong, for beer (mostly at Rocky mountain), as an editor to my documents, and ever ready to lend me his ear and wisdom about everything under the sun. Likewise, I am thankful that Yifu Ding has been like an elder brother and friend to me throughout the last seven years. I have been blessed with a large number of friends across the globe, and I thank them all. I specially thank Abhinav (Sexana and Singh), Akbar, Ajitabh, Amit Gupta, Anshuman, Arun, Farminder, Gagan, Hemabh, Ishwar, Sanjoy and Vikas Tomar who were encouraging me with their significant

comments about science and life. Likewise, I must thank my roommates and friends from Akron, especially Vikas, Shishir, Rajesh and Parag. The most significant role in my personal odyssey is played by Smita Sahoo, and I will have all my future years to acknowledge her contributions.

I particularly wish to thank everyone involved in Poetry at Tech: Travis Denton, Ginger, all the poets I met there, and above all, Gurudev Prof. Thomas Lux. I thank Bruce McEver as well as Henry and Margaret Bourne for instituting two chair positions in poetry, and ensuring that Gurudev Lux is present on the Tech campus. The first poem of Gurudev's new book (God Particles) says exactly what I will ever say about him: "The Gentleman who spoke like music/ was kind to me/ though he need not have to be." Gurudev Lux has been a mentor, a friend, a teacher to me and over last three years, he has transformed my poetry and personality. The role of poetry and imagination in science was best expressed by van't Hoff over a century ago, and personally I am indebted to Georgia Tech. for proving me the opportunity of working with professors who have guided me in the pursuit of excellence in both science and poetry.

My greatest gratitude is and always will be to my parents, who ensured that I always got the best possible education, and toiled throughout their life to make my life comfortable and worthwhile. I dedicate my dissertation and my every accomplishment to their dreams, determination and digilence. I also wish to acknowledge the confidence my sister, Vandana, my relatives and my childhood friends (Himanshu, Ashish, Shashi and Pooja,) expressed in me. Their faith kept me focussed and motivated always.

Lastly, I wish to thank National Science Foundation for supporting bulk of my graduate education.

TABLE OF CONTENTS

LIST OF TABLES

Page

LIST OF FIGURES

Page

SUMMARY

Water drops that nucleate and grow over an evaporating polymer solution exposed to a current of moist air remain noncoalescent and self-assemble into close packed arrays. The hexagonally close packed, nearly monodisperse drops, eventually evaporate away, leaving a polymer film, with ordered array of pores. Meanwhile, typical breath figures or dew that form when moist air contacts cold surfaces involve coalescence-assisted growth of highly polydisperse, disordered array of water drops.

This dissertation provides the first quantitative attempt aimed at the elucidation of the mechanism of the breath figure templated assembly of the ordered arrays of pores in polymer films. The creation and evolution of a population of close packed drops occur in response to the heat and mass fluxes involved in water droplet condensation and solvent evaporation. The dynamics of drop nucleation, growth, noncoalescence and self-assembly are modeled by accounting for various transport and thermodynamic processes. The theoretical results for the rate and extent of evaporative cooling and growth are compared with experiments. Further, the dissertation describes a rich array of experimental observations about water droplet growth, noncoalescence, assembly and drying that have not been reported in the published literature so far. The theoretical framework developed in this study allows one to rationalize and predict the structure and size of pores formed in different polymer-solvent systems under given air flow conditions.

While the ordered arrays of water drops present an example of dynamics, growth and assembly of spherical particles, the study on colloidal gold nanorods focuses on the behavior of rodlike particles. A comprehensive set of theoretical arguments based on the shape dependent hydrodynamics of rods were developed and used for centrifugation-

assisted separation of rodlike particles from nanospheres that are typical byproducts of seed mediated growth of nanorods. Since the efficiency of shape separation is assessed using UV-Vis-NIR spectroscopy and transmission electron microscopy (TEM), the present dissertation elucidates the shape dependent parameters that affect the optical response and phase behavior of colloidal gold nanorods. The drying of a drop of colloidal gold nanorods on glass slides creates coffee ring like deposits near the contact line, which is preceded by the formation of a liquid crystalline phase. The assemblies of rods on TEM grids are shown to be the result of equilibrium and non-equilibrium processes, and the ordered phases are compared with two dimensional liquid crystals.

The methodology of pattern characterization developed in this dissertation is then used to analyze the structure of the exocuticle of iridescent beetle *Chrysina gloriosa*. The patterns were characterized using Voronoi analysis and the effect of curvature on the fractions on hexagonal order of tiles was determined. Further, these patterns were found to be analogous to the focal conic domains formed spontaneously on the free surface of a cholesteric liquid crystal.

In summary, the dissertation provides the crucial understanding required for the widespread use of breath figure templated assembly as a method for manufacturing porous films, that requires only a drop of polymer solution (dilute) and a whiff of breath! Further, the dissertation establishes the physical basis and methodology for separating and characterizing colloidal gold nanorods. The dissertation also suggests the basis for the formation and structure of tiles that decorate the exoskeleton of an iridescent beetle *Chrysina gloriosa*.

CHAPTER 1

INTRODUCTION

'Before the beginning of great brilliance, there must be chaos': I Ching.
Quoted in *Chaos by* James Gleick [3]

1.1 Viewing complex fluids as fragile objects: Motivations

The study of fragile objects, according to Pierre-Gilles de Gennes [4, 5] includes polymers, colloids, emulsions, foams, liquid crystals, bubbles, drops, gels and granular media. This realm of matter is called soft condensed matter [6-10], for these materials are squishy and their response to stress is like that of semi-solids. A combination of spring-like elasticity and ability to flow makes their behavior viscoelastic. Their ability to flow is itself distinguished by behavior unlike that of common liquids or gases [4, 11]: the complexity comes from their time dependent, or stress dependent behavior. For example, a rubber ball can be squeezed slowly like a fluid, and if it is thrown at a wall, it bounces back like a solid. The response of soft mater is described by the laws of statistical mechanics. The moieties that constitute these materials have interaction forces of the order of k_BT, where k_B is the Boltzmann constant and T is the temperature, and thus their dynamics follows from the laws of Brownian motion [12]. Most of the living matter, food, our blood, cells, plastic, rubber, and laptop computer screens contain or are formed of complex fluids in some form. To understand the behavior of such materials requires one to study fluid mechanics [13-15], understand interaction of light with matter [16-22], thermodynamics [10, 23, 24] and statistical mechanics [25, 26].

While the physical appearance of various groups of soft matter is quite different, the physics bears similarities that help to identify the differences, as was demonstrated time and again by various researchers, including de Gennes [4, 5, 27-29], who was a

master at it. The life and work of Pierre-Gilles de Gennes is a testimony to his advice [4]: "…this transportation of methods between two apparently unrelated fields of science. What has been learned in one field can at times help solve completely different problems." The dissertation research presented here owes a lot to insights gained by reading remarkable textbooks from his work [4, 5, 27-29].

The domain of research explored in this dissertation lies in this realm of soft matter physics. The motivation is summed up in three questions: 1) Breathing on cold glass produces patterns called breath figures that consist of drops of many sizes, randomly arranged (surface coverage ~55%), but breathing on evaporating polymer solutions produces water drops that are noncoalescent, monodisperse, and closely packed (surface coverage in two dimensions ~90%), before they evaporate out leaving a polymer film full of ordered arrays of air bubbles or pores: *What is the mechanism for this breath figure templated assembly that makes water drops grow and organize without coalescence, and create porous or "holey" film?* 2) *How can one separate colloidal gold nanorods from nanoparticles of other shapes, and how can one ascertain that those were separated efficiently?* 3) *What causes the exoskeleton of the beetle Chrysina Gloriosa to display iridescent colors?* To find the answers, one must first understand these questions, why these are relevant questions, what knowledge exists already and then figure how to address the unresolved, by hypothesis or experiments, and by critical reasoning, expound on whatever was discovered. The rest of the thesis (hopefully) pertains to this sequence of thought and description of my research.

This dissertation is divided into twelve chapters: Chapters 2-7 are dedicated to breath figure templated assembly, chapters 8-10 to colloidal gold nanorods, chapter 11 to

the iridescent beetles, while chapter 12 provides a list of conclusions derived from the research presented in this dissertation. Before exploring each of these questions individually, let us step back and look at the broad ideas that have brought these three seemingly different realms of soft matter into one dissertation. While the literature review pertinent to the specific topics is incorporated into the respective chapters, the summary in this chapter provides a gist of ideas involved in this research.

1.2 Historical connection between colloidal gold, water drops and iridescent beetles

Historically speaking, the study of colloids begins in the middle of nineteenth century with a paper on colloidal gold by Faraday [30]. Colloidal gold sols were produced and used as colorants and medicines for centuries [31, 32], before they attracted Faraday's interest in 1857 [30], in a paper that can be called the most important article in both the history of experimental colloidal synthesis, as well as in the discussion of how light interacts with matter. While Faraday's body of work in electromagnetism set the stage for Maxwell's celebrated equations that describe the behavior of light [2, 33, 34], unfortunately Faraday's work on colloidal gold was forgotten for nearly forty years. Thereafter, Zsigmondy, who developed a different synthesis protocol became aware of it [35]. Zsigmondy combined his synthesis technique with Faraday's method, to devise two step "nuclear" method [35]. This method has been rediscovered and is now termed as the "seed-mediated" method, without any acknowledgement of the pioneering work by Zsigmondy and others.

Further Zsigmondy managed to design an ultramicroscope to view the size and mobility of nanometer size colloidal particles [35, 36], which were called ultramicrons at that time. Faraday tried to see colloidal particles using a Tyndall cone of light through the colloidal solution [30]. Zsigmondy conducted Faraday's experiment under a microscope, and his discovery not only established colloidal matter, but set the stage for multiple discoveries that form the basic thesis of soft matter. Tyndall himself probed scattering of light, but the explanation for blue tinge he noticed in artificial fogs and the explanation for the blue color of sky was given by Lord Rayleigh. While Lord Rayleigh explained blue color of the sky [37], the color of blue seas was explained partially by C. V. Raman, and by J. Aitken, as recounted in Bohren's 'Clouds in a glass of beer: Simple experiments in atmospheric physics' [38]. Maxwell himself was a pioneer in color science, and among his numerous contributions, he produced the world's first colored photograph. His work is equally fundamental in the realms of kinetic theory of gases, thermodynamics and mechanics [2].

Lord Rayleigh contributed to so many areas (fluid and solid mechanics, optics, sound, radiation to name a few [39]) that is easy to overlook his interest in color science, which put him on trail of butterflies. Lord Rayleigh's contributions to the understanding of fluid jets that bounce on collision [40, 41], instability of cylindrical fluid jets and convective instability created by temperature difference [39], are important for understanding the phenomenon described in this thesis. Lord Rayleigh also worried about breath figures, where again he got into a debate with Aitken (series of papers in Nature [42-44]). Aitken, along with Coulier, (see the review by Spurny [45]) established that fogs and clouds form by condensation of water over aerosols or particles dispersed in air.

The creation of cloud chambers and experiments using them was in fashion in the beginning of twentieth century, and innumerable experimentalists including Wilson, Millikan, Helmholtz, Aitken, J. J. Thomson, among others used it to establish key principles in particle physics, as was summarized in a long and interesting review by Dasgupta and Ghosh in 1946 [46].

Like Faraday and Zsigmondy, Svedberg made important contributions in the synthesis of colloidal gold [47, 48] and used these particles to show how ultracentrifuge designed by him can not only size separate them, but also reveal their size and shape-dependent mobility [47-49]. These experiments were done at an opportune time, for the basic theories of Brownian motion were being developed by Einstein [50-52], Smoluchowski [53-55] and Langevin [56] (also see Chandrasekhar's review [12] and recent perspectives [57-60]). The distribution of Brownian particles as a function of height predicted by these theories was used by Perrin [61-63], to experimentally determine Avogadro's number and establish the reality of molecular theory of matter. These experiments are reviewed in chapter 8, and provide inspiration for elucidation of separation of rods and spheres using centrifugation described in chapter 9. Further, Perrin [61-63] measured size of particles used in his experiment by allowing them to organize into a close packed array: the physics that drives colloidal assembly is relevant to both the assembly of non-coalescent water drops, described in chapter 6 and to the self-assembly of colloidal gold nanorods, discussed in chapter 9.

Around the same time (early twentieth century), Mie advanced his theory [64] in attempt to explain the color of colloidal gold dispersions and Gans proceeded to discuss the influence of ellipsoidal shape on colloidal gold [65]. The theories of Mie and Gans

allow one to understand the color of colloidal gold dispersions as well as their absorption and scattering behavior, which is key to characterizing their size dispersion, as well as for their use in sensors, as is discussed in chapter 8 and 9.

Zsigmondy drew the attention of von Smoluchowski to the problem of colloidal coagulation of gold particles, asking him to derive an experimentally verifiable formula. (Nobel Lecture [66]) Smoluchowski's theories for diffusion and coagulation [12, 53, 55, 67] are central to our understanding of collision and coalescence issues in both colloidal sols and other such systems including stability of fog. Smoluchowski computed the rate at which a diffusing particle arrives in a 'sphere of influence' of another particle. The assumption is that if the diffusing particle moves about in the region outside this sphere of influence, it moves unaffected, but if it enters the region, it sticks to the other particle [12]. Thus Brownian motion, together with the interparticle attractive and repulsive forces that form the physico-chemical basis for the sphere of influence, determines the phase behavior and stability of colloids. Non-coalescence or lack of aggregation of colloidal particles is critical to the stability of colloidal dispersions, as described in chapter 8. These theories also help in understanding the kinetic factors that make water drops noncoalescent in breath figure templated assembly, discussed in chapter 5.

The condensation of water vapor into drops is a ubiquitous phenomenon. It underlies the formation of dew, clouds, fog, rain, fogging of car windows, beads of water on a glass of cold beer and of breath figures [38, 68]. These have interested poets, philosophers and scientists for centuries [38, 42, 68, 69]. While Lord Rayleigh and Aitken studied breath figure patterns on solid surfaces in the beginning of last century, Augustus Waller in 1846 had reported experiments of water droplets trapped on liquids

and solids, including Canada balsam, turpentine oil, castor oil, etc. and on filaments of spider web, and he showed that fog was composed of water droplets and not vesicles as was believed then (even by Clausius) [68]. A very entertaining history of the theories of rain and other forms of precipitation [68], written by Middleton, introduces a cast of characters from Clausius, Aristotle, Maxwell, Langmuir, Kelvin, among others who studied the aspects related to precipitation, and interestingly made significant contributions to the fields of thermodynamics, fluid mechanics and optics. In recent times, Beysens and Knobler [70] revitalized the interest in breath figures. Though assembly of water drops had been observed to create ordered and disordered structures over evaporating polymer structures by Widawski et al [71], Limaye et al [72], Pitois and Francios [73, 74] among others, the connection to breath figures was first made in a report by Srinivasarao et al [75]. The different mechanisms that have been proposed to explain growth, non-coalescence and assembly of drops, and the range of polymer solvent systems that have been tried are reviewed in the next chapter.

Yet the initial studies of water drops deposited in liquid polymer films were done in the 1940s [76-78], where polymer solutions were passed though a fog chamber to trap water drops for measuring their sizes and size distribution. Atmospheric physics scientists used Formvar solution in chloroform, which was first exposed to fog formed in a cloud/ fog chamber, and then the polymer solution with water drops trapped on it was dried in a hot chamber. The droplets left craters on the plastic film which were counted and characterized to determine dimensions of the water drops in the cloud chamber [76-78]. In the present research, we rediscover the *forgotten* connection between atmospheric physics and the mechanistic aspects of breath figure template assembly. The kinetics of

nucleation and growth of water drops over evaporating polymer solutions derived and described in chapter 4 and the mechanism of noncoalescence described in chapter 5 involve the analogies from atmospheric physics.

The concepts related to optical properties of colloidal gold (and other particles) as well as to the formation of mixing clouds, fog, clouds, rain and blue color of sea and sky are explained in a very entertaining and insightful fashion by Bohren [16, 23, 38, 79]. The breath figure patterns are analogues to chemical vapor deposition, and this similarity is described in the work of Meakin [80, 81], whereas condensation growth of water drops is similar to growth of colloidal particles from solution, as was already identified by Sevdberg [47, 48] and Zsigmondy [35, 36]. The assembly water droplets over a two dimensional region, and the self-assembly of colloidal gold nanorods that are discussed in chapter 6 and chapter 10 are based on the pursuit of perfect packing: their differences arise primarily due to the difference their shape [82, 83]. The work of Pieranski features in the later chapters in context of colloidal crystallization [84-86] first and later his studies of the cholesteric focal conic domains [87] are relevant in the context of iridescent beetles. The color of beetles and butterflies is often due to the microstructure of their exoskeletons or wings [88-92]. The range of patterns that form in physical and biological systems, and their common basis itself has a long an interesting history, and the texts by Thomson [93], Ball [94] and Stevens [95] were key to my developing the eye for such patterns. The structural color in colloidal crystals that make opals, as well as the brilliant colors of cholesteric liquid crystals, are described by the use of Bragg's law, as is discussed in chapter 11 of this thesis. Isn't it amazing that the same Sir Lawrence Bragg (in collaboration with Nye and Lomer) [96-99] also studied bubble rafts, that form

ordered arrays and exhibit dynamical crystal structure exhibited by array of noncoalescent water drops?

Thus the sciences of colloidal matter, clouds and fogs, and color of beetles and butterflies seem to share a considerable history of thoughts and ideas. Personally, the reason why these topics feature in the same thesis is influenced greatly by the nature of research done by my advisor, Mohan Srinivasarao and my interactions with Jung O. Park and the students in this group: Jian Zhou on liquid crystals [100], Kyoungweon Park on colloidal gold [101], Lulu Song on breath figure templated assembly [102] and Matija Crne on butterflies and beetles [103, 104]. The quote of I Ching in the beginning of this chapter is taken from a book on Chaos by Gleick [3], which was responsible in part for my interest in nonlinear dynamics, and research effort on chaotic mixing, that is not included in this dissertation. The two years spend in imaging of chaotic mixing in microdroplets in the group of Mike Schatz (and in collaboration with Roman Grigoriev) [105] as well as my varied background and courses in polymers, physics and chemical engineering allowed this thesis to emerge in its present form. The sequence in which research is presented in this dissertation is outlined in the next section.

1.3 Thesis Outline

The present research attempts to provide the first quantitative attempt at theoretical understanding of the influence and role of parameters that guide the nucleation, growth, and self-assembled array of nearly monodisperse, non-coalescent water drops over evaporating polymer solutions exposed to moist air flow. Chapter 2 provides a comprehensive summary of the mechanisms proposed so far, and summarizes

experimental results from published literature. The chapter also lists the questions that will be addressed in context of breath figure templated assembly of air bubbles in polymer films.

Chapter 3 describes a model for evaporative mass loss that considers the diffusion of solvent through a polymer film with air flow at the top surface and compares it with the experiments. Thereafter, the change in the temperature of the surface during evaporation is modeled, and compared with the experimental measurements. The heat change associated with the latent heat of vaporization of the solvent and the heat flux at the surface is correlated with the conductive and convective heat transfer that takes place when the blast of air flows over the substrate are taken into account.

The variation of supersaturation over the substrate is computed next in chapter 4. Using the solvent vapor flux and temperature change of the substrate modeled herewith, the actual humidity or saturation level above the substrate is derived and related to water vapor flux due to the air flow. Thereafter the condensation growth of droplets is modeled and the apparent monodispersity of water droplets is shown to be a consequence of nucleation and growth kinetics derived in this study.

The non-coalescence of water drops over the evaporating polymer solutions is described chapter 5, where the role of collision statistics and hydrodynamics of draining films is elucidated.

Chapter 6 describes the assembly of water drops as a model system for studying pursuit of perfect packing in two dimensional systems. The various attractive and repulsive forces that act on water drops are computed.

In the last chapter on breath figure templated assembly, i. e. in chapter 7, various wetting and dewetting transitions are reported to occur before the water drops dry out. The observation of the wetting-dewetting transitions before drying in experiments as well as elucidation of why they occur are have not been reported before this dissertation research.

The question of how colloidal gold nanorods can be characterized for polydispersity in shape and size, and how these can be separated from a mixture of as-made particles, synthesized by seed mediated method are focus of next three chapters.

It is important to recognize that the physical properties of gold particles *including rodlike particles* were studied in the early twentieth century and these provided original and ground breaking advances in the field of colloidal matter. The importance of these historical studies is highlighted in chapter 8 for these include use of methods and concepts that are crucial for better understanding of rodlike particles. The parameters that affect colloidal stability of gold dispersions are outlined as well.

The theoretical arguments that allow successful centrifugation assisted separation of colloidal nanorods from nanospheres are described in chapter 9.

In chapter 10, the patterns formed on drying a drop of colloidal gold nanorods on TEM grids and glass slides are shown to involve a range of equilibrium and non-equilibrium effects, including formation of liquid crystalline phase and ring-like deposits at or near the contact line.

Chapter 11 described how the patterns on the exocuticle of iridescent beetle Chrysina gloriosa were characterized using Voronoi analysis and the effect of curvature on the hexagonal order of cells that tessellate the exocuticle was determined.

Chapter 12 lists the questions that were asked and answered during the course of this dissertation research and concludes with recommendations for future work.

1.4 References

1. Dinkar, R.S., *Sanchayita*. 1973, New Delhi.
2. Campbell, L. and W. Garnett, *The life of James Clerk Maxwell*. 1882, London: Macmillan & Co.
3. Gleick, J., *Chaos*. 1988: Penguin.
4. de Gennes, P.G. and J. Badoz, *Fragile Objects*. 1996, New York: Springer-Verlag.
5. de Gennes, P.G., *Simple views on condensed matter*. 3rd ed. 2003, Singapore: World Scientific Publishing Co.
6. Cates, M.E. and M.R. Evans, *Soft and Fragile Matter*. 2000, Bristol: Institue of Physics Publishing.
7. Kleman, M. and O.D. Lavrentovich, *Soft matter physics: an introduction*. 2003, New York: Springer-Verlag Inc.
8. Witten, T.A. and P.A. Pincus, *Structured Fluids: Polymers, Colloids, Surfactants*. 2004, New York: Oxford University Press.
9. Daoud, M. and C.E. Williams, eds. *Soft Matter Physics*. 1995, Springer: Berlin.
10. Chaikin, P.M. and T.C. Lubensky, *Principles of condensed matter physics*. 1995, Cambridge: Cambridge University Press.
11. Larson, R.G., *The structure and rheology of complex fluids*. Topics in chemical engineering, ed. K.E. Gubbins. 1999, New York: Oxford University Press.
12. Chandrasekhar, S., *Stochatic Problems in Physics and Astronomy.* Reviews of Modern Physics, 1943. **15**(1): p. 1-89.
13. Batchelor, G.K., *An Introduction to Fluid Mechanics*. 1967, Cambridge: Cambridge University Press.
14. Bird, R.B., W.E. Stewart, and E.N. Lightfoot, *Transport Phenomenon*. 1960, Singapore: John Wiley and Sons.

15. Happel, J. and H. Brenner, *Low Reynolds number hydrodynamics* 2nd ed. 1973, Leyden: Noordhoff International Publishing.

16. Bohren, C.F. and D.R. Huffman, *Absorption and scattering of light by small particles*. 1983, New York: John Wiley & Sons.

17. Born, M. and E. Wolf, *Principles of Optics: Electromagnetic Theory of Propagation, Interference and Diffraction of Light*. 7th ed. 1999, Cambridge: Cambridge University Press.

18. Kerker, M., *The scattering of light and other electromagnetic radiation*. 1969, New York: Academic Press, Inc.

19. Lipson, S.G., H. Lipson, and D.S. Tannhauser, *Optical Physics*. 1995, Cambridge: Cambridge University Press.

20. Michelson, A.A., *Studies in Optics*. 1927, Chicago: The University of Chicago Press.

21. Sommerfeld, A., *Optics: Lectures on Theoretical Physics, Volume 4*. 1954, New York: Academic Press.

22. van de Hulst, H.C., *Light Scattering by Small Particles*. 1981, Mineola: Dover Publications, Inc.

23. Bohren, C.F. and B.A. Albrecht, *Atmospheric Thermodynamics*. 1998: Oxford University Press, USA

24. Israelachvili, J., *Intermolecular and Surface Forces*. 2nd ed. 1992, San Diego: Academic Press.

25. Pathria, R.K., *Statistical Mechanics*. 2nd ed. 1996, Oxford: Butterworth-Heinemann.

26. Hill, T.H., *An Introduction to Statistical Thermodynamics*. 1986, New York: Dover Publications, Inc.

27. de Gennes, P.G., F. Brochard, and D. Quere, *Capillarity and Wetting Phenomena: drops, bubbles, pearls, waves*. 2004, New York: Springer-Verlag.

28. de Gennes, P.G. and J. Prost, *The Physics of Liquid Crystals*. 2nd ed. International Series of Monographs on Physics. 1995: Oxford University Press, USA.

29. de Gennes, P.G., *Scaling concepts in polymer physics*. 1979, Ithaca: Cornell University Press.

30. Faraday, M., *The Bakerian Lecture: Experimental Relations of gold (and other metals) to light.* Philosophical Transactions of the Royal Society of London, 1857. **147**: p. 36.

31. Ostwald, W., *An Introduction to Theoretical and Applied Colloid Chemistry*. 1917, New York: John Wiley & Sons, Inc.

32. Ray, P.C., *History of Hindu Chemistry*. 1903, Calcutta: The Bengal Chemical and Pharmaceutical Works, Limited.

33. Slater, J.C. and N.L. Frank, *Electromagnetism*. 1969, New York: Dover Publications, Inc.

34. Jackson, J.D., *Classical Electrodynamics*. 1962, New York: John Wiley & Sons, Inc.

35. Zsigmondy, R., *The Chemistry of Colloids*. 1917, New York: John Wiley & Sons, Inc.

36. Zsigmondy, R., *Colloids and the ultramicroscope*. 1909, New York: John Wiley & Sons, Inc.

37. Strutt, J.W.L.R., *On the light from the sky, its polarization and colour.* Philosophical Magazine, 1871. **107**: p. 274-279.

38. Bohren, C.F., *Clouds in a Glass of Beer: Simple Experiments in Atmospheric Physics*. 2001: Dover Publications.

39. Strutt, J.W.L.R., *Scientific Papers*. 1920, Cambridge: Cambridge University Press.

40. Rayleigh, L., *On the Capillary Phenomenon of Jets.* Proceedings of the Royal Society of London, 1879. **29**: p. 71-97.

41. Rayleigh, L., *Further Observations upon Liquid Jets, in Continuation of Those Recorded in the Royal Society's 'Proceedings' for March and May, 1879.* Proceedings of the Royal Society of London 1882. **34**: p. 130-145.

42. Rayleigh, *Breath figures.* Nature, 1911. **86**: p. 416-418.

43. Rayleigh, *Breath figures.* Nature, 1912. **90**: p. 436-438.

44. Aitkens, J., *Breath Figures.* Nature, 1911. **86**: p. 516-517.

45. Spurny, K.R., *Atmospheric condensation nuclei P. J. Coulier 1875 and J. Aitken 1880 (historical review).* Aerosol Science and Technology, 2000. **32**(3): p. 243-248.

46. Dasgupta, N.N. and S.K. Ghosh, *A report on the Wilson cloud chamber and its application in physics.* Reviews of Modern Physics, 1946. **18**(2): p. 225-290.

47. Svedberg, T., *The Formation of Colloids*. 1921, New York: D. Van Nostrand Company.

48. Svedberg, T. and A. Tiselius, *Colloid Chemistry*. Second ed. 1928, New York: The Chemical Catalog Company, Inc.

49. Svedberg, T. and K.O. Pedersen, *The Ultracentrifuge*. 1940, Oxford: Oxford University Press.

50. Einstein, A., *The motion of elements suspended in static liquids as claimed in the molecular kinetic theory of heat.* Annalen Der Physik, 1905. **17**(8): p. 549-560.

51. Einstein, A., *Investigation on the theory of Brownian movement*. 1956, New York: Dover Publications.

52. Einstein, A., *The theory of the Brownian Motion.* Annalen Der Physik, 1906. **19**(2): p. 371-381.

53. von Smoluchowski, M., *The kinetic theory of Brownian molecular motion and suspensions.* Annalen Der Physik, 1906. **21**(14): p. 756-780.

54. von Smoluchowski, M., *Three presentations on diffusion, molecular movement according to Brown and coagulation of colloid particles.* Physikalische Zeitschrift, 1916. **17**: p. 557-571.

55. von Smoluchowski, M., *Three lectures on diffusion, Brown's molecular movements and the coagulation of colloid parts.* Physikalische Zeitschrift, 1916. **17**: p. 585-599.

56. Langevin, P., *The theory of brownian movement.* Comptes Rendus Hebdomadaires Des Seances De L Academie Des Sciences, 1908. **146**: p. 530-533.

57. Haw, M.D., *Colloidal suspensions, Brownian motion, molecular reality: a short history.* Journal of Physics-Condensed Matter, 2002. **14**(33): p. 7769-7779.

58. Newburgh, R., J. Peidle, and W. Rueckner, *Einstein, Perrin, and the reality of atoms: 1905 revisited.* American Journal of Physics, 2006. **74**(6): p. 478-481.

59. Dhont, J.K.G. *Translational Brownian motion*. in *Physics meets biology: From Soft Matter to Cell Biology, 35th Spring School of the Institut fur Festkorperforschung*. 2004. Julich: Forschungszentrum.

60. Dhont, J.K.G. *Rotational Brownian motion of colloidal rods*. in *Soft Matter: Complex Materials on mesoscopic scales, 33rd IFF-Ferienschule*. 2002. Julich: Forschungszentrum Julich GmbH.

61. Perrin, J., *Brownian motion and molecular reality.* Annales De Chimie Et De Physique, 1909. **18**: p. 5-114.

62. Perrin, J., *Atoms*. 2nd ed. 1923, London: Constable & Company Ltd.

63. Nye, M.J., *The Question of the Atom*. The History of Modern Physics, 1800-1950. Vol. IV. 1984, Los Angeles: Tomash Publishers.

64. Mie, G., *Articles on the optical characteristics of turbid tubes, especially colloidal metal solutions.* Annalen Der Physik, 1908. **25**(3): p. 377-445.

65. Gans, R., *The shape of ultra microscopic gold particles.* Annalen Der Physik, 1912. **37**(5): p. 881-900.

66. Foundation, N., ed. *Chemistry 1922 - 1941 Nobel Lectures*. 1966, Elsevier Publishing Company: Amsterdam.

67. von Smoluchowski, M., *Outline of the coagulation kinetics of colloidal solutions.* Kolloid-Zeitschrift, 1917. **21**(3): p. 98-104.

68. Middleton, W.E.K., *History of the Theories of Rain and Other Forms of Precipitation*. 1966, New York: Franklin Watts, Inc.

69. Fuchs, N.A., *Evaporation and droplet growth in gaseous media*. 1959, London: Permagon Press.

70. Beysens, D. and C.M. Knobler, *Growth of breath figures.* Physical Review Letters, 1986. **57**(12): p. 1433-1436.

71. Widawski, G., M. Rawiso, and B. Francois, *Self-organized honeycomb morphology of star-polymer polystyrene films.* Nature, 1994. **369**(6479): p. 387-389.

72. Limaye, A.V., et al., *Evidence for convective effects in breath figure formation on volatile fluid surfaces.* Physical Review Letters, 1996. **76**(20): p. 3762-3765.

73. Pitois, O. and B. Francois, *Formation of ordered micro-porous membranes.* European Physical Journal B, 1999. **8**(2): p. 225-231.

74. Pitois, O. and B. Francois, *Crystallization of condensation droplets on a liquid surface.* Colloid and Polymer Science, 1999. **277**(6): p. 574-578.

75. Srinivasarao, M., et al., *Three-dimensionally ordered array of air bubbles in a polymer film.* Science, 2001. **292**(5514): p. 79-83.

76. Mason, B.J., *The Physics of Clouds, 2nd ed.* 1971, London: Oxford University Press.

77. MacCready, P.B. and C.J. Todd, *Continuous Particle Sampler.* Journal of Applied Meteorology, 1964. **3**(4).

78. Spyers-Duran, P.A. and R.R. Braham, *An Airborne Continuous Cloud Particle Replicator.* Journal of Applied Meteorology, 1967. **6**(6).

79. Bohren, C.F., *What light through yonder window breaks?: more experiments in atmospheric physics*. 1991, New York: John Wiley & Sons, Inc.

80. Meakin, P., *Droplet deposition growth and coalescence.* Reports on Progress in Physics, 1992. **55**(2): p. 157-240.

81. Meakin, P., *Fractals, scaling and growth far from equilibrium*. 1998, Cambridge: Cambridge University Press.

82. Aste, T. and D.L. Weaire, *The Pursuit of Perfect Packing*. 2000, London: Institute of Physics Publishing.

83. Hyde, S., et al., *The Language of Shape*. 1997, Amsterdam: Elsevier Science B. V.

84. Pieranski, P., *Two dimensional interfacial colloidal crystals.* Physical Review Letters, 1980. **45**(7): p. 569-572.

85. Pieranski, P., *Colloidal crystals.* Contemporary Physics, 1983. **24**(1): p. 25-73.

86. Pieranski, P., L. Strzelecki, and B. Pansu, *Thin colloidal crystals.* Physical Review Letters, 1983. **50**(12): p. 900-903.

87. Meister, R., et al., *Structure of the cholesteric focal conic domains at the free surface.* Physical Review E, 1996. **54**(4): p. 3771-3782.

88. Ghiradella, H., *Light and color on the wing - structural colors in butterflies and moths.* Applied Optics, 1991. **30**(24): p. 3492-3500.

89. Srinivasarao, M., *Nano-optics in the biological world: Beetles, butterflies, birds, and moths.* Chemical Reviews, 1999. **99**(7): p. 1935-1961.

90. Vukusic, P. and J.R. Sambles, *Photonic structures in biology.* Nature, 2003. **424**(6950): p. 852-855.

91. Parker, A.R., *515 million years of structural colour.* Journal of Optics a-Pure and Applied Optics, 2000. **2**(6): p. R15-R28.

92. Bertheier, S., *Iridescences: The Physical Color of Insects*. 2007: Springer.

93. Thompson, D.A., *On Growth and Form*. 1961, Cambridge: Cambridge University Press.

94. Ball, P., *The Self-made tapestry: pattern formation in nature*. 1999, Oxford: Oxford University Press.

95. Stevens, P.S., *Patterns in Nature*. 1974, Boston: Little, Brown and Company.

96. Bragg, L. and J.F. Nye, *A dynamical model of a crystal structure.* Proceedings of the Royal Society of London Series a-Mathematical and Physical Sciences, 1947. **190**(1023): p. 474-&.

97. Lomer, W.M., *A dynamical model of a crystal structure. III.* Proceedings of the Royal Society of London Series a-Mathematical and Physical Sciences, 1949. **196**(1045): p. 182-194.

98. Bragg, L. and W.M. Lomer, *A dynamical model of a crystal structure. II.* Proceedings of the Royal Society of London Series a-Mathematical and Physical Sciences, 1949. **196**(1045): p. 171-181.

99. Lomer, W.M. and J.F. Nye, *A dynamical model of a crystal structure IV. Grain boundaries.* Proceedings of the Royal Society of London Series a-Mathematical and Physical Sciences, 1952. **212**(1111): p. 576-584.

100. Zhou, J., *Study of anchoring behavior of nematic fluids at the interface of polymer dispersed liquid crystals*, in *School of Polymer, Textile and Fiber Engineering*. 2003, Georgia Institute of Technology: Atlanta.

101. Park, K., *Synthesis, characterization and self-assembly of size tunable gold nanorods*, in *School of Polymer, Textile and Fiber Engineering*. 2006, Georgia Institute of Technology: Atlanta.

102. Song, L., *Study of ordered macroporous polymer films by templating breath figures*, in *School of Polymer, Textile and Fiber Engineering*. 2005, Georgia Institute of Technology: Atlanta. p. 193.

103. Sharma, V., et al., *Cholesteric focal conic domains decorate the exocuticle of iridescent beetle Chrysina Gloriosa.* to be submitted.

104. Crne, M., et al., *Mimicry of Papilio Palinurus butterfly optical effects* To be submitted.

105. Grigoriev, R.O., M.F. Schatz, and V. Sharma, *Chaotic mixing in microdroplets.* Lab on a Chip, 2006. **6**(10): p. 1369-1372.

CHAPTER 2

BREATH-FIGURE-TEMPLATED ASSEMBLY

The dew-drop carries in its eye
Mountain and forest, sea and sky,
With every change of weather;
(*Dew-drop and diamond* by Robert Graves [1])

Breath figures or dew forms over cold solid or liquid substrates in contact with humid air [2-14]. The growing water drops coalesce with each other, and several generations of drops coexist in a fractal pattern as shown in Figure 2.1. When the breath figures form over a pre-cooled liquid substrate (immiscible with water), they first self-organize into locally ordered state, and then coalescence sets in, giving a pattern with polydisperse drop sizes [9, 10, 14]. Breath figure like patterns of water droplets appear on evaporating polymer solution, exposed to a blast of moist air, and once the solvent evaporation is complete, the water drops evaporate away as well, leaving (under appropriate conditions, discussed later) a highly ordered array of holes in polymer film as illustrated in Figure 2.2 [15].

(a) (b) (c)

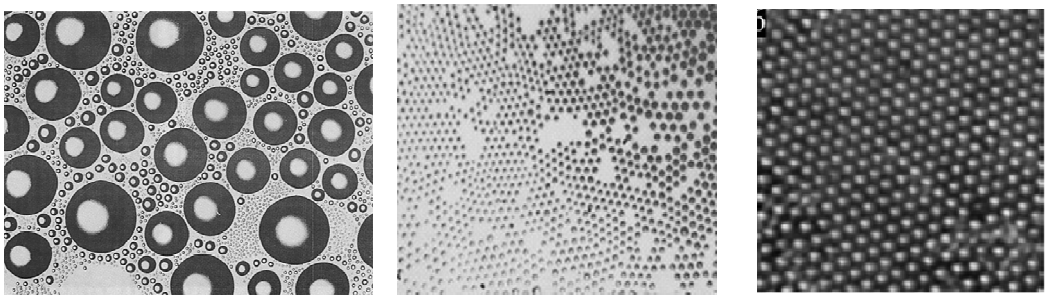

Figure 2.1 (**a**) Breath figure formed over solid substrate [9, 10, 14]. (**b**) Breath figure formed over liquid substrate, showing the intermediate hexatic phase [9, 10, 14]. ; The final pattern over liquid substrate is similar to (a), for eventually drops coalesce (**c**) Water droplets self-assembled over evaporating polymer solution of polystyrene in carbon disulfide [16]. The drops pack without coalescing, and all drops have nearly the same size.

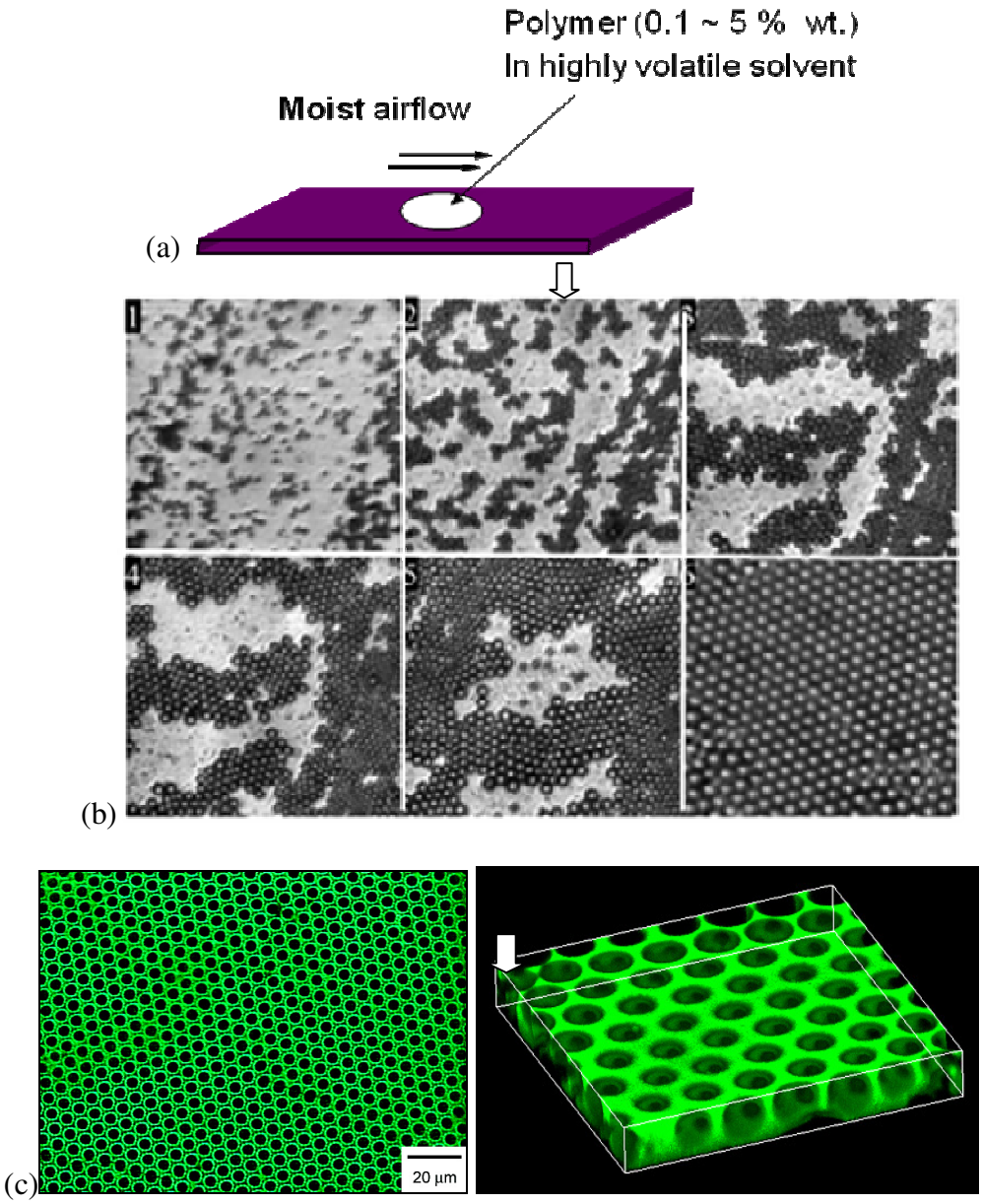

Figure 2.2 (**a**) Moist air flows over a drop or film of polymer solution placed over a glass slide. (**b**) Stages in the growth and assembly of water drops, where growth and assembly from image 1-5 takes place in ~50 s [16]. c) Holey film imaged in reflection mode on an optical microscope, followed by a three-dimensional reconstruction using confocal microscopy. Image is 29.7 × 29.7 × 3.7 μm^3 in dimension [17]. Notice that the pores are interconnected.

To note that the formation of the porous structure is attributable to the presence of water droplets formed by a condensation process is to follow a wealth of evidence that shows noncoalescent water drops grow and assemble over evaporating polymer solutions.

To name the process as breath-figure-templated assembly is to recognize that the nucleation and growth of water drops occur when the evaporation of volatile solvent cools the solution below the critical dew point temperature. Figure 2.2 (b) shows a series of snapshots that reveal how water drops grow and assemble, and Figure 2.2 (c) shows the typical holey film as it appears under the microscope. The confocal image shows that the pores are interconnected. In this chapter, the experimental evidence will be weighed against the mechanisms that have had been proposed to explain the formation of macroporous, 'holey' film from a dilute polymer solution exposed to a blast of moist air. In this thesis, the physical processes involved in every step of breath figure templated assembly are assessed to develop a framework for understanding the mechanism, and for using it to design holey films with desired pore sizes.

2.1 Breath figures: The story of dew formation

Breath-figure-templated-assembly (BFTA) involves condensation of water vapor into droplets of water. The condensation of water vapor into drops underlies the formation of dew, clouds, fog, rain, fogging of car windows, beads of water on a glass of cold beer and of breath figures [18, 19]. In each of these processes, the specific patterns observed and size distributions reached are a result of the interplay between mass and heat transfer associated with the phase transition from the vapor to the liquid phase, as well as on the wetting properties of the substrate. The nucleation and growth of droplets on solid substrates exposed to nearly saturated vapor has been studied extensively in the context of the formation of dew and breath figures [2-14] as well as in developing a greater understanding of chemical vapor deposition [20]. Atmospheric air is a mixture of dry air and water vapor. If the mixture is placed in a closed vessel in contact with liquid

water, the mixture is said to be saturated at a certain temperature if the rate of condensation to the liquid equals the rate of evaporation from it. The partial pressure of water vapor in this case corresponds to the saturation vapor pressure, which is a function of temperature only. On a typical day, the air around us has a partial pressure lower than this saturation vapor pressure, and the relative amount of moisture is expressed as relative humidity.

The condensation of water vapor on cold surfaces – look at a cold, soft drink can, for example – is visible on most days. The supersaturation, in this case, results from the cooling of the vapor within the immediate vicinity of the surface. Likewise, the formation of dew during the night occurs when cold surfaces – petals, leaves, twigs, cobwebs – are brought in contact with air. The temperature at which condensed drops appear on a surface is called the dew point. Ideally, if moist air, with constant mass of water vapor per unit mass of dry air, is cooled isobarically, the dew point temperature will be that unique value when the moist air with specified water vapor content reaches saturation. Practically every cold surface can get covered with water drops. But the temperature at which dew forms or becomes visible also depends upon the nature of surface, and the experimentally determined “dew point” reflects the effect of the wetting behavior of the substrate.

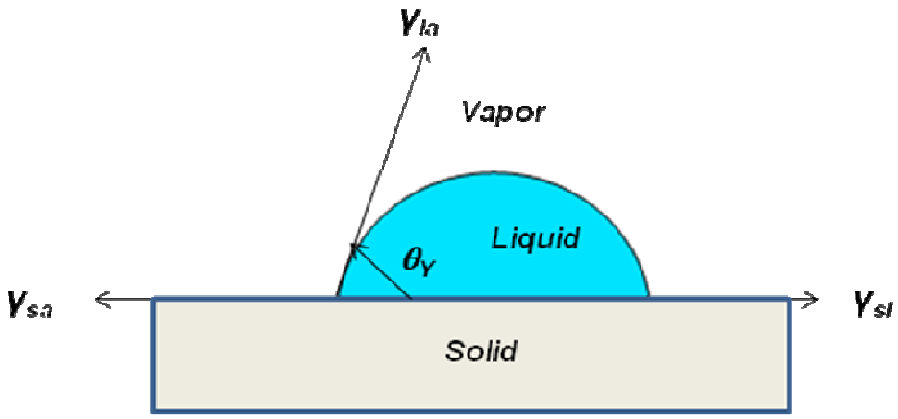

Figure 2.3 A partial wetting drop in contact with a solid substrate, where the contact angle is at the three phase line is dictated by the interfacial energies.

The nature or the choice of surface sets the contact angle at the three phase contact line, as shown schematically in the Figure 2.3. The contact angle, θ_Y given by Young's equation [21-25] as :

$$\cos\theta_Y = \frac{\gamma_{sa} - \gamma_{sl}}{\gamma_{la}} \tag{2.1}$$

where γ_{ij} represents the interfacial energy between phases *i* and *j*, i.e. air, liquid and solid. The contact angle is close to zero for wetting surface, where given an adequate volume of fluid, it just wets the surface completely. The contact angle of π corresponds to the other extreme where drops are nearly spherical, and form vanishingly small contact with the surface [21] (this holds strictly of the small drops where the effect of gravity is small compared to capillary forces). Most surfaces are partially wetting, though by suitable choice of chemical substance and by incorporating roughness or texture, surfaces can be constructed to have contact angles close to π [21, 26, 27]. A lotus leaf is such a surface, and hence, the drops appear as beads that roll off [27, 28]. But even a lotus leaf allows condensation of water on it, and this will be remarked on in more detail in Chapter 7. The main thing to remember is that condensation of vapor as dew or breath figures is

influenced by both the phase transition – involving diffusion of water vapor to droplets and heat of condensation – and the wetting characteristics of the surface.

While dew and breath figures have been observed since antiquity, their scientific study can be traced to early work by Waller in 1846 [19] and by a series of articles by Aitken and Rayleigh in 1911 (and letters back and forth in Nature for next couple of years) [2-4]. Several papers published in the next seventy five years mention breath figures in the context of either looking at purity of surfaces [29, 30] or for generating patterns of randomly distributed drops for studying diffraction [31]. However the first quantitative study of the breath figures, as representative systems of phase transitions involving formation of liquid drops over solid substrates, as dictated by heat and mass transfer and wetting characteristics of the surface, was conducted by Beysens and Knobler in 1986 [5]. These researchers and collaborators have studied breath figure formation over many different solid as well as liquid substrates [10]. Their essential observations are summarized next, to provide the background necessary for understanding the breath-figure-templated assembly.

2.1.1 Heterogeneous nucleation for dew formation

In breath figures, water drops nucleate heterogeneously, grow first by condensation and eventually by coalescence, forming a fractal-like pattern of many generations of drops, with a random packing fraction of 0.55 [5, 10]. As a cold substrate at temperature T_s comes in contact with an air saturated at T_r, where T_s-T_r < 0, heterogeneous nucleation of drops occurs on the surface. For a partially wetting surface, the nucleation rate (number *dn* of drops nucleated in time *dt*) over the surface is

controlled by an activation energy of the droplet of critical size, $F(r_c)$ and a function $\Phi(\theta_Y)$ that depends upon contact angle [14]:

$$\frac{dn}{dt} \sim \exp\left[F(r_c)\Phi(\theta_Y)\right] \tag{2.2}$$

The energy barrier is calculated by noting that the formation of a drop involves the creation of liquid-vapor interface, that incurs a surface energy cost proportional to the surface area and surface tension, γ and volume contribution proportion to ΔE such that energy of a drop [14] is

$$F = -\frac{4\pi r^3}{3}\Delta E + 4\pi r^2 \gamma \tag{2.3}$$

The energy is minimized at the critical radius, $r_c = 2\gamma / \Delta E$. The energy for critical radius, $F(r_c)$ [14], is

$$F(r_c) = \frac{16\pi}{3}\frac{\gamma^3}{\Delta E^2} \tag{2.4}$$

The term that depends upon the contact angle is described [14] as

$$\Phi(\theta_Y) = 2\frac{3 - \cos\theta_Y + \cos^3\theta_Y}{3\sin^3\theta_Y} \tag{2.5}$$

Heterogeneous nucleation occurs at much higher temperatures than homogeneous nucleation, which is the reason why condensed drops appear on cold surfaces. Homogeneous nucleation would occur around 0°C if clean air is saturated at 20°C, but as long as there is a surface, heterogeneous condensation takes place, and it occurs at relatively higher temperatures [32, 33]. The presence of chemical and physical defects enhances the rate of nucleation further [10].

2.1.2 Growth of breath figures

After nucleation, the growth of water drops on a surface depends upon the rate at which moisture is supplied to it and the rate at which heat of condensation is released. The growth of a single droplet over a substrate, with moist air flowing at a rate U parallel to substrate is given by (expression based on ref. [14])

$$r(t) \sim (U^{0.5}\, \upsilon_a^{-1/6} D^{2/3} \Delta e)^{1/3} t^{1/3} \qquad (2.6)$$

Here D is the diffusion coefficient of water vapor, $\Delta e = e_r - e_s$ is the difference between vapor pressure of air and saturation pressure, υ_a, is the kinematic viscosity of air, and the growth law is applicable whenever air flow creates a slim boundary layer over growing drops. Note that the growth law implies that radius grows as cube root of time, and the rate of growth increases with increase in velocity of the air flow. For a population of drops, the coalescence events enhance the growth rate and the scaling of $r(t) \sim t$ is said to exist on a planar substrate [14].

2.1.3 Breath figures over liquid surfaces

When experiments are conducted with liquid substrates the drops are mobile and tend to form rafts with partial ordering prior to coalescence [9, 13, 34]. The surface of a liquid is chemically and physically smooth (up to the capillary length) and hence, the nucleation as well as growth stages are delayed compared with the breath figures on the solid substrate. Further, the growing drops have to drain out the fluid separating them, before coalescence can set in, and the coalescence stage is also delayed for the liquid substrate. The partially ordered drops interact with each other, and reorganize, while trying to form crystal patterns. A combination of coalescence and random nucleation-

growth prevents the drops from forming a two-dimensional crystal, though the hexatic phase exists and has been characterized as fat fractal before [13].

In both these scenarios, breath figures were formed over solid or liquid substrates that were precooled by placing the substrate on a cold stage. In 1996, Limaye et al [35] published a study of breath figures formed on volatile liquids. In their study they used chloroform and benzene and determined that the growth rate observed for benzene was $r \sim t^{1/3}$ whereas in case of chloroform there were two regions of growth: early stage without coalescence with growth rate as $r \sim t^{1/2}$ and at the late stage, $r \sim t$. The maximum size of drops was 10 μm for benzene and the distribution for chloroform was bimodal, with drops that were 11.5 μm and 14.5 μm respectively. According to Limaye et al [35], the larger drops in chloroform are formed by coalescence of two smaller drops. The experimental set-up in Limaye et al [35] involved an atmosphere with constant supersaturation or humidity, though no air flow was mentioned. Curiously, in this first study on breath figures forming on volatile fluids, 5% polystyrene was added to the solvents, and the drops organized into a pattern with up to 70% with six neighbors.

In breath-figure-templated assembly, the breath figures are formed likewise on volatile solutions containing polymers, though the water drops in this case organize into patterns with greater number of drops in ordered state (or six close packed neighbors), and when the solvent and water drops evaporate away, they leave behind an ordered macroporous film, as discussed in the sections that follow.

2.2 Which polymers and solvents form these patterns?

Breath-figure-templated assembly has been shown to work for a wide variety of polymer solvent systems. The solvents used include carbon disulfide (CS_2), chloroform ($CHCl_3$), benzene, toluene, dichloromethane (DCM), tetrahydrofuran (THF), and Freon. These solvent are highly volatile, have low boiling points, have low or limited water miscibility, and are good solvents for the polymers chosen. The range of the polymer-solvent and inorganic particle systems investigated in literature along with the corresponding air flow and humidity conditions used are summarized in Table 1. Intended applications, and pore sizes obtained are also listed for completeness.

Table 2.1 A summary of the studies that have used breath-figure-templated assembly of pores in polymers or inorganic nanoparticles. The table includes the airflow and humidity conditions employed, the results from pore characterization, and the applications suggested in each reference.

Material and Air Flow conditions **Polymer; Mw; concentration** **Solvent** **Humidity/ Temperature/ Airflow speed**	**Comments on morphology and mechanism** **(Intended or proposed) Applications**	**Ref.**
PS-b-PPP 30k-b-7k PS star shaped 1.5 k – 50 k 1; Carbon disulfide Moist air/moist inert gas	Argues that linear PS cannot make holes; Argues for gelation & Phase inversion; Says only CS_2 works Controlled release of drugs; model substrates for surface science	[36]
Poly(p-phenynlene)-b-PS 3k-30k Star PS 0.002; Carbon disulfide	Invokes mechanism of droplet encapsulation by polymer film	[37] [38]
PPQ-b-PS (rod coil) 0.005- 1; Carbon disulfide	Invokes miscelle like assembly of rod-coil polymer Photonics, optoelectronics, insulation	[39]
Five arm star PS, (glucose initiated) 4k, 20k, 33k 10 % in Chloroform RH >80%; 5, 10, 15, 17.5 & 20 ^{o}C	Lower temperature, higher order Statistics on pore sizes Self-organizing membranes	[40]

Table 2.1 contd.

PS 190 k 30 % in CS_2 18-35 % in THF 30% in Acetone/ Cyclohexane Polycarbonate (PC) 60 k 20 % in Chloroform 20; THF Poly(methyl methacrylate) (PMMA) 10% in THF 10% in Acetone 10% in $CHCl_3$ 0.07 ml/min at 25 ^oC	 0.1-.75 µm 0.05-.15 µm 0.3-1 µm 0.1-0.25 µm Few µm Few µm ~0.25 µm ~0.25 µm Electrospun fibers for filtration, sensors and scaffolds	[41]
PMMA 102 k; PS 223k PS-cr-PS 5.7k or PMMA-cr-PMMA 0.5 or 1% in Toluene RH 60% in N_2 flow -cr-: -(crown ether)-	Invoke Marangoni flow; Polymer bag; Drops assemble by capillary forces	[42]
PS_{400}-b-$POTI_{25}$ (Rod coil block copolymer of styrene (PS, 400 monomers) & isoprene with oligothiopene-modified side chains (POTI with 25 monomers)) 0.25 % in Carbon disulfide RH 85%; 3 L/min	0.1wt% : single layer of pores, 1% multiple; d_{pore} increases 1.2 to 4.5 µm with conc. Tunable diffraction gratings and holograms	[43]
Perfluoropolyether thiol-coated (PFPE-SH coated) 5 nm Au nano-crystals in Freon TOP coated InMnAs (Inorganic) in Chloroform RH 60%; 22-23 ^oC; No flow	~0.5 µm Self-organized superlattice of nanocrystals for photonics, catalysis, sensors and separations	[44]
Polyimide (PI) 0.1; Chloroform RH 50-70%	Increase in volume of casting from 20 µL to 5 mL, d_{pore} from 0.5 to 9 µm; Decrease in T from 20 to 4 ^oC, decreases d_{pore} from 5.2 µm to 18 µm; Assemble at contact line by capillary effects; Separation membranes, microreactors, templates for chemical etchings and 2-D photonic crystals	[45]
0.1 % PCL 67k or 0.01% Amphiphilic polymer 22k In Benzene; RH 75%; 20 ^oC; 1.2 L/min	5 µm pores; films stretched to alter pore shapes to elliptical; Shimomura's Cell culture substances	[46]
Cellulose Acetate 2 % in Benzene	With acetone, disordered patterns form Inverse opal structure	[47]

Table 2.1 contd.

Carbohydrate based PS through RAFT (Star, comb, linear) 40 - 220 k 0.3 – 4 % in CS_2 or DCM Humid airflow		0.5 to 4 µm Head group, Mw, conc. and star vs linear differences in pore size		[48]
0.1 % poly(D,L-lactic-co-glycolic acid) (PLGA) in Chloroform RH 75-95%; 5 - 25 ^oC		Disordered pores; decrease substrate T; or increase RH to increases d_{pore}		[49]
1% PS 1970k, 223.2 k or 29.3 k (linear; no polar end group) Toluene; Carbon Disulfide; THF or Chloroform @ RH 45-95% N_2 flow		d_{pore} increases with RH; Square packing of holes seen; PS with Toluene and $CHCl_3$ give ordered, with CS_2, THF disordered films at 60% RH Potential for photonic bandgap and patterned LEDs		[50]
PS 31.6k, 171k, 190k, 560k 35% in THF	RH % 31-38 40-45 50-59 66-72	Mean Pore 85 nm 115 nm 115 nm 135 nm	Electrospun fibers for filtration, protective clothing	[51]
PS 76k +1% CdSe 4 nm particles 7 % in Chloroform RH 80%; N_2 flow at 30^oC		CdSe particles segregate to pores Naoparticles microarrays for sensory, separation or catalysis		[52]
Cellulose Acetate Butyrate (CAB) 11k; PS-COOH 30k or PMMA 26k .001-0.02 % in THF; THF/Water or $CHCl_3$ RH 35-95%		THF/water mixture in low RH gives pores on spin coating at 1100 rpm; Dec RH dec size, No pores below 40% RH for THF; Inc water content, Inc pore size		[53]
P(MMA-co-$(HFPO)_3$MA (Copolymer of methyl methacrylate & a methacylate with a trimeric hexafluoropropyleneoxide substitute) 180k; 0.1 mg/ml in Freon RH ~90%		Used to structure semiconductor surfaces & make Au, Al dichroic filters; Invoke polymer bags; Photonic crystals and dichroic masks.		[54]
PMMA-cr-PMMA 7.2k, 36.7k THF No airflow *PMMA-dibenzo-18 crown-6-PMMA		Pore diameter (d) decreases with polymer conc. $d \sim 518c^{-0.61}$; Argue THF dissolves water, & so it is not breath figure templated assembly.		[55]
Fluorooctyl methacrylatethiol (FOMA-SH) coated Au nanocrystals Freon; RH 70-90%; 24^oC		Nanocrystal superlattice films with ordered arrays of holes; bigger, closed pack holes at higher RH 2-D Waveguides with tunable optical properties		[56]

Table 2.1 contd.

P2VP/PS blends 11k with 11k, 114k, 212k, 582k 4% Toluene; Air flow 0.3-0.8 L/min	Marangoni flow, phase separation hydrodynamics invoked to explain the structures; Increase in air flow, decreases drop size and drop distance & believe increase in air flow, increases temperature difference.	[57]
PMMA-LC based polymer and copolymer DCM; No air flow, 0, 5, 10, 15 ^{o}C	Believe regularity of pores from polymer bags Molecular composites with porosity	[58]
PCL with CAP (10:1) 0.1 – 2.0 % in Toluene, Xylene, Benzene or Chloroform Air flow 0.09-3 L/min	Cast volume and solvent choice influences pore size; larger volume, larger pores; Biointerfaces; Blood cell separations	[59]
Polysulfone 44k, 56k, 75k 0, 0.6 or 1% in Chloroform RH 65%; 85%;	Higher pore size for lower concentration and higher Mw Membranes resistant to acidic and salt solutions	[60]
Dodecanethiol capped 2.1 nm Au nanoparticles 0.5-1.0 % in Toluene RH 60-80%; Air flow 30-70 m/min	By changing velocity and direction of aiflow, get elliptical pores	[61]
PS 280K & Amphiphic copolymer 9:1 ratio 0.5% in Chloroform	Microlens arrays	[62]
5% PS; PC or PMMA in DCM or Chloroform Fast process dip coating; 47 cm/min Air or N_2 flow for drying	Mesoscopic structures with length scale ~50 µm with µm size pores Full dielectric long period gratings	[63]
Poly(acrylic acid)-block-poly(styrene) 0.05-0.1 % in Carbon disulfide RH 75 or 100% bubbled through saturated NaCl or water; Flow rate 5-20 L/min	d_{pore} increases with flow rate; 2.5 µm for 5 L/min and ~5 µm for 20L/min Used as templates for making polyaniline dots	[64]
P2VP/PS blends of 11k with 11k, 114k, 212k, 582k 4 % in THF with RH 10-70%; Air flow 0.2 L/min	Holes form above RH of 30%; Mw and Blend ratio effects; Increasing RH increases size and depth of holes	[65]
SiO_2- grafted-PS with PS with 23.4 k; SiO_2- grafted-PS-b-PMMA 2 mg/ml polymer + 10 mg hybrid nanoparticles; Carbon disulfide; CS2/CHCl3 mixture Ambient, humid conditions	d_{pore} increases from 2-8 µm by changing humdity and airflow (unspecified); Polymer ppt. argument; Isoporous membranes	[66]

Table 2.1 contd.

PS 10 % in THF Chloroform 25^{o}C	1.5-2 µm ***concavity;*** drops were spread on EG and phase separation arguments invoked; Templates to pattern convex – patterned polymer films, TiO_2 microparticles and NaCl nanocrystals	[67]
Polyoxometalate 0.2 mM in Chloroform	1.3 µm holes, with walls of 100 nm; nanophase separation; Semiconducting devices and separation devices	[68]
PS or PC 5 % in DCM or Chloroform (and mixtures) Fast process dip coating; 47 cm/min Air or N_2 flow for drying	Mesoscopic structures with length scale ~50 µm with micron size pores; Attribute assembly to "boiling of solvent"; Invoke capillary forces for bringing vapor bubbles together; Membranes and photonic bandgap structures	[69]
PS 4.8k, 42.5k, 227k, 1000k 2.5, 5.0; DCM/ Chloroform (92:8) Fast process dip coating; IR lamps for drying; RH 30-40% for airflow at 60 deg	d_{pore} increases with increase in molecular weight	[63]
Au nanoparticles end capped with 1-dodecanethiol (Inorganic) Chloroform		[70]
PPQ-b-PMMA (Rod-coil polymer) 1 % in DCM; RH > 60%; Air flow 2 m/s at room temperature	d_{pore} increases with Mr (ratio of Mw of PPQ with PMMA) (No mention of the fact that Mw are different); recourse to precipitate effect Heterojunction devices and picoliter beakers	[71]
PS-b-4T Rod coil & 4T-PS-4T Rod-coil-rod 0.2 – 5 % in Carbon disulfide RH 85%; Flow rate 3.0 L/min	Evoke micelle formation; Show 4T confined to pores. Chemically heterogeneous patterned surfaces	[72]
PS 274 k ; PMMA 103 k 10 in THF /water; Or THF/ethylene Glycol RH 30-40%	d_{pore} increased with water fraction; Decreasing temperature increased d_{pore} Micropatterned surface	[67]

Table 2.1 contd.

PEO-b-PFOMA 10k, 25k, 75k, 140k 0.1% in Freon		[73]
Cycloaliphatic polyurethanes 5 % in Chloroform	Membranes for biomedical application	[74]
Cellulose acetate butyrate 0.015 % in THF/ Chloroform		
Block, Liquid Crystalline, comb polymers, with PS as a component	Credits Rayleigh with observing hexagonal arrays (!!); Polymer bag effect for assembly; Mentions temperature fall to -12 ^{o}C during evaporative cooling	[75]
Poly(TDCM) 20K 1% in THF/ water (9:1)	Propose a mechanism similar to micelle formation, with role of H-bonding sidegroups; Believe amphiphilic required	[76]
Star shaped PDLLA 25k, 36k, 58k 1-10 % in DCM RH 65-90%; Nitrogen flow	Ordered films above 7% wt conc for 58k, RH 76%; d_{pore} increases with viscosity and humidity; thinner walls for lower concentrations Biosensing and biomedical applications	[77]
Poly(vinyl phenol)-block-polystyrene (PVPh-b-PS) THF/Toluene	Micelle formation as intermediate in holey film formation and packing by capillary forces Surface roughness induced water repellency	[78]
Surfactant encapsulated polyoxometalate complexes 1% in Chloroform; Moist airflow	No pores below 30% RH; Argue contact angle >90 required; Microporous films for hybrid materials	[79]
Poly(flourene-arylene) copolymer 3 % in Chloroform; Moist N_2, 2L/min	Pore size difference in side and edges; Microstructured OLEDs	[80]
PS-b-poly(tert-butyl methacylate) or PS-b-PBMA; 2 % in Cyclohexane	Micelle formation mechanism	[81]
PDTG Rod-coil block copolymer Chloroform 48% RH	Capillary mechanism of Shimomura; 1.3 µm pores; multilayers by "conflux"; Enhancement of photocurrent by porous organic thin films	[82]
P2VP/PS + Triton X-100 4 % in Toluene AF: 0.5 L/min	Invoke role of surfactant, phase separation and breath figures, all simultaneously	[83]

Table 2.1 contd.

0.1 g P2VP 159k & 0.1 ml of DIB in 5mL Nitromethane/THF (9:1) DIB content varied from 2-6%	d_{pore} increases with DIB content; Said to be mechanistically different involving formation of DIB drops	[84]
PS, PBA, PBA-b-PS in CS_2 PBA: Poly(butyl acrylates)	Questions polymer bag mechanism	[85]
PS-b-PAA 10mg/mL in THF	d_{pore} increases with RH; Smart stimuli-responsive materials, biosensors and microfluidic devices	[86]
PMMA14.4 k; PS 18 K; PMMA & PS blend 100 mg/mL in THF/Water RH 5-85%, Spin casting at 1000rpm	Pores form in low humidity airflow if Water in THF/Water is >6%; Size increases with Water content	[87]
5g/L PMMA 177.8 k with 0.65 g/L amphiphilic copolymer in chloroform	Nanoparticles deposited into pores;	[88]
20 % Polycarbonate (with 6% PDMS component) in DCM, 24^{o}C, RH 65%	Anamorphic microlens arrays	[89]

PMMA-LC based copolymer: Side-chain liquid crystalline block copolymers containing a poly[6-[4-(4`-methoxyphenyl)phenoxy]hexyl methacrylate] (PMMA-LC) segment and a styrene-co-maleic anhydride segment (alternating structure) made by RAFT (homopolymer was just PMMA-LC);
PCL with CAP: Poly(e-caprolactone) and a copolymer of dodecylacrylamide and w-carbonxyhexylacrylamide (CAP)

The process forms ordered arrays of holes in polymers ranging from linear polymers like polystyrene (PS) [15, 42, 50, 52, 67], poly(methyl methacrylate) (PMMA) [42, 53, 55, 90], polysulfone [60], cellulose acetate butyrate [53] to the polymers with star or comb architectures [36-38, 48, 75]. Further, studies have been carried out for rodlike polymers, amphiphilic and rod-coil block polymers [36-38, 46] as well as polymer blends [57, 59, 62, 65]. The applications that motivated these studies include 2D and 3D photonic materials, membranes for catalysis, separations or tissue engineering, among others, although in most of these papers, the applications were only suggested and not realized in practice. Recently inorganic nanoparticles dispersed in a volatile solvent have also been used to produce porous films that on one hand carry the functionality of

the nanoparticles and on the other hand feature highly organized pores [44, 56, 61]. The physical and chemical properties of the inorganic nanoparticles, combined with their arrangement into well defined pattern or superstructure, is expected to prove useful in catalysis, photonic and electronic applications.

2.3 What are the mechanisms proposed for the formation of holey polymer films from moist airflow over evaporating polymer solutions?

Breath figure templated assembly differs from the experiments and models described for breath figures [2-14], in at least two important aspects: 1) For breath figures or dew formation, the substrate is pre-cooled below the dew-point and 2) Coalescence is the dominant growth mechanism in the late stages of breath figures, limiting the maximum surface coverage to 55% and creating a distribution of drop sizes. *In the breath figure templated assembly over polymer solutions, cooling is evaporation driven, the drops can remain non-coalescent and grow and assemble into a close-packed, highly ordered array of similar size drops* [15]. For the case with one layer of pores, the packing fraction approaches 0.907 [17], which is the theoretical limit for closely packed circles or spheres in two dimensions [91, 92]. The significant difference in growth kinetics and patterns formed necessitates the quantitative analysis of factors underlying droplet growth and assembly over evaporating polymer solutions, and this is the motivation for the research outlined here. Besides the need for quantitative analysis of factors, the hope is to better understand the mechanism. But before proceeding further, the mechanisms that have been postulated and cited by various authors (listed in Table 2.1 for example) are mentioned here only briefly.

Initial studies on the breath figure templated assembly were carried out with star-PS or the diblock PS-PPP (copolymer of polystyrene and poly(p-phenylene) dissolved in carbon disulfide) [36-38], and PS-PPQ (block polymer with polystyrene and poly(phenylquinoline)) [39]. It was claimed that the linear PS does not give ordered array of holes [36, 38]. In the 1994 paper, Widawski et al [36] proposed that the assembly of these pores requires presence of either star-shaped or block copolymer, and droplet assembly is a consequence of phase inversion process, assisted by gelation of PS in carbon disulfide. Phase inversion requires the non-solvent to diffuse into the polymer, and this non-solvent is supposed to be miscible with the solvent it extracts from the polymer. Since water is immiscible with the solvents used, phase inversion is ruled out, which was recognized in the next set of papers by Pitois and Francois [37, 38], who also recognized that gelation does not play a role as originally thought by Widawski et al [36].

Jenekhe and Chen [39] surmised that the pattern formation results from the self-assembly of rod-coil polymers into micelles. For this mechanism to exist, the polymer solution must contain micelles that are few microns in size, which would make the solution appear cloudy! The polymer solutions are typically clear and the micelle formation does not occur. Most of these initial studies used block copolymers and thus envisioned some role for the presence of two distinct, covalently linked polymer chains, and an ability to make spherical micelles in solution. The range of polymer and solvents that have been used since (see Table 2.1) to make holey films using breath-figure-templated assembly bear evidence to the fact that gelation, phase inversion and micelle formation are unlikely candidates for explaining what is observed.

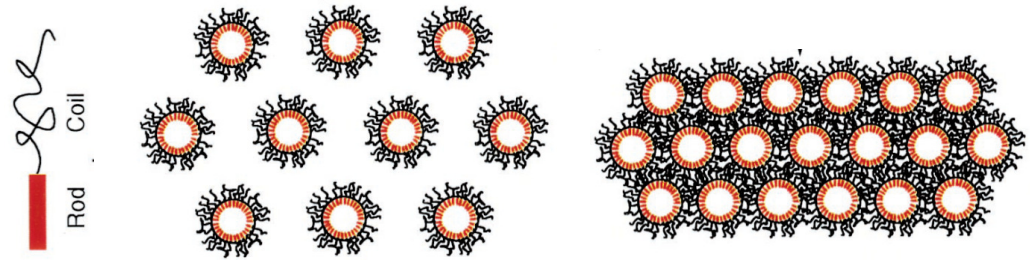

Figure 2.4 Schematic of the hierarchical self-assembly mechanism by Jenekhe and Chen [39]. (**a**) The rod-coil polymers aggregate into micelles (**b**) that eventually pack together (**c**) to form the macroporous polymer films.

While Pitois and Francois [37, 38] recognized that gelation and phase inversion are not required, they envisioned that polymer must precipitate around water drops, to prevent water drop coalescence, as shown in Figure 2.5. Their hypothesis rested on their results that holey films result only from the use of Polystyrene-b-poly(p-phenylene) (PS-PPP) in CS_2 and since linear polystyrene cannot make such precipitates on water drops, they did not form holey films. The subsequent studies have shown the formation happens in linear, non-amphiphilic polymers as well as in polystyrene in carbon disulfide [15]. Further, the arguments of polymer precipitation were made using the following experiment: drops of PS-b-PP/CS_2 solution immersed in water did not coalesce as easily as drops of PS/CS_2 solution. The authors also conducted a pendant drop experiment where the solution drop immersed in water bath was found to form a polymer film, though in this case film forms at around the polymer solution, and not over water drops (thus schematic portrays a scenario with polymer around water drops, while experiment is for polymer around solution drop!). While numerous authors cite these papers [42, 54, 58, 75, 93], they seem to do so without recognizing that the evidence presented is not for water drops immersed in polymer solution, drop sizes used in experiments (~1 mm) are

three orders of magnitude larger, and in spite of the assertion that lack of "precipitation" implies that ordered holey films cannot form for PS/CS_2, the contrary has been observed time and again. In fact, as pointed out earlier, in the study by Limaye et al [35] on breath figures on volatile liquids, the assertions about water drops forming ordered arrays was already present, though these authors did not report the formation of holey films, they seem to have observed the imprints of water on polystyrene that was dissolved in benzene and chloroform. Pitois and Francois [37, 38] do not cite this paper or comment about it, implying that their conclusions could have been otherwise, had they known how regular the patterns observed were. The polymer bag or precipitation argument could have been nipped in the bud!

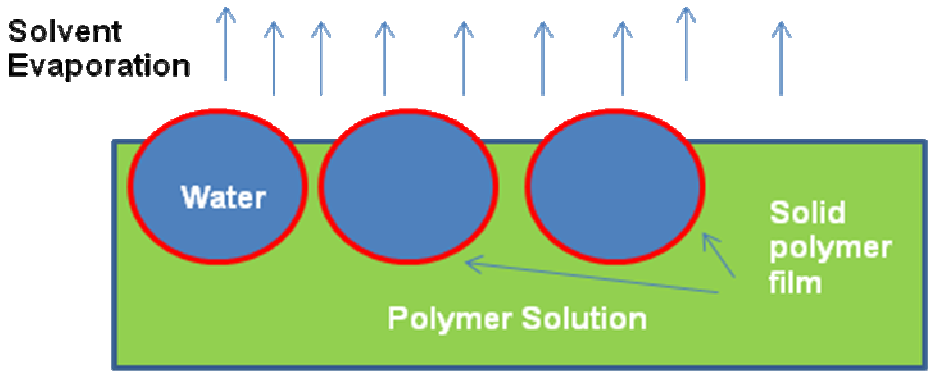

Figure 2.5 Polymer precipitation mechanism advanced by Pitois and Francois [37, 38]. A solid polymer film is postulated to precipitate at the water/organic solvent interface.

As early as 2000, a paper by Karthaus et al [94] presented further experimental evidence that water drops can form a hexagonally ordered assembly on pure chloroform, implying that the presence of polymer precipitation is unnecessary for the assembly (though without the polymer, coalescence eventually sets in, as was noted for breath figures on precooled, nonvolatile liquids earlier). One of the coauthors of this paper,

Shimomura [95, 96], has published dozens of articles that propagate another mechanism, based on evaporation induced convective assembly, derived from studies of colloidal crystallization. In this mechanism, condensed water drops migrate to the contact line, and assemble there due to capillary immersion forces. Experimental observations of growing drops by Karthaus et al [94], Limaye et al [35], Pitois and Francois [37, 38] and on breath figures over liquids [9, 10, 14] into rafts contradicted this mechanism based on assembly at contact line (see Figure 2.6, based on [96]) when it was first made, and observations thereafter show that assembly of drops does not occur only at the edge, and pores formed at the center of the substrate typically have higher order.

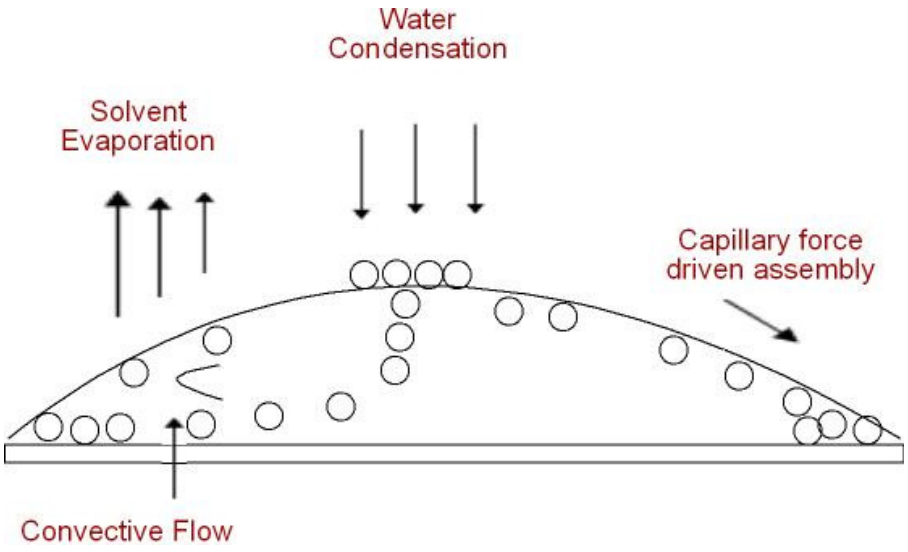

Figure 2.6 Capillary force driven assembly at contact line, (Shimomura and coworkers [95, 96]).

The wealth of evidence imparted by just looking at polymers and solvents for which the process works allows these conclusions: 1) Breath-figure-templated assembly does not require presence of amphiphilic components for non-coalescence. 2) Polymer precipitation mechanism or polymer bag mechanism is as unlikely explanation of observations, as is micelle formation, phase inversion or gelation. 3) BFTA involves

stages similar to formation of breath figures over liquids [9, 10, 14]: delayed droplet coalescence and local hexagonal assembly (hexatic phase) were both studied in those systems.

The assertion that water drops forming hexagonal arrays on evaporating polymer solutions is akin to breath figure formation was made first in the paper by Srinivasarao and coworkers [15]. The authors proposed that the water droplets form due to condensation over the evaporatively cooled substrate, and as long as the solvent is sufficiently volatile and water insoluble, the formation of droplets and resulting pores in films is generic for any polymer solution exposed to moist air, see Figure 2.7. Evaporative cooling drives the nucleation and growth of water droplets. In analogy to Limaye et al [35], the authors postulated that the evaporative cooling induces convection currents within the sample, which in conjunction with the airflow across the surface, drive ordering of the water droplets [15]. The non-coalescence of water drops in PS/CS_2 systems was attributed to the temperature gradients present in the system, which could produce thermocapillary convection, keeping droplets apart by replenishing the fluid layer that needs to be drained for drops to come together. An alternative hypothesis was also proposed that evaporation flux is able to maintain droplets apart by providing a non-vanishing, replenished vapor layer between them [15]. The schematic for the postulated mechanism is shown below.

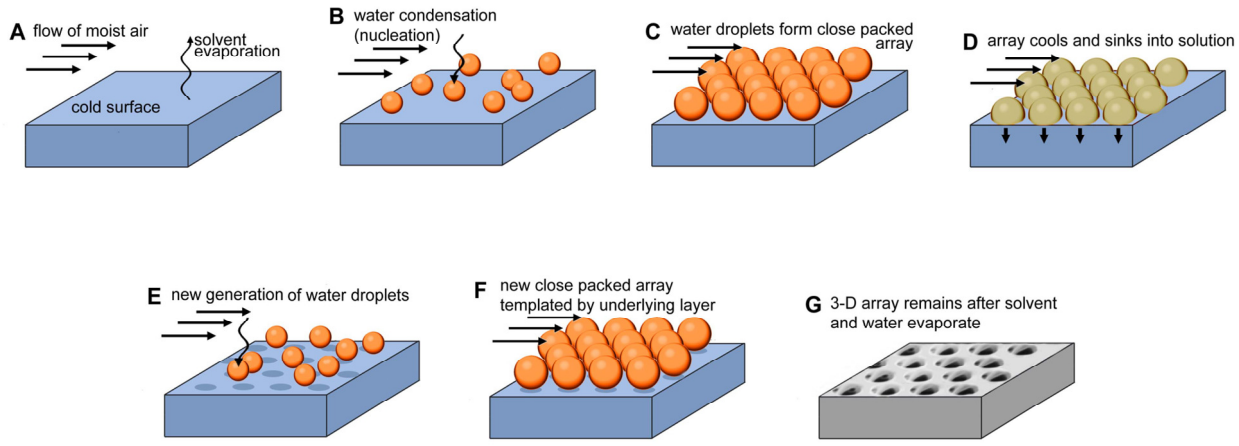

Figure 2.7 Mechanism for breath-figure-templated assembly suggested by Srinivasarao et al [15].

The diverse range of polymers and solvents listed in Table 1 shows that BFTA can be carried out in a simple and universal manner. The list of researchers who repeat the phase inversion, convective assembly driven by capillary effects, gelation, polymer bag effect, micelle formation arguments might be long, but the series of counter-examples provided by experiments and researchers themselves imply that these postulates are not valid.

At the same time, it is important to develop a theoretical framework to critically assess the value of various explanations and hopefully that will clear out the fog of ideas that has engulfed this research area. Most applications require us to have a certain pore size, and hence it is necessary for us to know how to control the experimental conditions to achieve these. This requires a thorough understanding of mechanistic aspects of this pattern formation. The formation of pores is coupled to the questions about what dictates droplet nucleation and growth. The growth occurs under the moist air flow over an evaporatively cooled solution substrate, implying that the knowledge of the extent and rate of cooling itself is required. The next five chapters are dedicated to aspects related to

the 1) evaporative cooling, 2) nucleation and growth, 3) noncoalescence, 4) assembly and 5) drying of water and pore formation in the context of breath-figure-templated assembly. Each of these chapters will form an important episode in the exploration of answers to questions listed next.

2.4 Questions that motivated the study of mechanistic aspects of breath-figure-templated assembly

The thesis was motivated by a number of questions that need to be answered with respect to breath-figure-templated assembly, such as:

- What is effect of changing air speed and humidity on the pore size?
- What is the lowest humidity at which these structures can form?
- What is the role of solvent?
- What is the reason for non-coalescence of water droplets when they assemble on or above the evaporating polymer solutions?
- Is the presence of amphiphilic polymer, surfactant or hydrophilic group necessary for getting an ordered assembly of pores?
- Is the architecture or molecular weight of the polymer important?
- Why are the drops and pores nearly monodisperse in size?
- What is the minimum and maximum size of pores that can be reached using this method?
- Where, how and why do the drops nucleate?
- When are the pores formed?
- What causes the drop assembly?

2.5 References

1. Graves, R., *The Complete Poems*. 2003, London: Penguin Books Ltd.

2. Rayleigh, *Breath figures.* Nature, 1911. **86**: p. 416-418.

3. Aitkens, J., *Breath Figures.* Nature, 1911. **86**: p. 516-517.

4. Rayleigh, *Breath figures.* Nature, 1912. **90**: p. 436-438.

5. Beysens, D. and C.M. Knobler, *Growth of breath figures.* Physical Review Letters, 1986. **57**(12): p. 1433-1436.

6. Briscoe, B.J. and K.P. Galvin, *Breath figures.* Journal of Physics D-Applied Physics, 1990. **23**(9): p. 1265-1266.

7. Briscoe, B.J. and K.P. Galvin, *The evolution of a 2D-constrained growth system of droplets - breath figures.* Journal of Physics D-Applied Physics, 1990. **23**(4): p. 422-428.

8. Steyer, A., et al., *Growth of droplets on a one dimensional surface - experiments and simulation.* Europhysics Letters, 1990. **12**(3): p. 211-215.

9. Steyer, A., et al., *Two-dimensional ordering during droplet growth on a liquid surface.* Physical Review B, 1990. **42**(1): p. 1086-1089.

10. Beysens, D., et al., *How does dew form.* Phase Transitions, 1991. **31**(1-4): p. 219-246.

11. Fritter, D., C.M. Knobler, and D.A. Beysens, *Experiments and simulation of the growth of droplets on a surface (breath figures).* Physical Review A, 1991. **43**(6): p. 2858-2869.

12. Beysens, D. and C.M. Knobler, *Dew Formation.* Recherche, 1992. **23**(245): p. 808-817.

13. Steyer, A., P. Guenoun, and D. Beysens, *Hexatic and fat fractal structures for water droplets condensing on oil.* Physical Review E, 1993. **48**(1): p. 428-431.

14. Beysens, D., *The formation of dew.* Atmospheric Research, 1995. **39**(1-3): p. 215-237.

15. Srinivasarao, M., et al., *Three-dimensionally ordered array of air bubbles in a polymer film.* Science, 2001. **292**(5514): p. 79-83.

16. Barrow, M.S., et al., *Physical characterisation of microporous and nanoporous polymer films by atomic force microscopy, scanning electron microscopy and*

high speed video microphotography. Spectroscopy-an International Journal, 2004. **18**(4): p. 577-585.

17. Song, L., *Study of ordered macroporous polymer films by templating breath figures*, in *School of Polymer, Textile and Fiber Engineering*. 2005, Georgia Institute of Technology: Atlanta. p. 193.

18. Bohren, C.F., *Clouds in a Glass of Beer: Simple Experiments in Atmospheric Physics*. 2001: Dover Publications.

19. Middleton, W.E.K., *History of the Theories of Rain and Other Forms of Precipitation*. 1966, New York: Franklin Watts, Inc.

20. Meakin, P., *Droplet deposition growth and coalescence.* Reports on Progress in Physics, 1992. **55**(2): p. 157-240.

21. de Gennes, P.G., F. Brochard, and D. Quere, *Capillarity and Wetting Phenomena: drops, bubbles, pearls, waves*. 2004, New York: Springer-Verlag.

22. Kralchevsky, P.A. and K. Nagayama, *Particles at fluid interfaces and membranes*. Studies in interface science, ed. D. Mobius and R. Miller. 2001, Amsterdam: Elsevier Science B. V.

23. Starov, V.M., M.G. Velarde, and C.J. Radke, *Wetting and Spreading Dynamics*. Surfactant Science Series, ed. A.T. Hubbard. 2007, Boca Raton: Taylor & Francis Group, LLC.

24. Rowlinson, J.S., *Cohesion: A Scientific History of Intermolecular Forces*. 2002, Cambridge: Cambridge University Press.

25. Rowlinson, J.S. and B. Widom, *Molecular Theory of Capillarity*. 2003: Dover Publications.

26. Herminghaus, S., M. Brinkmann, and R. Seemann, *Wetting and Dewetting of Complex Surface Geometries.* Annual Review of Materials Research, 2008. **38**: p. 101-121.

27. Quere, D., *Wetting and Roughness.* Annual Review of Materials Research, 2008. **38**: p. 71-99.

28. Barthlott, W. and C. Neinhuis, *Purity of the sacred lotus, or escape from contamination in biological surfaces.* Planta, 1997. **202**(1): p. 1-8.

29. Baker, T.J., *Breath figures.* Philosophical Magazine, 1922. **44**(262): p. 752-765.

30. Spurr, R.T. and J.G. Butlin, *Breath figures.* Nature, 1957. **179**(4571): p. 1187-1187.

31. Sommerfeld, A., *Optics: Lectures on Theoretical Physics, Volume 4*. 1954, New York: Academic Press.

32. Rogers, R.R. and M.K. Yau, *Short Course in Cloud Physics, Third Edition*. 3 ed. 1989: Butterworth-Heinemann.

33. Pruppacher, H.R. and J.D. Klett, *Microphysics of Clouds and Precipitation*. 2nd ed. 1996: Springer.

34. Knobler, C.M. and D. Beysens, *Growth of breath figures on fluid surfaces.* Europhysics Letters, 1988. **6**(8): p. 707-712.

35. Limaye, A.V., et al., *Evidence for convective effects in breath figure formation on volatile fluid surfaces.* Physical Review Letters, 1996. **76**(20): p. 3762-3765.

36. Widawski, G., M. Rawiso, and B. Francois, *Self-organized honeycomb morphology of star-polymer polystyrene films.* Nature, 1994. **369**(6479): p. 387-389.

37. Pitois, O. and B. Francois, *Crystallization of condensation droplets on a liquid surface.* Colloid and Polymer Science, 1999. **277**(6): p. 574-578.

38. Pitois, O. and B. Francois, *Formation of ordered micro-porous membranes.* European Physical Journal B, 1999. **8**(2): p. 225-231.

39. Jenekhe, S.A. and X.L. Chen, *Self-assembly of ordered microporous materials from rod-coil block copolymers.* Science, 1999. **283**(5400): p. 372-375.

40. Angus, S.D. and T.P. Davis, *Polymer surface design and infomatics: Facile microscopy/image analysis techniques for self-organizing microporous polymer film characterization.* Langmuir, 2002. **18**(24): p. 9547-9553.

41. Megelski, S., et al., *Micro- and nanostructured surface morphology on electrospun polymer fibers.* Macromolecules, 2002. **35**(22): p. 8456-8466.

42. Peng, J., et al., *Formation of regular hole pattern in polymer films.* Macromolecular Chemistry and Physics, 2003. **204**(1): p. 125-130.

43. Hayakawa, T. and S. Horiuchi, *From angstroms to micrometers: Self-organized hierarchical structure within a polymer film.* Angewandte Chemie-International Edition, 2003. **42**(20): p. 2285-2289.

44. Shah, P.S., et al., *Single-step self-organization of ordered macroporous nanocrystal thin films.* Advanced Materials, 2003. **15**(12): p. 971-+.

45. Yabu, H., et al., *Preparation of honeycomb-patterned polyimide films by self-organization.* Langmuir, 2003. **19**(15): p. 6297-6300.

46. Nishikawa, T., et al., *Micropatterns based on deformation of a viscoelastic honeycomb mesh.* Langmuir, 2003. **19**(15): p. 6193-6201.

47. Cai, M.M., et al., *Synthesis of inverse opal polymer films.* Journal of Materials Science Letters, 2003. **22**(18): p. 1295-1297.

48. Stenzel, M.H., T.P. Davis, and A.G. Fane, *Honeycomb structured porous films prepared from carbohydrate based polymers synthesized via the RAFT process.* Journal of Materials Chemistry, 2003. **13**(9): p. 2090-2097.

49. Zhao, X.Y., et al., *Formation of ordered microporous films with water as templates from poly(D,L-lactic-co-glycolic acid) solution.* Journal of Applied Polymer Science, 2003. **90**(7): p. 1846-1850.

50. Peng, J., et al., *The influencing factors on the macroporous formation in polymer films by water droplet templating.* Polymer, 2004. **45**(2): p. 447-452.

51. Casper, C.L., et al., *Controlling surface morphology of electrospun polystyrene fibers: Effect of humidity and molecular weight in the electrospinning process.* Macromolecules, 2004. **37**(2): p. 573-578.

52. Boker, A., et al., *Hierarchical nanoparticle assemblies formed by decorating breath figures.* Nature Materials, 2004. **3**(5): p. 302-306.

53. Park, M.S. and J.K. Kim, *Breath figure patterns prepared by spin coating in a dry environment.* Langmuir, 2004. **20**(13): p. 5347-5352.

54. Haupt, M., et al., *Breath figures: Self-organizing masks for the fabrication of photonic crystals and dichroic filters.* Journal of Applied Physics, 2004. **96**(6): p. 3065-3069.

55. Fu, J., et al., *Ordered macroporous films from self-assembly of two-armed polymer with a crown ether core.* Polymer, 2004. **45**(22): p. 7389-7394.

56. Saunders, A.E., et al., *Inverse opal nanocrystal superlattice films.* Nano Letters, 2004. **4**(10): p. 1943-1948.

57. Cui, L., et al., *Tunable ordered droplets induced by convection in phase-separating P2VP/PS blend film.* Polymer, 2004. **45**(24): p. 8139-8146.

58. Hao, X.J., et al., *Molecular composite materials formed from block copolymers containing a side-chain liquid crystalline segment and an amorphous styrene/maleic anhydride segment.* Polymer, 2004. **45**(22): p. 7401-7415.

59. Tanaka, M., et al., *Design of novel biointerfaces (II). Fabrication of self-organized porous polymer film with highly uniform pores.* Bio-Medical Materials and Engineering, 2004. **14**(4): p. 439-446.

60. Xu, Y., B.K. Zhu, and Y.Y. Xu, *A study on formation of regular honeycomb pattern in polysulfone film.* Polymer, 2005. **46**(3): p. 713-717.

61. Li, J., et al., *Ordered honeycomb-structured gold nanoparticle films with changeable pore morphology: From circle to ellipse.* Langmuir, 2005. **21**(5): p. 2017-2021.

62. Yabu, H. and M. Shimomura, *Simple fabrication of micro lens arrays.* Langmuir, 2005. **21**(5): p. 1709-1711.

63. Bormashenko, E., et al., *Formation of honeycomb patterns in evaporated polymer solutions: Influence of the molecular weight.* Materials Letters, 2005. **59**(28): p. 3553-3557.

64. Maeda, Y., Y. Shimoi, and K. Ogino, *Fabrication of microporous films utilizing amphiphilic block copolymers and their use as templates in poly(aniline) preparation.* Polymer Bulletin, 2005. **53**(5-6): p. 315-321.

65. Cui, L., et al., *Ordered porous polymer films via phase separation in humidity environment.* Polymer, 2005. **46**(14): p. 5334-5340.

66. Nystrom, D., et al., *Highly-ordered hybrid organic-inorganic isoporous membranes from polymer modified nanoparticles.* Macromolecular Rapid Communications, 2005. **26**(7): p. 524-528.

67. Wang, Y., et al., *Phase-separation-induced micropatterned polymer surfaces and their applications.* Advanced Functional Materials, 2005. **15**(4): p. 655-663.

68. Bu, W.F., et al., *Polyxometalate-based vesicle and its honeycomb architectures on solid surfaces.* Journal of the American Chemical Society, 2005. **127**(22): p. 8016-8017.

69. Bormashenko, E., et al., *Mesoscopic and submicroscopic patterning in thin polymer films: Impact of the solvent.* Materials Letters, 2005. **59**(19-20): p. 2461-2464.

70. Cai, X.M., et al., *Porous metallic films fabricated by self-assembly of gold nanoparticles.* Thin Solid Films, 2005. **491**(1-2): p. 66-70.

71. Lin, C.L., P.H. Tung, and F.C. Chang, *Synthesis of rod-coil diblock copolymers by ATRP and their honeycomb morphologies formed by the 'breath figures' method.* Polymer, 2005. **46**(22): p. 9304-9313.

72. Hayakawa, T. and H. Yokoyama, *Fabrication of self-organized chemically and topologically heterogeneous patterns on the surface of polystyrene-b-oligothiophene block copolymer films.* Langmuir, 2005. **21**(23): p. 10288-10291.

73. Saunders, A.E., et al., *Breath figure templated self-assembly of porous diblock copolymer films.* Physical Review E, 2006. **73**(3).

74. Deepa, P. and M. Jayakannan, *Microporous polyurethanes: Synthesis and investigation of the mechanism of the pore formation.* Journal of Polymer Science Part B-Polymer Physics, 2006. **44**(9): p. 1296-1308.

75. Stenzel, M.H., C. Barner-Kowollik, and T.P. Davis, *Formation of honeycomb-structured, porous films via breath figures with different polymer architectures.* Journal of Polymer Science Part a-Polymer Chemistry, 2006. **44**(8): p. 2363-2375.

76. Deepak, V.D. and S.K. Asha, *Self-organization-induced three-dimensional honeycomb pattern in structure-controlled bulky methacrylate polymers: Synthesis, morphology, and mechanism of pore formation.* Journal of Physical Chemistry B, 2006. **110**(43): p. 21450-21459.

77. Karikari, A.S., et al., *Porous thin films based on photo-cross-linked star-shaped poly(D, L-lactide)s.* Langmuir, 2006. **22**(23): p. 9687-9693.

78. Tung, P.H., et al., *Regular honeycomb porous polymer films based on amphiphilic block copolymer.* Desalination, 2006. **200**(1-3): p. 55-57.

79. Sun, H., et al., *Self-organized microporous structures based on surfactant-encapsulated polyoxometalate complexes.* Journal of Physical Chemistry B, 2006. **110**(49): p. 24847-24854.

80. Pintani, M., et al., *Breath figure pattern formation as a means to fabricate micro-structured organic light-emitting diodes.* Journal of Physics-Condensed Matter, 2007. **19**(1).

81. Ishizu, K., Y. Tokuno, and M. Makino, *Microporous films from diblock copolymer micelles based on solvent-induced mechanism by temperature control of casting solution.* Macromolecules, 2007. **40**(3): p. 763-765.

82. Heng, L.P., et al., *Enhancement of photocurrent generation by honeycomb structures in organic thin films.* Chemphyschem, 2006. **7**(12): p. 2520-2525.

83. Cui, L., B.Y. Li, and Y.C. Han, *Transformation from ordered islands to holes in phase-separating P2VP/PS blend films by adding triton X-100.* Langmuir, 2007. **23**(6): p. 3349-3354.

84. Orlov, M., et al., *pH-Responsive thin film membranes from poly(2-vinylpyridine): Water vapor-induced formation of a microporous structure.* Macromolecules, 2007. **40**(6): p. 2086-2091.

85. Ghannam, L., et al., *A versatile route to functional biomimetic coatings: ionomers for honeycomb-like structures.* Soft Matter, 2007. **3**(12): p. 1492-1499.

86. Wang, C.Y., et al., *Fabrication of highly ordered microporous thin films by PS-b-PAA self-assembly and investigation of their tunable surface properties.* Journal of Materials Chemistry, 2008. **18**(6): p. 683-690.

87. Madej, W., et al., *Breath figures in polymer and polymer blend films spin-coated in dry and humid ambience.* Langmuir, 2008. **24**: p. 3517-3524.

88. Tamaki, K., S. Matsushita, and M. Shimomura, *Fabrication of polymeric particles composed of two-dimensionally self-assembled nanoparticles by use of a microporous film as a template.* Colloids and Surfaces a-Physicochemical and Engineering Aspects, 2008. **313**: p. 630-635.

89. Chari, K., C.W. Lander, and R.J. Sudol, *Anamorphic microlens arrays based on breath-figure template with adaptive surface reconstruction.* Applied Physics Letters, 2008. **92**(11).

90. Wang, Y., et al., *Micropatterned polymer surfaces enduced by nonsolvent.* Langmuir, 2006. **22**(4): p. 1928-1931.

91. Aste, T., *Circle, sphere, and drop packings.* Physical Review E, 1996. **53**(3): p. 2571-2579.

92. Aste, T. and D.L. Weaire, *The Pursuit of Perfect Packing*. 2000, London: Institute of Physics Publishing.

93. Bunz, U.H.F., *Breath figures as a dynamic templating method for polymers and nanomaterials.* Advanced Materials, 2006. **18**(8): p. 973-989.

94. Karthaus, O., et al., *Water-assisted formation of micrometer-size honeycomb patterns of polymers.* Langmuir, 2000. **16**(15): p. 6071-6076.

95. Shimomura, M. and T. Sawadaishi, *Bottom-up strategy of materials fabrication: a new trend in nanotechnology of soft materials.* Current Opinion in Colloid & Interface Science, 2001. **6**(1): p. 11-16.

96. Maruyama, N., et al., *Mesoscopic patterns of molecular aggregates on solid substrates.* Thin Solid Films, 1998. **329**: p. 854-856.

CHAPTER 3

EVAPORATIVE COOLING

The answer, my friend, is blowin' in the wind.
Bob Dylan [1]

The essential processes known to be involved in breath-figure-templated assembly of holes in polymer films can be summarized in two sentences. A blast of moist air over a dilute solution of polymer in a volatile solvent results in condensation and growth of non-coalescent water droplets that self assemble into a close packed structure. Following complete evaporation of the solvent, the water droplets evaporate, leaving an imprinted array of 0.3–10 μm holes in the polymer film. [2-7] The process is completed in a few minutes and results in the creation of a highly ordered mesoporous structure. The templating process has been successfully applied to a wide variety of polymers (coil-like, rod-coil, star-shaped) and solvents (chloroform, toluene, carbon disulfide, dichloromethane, benzene, THF) to create the holey films for applications such as non-wetting or superhydrophobic surfaces, picoliter beakers, microlenses, substrates for cell growth and photovoltaics, among others as was summarized in Chapter 2. Since applications require microporous films with well-defined structure, the understanding of how the pore size depends upon the parameters like humidity, air temperature and velocity as well as the choice of solvent and polymer is essential for widespread use of the process.

Despite a general consensus that the fabrication process is simple to perform, [2-10] models capable of quantitatively predicting final structure in terms of these aforementioned variables are not yet available, partially due to the complex interplay of

several physical processes [2]. However it is clear that both heat and mass transfer are predominantly influenced by the choice of solvent. It is therefore useful in the first instance to examine the correlation between solvent properties and the final product structure. The problem has been cited to be very complex [2, 4, 7], not only because it requires an understanding of mass and heat changes taking place during solvent evaporation, but possibly because it also involves convection within the polymer solution substrate. The temperature and/or concentration -gradient-induced phenomena of Rayleigh–Bernard and/or Maragoni-Bernard convention [2, 11-13] could become important during solvent evaporation. In this chapter, a model for computing the concentration and temperature changes occurring in breath-figure-templating is described, capturing the experimentally observed behavior for PS/CS_2 system. The present study is a crucial step in elucidating the role of parameters in the breath-figure templated assembly of holes in polymer films.

The rate of solvent evaporation and the associated concentration and temperature dependent properties of a polymer solution affect the morphology obtained in a range of other systems. Examples include functional adhesives, porous membranes and anti-reflection coatings [14, 15], fibers spun from solution (for example in electrospinning [16, 17]), spin casting [18, 19] and in our case, the breath-figure templating of microporous polymer films [2-10]. Changes in concentration and temperature influence the kinetics and dynamics of phase transitions, and are of importance in processes such as the casting of immiscible polymer blends and block copolymers [20] and in the electrospinning of solutions near critical behavior.

The templating mechanism for the formation of microporous films in our case is driven by the evaporation of a high volatility solvent (aided by a flow of moist air over the solution). Evaporative cooling drives the nucleation and growth of water droplets. It has been suggested by Limaye et al [11] and Srinivasarao et al [2] that evaporative cooling induces convection currents within the solution which in conjunction with the airflow across the surface drive ordering of the water droplets. The non-coalescence of water drops has been attributed to several factors (micelle formation, thermocapillary flows, polymer bags, described in Chapter 2) although the dominant mechanism is currently being studied. Srinivasarao et al [2] suggested that the temperature gradient present in the system may produce thermocapillary convection such that the droplets are kept apart by replenishing the fluid (air) layer that needs to be drained for drops to come together [21]. An alternative hypothesis is that evaporation flux may be providing a non-vanishing, replenished vapor layer to keep drops from coalescing [2]. Both the rate at which vapor flux is generated and how the temperature above the solution changes as a function of time are derived in this chapter, while their role in non-coalescence and self-assembly will be described in detail in Chapter 5. The nucleation and growth of droplets on solid substrates has been studied extensively in the context of the formation of dew and breath figures [22-26], where condensation occurs over a precooled substrate when moist air passes over it. To correlate the growth over polymer solutions to breath figure laws also requires elucidation of the evaporation driven cooling. In the following sections, the mass transfer and heat transfer associated with evaporation of solvent from the polymer solution is modeled and compared to experiments.

3.1 What influences the rate of mass loss during solvent evaporation?

A thin film of polymer solution, with polymer content C, ($C < 5\%$) is deposited on a solid substrate. The film is initially at the ambient temperature, T. Let us assume that the solution is spread into a rectangular block of area, S, initial height, h_o and initial volume V_o. The presence of the polymer retains the boundary of the film, thus maintaining the area of film constant, while the volume of the fluid decreases with time. A flow of humidified air, with velocity v_∞ and kinematic viscosity, υ_a is considered to move in a direction x such that a laminar boundary layer is formed close to the surface of polymer solution according to the Reynolds number condition ($Re \sim v_\infty x/\upsilon_a > 10^5$) for boundary layer flow which presently corresponds to velocities, $v_\infty \sim 1$ m/s (typical velocities from experiments).

Using the classic boundary layer approach [27, 28] and assuming a steady state exchange, it is possible to calculate the temperature, solvent mole fraction, and velocity profiles in the boundary layer for a given temperature and concentration of polymer at the solution surface. A steady state approach provides useful information about the volume fraction and temperature gradients in the boundary layer [27, 28], (the latter being required to model thermocapillary flow and its potential to suppress coalescence). However, in the process involved in breath figure templated assembly, both the temperature and concentration at the surface evolve with time, thereby necessitating the use of an unsteady-state evaporation model.

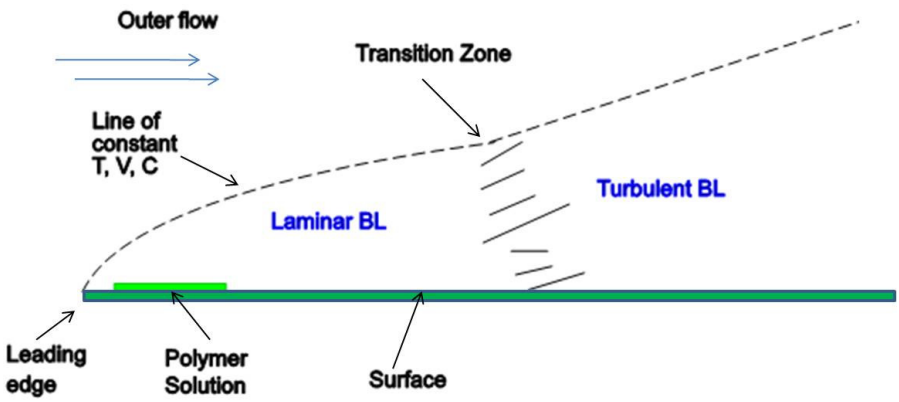

Figure 3.1 Boundary layer flow over a polymer solution substrate, showing regions of laminar and turbulent boundary layer, as well as region outside boundary layer region that has temperature, concentration and velocities as dictated by the air flow.

Let us consider the evaporative mass loss problem, by proposing that the liquid solvent diffuses through the polymer solution to arrive at the surface, where it is removed by the blast of moist air. The problem is therefore considered to be predominantly diffusion limited and may be conveniently described by Fick's law, such that the diffusion process within the polymer solution is represented by [29, 30],

$$D_L \frac{\partial^2 C_L}{\partial z^2} = \frac{\partial C_L}{\partial t} \tag{3.1}$$

D_L is the diffusion coefficient of the solvent, and C_L is the concentration of the solvent at position z in the film. At the bottom surface of the film, z =0, no solvent loss takes place through the supporting substrate and hence the boundary condition at this surface,

$$\frac{\partial C_L}{\partial z} = 0 \;\; at \;\; z = 0 \;\; \forall t \tag{3.2}$$

As the sample is sufficiently thin, mass loss is considered to occur only at the top surface due to the negligible area for mass transfer presented by the sample edges. At the

top surface, $z = l$, the solvent is considered to be continuously removed by mass transfer to the air flow, and hence the appropriate boundary condition [29, 30] is

$$\frac{\partial C_L}{\partial z} = \frac{k_{MT}}{D_L K}(C_L^* - C_L) \; at \; z = l, \; t > 0 \tag{3.3}$$

K is the equilibrium distribution coefficient and $C_L^* = KC_{L\infty}$. In effect, we use the Henry law, and the term $KC_{L\infty}$ is replaced by the concentration inside the film substrate in equilibrium with the bulk concentration in vapor [29, 30]. The mass transfer coefficient, k_{MT}, for the transfer of component A into the free stream of B is defined in terms of the diffusion at the interface as

$$k_{MT} = -\frac{D_L(\partial C_L/\partial z)|_{z=0}}{C_{L1} - C_{L\infty}} \tag{3.4}$$

For laminar flow, the mass transfer coefficient can be estimated from the Sherwood number, $Sh_{LAMINAR} = k_c l/D_L = 0.664\,\mathrm{Re}^{1/2}\,Sc^{1/3}$, where $Sc = \nu/D$ [30], is the Schmidt number and where Re (~ 1000) and Sc (= 1.2) correspond to measures with respect to air diffusivity, viscosity and velocity. The mass transfer coefficient for the turbulent flow has a different correlation [30].

The diffusion equation, with aforementioned boundary and initial conditions has a solution of the form [29],

$$\frac{M_t}{M_0} = \sum \frac{2\alpha^2}{(\beta_i^2 + \alpha^2 + \alpha)} \exp\left(-\frac{\beta_i^2 D_L t}{l^2}\right)$$

(3.5)where β_n values are roots of $\beta_i \tan\beta_i = \alpha = k_{MT} l/KD_L$ [29, 30] and M_t/M_0 denotes the mass of the polymer solution relative to the initial mass as a function of time. The transient depletion of solvent calculated above depends upon the velocity of air flow

and solvent properties, for these determine the values of mass transfer coefficient and hence that of coefficients α and β. The rate of solvent loss is mainly limited by the diffusion coefficient of the solvent. Figure 3.2 shows the calculated mass loss as a function of time, and Figure 3.3 shows the corresponding experimentally measured evaporation profile for PS/CS_2 solution (adapted from experiments done by Song [7]). The calculated rate of mass loss appears to closely resemble the experimentally measured profiles with the exception of the more dilute solutions, where the surface area itself was not constant. The magnitude of β is quite insensitive to change in velocity (for typical airflows employed) and the model computed mass loss occurs nearly at the same rate, in agreement with the experimental results of Song [7]. It is inherently assumed in the model that the choice of polymer and the molecular weight do not affect the time required for mass loss, and studies conducted to date on a range of polymers used to form breath figures appear to support the validity of this assumption.

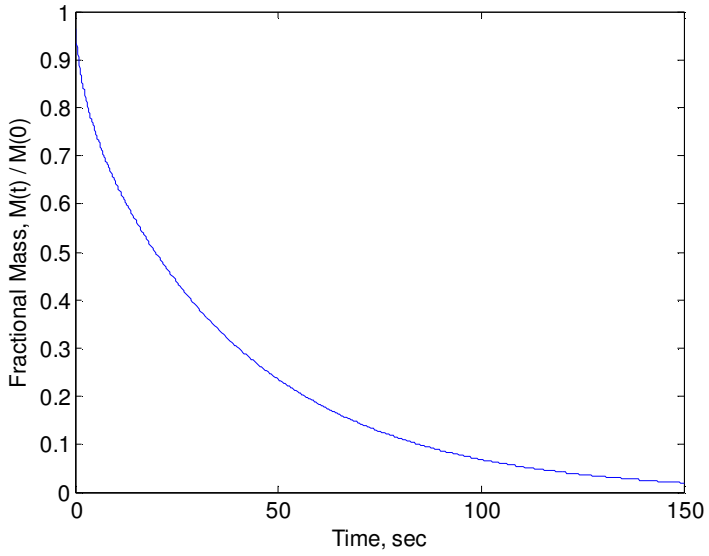

Figure 3.2 Theoretically predicted mass loss as a function of time for PS/CS_2; using flow rate of 0.75 m/s, and thickness corresponding to 0.12 g of polymer solution, area 1 cm^2 (typical experimental values).

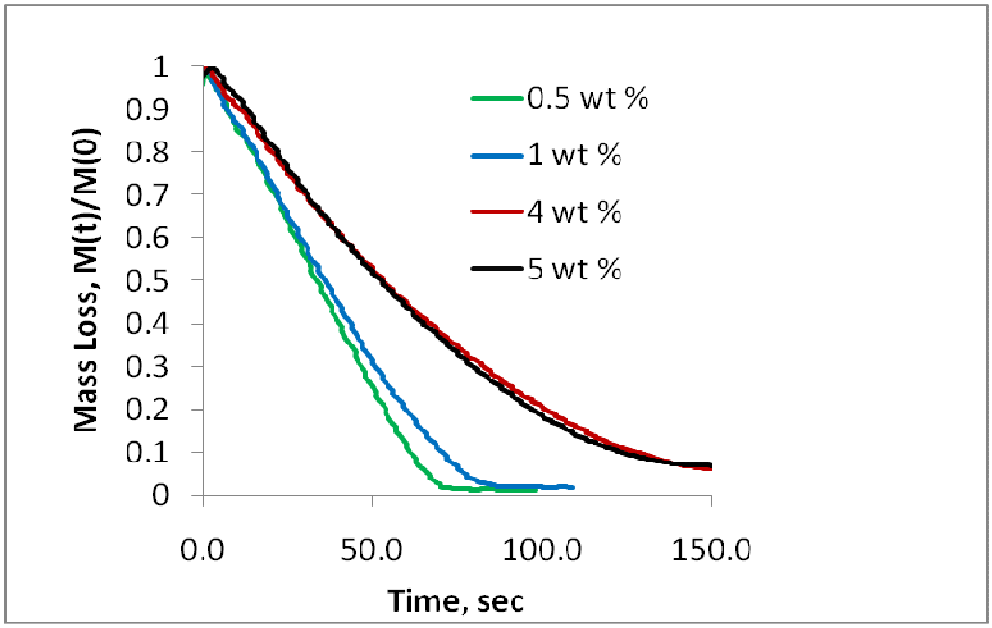

Figure 3.3 Experimentally determined mass profiles, for PS/CS_2 solutions, where for polystyrene is mono-carboxy terminated (M_w =50K), and airflow is 0.75 m/s, with varying PS content.

3.2 How does the polymer solution temperature vary during solvent evaporation?

The variation of surface temperature as a function of time during the evaporative period is essentially a heat diffusion problem and may be described by the equation [29]:

$$D_T \frac{\partial^2 \theta}{\partial z^2} = \frac{\partial \theta}{\partial t} \tag{3.6}$$

We consider the polymer solution to be thin enough such that the dominant heat exchange takes place in the z direction, and that the heat of mixing of solvent vapor and moist air is negligible. Let us define θ as the difference between the temperature of the solvent and the temperature of the airflow, D_T is the thermal diffusion coefficient, given by $D_T = K_T / \rho_L \alpha_L'$, K_T is the heat conductivity and α' is the specific heat of the solvent. Any circulation within the polymer solution is neglected in this model.

At the bottom surface, which is in contact with a solid insulating substrate, boundary condition of zero flux is applied, implying

$$\partial\theta/\partial z = 0 \ at \ z = 0 \quad \forall t \tag{3.7}$$

Heat is continuously exchanged at the top surface. The heat exchange associated with enthalpy of evaporation is $\frac{1}{2}\rho l L_{vap}\left(d\Re(t)/dt\right)$ where $\Re(t) = M(t)/M(0)$ is the relative mass at time, *t*, and L_{vap} is the heat of vaporization [29]. Radiative heat loss is equal to $k_1\theta$, where $k_1 = 4\sigma_0\theta_0^3$, where σ_0 is Stephan's constant. Heat loss due to air flow is equal to $k_{HT}\theta$, where k_{HT} is dependent upon both Reynolds number, *Re* and Prandtl number, *Pr* and is calculated using the Nusselt number, $Nu_L = k_{HT}L_{vap}/K_T = 0.664\,\mathrm{Re}^{1/2}\,\mathrm{Pr}^{1/3}$. Lastly, conductive heat exchange is equal to $K_T\frac{\partial\theta}{\partial z}$. Taking all the heat exchange terms into account, the boundary condition turns out to be:

$$\frac{1}{2}\rho l L_{vap}\frac{d\Re}{dt} + K_T\frac{\partial\theta}{\partial z} - k_{HT}\theta = 0 \ at \ z = h, \ t > 0 \tag{3.8}$$

.

The k_1 is dropped as the term is much smaller than the heat transfer coefficient, k_{HT}. By defining, $\phi = \theta/\theta'$; $\theta' = \beta^2 D_L \rho L_{vap}\xi/2K_T$, X=z/l, $\tau = t/\tau'$; $\tau' = \rho\alpha l^2/K_T$, ξ as the pre-factor for *M(t)/M(0)* and $\gamma = \rho\alpha\beta^2 D_L/K_T$, the heat equation becomes

$$\frac{\partial\phi}{\partial\tau} = \frac{\partial^2\phi}{\partial X^2} \tag{3.9}$$

with the initial condition and the boundary conditions as

$$\phi = 0; 0 < X < 1; \tau = 0 \tag{3.10}$$

$$\frac{\partial\phi}{\partial X} = 0 \ at \ X = 0$$

$$\frac{\partial \phi}{\partial X} - \frac{k_T l}{K_T}\phi + \exp(-\gamma\tau) = 0 \; at \; X = 1, \; \tau > 0$$

.

The heat equation, with the aforementioned boundary and initial conditions was solved numerically for the PS/CS_2 system as shown in Figure 3.4. The predicted temporal variation of temperature shows a remarkable similarity to the corresponding temperature profile measured experimentally as shown in Figure 3.5. The experimental profile was obtained using an embedded thermocouple probe, see SEM image in Figure 3.6, (experimental result from our collaborators Richard Jones, Mathew Barrow and P. R. Williams, University of Wales, Swansea). Notice that the temperature first decreases much below room temperature and as the evaporation of the solvent slows down and ceases, the temperature starts to rise back again. The magnitude of the temperature drop and its duration appears to be controlled by the magnitude of thermal and mass diffusivity of the solvent and by the convective losses as incorporated in the magnitude of the heat transfer coefficient, k_{HT}.

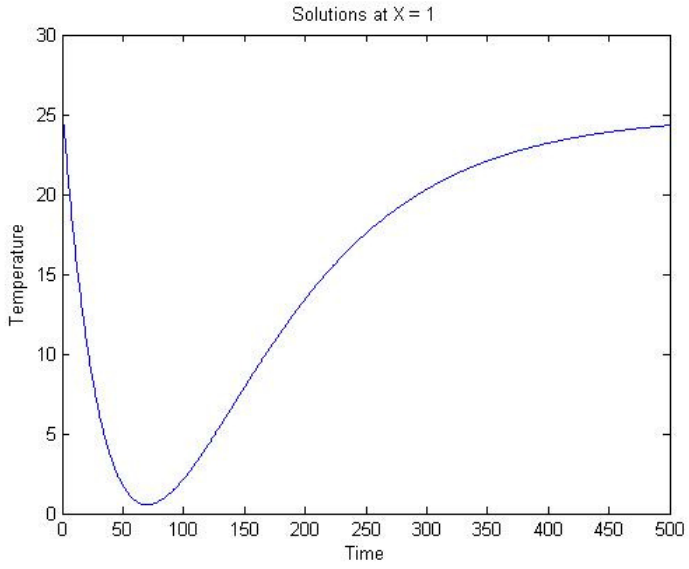

Figure 3.4 Model prediction of the temperature profile for PS/CS_2 for flow rate of 0.5 m/s. The temperature shown is calculated for the top of the substrate.

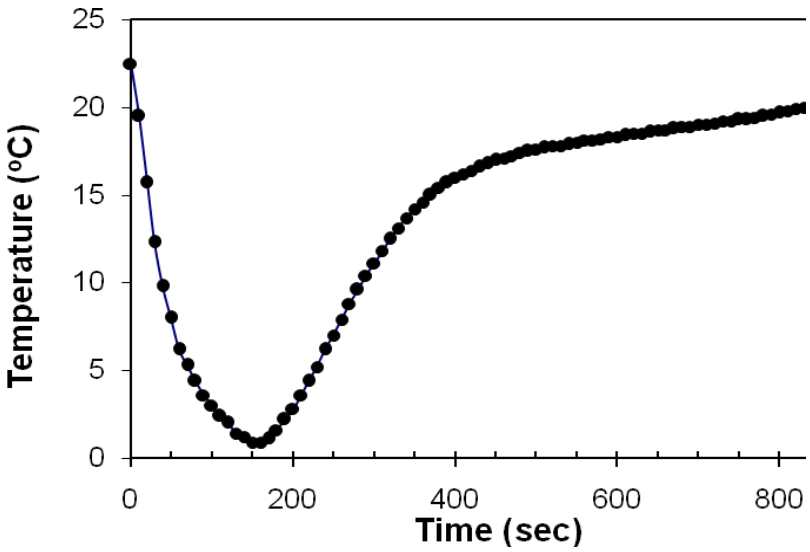

Figure 3.5 Experimentally measured temperature profile, for flow rate of 0.5 m/s, humidity 52 %, PS 3% by weight in CS_2. Thermocouple was placed close to the substrate.

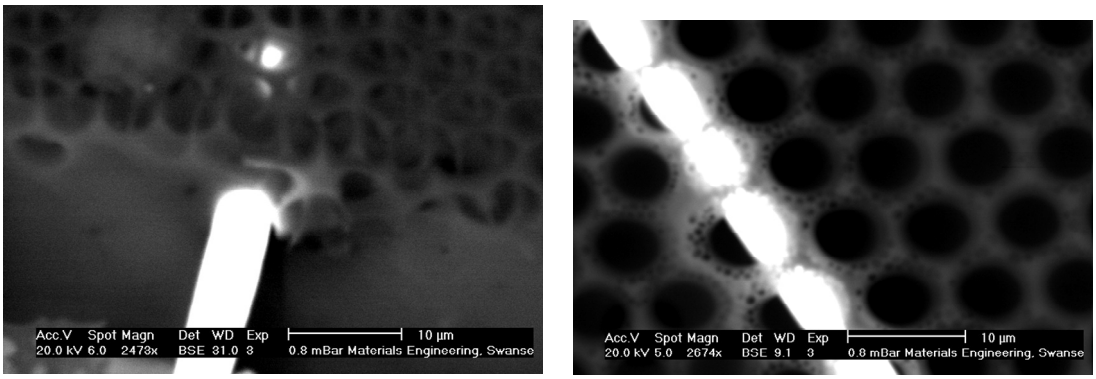

Figure 3.6 SEM images for microporous films with an embedded wire.

3.3 How does the choice of solvent or air flow effect the rate and extent of evaporative cooling?

Evaporation of solvent leads to a temperature drop that depends upon the air flow velocity, as is plotted in Figure 3.7 for the typical air flow speeds used in the experiments. The absolute value of temperature drop as well as its evolution with time is

dependent on the chosen air flow velocity. Interestingly, a higher airflow velocity produces a smaller temperature change. The explanation is simple and as follows. Evaporative cooling is counteracted by an increased and opposing conductive heat flux, from the warmer air that flows over the colder substrate. By changing the depth and width of the curve that represents the variation in temperature with time, the time available for drops to nucleate and grow must change. The growth of drops is modeled and described in next chapter, but even without formulating a growth law, one can expect that increase in velocity implies lower drop sizes, for the drops can grow only for a shorter duration. This is in accord with the experimental observations reported by various groups [2, 31, 32].

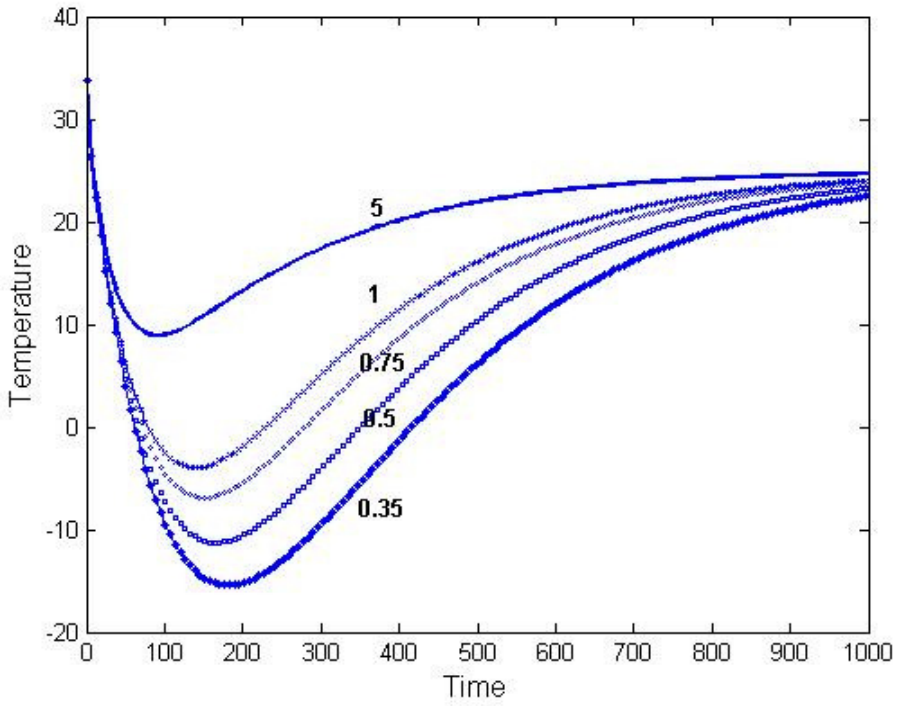

Figure 3.7 The temperature variation (in ^{o}C) as a function of time (in seconds) plotted for range of velocities for CS_2 solution; 0.35 m/s (dots), 0.5 m/s (open circles), 0.75 m/s (squares), 1 m/s (crosses) and 5 m/s (bold line).

By using the corresponding physical properties of the solvent (heat diffusivity, mass diffusivity, conductivity, enthalpy of vaporization, etc. provided in Appendix I) in the numerical model developed here, the temperature changes can be predicted for any given solvent, and for different air velocities. Since the physical properties of dry air are quite similar to the moist air or nitrogen atmosphere, qualitatively, the effect of changing the solvent or flow rate is similar. Figure 3.8 shows how the model profiles change when the flow rate is varied for two different solvents, chloroform and carbon disulfide, from which it can be seen that the temperature change is always higher for carbon disulfide. The effect of changing air flow velocity for both the solvents is also plotted in Figure 3.8. The higher air flow speed diminishes the effect of evaporative cooling, though the absolute variations are more dramatic for carbon disulfide. The temperature drop for carbon disulfide is not only greater in magnitude, it also occurs at a much faster rate.

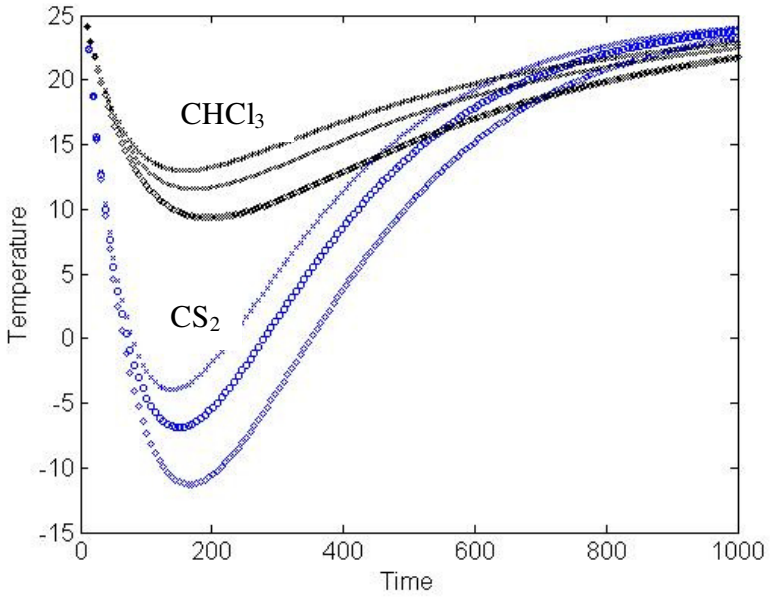

Figure 3.8 Comparison of the model profiles of the temperature variation (in ^{o}C) as a function of time (in seconds) plotted for carbon disulfide, CS_2 (blue) and chloroform, $CHCl_3$ (black) for flow rates of 0.5 (squares), 0.75 (circles) and 1 (crosses) m/s, respectively.

Carbon disulfide is one of the most commonly used solvents for studies on breath figures. The success story of this solvent lies in its extent of evaporative cooling itself. When the corresponding temperature drops are compared for four of the most commonly used solvents (see Figure 3.9), the extent of cooling is found to be carbon disulfide > benzene > chloroform > toluene. It is tempting to draw conclusions about a number of results summarized for solvents in Table 2.1 and, to a large extent, the depth and width of cooling curve dictates the duration of drop growth. But a detailed discussion about how drop size depends upon solvent parameters and on the air flow conditions can be and will be made only after the corresponding models for droplet growth are described in the next chapter.

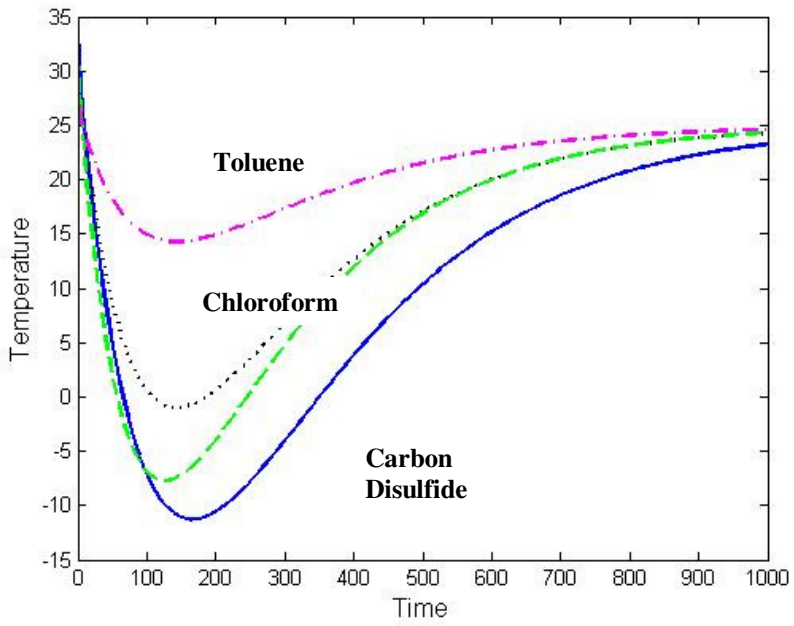

Figure 3.9 Temporal variation of temperature (^{o}C) as a function of time (seconds) plotted for different solvents. Carbon disulfide (blue, bold line) has the biggest temperature drop, followed by benzene (green, broken line), chloroform (black, dotted line) and toluene (magenta, dash-dots). The velocity of air flow is 0.5 m/s for all solvents.

It is worth noting that as the temperature of the solution and the polymer concentration change, the absolute values of the physical properties of the solvent will vary accordingly. These effects may be considered in future work but our present understanding is that the variation of the key parameters (including vapor pressure, heat of vaporization, specific heat and diffusivity of the liquid) is sufficiently low (i.e. within a few percent of those of the pure solvent) to justify omission from the present approximations. Despite this and even with the stated simplifying approximations, the model appears to capture most of aspects of the evaporation behavior occurring within the context of breath figure templated assembly.

3.4 What is the role of architecture, molecular weight and concentration of the polymer?

The viscosity of the polymer solution depends upon the molecular weight, concentration and the architecture of polymer. The evaporative cooling for a given solvent is primarily dependent upon the physical properties of the solvent, and hence the initial nucleation and growth of water droplets is not influenced by the choice of polymer molecular weight or architecture. As the polymer solutions progress from a dilute to semi-dilute state during evaporation, the associated viscosity increases by approximately three orders of magnitude [33]. In breath figures formed on nonvolatile, precooled liquids, the delayed coalescence of drops, which allows for their assembly into rafts, is attributed to the draining time required for the solvent to move out which scales linearly with viscosity. In the late stages, where droplets are closely packed and lie within the polymer solution, the draining time for the increasingly viscous polymer solution will be

several orders of magnitude larger than that of the pure solvent. An alternative mechanism preventing coalescence may be present during the early stages, where replenished fluid layer between interacting drops keeps them apart. The detailed physics of why water drops exhibit non-coalescence in early stages and the effect of solvent vapor flux and temperature dependences will be examined in subsequent chapters. Since the calculation of solvent vapor flux and the temperature of the substrate can be computed for given solvent and air flow, the present study provides a good basis for evaluating growth, noncoalescence and assembly processes qualitatively as well as quantitatively.

3.5 Conclusions and outlook

A theoretical framework was developed to model the effect of the choice of solvent and velocity of air flow on the extent of evaporative cooling that creates the conditions for breath figure templated assembly. This study shows how the choice of solvent determines the rate and extent of evaporative cooling. The rate of mass loss and temperature change measured for a polymer solution, PS/CS_2 system, exposed to a stream draft of moist air are captured quite well by the model presented here. The extent of evaporative cooling is contrasted for various solvents, and it was determined that for the same air flow velocity, the depth and width of curve representing the temperature drop as a function of time is in the following sequence: carbon disulfide > benzene > chloroform > toluene. Carbon disulfide solutions have a greater temperature drop than the chloroform solutions for the whole range of typical air flow velocities employed in the experiment. The elucidation of how the choice of solvent and airflow velocity determines

the time scales as well as heat and mass fluxes is an essential step towards our goal of unraveling the physics of nucleation, growth, non-coalescence and assembly of water drops and as a result, establishing how pore sizes can be manipulated using the process parameters. These will be examined in detail in the following chapters of the thesis.

3.6 References

1. Dylan, B., *The Definitive Bob Dylan Songbook*. 2001, New York: Amsco Publications.

2. Srinivasarao, M., et al., *Three-dimensionally ordered array of air bubbles in a polymer film.* Science, 2001. **292**(5514): p. 79-83.

3. Widawski, G., M. Rawiso, and B. Francois, *Self-organized honeycomb morphology of star-polymer polystyrene films.* Nature, 1994. **369**(6479): p. 387-389.

4. Pitois, O. and B. Francois, *Formation of ordered micro-porous membranes.* European Physical Journal B, 1999. **8**(2): p. 225-231.

5. Pitois, O. and B. Francois, *Crystallization of condensation droplets on a liquid surface.* Colloid and Polymer Science, 1999. **277**(6): p. 574-578.

6. Barrow, M.S., et al., *Physical characterisation of microporous and nanoporous polymer films by atomic force microscopy, scanning electron microscopy and high speed video microphotography.* Spectroscopy-an International Journal, 2004. **18**(4): p. 577-585.

7. Song, L., *Study of ordered macroporous polymer films by templating breath figures*, in *School of Polymer, Textile and Fiber Engineering*. 2005, Georgia Institute of Technology: Atlanta. p. 193.

8. Englert, B.C., et al., *Templated ceramic microstructures by using the breath-figure method.* Chemistry-a European Journal, 2005. **11**(3): p. 995-1000.

9. Erdogan, B., et al., *Permanent bubble arrays from a cross-linked poly(para-phenyleneethynylene): Picoliter holes without microfabrication.* Journal of the American Chemical Society, 2004. **126**(12): p. 3678-3679.

10. Song, L., et al., *Facile microstructuring of organic semiconducting polymers by the breath figure method: Hexagonally ordered bubble arrays in rigid-rod polymers.* Advanced Materials, 2004. **16**(2): p. 115-+.

11. Limaye, A.V., et al., *Evidence for convective effects in breath figure formation on volatile fluid surfaces.* Physical Review Letters, 1996. **76**(20): p. 3762-3765.

12. Weh, L. and A. Venthur, *Crack patterns in thin polymer layers.* Macromolecular Materials and Engineering, 2004. **289**(3): p. 227-237.

13. Bormashenko, E., et al., *Mesoscopic Patterning in thin polymer films formed under the fast dip-coating process.* Macromolecular Materials and Engineering, 2005. **290**(2): p. 114-121.

14. Vrentas, J.S. and C.M. Vrentas, *Drying of solvent-coated polymer films.* Journal of Polymer Science Part B-Polymer Physics, 1994. **32**(1): p. 187-194.

15. Guerrier, B., et al., *Drying kinetics of polymer films.* AIChE Journal, 1998. **44**(4): p. 791-798.

16. Megelski, S., et al., *Micro- and nanostructured surface morphology on electrospun polymer fibers.* Macromolecules, 2002. **35**(22): p. 8456-8466.

17. Casper, C.L., et al., *Controlling surface morphology of electrospun polystyrene fibers: Effect of humidity and molecular weight in the electrospinning process.* Macromolecules, 2004. **37**(2): p. 573-578.

18. Hall, D.B., P. Underhill, and J.M. Torkelson, *Spin coating of thin and ultrathin polymer films.* Polymer Engineering and Science, 1998. **38**(12): p. 2039-2045.

19. Flack, W.W., et al., *A mathematical-model for spin coating of polymer resists.* Journal of Applied Physics, 1984. **56**(4): p. 1199-1206.

20. Bang, J., et al., *Effect of humidity on the ordering of PEO-based copolymer thin films.* Macromolecules, 2007. **40**(19): p. 7019-7025.

21. Neitzel, G.P. and P. Dell'Aversana, *Noncoalescence and nonwetting behavior of liquids.* Annual Review of Fluid Mechanics, 2002. **34**: p. 267-289.

22. Beysens, D. and C.M. Knobler, *Growth of breath figures.* Physical Review Letters, 1986. **57**(12): p. 1433-1436.

23. Beysens, D., *The formation of dew.* Atmospheric Research, 1995. **39**(1-3): p. 215-237.

24. Fritter, D., C.M. Knobler, and D.A. Beysens, *Experiments and simulation of the growth of droplets on a surface (breath figures).* Physical Review A, 1991. **43**(6): p. 2858-2869.

25. Steyer, A., P. Guenoun, and D. Beysens, *Hexatic and fat fractal structures for water droplets condensing on oil.* Physical Review E, 1993. **48**(1): p. 428-431.

26. Steyer, A., et al., *Two-dimensional ordering during droplet growth on a liquid surface.* Physical Review B, 1990. **42**(1): p. 1086-1089.

27. Bird, R.B., W.E. Stewart, and E.N. Lightfoot, *Transport Phenomenon*. 1960, Singapore: John Wiley and Sons.

28. Deen, W.M., *Analysis of Transport Phenomena*. Topics in Chemical Engineering, ed. K.E. Gubbins. 1998, New York: Oxford University Press.

29. Crank, J., *The Mathematics of Diffusion*. 2nd ed. 1975, New York: Oxford University Press.

30. Hines, A.J. and R.N. Maddox, *Mass Transfer: Fundamental and Applications*. 1985, New Jersey: Prentice Hall.

31. Cui, L., et al., *Tunable ordered droplets induced by convection in phase-separating P2VP/PS blend film.* Polymer, 2004. **45**(24): p. 8139-8146.

32. Maeda, Y., Y. Shimoi, and K. Ogino, *Fabrication of microporous films utilizing amphiphilic block copolymers and their use as templates in poly(aniline) preparation.* Polymer Bulletin, 2005. **53**(5-6): p. 315-321.

33. Doi, M. and S.F. Edwards, *The Theory of Polymer Dynamics*. 1986, Oxford: Oxford University Press.

CHAPTER 4

NUCLEATION AND GROWTH

TRICKLE, drops! my blue veins leaving!
O drops of me! trickle, slow drops,
Candid, from me falling—drip, bleeding drops,
From wounds made to free you whence you were prison'd,
From my face—from my forehead and lips,
From my breast—from within where I was conceal'd—press forth, red drops—confession drops;

Stain every page—stain every song I sing, every word I say, bloody drops;
Let them know your scarlet heat—let them glisten;
Saturate them with yourself, all ashamed and wet;
Glow upon all I have written, or shall write, bleeding drops;
Let it all be seen in your light, blushing drops.
(*Trickle drops* by Walt Witman [1])

The formation of liquid water from water vapor involves one of the most commonly observed phase transitions, underlying the formation of fogs, clouds and rain [2-10], breath figures and dew [11-19], breath fog and drops that form on the cold glass of a soft drink or beer. The condensation process is accompanied by transfer of heat and mass and is crucial to many industrial and natural processes, including precipitation [2-10], chemical vapor deposition [19, 20], colloidal synthesis [21, 22], etc. In fact, breath figures [12, 15-19], which form when one breathes over a cold glass or mirror for example, have been found to be good analogues to chemical vapor deposition [19, 20]. In these cases, the nucleation of water drops occurs at the surface, implying that the condensation growth is assisted by presence of a surface, and such nucleation process is called heterogeneous nucleation [7, 8]. In the absence of any external surface, the condensation process is initiated by formation of a stable cluster of water molecules that

can grow if the supply of vapor is abundant and the condensation process is favored [7, 8]. In breath figures, the pre-cooled substrate acts as both the nucleation site and as the location of subsequent growth of the drops [11, 12, 14]. In breath-figure-templated assembly, we start with a substrate at ambient temperature, and the cooling is a result of evaporation as described in the preceding chapter. For drops to nucleate and grow, the local supply of vapor must be evaluated for each drop, which is an intricate problem. To make the problem more tenable, a mean field approach was adopted, where the temperature and concentration of vapor in the vicinity of the substrate was computed first. Thereafter the mechanism and kinetics of nucleation and growth of drops is derived and discussed.

4.1 How does supersaturation available for drops to grow vary?

Since the water droplets nucleate and grow due to condensation, it must be emphasized that the important parameter is the level of supersaturation present in the vicinity of growing drops. Relative humidity of the air refers to the ratio of the partial pressure of water vapor to the saturation vapor pressure at that temperature. The air is said to be saturated with water vapor when the partial pressure of the vapor is equal to the saturation value, e_s, that is computed using Clausius-Clapeyron equation, as shown in Figure 4.1, using the formula [8],

$$e_s(T) = 6.112 \ \exp\left([17.67 * T]/[T + 243.5]\right) \tag{4.1}$$

which is valid between -30 ^{o}C and 35 ^{o}C , and e_s here is in mb (millibar) and T in ^{o}C [8]. Physically, the rates of evaporation and condensation are the same for a saturated vapor. The vapor is said to be supersaturated when the partial pressure of vapor is higher than

the saturation value. The kinetics of droplet nucleation, growth and assembly are determined by the mass and heat flux of water vapor [4, 10, 11, 14], which are directly influenced by the local conditions controlled by the solvent evaporation. We already have derived the solvent flux and temperature change in substrate in the chapter 3. For air with temperature and partial pressure of water vapor given by point A on Figure 4.1, the theoretical dew point can be reached by cooling to T_{dA}. The temperature at which dew actually forms is dependent on the substrate surface condition [11, 14], as was discussed in Chapter 2.

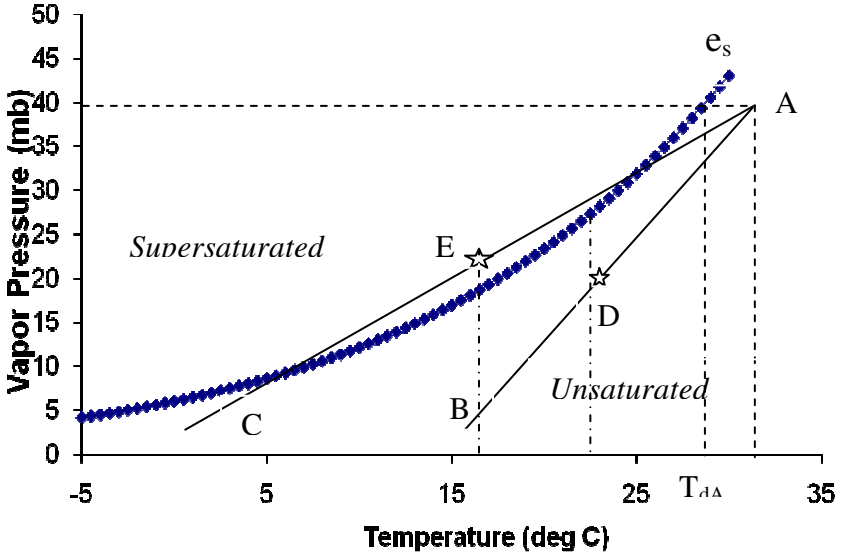

Figure 4.1 Saturation vapor pressure as a function of temperature computed for water vapor. (See text for details)

When the moist air flow comes in contact with the flux of evaporating solvent vapor, the humidity and temperature of the mixture become the relevant parameters for nucleation and growth of the drops. Before deriving the mathematical expression for the supersaturation of the mixture, the effect of mixing is illustrated with Figure 4.1. In the present situation, the supersaturation is caused by the same phenomenon that causes

mixing clouds that appear as fogging of breath in winter. The physical origin of supersaturation in these cases can be understood by looking at Figure 4.1. The mixing of two unsaturated parcels of air with different temperature and vapor pressure, say point, A and C on the graph, can lead to a supersaturated mixture, E [3, 8, 23].

For any experiment carried out with a constant air stream velocity and humidity, the amount of water vapor supplied is constant (given by equation 4.5, discussed later). This determines the flux of the water vapor for breath figures formed on solid and liquid substrates, and in *that* case, the supersaturation results from conductive cooling in air stream that contacts the cold surface. But in the present case, the mixing of water vapor with evaporating solvent above the substrate implies that the change in the "relative humidity" and temperature of the mixed volume is similar to progressively moving from the point D to E on Figure 4.1. Thus not only the absolute magnitude of supersaturation would be different from the case of breath figures, the supersaturation must vary with time, for evaporation rate and temperature of the substrate vary with time as described in the previous chapter.

A slight change in relative humidity or temperature of incoming air flow changes the position of A, and hence changes the value and time evolution of supersaturation. In a delightful chapter on mixing clouds, Bohren [3] remarks that since the exhaled air from dogs is hotter and more humid than from a woman, on a certain cold day only the dog's breath yielded a mixing cloud, while his wife failed to produce a breath fog. The contrails created by the flying planes are also examples of mixing clouds.

For the isobaric mixing of two volumes at pressure P, having initial temperature T_1 and T_2, and water vapor pressure e_1 and e_2, respectively, the resulting supersaturation, s_m, from mixing [23] is

$$s_m = \left(e_m / e_s(T_m)\right) - 1 \tag{4.2}$$

Here $e_s(T_m)$ is the saturated vapor pressure at temperature T_m, which is the temperature of the mixed volume. The ratio of the two vapor pressures is hereafter called Saturation Ratio, S and it is related to the supersaturation, s by the relation $s = S\text{-}1$. The temperature of the mixed volume, T_m, is written using mixing rule as

$$T_m = kT_1 + (1 - f)T_2 \tag{4.3}$$

The mixing ratio, f, is the ratio of the flux of water vapor to the surface of the substrate and the flux of evaporating solvent that mixes with it. Vapor pressure of the mixed volume, e_m is given by the mixing rule to be

$$e_m = e_1 \frac{1}{1+f} \tag{4.4}$$

Since the solvent flux has no water vapor, $e_2 = 0$, only e_1 contributes to the partial pressure of vapor in the mixed volume. The flux of evaporating solvent vapor is computed from rate of the mass loss, or from $\Re(t) = M(t)/M(0)$, determined in the previous chapter. The flux of the vapor is determined by using the correlation for the laminar boundary layer transport equation, where the Sherwood number, Sh defined [24] as

$$Sh = j\delta_{BL} / D_0 c_0 \sim \mathrm{Re}^{1/2}\, Sc^{1/2} \tag{4.5}$$

correlates j, the flux of water vapor molecules from the gas phase to the interface on the substrate, to Re and Sc. Here c_0 is the concentration of water vapor at the edge of bounder

layer of thickness, δ_{BL}, and D_0 is the bulk diffusion coefficient of water vapor in the gas phase. The correlation is based on the assumption that the vapor flux is determined by the diffusion from the gas phase and all the water molecules are absorbed at the substrate. The mixing of solvent vapor and of water vapor laden moist air is assumed to be ideal mixing. *While the actual flux of water vapor might be lower than estimated by equation 4.5, the variation of supersaturation with time and its dependence on air flow velocity and humidity will be qualitatively quite similar.*

The solvent properties influences the saturation ratio achieved. The difference is a result of both the difference in the temperature of the substrate as well as in the solvent vapor flux, which changes the parameter *f* that determines both the mixture temperature and supersaturation. Since $e_m = e_1(1+f)^{-1}$, the supersaturation is directly proportional to the relative humidity of the air flow. Figure 4.2 illustrates how changing solvent from carbon disulfide to chloroform impacts the saturation ratio. The figure also shows a comparison of saturation ratio as determined by the humidity of incoming air flow. The variation and magnitude of supersaturation in the mixed vapor for the given solvent, carbon disulfide, can be thus changed by varying the relative humidity of the incoming air flow.

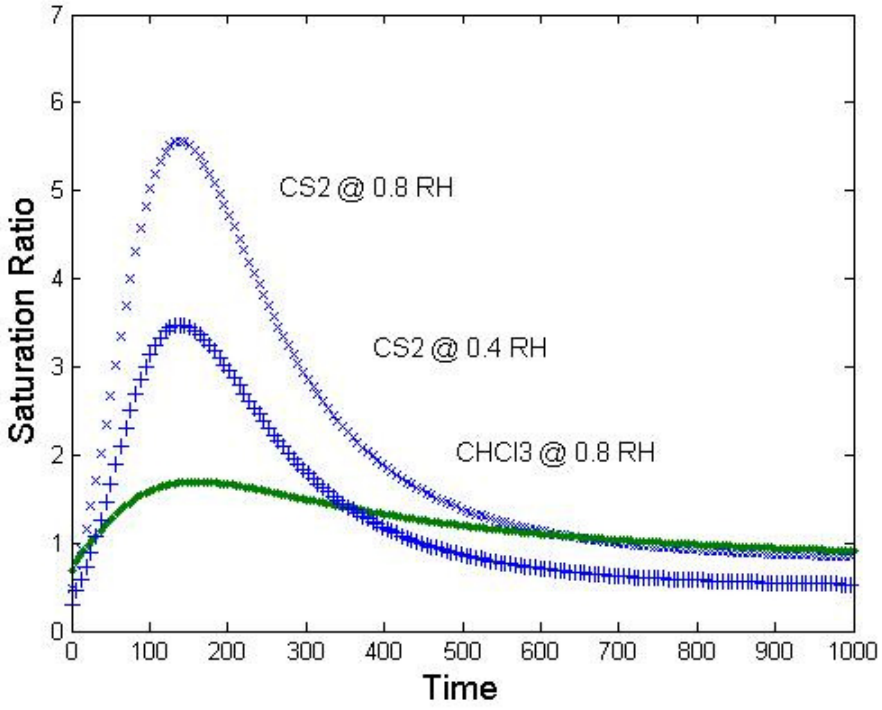

Figure 4.2 Saturation ratio computed for chloroform and carbon disulfide, for moist air at room temperature flowing with velocity of 1 m/s over evaporating polymer solution. Time is in seconds.

The theoretical model developed here provides the temporal variation of supersaturation for a given set of conditions (speed and humidity of airflow) for any given solvent, as long as the physical properties of the solvent are known. Figure 4.3 shows how the saturation ratio depends upon the choice of the solvent. The saturation ratio achieved for a given airflow and humidity for these solvents shows the following sequence: carbon disulfide > benzene > cholorform > toluene. Note that the two sets of curves present the same data, but the first one is plotted on a linear axis to allow comparison with the temperature variations plotted earlier. The second curve is plotted on a log-log plot and this is the way saturation ratio or supersaturation is typically represented by cloud physicists [7, 25].

(a)

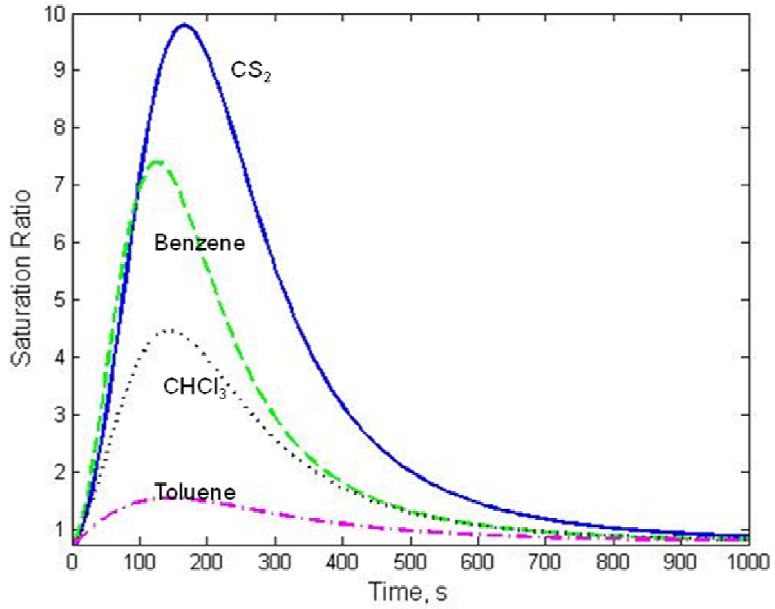

(b)

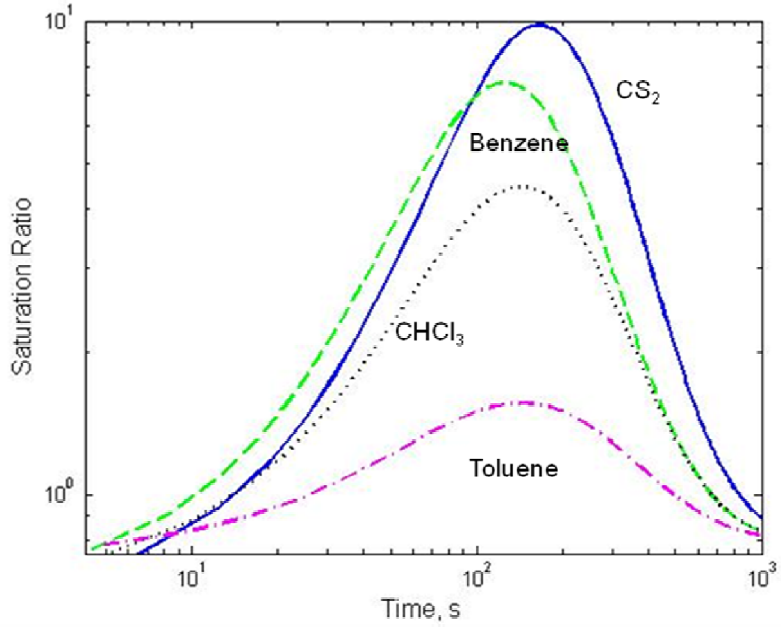

Figure 4.3 Temporal variation of supersaturation, plotted for different solvents. Carbon disulfide (blue, bold line) has the biggest supersaturation peak, followed by benzene (green, broken line), chloroform (black, dotted line) and toluene (magenta, dash-dots). The velocity of air flow is 0.5 m/s for all solvents. Curve (**a**) shows everything on linear scale, and curve (**b**) on log-log plot.

Since the parameter *f*, for the same solvent and humidity also depends upon the air flow velocity, the temporal variation of supersaturation can be varied by changing the air flow velocity. For a given solvent, the peak saturation ratio achieved decreases with increase in velocity of the air flow. Figure 4.4 illustrates how the variation of supersaturation depends on air flow velocity for two different solvents, carbon disulfide and chloroform. While the amount of water vapor arriving at the substrate increases with an increase in air flow, the corresponding supersaturations are lower because the higher velocity of air flow leads to a higher temperature of the mixed volume (and of the substrate as described in chapter 3). It was remarked earlier that the experiments reported by various groups show increase in air flow leads to decrease in the drop size, and the lower peak supersaturation value as well as shorter duration for which the supersaturation exists for higher velocity, definitely indicate that the drops size will be smaller, when the velocity of air flow is increased.

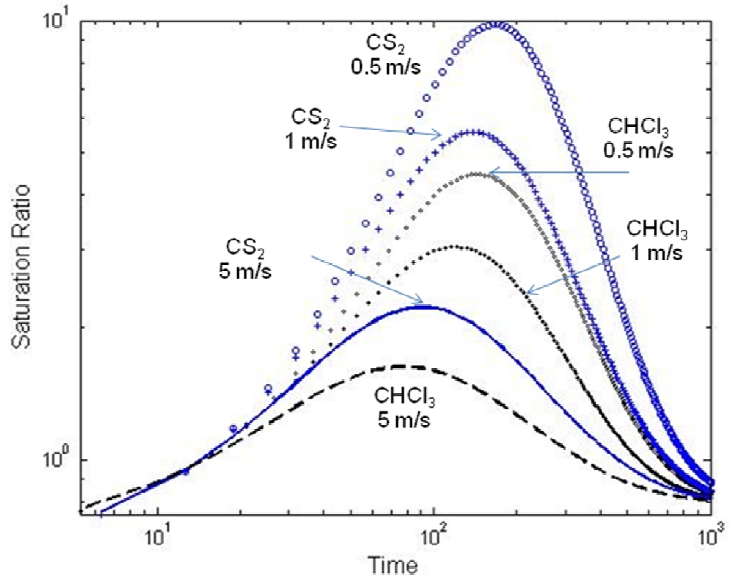

Figure 4.4 Comparison of supersaturation for Chloroform (black) and Carbon Disulfide (blue; wider lines/symbols) for 0.5 m/s (circles), 1 m/s (crosses) and 5 m/s (lines). Supersaturation over carbon disulfide is always larger than that for chloroform. Time is in seconds.

When the solvent evaporation flux starts to vanish, the temperature of the substrate starts to rise, as shown by theoretical and experimental results discussed earlier. Soon the water drops are in contact with an undersaturated air current. This causes evaporation of the water drops embedded in the substrate. The corresponding evaporation model for drops in air is qualitatively similar to the condensation model, but in the present case, since the evaporating drops are suspended in polymer rich substrate, they are expected to experience different boundary conditions. The evaporation of water drops is described in detail later in Chapter 7, though it seems intuitive that the pore sizes observed are a direct result of drop sizes achieved during growth.

4.2 What is the mechanism for nucleation?

Nucleation of liquid water from vapor requires formation of an embryonic droplet that is stable under the given environmental conditions, dictated by temperature and vapor pressure in the vicinity of the droplet. The embryo itself is formed by chance collisions and aggregation of molecules, and it is stable only when the size exceeds a certain critical value. The critical stable size of embryo depends upon the competing factors that assist in condensation growth or evaporative decay. The growth and decay occur at different rates depending upon whether the nucleation is homogeneous or heterogeneous. In the homogeneous nucleation of pure water, the rate at which water molecules impinge on the droplet is set by the partial pressure of vapor in the vicinity of the droplet, and this eventually determines the growth rate. The evaporative decay is a

function of temperature and surface tension of the droplet, for molecules can escape from liquid state only if they overcome the energy barrier [5, 7, 8].

The growth or decay of drop occurs in a given environment depending upon whether it is supersaturated or undersaturated. In equilibrium, the rate of condensation and evaporation are matched, and the vapor is said to be saturated at that temperature. Since the embryonic drops are typically small and have large surface energy, the equilibrium vapor pressure of a droplet is affected by the curvature and depends upon its size, r_d and is given [5, 7, 8, 10] by

$$e_s(r) = e_s(\infty) \exp\left(2\sigma_d / r_d R_v \rho_d T\right) \tag{4.6}$$

where $e_s(r)$ is the saturation vapor pressure of a spherical drop of density ρ_d at temperature T, and R_v (461.5 J kg^{-1} K^{-1}) is the individual gas constant for water vapor. The vapor pressure required for equilibrium increases with a decrease in drop size. Hence, for a given distribution of drop sizes, evaporation or growth is linked to the local vapor pressure. The size dependence of vapor pressure is based on a derivation by Lord Kelvin, who was trying to explain the rise of a fluid in a capillary tube [8]. The net rate of condensation growth or evaporative decay is proportional to $e - e_s(r)$ where e represents the actual ambient vapor pressure, and growth occurs if $e > e_s(r)$. The critical size thereof is defined by $e\text{-}e_s(r_c)=0$, which implies that for the saturation ratio, S is defined as $S = e/e_s(\infty)$, the critical size, r_c [5, 7, 8, 10] is

$$r_c = 2\sigma/(R_v \rho_d T \ln S) \tag{4.7}$$

The higher the supersaturation, the lower is the critical radius. For example, for saturation ratio, S = 1.01 the critical radius is 0.12 microns, while it is only 0.52 nm for S of 10 [8]. Once the critical size is reached, addition of more molecules makes the droplet

supercritical. Since $e_s(r_d)$ decreases with the increase in radius, the rate of growth which depends upon the local supersaturation increases, and beyond the critical size, the drops grow spontaneously. Thus the calculation of nucleation rate amounts to the computation of the rate at which supercritical drops form. This depends upon the concentration of critical drops as well as on the rate at which more molecules accrue on this droplet, making it supercritical. The nucleation rate per unit volume, J_c, is approximately[8]

$$J_c = 4\pi r_c^2 \frac{e}{\sqrt{2\pi\, m_{H_2O}\, k_B T}} Z\, n_v \exp\left(-\frac{4\pi r_c^2 \sigma}{3 k_B T}\right) \tag{4.8}$$

where m_{H2O} is the mass of a water molecule, k_B is the Boltzmann's constant, n_v is the number density of the vapor molecules and Z (~0.01 if CGS units are used) is numerical factor [8]. The detailed discussion of homogeneous nucleation of water can be found in any standard atmospheric physics textbook [5, 7, 8, 10] and is not necessary to the arguments that follow.

Nepomnyashchy et al [24] argued that in the case of breath figure templated assembly, the heterogeneous condensation on the polymer solution is more favored thermodynamically than homogeneous nucleation and condensation in the air above it. For heterogeneous nucleation over a planar substrate with the air flow over it, the conditions are similar to the formation of dew or breath figures. The hydrophobicity of the surface enters through the term that depends upon the contact angle, $\cos\theta$ and breath figure templated assembly typically involves condensation over an organic fluid. Since the nucleation over substrate is more likely than the homogeneous nucleation in air, when moist air contacts a pre-cooled, nonvolatile liquid substrate, breath figures or dew form at the substrate. But in this case, as is discussed next, the hygroscopic and non-hygroscopic

particles that are ever present in humid air can be activated as soon as the critical supersaturation is reached in air [4-8, 10]. Ever since the experiments of Coulier and Aitken [26], it is known that in a supersaturated volume of air, heterogeneous nucleation can occur over the aerosol particles [6-8, 10]. Thus the rate of droplet formation is controlled by the number of such hygroscopic or condensation nuclei, and not by collision statistics.

At a particular supersaturation, for both homogeneous and heterogeneous nucleation, there exists a minimum nuclei radius that is in equilibrium with the vapor surrounding it. Under appropriate conditions of vapor and temperature flux, the transition to the regime of high growth rate occurs. Aerosols can themselves be hydrophobic, hygroscopic or neutral. The neutral aerosol particles require nearly the same supersaturation as homogeneous nucleation and the hydrophobic particles, because of their wetting properties also require significant supersaturation values. The hygroscopic particles on the other hand, can be in equilibrium with an environment at much lower supersaturation than the corresponding drops of the pure water. The reduction in the vapor pressure due to presence of dissolved nonvolatile particles or solute over a flat surface is given in terms of a van't Hoff factor [7, 8, 10]. For dilute solutions, the saturation ratio is simply $S = 1- b/r^3$ where $b \sim 4.3\ iM/m_s$ (cm^3) depends upon i, degree of ionic association (~2 for most salts in atmosphere) [8], M is the mass of the solute or salt present in water droplet and m_s is the molecular weight of the solute. Taking curvature effect for small drops into account, as given by Kelvin's relation, the saturation ratio can be written as $S = 1+ a/r - b/r^3$, where $a \sim 3.3 \times 10^{-5}/T$ (cm) is the curvature term that

incorporates the value of surface tension [8]. The variation of saturation ratio over a drop with radius is given in Figure 4.5, which is historically called the Köhler curve [8].

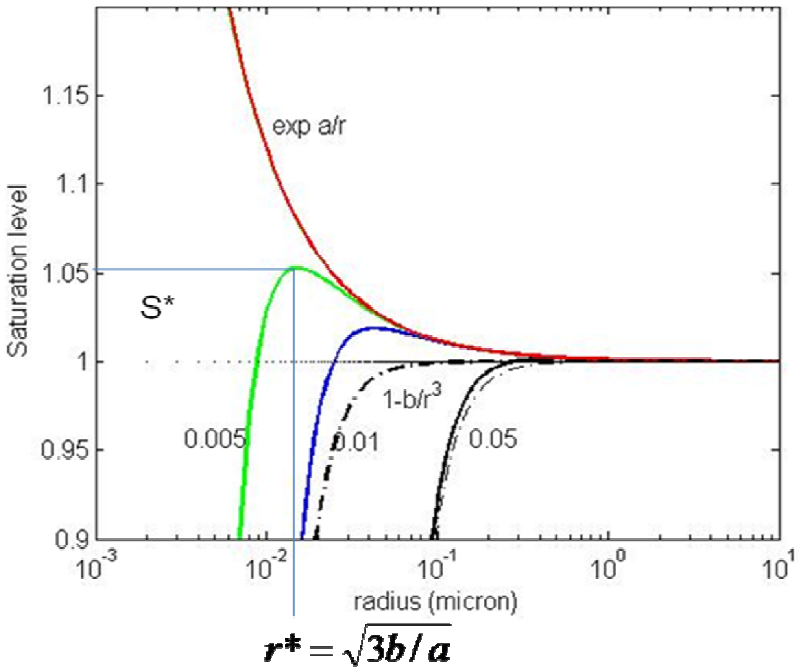

Figure 4.5 Köhler curve showing the dependence of saturation ratio as a function of radius. Here the three numbers denotes different initial salt content, solid lines show the combined effect of surface tension or Kelvin factor and solution or van't Hoff factor. The dotted lines show only van't Hoff factor, and red curve shows the effect of Kelvin factor, that does not change with variation in salt content.

The essential point to note about Köhler curve is that the solution and surface tension effects dominate at small size (< 1 µm). Remember here the solution refers to an aqueous solution that constitutes the growing drops. Very small solution drops are in equilibrium with humidity below 100% and as the saturation ratio increases, the drops continue to grow up till the peak saturation value, S^* is crossed. Thereafter, the droplets grow without need of increasing saturation ratio. Thus two regimes exist: for a drop with size $r_d < r^*$ where r^* is typically of the order of 0.1-1 µm, the drops are in a stable equilibrium with its environment, and adjusts its size by evaporation or condensation for

any change in the ambient humidity. Such drops constitute the haze. Once the drops grow beyond the critical radius, these drops are said to be activated, and then the drops continue to grow [7, 8, 10].

The transformation of condensation nuclei to droplets and the development of resulting droplet spectrum is controlled both by the spectrum of condensation nuclei and by the time dependence of supersaturation. For the present case, mixing causes supersaturation and hence, as for breath fog, the nucleation will be predominantly taking place in vapor phase. *The mixing of warm moist air with the cooler solvent vapor flux creates conditions akin to breath fog and hence the water nucleation occurs over the dispersed particles in the air and thus the activated cloud condensation nuclei are the ones that grow into the drops.*

In cloud microphysics, the available water vapor in a parcel of ascending air is consumed by the distribution of nuclei that become active at certain critical supersaturations, and the number of possible nuclei is finite. For different salt concentrations, the Köhler curves are shown in Figure 4.6 [27]. The salt particles that follow the green curve will be activated only if the supersaturation goes beyond 0.45 for example, though the salt particles that follow the magenta curve will be active as soon as supersaturation gets to 0.2 or higher.

The influx of moist air in our case brings a constant stream of nuclei, and hence the source term of nucleation will be qualitatively different from cloud microphysics. As shown before, in breath figure templated assembly the supersaturation rises to a peak value and then it decreases. In cloud physics, the nuclei are typically activated in a short initial burst, and these activated nuclei consume the supply of vapor at a fairly rapid rate

[10]. In the context of breath figure templated assembly, the likelihood of this happening is even higher. Moreover, if small drops get generated during later stages, the hydrodynamics of the problem is such, as explained in greater detail in the chapter on noncoalescence, that these fresh droplets are likely to escape, without getting close enough to substrate to be sustained there for growth and assembly.

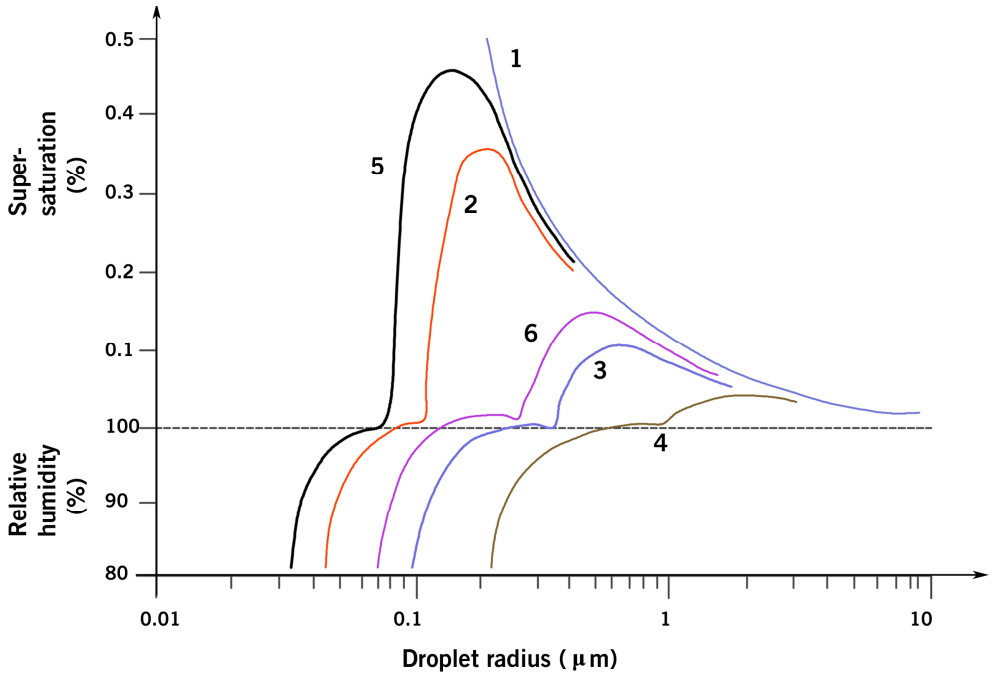

Figure 4.6 Supersaturation and relative humidity as a function of salt type and salt concentration. (1) Pure water, (2) 10^{-19} kg of NaCl, (3) 10^{-18} kg of NaCl, (4) 10^{-17} kg of NaCl, (5) 10^{-19} kg of $(NH_4)_2SO_2$ and (6) 10^{-18} kg of $(NH_4)_2SO_2$. Note the discontinuity in ordinate at relative humidity of 100% and note that pure water lies above all the solution drops. (Adapted from ref. [27]).

It must be remarked here that cloud physicists have characterized the propensity of the air present in different place, over sea and in cities, in desert and over mountains, to determine the number of particles per unit volume, N_c that are activated as a function of supersaturation, s. The nucleus counts follow a power law, $N_c \sim A_c s^k$ where A_c = 30 to 300 cm^{-3}; k = 0.3 to 1.0 for maritime air, and 300 to 3000 cm^{-3}; 0.2 to 2.0 for continental

air respectively [5, 7, 8]. The coefficient and the exponent have been found to vary with location and season, which are tabulated in most atmospheric science textbooks [5, 7, 8]. The knowledge that the number and size distribution of condensation nuclei present is itself a variable implies that realistic comparisons between the effect of humidity or airflow can be made only if the number of nuclei coming in are controlled.

4.3 Growth of individual droplets

The growth of water droplet is governed by a complex interplay of heat and mass transfer. Corresponding equations that determine droplet growth in the presence of convective flow of air around it, for vapor and heat transport respectively [10, 28] are

$$\frac{\partial \rho}{\partial t} + v_1 \nabla \rho = D_v \frac{\partial^2 \rho}{\partial r^2} \tag{4.9}$$

$$\frac{\partial T_i}{\partial t} + v_i \nabla T_i = D_{Ti} \frac{\partial^2 T_i}{\partial r^2} \tag{4.10}$$

with the mass balance described [10, 28] as

$$\frac{dm_d}{dt} = D_v \iint_s \left. \frac{d\rho}{dr} \right|_{r=r_d} dS_d \tag{4.11}$$

where ρ and D_v are the density and coefficient of diffusion of vapor. T_i, v_i and D_{Ti} are the temperature, velocity and thermal diffusivity of air (i = 1) and liquid (i=2), while m_d and S_d are respectively the mass and surface area of the liquid drop. In the present form, the equations require determination of velocity field inside and outside the droplet. The relative role of the convection and diffusion can be estimated using dimensionless parameters: The Reynolds number $\mathrm{Re} = \rho v r_d / \eta$ and Peclet numbers, diffusional and thermal, $Pe_D = v r_d / D_v$ $Pe_T = v r_d / D_T$ respectively, calculated for both air and the liquid

phase, (for v ~ 0.01-10 m/s, r_d ~ 0.1-10 μm, and air and water properties listed in Appendix), are for present case are much smaller than unity. Thus in considering the growth or evaporation of droplets of within our size range and for the range of parameters used in these experiments, we can neglect the circulation within the drop and air motion outside it. This results in considerable simplification in the equations that describe the heat and mass transfer in the droplet growth or evaporation.

The equation for diffusional growth for an isolated drop [10],

$$\frac{\partial \rho}{\partial t} = D_v \frac{\partial^2 \rho}{\partial r^2}$$

(4.12)is similar to the equation for a drop, which is at rest in a vapor field, and the temperature field within and around droplet is described [10] by

$$\frac{\partial T_i}{\partial t} = D_{Ti} \frac{\partial^2 T_i}{\partial r^2}. \tag{4.13}$$

The mass change equation is

$$\frac{dm_d}{dt} = 4\pi r^2 D_v \frac{d\rho}{dr}\Big|_{r=r_d} \tag{4.14}$$

and the boundary conditions at drop surface [10]

$$LD_v \frac{\partial \rho}{\partial r} + k_1 \frac{\partial T_1}{\partial r} + k_2 \frac{\partial T_2}{\partial r} = 0 \qquad r = r_d \tag{4.15}$$

Both the heat change during condensation and conductive heat transfer are accounted for. Here $\rho = \rho_\infty$, $T_1 = T_\infty$ $r \to \infty$ and $\rho = \rho_o$, $T_1 = T_2 = T$ for $r = r_d$. These equations turn out to be quite similar to the initial condensation growth regime of droplets in clouds [10] and even though they were derived independently from mass and heat transport equations written down for spherical drops, the derivation and the resulting system of equations are quite analogous to physics of drop formation in the atmosphere.

The critical difference is in the time variation of supersaturation, which in the case of breath-figure-templated assembly was calculated as described in the previous section.

In cloud formation, the supersaturation arises in a parcel of air mainly due to the adiabatic expansion of air [5-8, 10]. It can also be brought about by either radiative cooling or by the mixing of air masses with different humidity and temperatures, mechanisms that typically create fogs and smog [7, 8]. The rate of cooling, and the volume of air affected determine the amount of condensation, and hence the amount of precipitation a cloud can produce [5-8, 10]. While qualitatively our equations look similar to the growth equations for initial growth regime dominated by condensation in the cloud microphysics (the other regime is coalescence assisted growth), significant differences exists in how condensing vapor is made available to the growing droplets, as well as in the occurrence of coalescence in clouds.

The generic growth law that results from the simplified mass and heat transfer equations is reminiscent of Maxwell's equation for diffusional growth of droplets [4, 10]. On incorporating the effect of surface tension and dissolved substances in the water drop, the growth law [10] is given by

$$\frac{\partial r}{\partial t} = K_G \frac{s_0 - \frac{B}{r} + \Phi(c)}{r} \tag{4.16}$$

$$K_G = D_v \rho_0 \Big/ \rho_2 \left[1 + \frac{\rho_0 L D_v}{k_1 T} \left(\frac{L}{R_v T} - 1 \right) \right] \tag{4.17}$$

The factor K_G incorporates the heat and mass diffusion terms as well as the heat change due to enthalpy of vaporization [10]. Here ρ_0, ρ_1 and ρ_2 are the densities of saturated water vapor, water and air respectively; k_1 is the thermal conductivity of the air,

B takes into account the effect of surface tension ($B = 2\sigma/\rho R_v T$) and $\Phi(c)$ is a function characterizing the drop in saturated vapor pressure due to soluble substances with surface concentration c. [10] Now using the time dependence of supersaturation computed as described earlier, the growth of drop of certain initial size can be described as a function of time. Figure 4.7 illustrates the growth computed for three drops with different initial size. As the drops grow under the given supply of supersaturation, each of the drop is seen to evolve to same size. *Since the growth rate scales inversely with radius of the drop, the smaller drops grow faster than the bigger drops and this in absence of coalescence leads to size narrowing*.

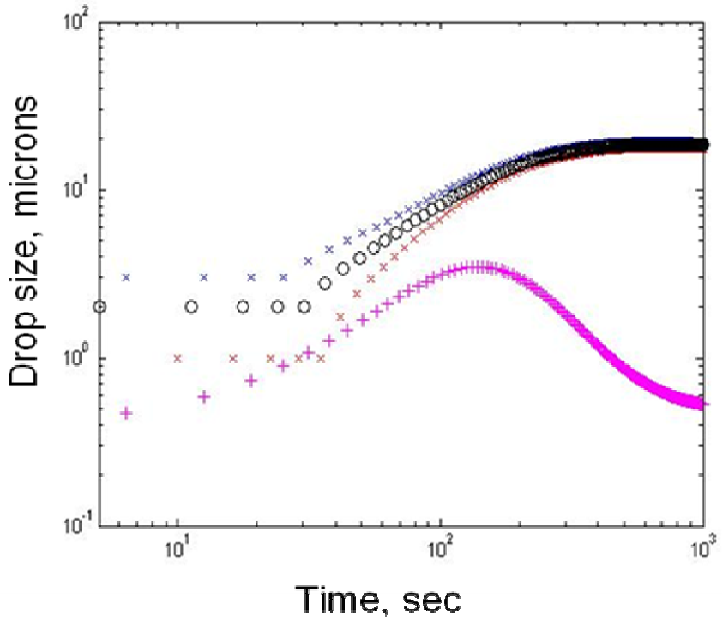

Figure 4.7 Growth of three water drops, with different initial nuclei diameter, computed for variation in supersaturation shown in pink. Saturation ratio is computed for carbon disulfide as solvent and air flow of 1 m/s, with 80% relative humidity.

In this case, the analogy with cloud physics is instructive, for the supersaturation variation is very similar to our case, though the variation there occurs because of cooling by expansion of a rising plume of moist air. Figure 4.8 sketches the supersaturation and

radius of drops, as calculated by Howell [25] and others [5, 7, 8] for drops growing by condensation process during the formation of clouds. Only the drops that have a certain minimum size are able to grow, and these drops converge to common size under the given conditions. In cloud physics, the growing drops consume the water vapor present in that plume, and the fall in supersaturation is related to the size and width of population distribution of the drops. In breath figure templated assembly, water vapor is continuously brought in by humid air flow, but the supersaturation variation is brought about by the mixing of air flow and solvent vapor.

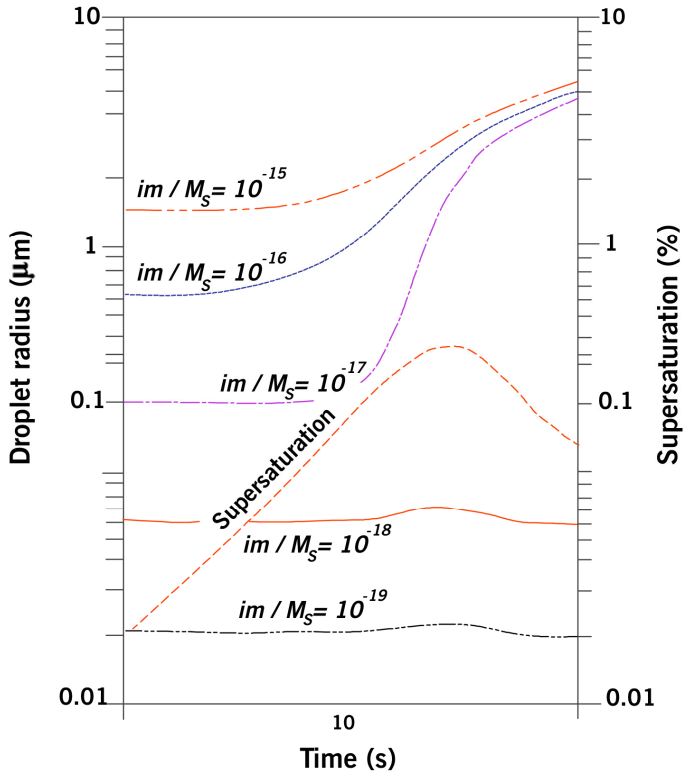

Figure 4.8 Growth of water drops with different critical radius, (with different initial nuclei diameter or different salt content), computed for variation in supersaturation that occurs during formation of the clouds (Adapted from [27]).

4.4 How does the choice of solvent and air flow influence the final drop or pore size?

The growth of drops over carbon disulfide solutions exposed to different air flow velocities changes is illustrated in Figure 4.9. Note that since most of the activated drops grow to nearly same size under identical air flow speed and humidity, the results do not depend upon the choice of initial nuclei size. The crucial aspect of the growth here is that increase in velocity of air flow results in a decrease in droplet size. According to the model used for description of droplet growth in case of breath figures [11], $r(t) \sim (U^{0.5}\, \upsilon_a^{-1/6} D^{2/3} \Delta e)^{1/3} t^{1/3}$, the radius of drops scales with $U^{1/6}$, implying that even a ten-fold increase in velocity increases the drop size only by a factor of 1.5 times. In breath-figure-templated assembly, the increase in flow rate results in a decrease in drop size [29-31] and the effect of velocity change is much stronger than in case of breath figures. This is in accordance with what is predicted by the framework developed here.

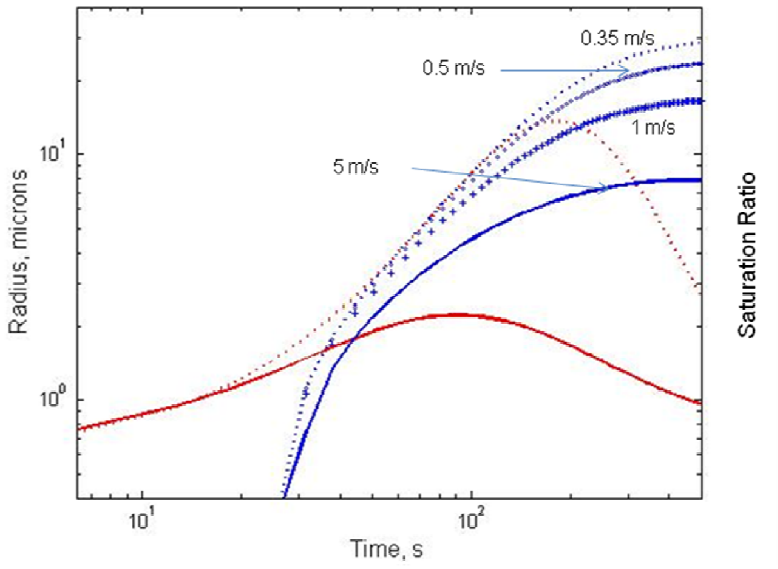

Figure 4.9 The radius of growing drop as a function of time, plotted for a range of air flow velocities over CS_2 solution; 0.35 m/s (dots), 0.5 m/s (open circles), 1 m/s (crosses) and 5 m/s (bold line). The dotted red line shows saturation ratio for 0.35 m/s and bold red line in for 5 m/s. Increase in velocity of air flow decreases the drop size.

Since the growth of drops depends upon the amount of supersaturation available to them, for the same humidity and speed, the amount of supersaturation available is determined by the solvent, the average drop size also follows the sequence: carbon disulfide > benzene > chloroform > toluene, as revealed by Figure 4.10.

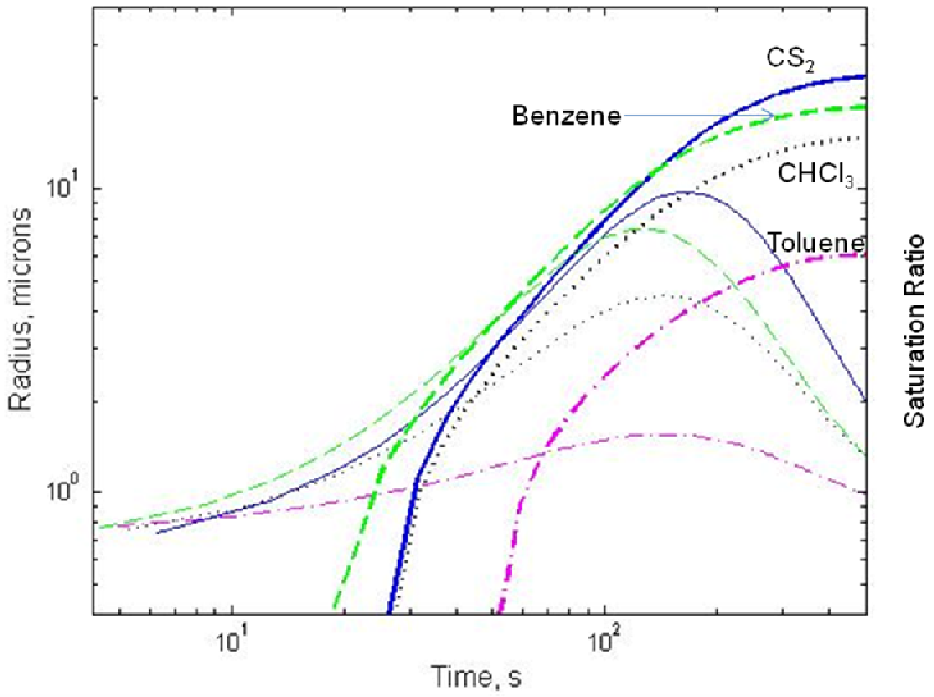

Figure 4.10 Temporal variation of supersaturation and representative radius of a drop as a function of solvent. Carbon disulfide (blue, bold line) has the biggest supersaturation peak and drop size, followed by benzene (green, broken line), chloroform (black, dotted line) and toluene (magenta, dash-dots). The velocity of air flow is 0.5 m/s for all solvents. The radius corresponds to thicker lines and drop growth takes off only after saturation ratio is slightly more than one.

Further, in literature, we find instances, typically for airflow at room temperature [32-37], where the relative humidity is reported to be low (35-50%). If the substrate is cooled using a cooling stage or due to evaporative cooling, the "relative humidity" in the vicinity of growing drops is different (much higher) than that measured for the incoming

airflow. While evaporative cooling promotes condensation, if the polymer solution is placed over a cooling stage, the condensation of drops, and time of growth is enhanced. This resulted in observed increase in final drop sizes from 5.2 micron at 20^{o}C to 18 micron at 4 ^{o}C, keeping everything else the same for polyimide in chloroform [33]. PS, with five arm star, glucose initiated were likewise shown to have higher order for lower temperature. Increase in pore size with lowering of temperature was also reported for PLGA in chloroform. Similarly, higher humidity results in bigger pore size [34, 38, 39]. Again, if the $r \sim \Delta e^{1/3}$ scaling for breath figures is used, the change in relative humidity of incoming air flow will not have as dramatic effect on the drop or pore sizes in our case as observed experimentally, and is predicted by the framework described here.

Some reports state that if experiments are done in low ambient humidity, porous polymer films can be formed by using THF/water mixture as the solvent [36, 37]. In these cases, where THF is mixed with water, additional contribution to available supply of vapor comes from the evaporation of water in the solvent. Not surprisingly the experiments reveal that for lower humidity air flow, the higher water content in THF/water leads to better results [36, 37]. The fact is that relative humidity only expresses the percentage of undersaturation at the temperature, and as our daily experience illustrates, water can deposit on a cold glass of beer or soft drink on seemingly dry days as readily as on oppressively humid days. Figure 4.2 illustrates how even at 40% humidity of incoming air, high degree of supersaturation can exist above carbon disulfide solution. Lower humidity of air flow implies lower supersaturation, and hence the growth of drops is inhibited.

Song [40] measured the size of water drops as a function of time, by using the movies that capture the growth and assembly of water drops over the evaporating solutions with carbon disulfide as a solvent. The smallest drop that was visualized using optical microscope was ~ 1 μm, for experimentally not only the resolution of the microscope used is limited, but the focusing on drops itself requires at least a few seconds. The growth regime as well as the initial nucleation cannot be visualized easily. Song argued that the counter for time for growth must be set at the instant the drops are nucleated, and since it is hard to point out the time instant when nucleation happens, the plot of growth against time cannot be used for figuring out the growth law. Essentially the argument was that during the experiment, depending upon the choice of time at which growth is assumed to begin, say at t_1 or t_2, the diameter grows as either $d \sim (t-t_1)^{\alpha}$ or $d \sim (t-t_2)^{\beta}$ giving different exponents, $\alpha \neq \beta$ and so the growth law cannot be determined.

The growth law in a generic sense for a case with constant supersaturation or for steady state can be described by $r^n \sim t$, implying that if the growth of drops is known at any three instants of time, the scaling constant for the growth law applicable can be computed as

$$r_2^{\,n}(t) = \frac{r_3^{\,n}(t) + r_1^{\,n}(t)}{2} \tag{4.18}$$

In context of breath figure templated assembly, many researchers cite the corresponding growth law from the breath figures. In this context, if the radii of drops are plotted as a function of time, the Figures 4.7-4.9 reveal that because of the nature of variation of supersaturation, it is not meaningful to expect a constant exponent "*n*" for breath figure templated assembly. But if, for argument's sake, the exponent needs to be evaluated, the method of differences applied to the experimental data (extracted from movies collected

by Lulu Song, unpublished), the growth law of $r^2 \sim t$ is applicable for a certain interval of time. This is different from expected from the scaling $r^3 \sim t$ for breath figures when drops grow independently from each other and from $r \sim t$ when drops grow through coalescence [11]. Further, even though there is no coalescence involved, the fall in supersaturation creates a regime where the rate of growth corresponds to $r \sim t$. The bottomline here is to recognize that the growth law for breath figure templated assembly depends upon a supersaturation that is itself a function of time, whereas the growth law calculated for the breath figures or dew relies on a supersaturation that is supposed to be constant.

4.5 How does a distribution of drop sizes evolve?

Mathematically, the observed growth to similar size is easy to show. The growth law derived here, can be simplified to the form

$$\frac{\partial r}{\partial t} = K_G \frac{s_0}{r} \tag{4.19}$$

when the drop size is over a micron or so. This can be integrated to show that for two drops with initial sizes $r_1(0)$ and $r_2(0)$ (such that $r_2(0) > r_1(0)$) growing under the same conditions, the difference between the size of drops at any time, t, is

$$r_2(t) - r_1(t) = \frac{r_2^2(0) - r_1^2(0)}{r_2(t) + r_1(t)} \tag{4.20}$$

Since the difference between the squares of initial radius is a constant, the difference in the radii of drops, 1 and 2, becomes smaller as they grow. *Thus the nearly monodisperse size spectrum of the drops and resulting pores can be traced to the growth law during condensation, which leads to different drop sizes evolving to similar size as smaller drops exhibit faster growth.*

Any distribution of droplets forming on polydisperse condensation nuclei is inherently thermodynamically stable. At any given supersaturation, if some drops are in equilibrium, others will have a positive or negative growth rate, with the former growing at the expense of the latter. The time history of the droplet size distribution is coupled to the corresponding time dependence of the supersaturation. For a given distribution of nuclei present during the process, the overall distribution function reflects why and how size distribution reacts to change in external control parameters like humidity or air velocity as well as to the choice of the solvent (for it affects time variation of supersaturation).

For a generic case, the functional form of the initial population of drops depends upon the condensation nuclei generated as a function of time, which depends both on the supersaturation and number density of Aitken nuclei or aerosol particles present in the volume of air. Assuming that the drops present at the end of breath figure templated process are all present at a time $t_{initial}$, and no new nuclei are generated thereafter, the evolution of distribution function for drops, Ω, can be described quite generally as follows [10]:

$$\frac{\partial \Omega}{\partial t} + \frac{\partial}{\partial r}\left(\frac{dr}{dt}\Omega(r,t)\right) = \Psi(r,t) \tag{4.21}$$

Here the distribution function satisfies the following condition [10]:

$$\int_0^\infty \Omega(r)\, dr = n \tag{4.22}$$

where n is the particle concentration and the term $\Psi(r,t)$ represents a source term that specifies how drops appear and disappear in the volume under consideration.

Under the condition, that no new drops are being generated, or when $\Psi(r,t)$=0 the distribution function just satisfies the condition

$$\frac{\partial \Omega}{\partial t} + \frac{\partial}{\partial r}\left(\frac{dr}{dt}\Omega(r,t)\right) = 0 \tag{4.23}$$

which can then be solved for a given growth law, if the initial shape of the distribution function is known. If we consider only the first term of the growth law, $\frac{\partial r}{\partial t} = K_G \frac{s_0}{r}$ and solve for the distribution function, the evolution of the distribution function can be described by the following:

$$\Omega(r,t) = A_f r \exp(-B_f (r^2 - \int K_G s(t)\, dt)) \tag{4.24}$$

where A_f is a constant that depends upon the initial distribution function and B_f is a numeric constant. The distribution function narrows as a function of time in a fashion shown in Figure 4.10, where arbitrary values of A_f and B_f were picked to illustrate the spectrum narrowing.

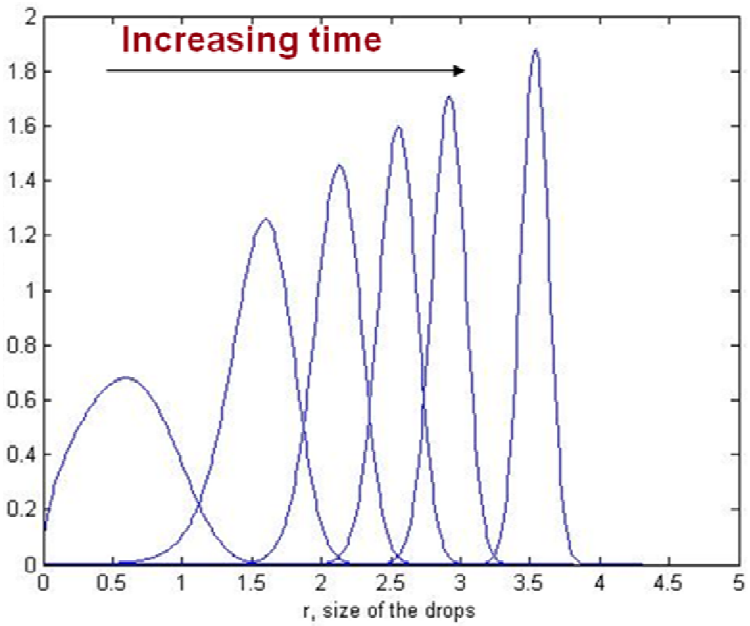

Figure 4.11 The droplet distribution function, Ω(r, t), becomes narrower with time.

Alternatively in the approach described by Rogers [8], drops can be thought of as flowing through *r* space as they grow and number of droplets per unit time per unit mass of air passing through *r* in radius space can be described in terms of the droplet current, *I(r,t)*. The rate of change of the number of droplets is then given by [8]

$$\frac{\partial}{\partial t}\left(\Omega(r,t)\delta r\right) = -\frac{\partial I}{\partial r}\delta r \tag{4.25}$$

and by using the simplified rate law and by noting that the droplet current can be related to distribution function by [8]

$$I(r,t) = \Omega(r,t)\frac{dr}{dt} \tag{4.26}$$

we obtain the same continuity equation for the distribution function as described earlier. According to Rogers [8], the solution to this can be written as

$$\Omega(r,t) = \frac{r}{\sqrt{r^2 - 2s_0 K_G t}}\Omega_0\left(\sqrt{r^2 - 2s_0 K_G t}\right) \tag{4.27}$$

and this function also shows narrowing of the spectrum as a function of time.

4.6 Summary

A theoretical framework was developed to illustrate the effect of the choice of solvent as well as humidity and velocity of air flow on the breath figure template assembly of pores in a polymer film, formed when a blast of moist air passes over the evaporating polymer solution. The supersaturation over the substrate is computed and correlated to solvent properties and air flow conditions. The mixing of two unsaturated volumes (solvent flux and moist air flow) of vapor creates a supersaturated mixture and

hence allows nucleation and growth of water droplets in air, in fashion similar to the formation of breath fog. *The similarity to breath fog, rather than dew or breath figures represents a paradigm shift in our understanding of nucleation and growth of water droplets over evaporating polymer solutions.* The growth kinetics for the drops formed in breath figure templated assembly is quite different from that followed by drops formed in breath figures. The growth kinetics was derived, and it was shown that the condensation growth mechanism itself is responsible for the observed monodipersity of pores.

4.7 References

1. Whitman, W., *The Complete Poems*. 2004, London: Penguin Books Ltd.
2. Tricker, R.A.R., *The Science of the Clouds*. 1970, New York: American Elsevier Publishing Co, Inc.
3. Bohren, C.F., *Clouds in a Glass of Beer: Simple Experiments in Atmospheric Physics*. 2001: Dover Publications.
4. Fuchs, N.A., *Evaporation and droplet growth in gaseous media*. 1959, London: Permagon Press.
5. Mason, B.J., *The Physics of Clouds, 2nd ed.* 1971, London: Oxford University Press.
6. Middleton, W.E.K., *History of the Theories of Rain and Other Forms of Precipitation*. 1966, New York: Franklin Watts, Inc.
7. Pruppacher, H.R. and J.D. Klett, *Microphysics of Clouds and Precipitation*. 2nd ed. 1996: Springer.
8. Rogers, R.R. and M.K. Yau, *Short Course in Cloud Physics, Third Edition*. 3 ed. 1989: Butterworth-Heinemann.
9. Mason, B.J., *Clouds, rain and rainmaking*. 2nd ed. 1975, Cambridge: Cambridge University Press.
10. Sedunov, Y.S., *Physics of Drop Formation in the Atmosphere*. 1974, New York: Wiley. 234.
11. Beysens, D., *The formation of dew.* Atmospheric Research, 1995. **39**(1-3): p. 215-237.

12. Beysens, D. and C.M. Knobler, *Growth of breath figures.* Physical Review Letters, 1986. **57**(12): p. 1433-1436.

13. Beysens, D., *Dew nucleation and growth.* Comptes Rendus Physique, 2006. **7**(9-10): p. 1082-1100.

14. Beysens, D., et al., *How does dew form.* Phase Transitions, 1991. **31**(1-4): p. 219-246.

15. Aitkens, J., *Breath Figures.* Nature, 1911. **86**: p. 516-517.

16. Rayleigh, *Breath figures.* Nature, 1911. **86**: p. 416-418.

17. Rayleigh, *Breath figures.* Nature, 1912. **90**: p. 436-438.

18. Baker, T.J., *Breath figures.* Philosophical Magazine, 1922. **44**(262): p. 752-765.

19. Briscoe, B.J. and K.P. Galvin, *Breath figures.* Journal of Physics D-Applied Physics, 1990. **23**(9): p. 1265-1266.

20. Meakin, P., *Droplet deposition growth and coalescence.* Reports on Progress in Physics, 1992. **55**(2): p. 157-240.

21. Svedberg, T., *The Formation of Colloids*. 1921, New York: D. Van Nostrand Company.

22. Evans, D.F. and H. Wennerstrom, *The Colloidal Domain*. Advances in Interfacial Engineering Series. 1999, New York: Wiley-VCH.

23. Bohren, C.F. and B.A. Albrecht, *Atmospheric Thermodynamics*. 1998: Oxford University Press, USA

24. Nepomnyashchy, A.A., et al., *Nucleation and growth of droplets at a liquid-gas interface.* Physical Review E, 2006. **74**(2).

25. Howell, W.E., *The growth of cloud drops in uniformly cooled air.* Journal of the Atmospheric Sciences, 1949. **6**(2): p. 134–149.

26. Spurny, K.R., *Atmospheric condensation nuclei P. J. Coulier 1875 and J. Aitken 1880 (historical review).* Aerosol Science and Technology, 2000. **32**(3): p. 243-248.

27. Wallace, J.M. and P.V. Hobbs, *Atmospheric science: an introductory survey*. 2nd ed. 2006, Amsterdam: Elsevier.

28. Bird, R.B., W.E. Stewart, and E.N. Lightfoot, *Transport Phenomenon*. 1960, Singapore: John Wiley and Sons.

29. Srinivasarao, M., et al., *Three-dimensionally ordered array of air bubbles in a polymer film.* Science, 2001. **292**(5514): p. 79-83.

30. Cui, L., et al., *Tunable ordered droplets induced by convection in phase-separating P2VP/PS blend film.* Polymer, 2004. **45**(24): p. 8139-8146.

31. Maeda, Y., Y. Shimoi, and K. Ogino, *Fabrication of microporous films utilizing amphiphilic block copolymers and their use as templates in poly(aniline) preparation.* Polymer Bulletin, 2005. **53**(5-6): p. 315-321.

32. Peng, J., et al., *Formation of regular hole pattern in polymer films.* Macromolecular Chemistry and Physics, 2003. **204**(1): p. 125-130.

33. Yabu, H., et al., *Preparation of honeycomb-patterned polyimide films by self-organization.* Langmuir, 2003. **19**(15): p. 6297-6300.

34. Peng, J., et al., *The influencing factors on the macroporous formation in polymer films by water droplet templating.* Polymer, 2004. **45**(2): p. 447-452.

35. Casper, C.L., et al., *Controlling surface morphology of electrospun polystyrene fibers: Effect of humidity and molecular weight in the electrospinning process.* Macromolecules, 2004. **37**(2): p. 573-578.

36. Park, M.S. and J.K. Kim, *Breath figure patterns prepared by spin coating in a dry environment.* Langmuir, 2004. **20**(13): p. 5347-5352.

37. Wang, Y., et al., *Micropatterned polymer surfaces enduced by nonsolvent.* Langmuir, 2006. **22**(4): p. 1928-1931.

38. Saunders, A.E., et al., *Inverse opal nanocrystal superlattice films.* Nano Letters, 2004. **4**(10): p. 1943-1948.

39. Cui, L., et al., *Ordered porous polymer films via phase separation in humidity environment.* Polymer, 2005. **46**(14): p. 5334-5340.

40. Song, L., *Study of ordered macroporous polymer films by templating breath figures*, in *School of Polymer, Textile and Fiber Engineering*. 2005, Georgia Institute of Technology: Atlanta. p. 193.

CHAPTER 5

NONCOALESCENCE

"We do not believe in miracles at all but that apparently strange things may be accomplished under the operation of natural laws. There is a vast amount of literature in India on these subjects, and the people there have made a study of these things. As to levitation, I have never seen anyone overcome gravitation and rise by will into the air, but I have seen many who were trying to do so. They read books published on the subject and spend years trying to accomplish the feat." (Swami Vivekananda, *The Memphis Commercial, 15th January, 1894* [1]*)*

The natural laws that govern the ability of drops to levitate or linger over a fluid bath, (reviewed in [2-5]) or to collide with each other without coalescence (see [4-12] and references therein) are of current and long standing interest as scientific curiosity and for their industrial applications, in fields as diverse as studies of rainfall [5, 13], fuel spray systems for combustion [12], colloidal, emulsion and foam stability [10, 14-20] and polymer-polymer blends [11, 21-24]. In the breath-figure-templated assembly, as moist air flows over a dilute polymer solution in a volatile solvent, evaporation cools the solution. The mixing of the solvent vapor with humid air creates a supersaturated vapor mixture. In the previous chapters, a theoretical framework was developed to illustrate the effect of the choice of solvent as well as humidity and velocity of air flow on the extent of evaporative cooling and the level of supersaturation. The initial nucleation and growth occurs in the supersaturated vapor mixture above the liquid substrate. The growth law for this scenario was derived, assuming drops grow without coalescence, and the condensation growth mechanism itself was found to be responsible for the observed monodispersity of pores. The key difference between breath figures that form on non-evaporating, pre-cooled liquid or solid substrates, and ordered arrays of drops that form on polymer solutions, is the absence of coalescence in the latter case. In fact, it is the

growth of droplets as independent entities that allows the size distribution of drops to evolve to the monodisperse distribution. The question addressed in this chapter is: *What is the reason for non-coalescence of water droplets when they assemble on or above the evaporating polymer solutions?*

Srinivasarao et al [25] ascribed noncoalescence to the thermocapillary convection caused by temperature gradients present in the system, which create a temperature difference between interacting drops, that keeps them from coalescing with each other. Further it was postulated that the thermocapillary flows "stabilize the condensing water drops on or at the polymer solution surface". Thus it was proposed [25] that the temperature difference between drops and the substrate can allow drops to levitate or float over the substrate. Further, the authors postulated that the temperature difference between interacting drops is able to keep droplets apart by replenishing the fluid layer that needs to be drained out before drops contact each other and start to coalesce, quite like the non-coalescence demonstrated by silicone oil drops in experiments by Dell'Aversana and coworkers [6, 26-28]. An alternative hypothesis states that the evaporation flux of solvent vapor is able to maintain droplets apart by providing a non-vanishing, replenished vapor layer between them [25]. On the other hand, Pitois and Francois [29] argued that a thin polymer film forms over the drops, which prevents them from coalescing, and in the last stage, the water evaporates by bursting this film. This argument has had its adherents, who call this either a polymer precipitation effect or polymer bag formation [30-34]. Other possibilities mentioned in literature include electrostatic effects [7], convective instabilities, micelle formation [35-39], etc. Their failure to capture the experimental observations was described in chapter 2.

In the previous chapters, we established that the condensation growth of drops must occur in the mixed vapors close to the substrate, rather than on the substrate. Therefore the reasons for non-coalescence need to be investigated in detail for both the time when drops are growing in air, and when they self-assemble in or on the solution substrate. The framework presented so far also provides us with the knowledge of mass and heat fluxes over the substrate to test the hypothesis of Srinivasarao et al [25] described above. Since water drops first form above the substrate, the possibility of levitation in the intermediate stage of growth itself will be examined. Recently Fisher and Golovin [40] examined the possibility of thermocapillary levitation of drops over evaporating liquid gas interface, which will be discussed in the context of temporal variation of temperature described in Chapter 3. While the noncoalescence of drops that come in vicinity of each other or collide elastically is easily observed, apart from the paper on thermocapillary induced levitation [40], the mystery surrounding the question of what makes it possible is not assessed carefully.

In this chapter, noncoalescence of drops is described for the following stages: 1) Initial stage where drops nucleate and grow over activated aerosols in vapor phase, when their size and volume fraction is low; 2) Intermediate stage when growing drops approach the polymer solution interface, and interact with each other and the substrate without merging with the fluid volumes; and 3) Last stage, where drops are partially or fully immersed in the polymer solution and the concentration of drops is the highest, as is the viscosity of the polymer solution. The objective of this chapter is to evaluate the forces or interactions that act to promote or prevent coalescence at each stage of the drop growth,

and by doing so, illustrate that noncoalescence is brought out by the nature of the breath-figure-templated assembly.

5.1 Collision, draining fluid and coalescence

The coalescence of two fluid volumes is typically described to occur in three consecutive stages: collision of drops, flow of the draining fluid and coalescence after contact. Let us first focus on these stages as defined for two drops. The first step involves the approach and collision of two drops, which come into the vicinity of each other either due to stochastic processes, as in the case of colloidal particles undergoing Brownian motion or by virtue of an external forces that pushes them towards each other, like billiard balls colliding as directed by the cue of a skilled player. The model for the coagulation of colloidal particles given by Smoluchowski involves the calculation of the probability of Brownian particles to encounter each other [41, 42]. While Smoluchowski neglected all particle interactions, the theories of particle capture developed later formulate hydrodynamic interaction as well as other particle-particle interactions [14, 43]. The efficiency of collision between drops is an important parameter for rain, and the efficiency is based upon their impact parameter. Langmuir [44] developed a collision model based on Stokes law governing the drop dynamics, which takes the effect of hydrodynamics into account.

The pioneer of pioneers, Lord Rayleigh noted in 1882: “With respect to the persistent scattering of very fine jets, however, it would appear that the principal cause is simply that many of the fine drops fail to come into contact in any case. The capillary forces act with exaggerated power, and doubtless impress upon the minute drops irregular

lateral velocities, which may easily reach a magnitude sufficient to clear each other as they pass." Figure 5.1 illustrates a sketch from Lord Rayleigh's studies conducted in 1882 [45], which were a follow up to an earlier paper in 1879 [46].

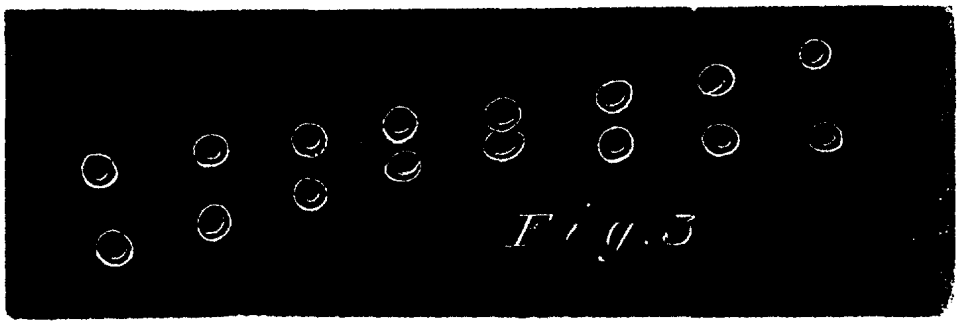

Figure 5.1 Lord Rayleigh's colliding water jets: drops bounce off, without coalescing [45].

The second stage involves draining flow of the fluid surrounding the drops that is required to allow the drops to come in contact with each other. This stage sets in if collisions are successful in bringing drops close to each other, say to a distance smaller than their size. While this happens, the relative velocity of drops towards each other decreases at first, and depending upon the forces or interactions that push or pull the drops together, the draining film is able to thin down. Eventually, the attractive van der Waals forces (for example), cause the film to rupture and bring the drops in close contact with each other. Interaction forces between two spheres or drops can be calculated using Derjaguin approximation [47], and in general depend upon contributions from the interparticle interaction potentials that could arise from electrostatics, van der Waals forces, solvation effects, etc [10, 14, 47]. The magnitude of external forces relative to the capillary forces within the drop determines whether the drops remain spherical or deform, making the apparent contact region look-like a disc of disperse phase fluid [10]. If the drops approach each other head-on, the possibility of collision is higher than in the case

where the drops are off-center and just glide over each other, before the draining film is able to thin. The role of draining film was apparent to Lord Rayleigh by 1899, where he followed up the jet collision papers mentioned earlier [45, 46, 48]. The role of draining film is examined later for drop-drop and drop-substrate scenarios observed in the growth and assembly of ordered arrays of noncoalescent drops that concern us.

Only when the drops have enough time to get within a critical distance of each other, the third stage of actual coalescence sets in. The third stage itself involves drops touching each other and then the higher interfacial cost (due to the higher surface tension of two drops in contact compared with a single drop) drives them into a single, bigger volume. (See Eggers, et al for a discussion on coalescence [49]) Once the interfacial forces become involved, the coalescence is instantaneous if the colliding drops are surrounded by a gas, though in certain cases, drop can break apart after coalescence as well, so stability analysis of compound drop is required [12].

The ability of coalescence is thus determined by the efficiency and time scales involved in each of these three stages. In the sections that follow, each stage for drops in vapor phase as well as when they are dispersed in polymer solution is examined. Since the first problem is basically of liquid drops dispersed in vapor phase, analogies from atmospheric physics will be presented for collision and coalescence in air [5, 13, 50]. In fact, the binary collisions of small drops and their coalescence is of interest not only in atmospheric physics, but also in spray combustion [12], ink-jet printing, spray paints, aerosol coagulation [5], etc. In recent years, noncoalescence of drops that takes place to the continuous renewal of draining film has received particular attention from the engineering community, as summarized in the review by Neitzel and Dell'Aversena [7]

(and the references therein). The kinetics of coalescence of the lower viscosity water drops immersed in much higher viscosity polymer solution should be similar to the coalescence behavior of phase separating polymer fluids or polymer blends, which is of particular interest in the field of polymer blends that aim to produce materials with required properties [11, 21-24]. In both cases, the underlying problem of aggregation resembles the similar problem of aggregation that has been investigated in greatest detail to explain colloidal instability [14, 43]. The dynamics of coalescence, including the drainage film flows, is crucial to the understanding of foams and emulsions as well [10, 15-20].

5.2 Collision Efficiency

5.2.1 Smoluchowski's coagulation rate

Colloidal particles are typically stabilized against aggregation by the use of electrostatic repulsion or through steric hindrance [14, 51]. Aerosols are colloidal in nature, as are small drops dispersed in vapor or liquid phase and hence their coalescence behavior can be understood using the same coagulation kinetics that applies to colloidal matter [5, 52]. Smoluchowski [41, 42] was first to model the rate of coagulation of colloidal particles in terms of the diffusion constant of the particles in question, D_{ij} and their concentration ϕ_i and ϕ_i to be

$$J \approx \phi_i \phi_j D_{ij} \tag{5.1}$$

This thesis discusses the development of colloidal physics at great length in context of colloidal gold nanorods in a later chapter, and the interested reader may wish to delve into the aspects related to Brownian motion and colloidal stability described in chapter 8.

Smoluchowski's argument implies that, since for the initial stages the number density of drops as well as their average size is small, the probability of drops encountering each other turns out to be vanishingly small. Since the collision probability by the simplest diffusion based process is itself small, even without considering the effectiveness of the collision in making drops coalesce, the lack of coalescence in initial stages is likely. Given the fact that Smoluchowski's model amount to considering collision process as a ballistic process, as shown in Figure 5.2 (a) similar to ideal molecular collision theory, and all drop-drop interaction including hydrodynamic interactions are neglected, various researchers have formulated the problem of the collision efficiency by taking hydrodynamics into account [5, 10, 11, 13, 14, 44, 53]. In this case, as the drops follow the trajectory or the streamlines around other drop, as shown in Figure 5.2 (b), the chances of collision are even lower.

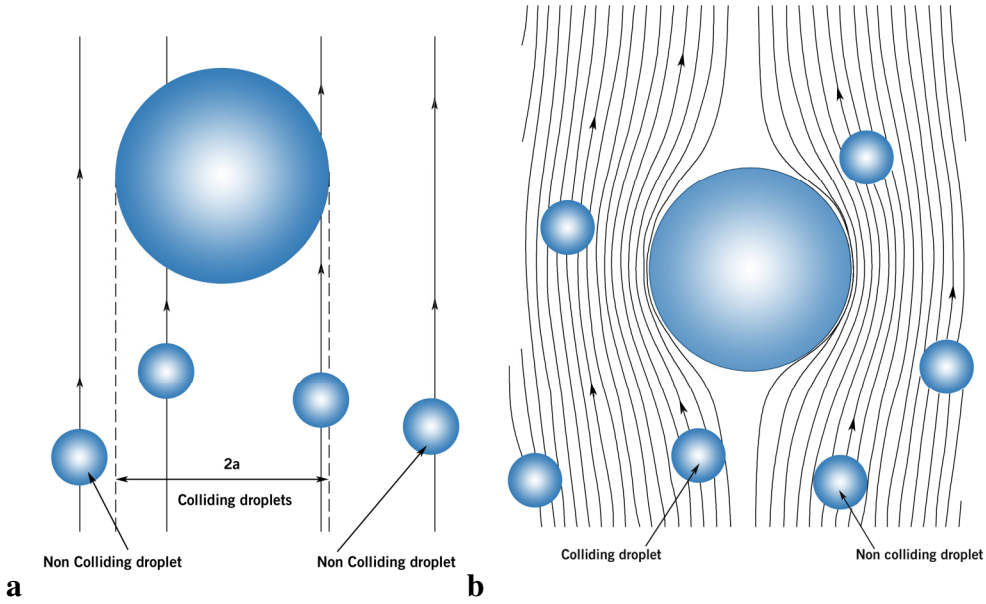

Figure 5.2 (**a**) Drops colliding in a ballistic fashion. Collision occurs if smaller drops lie in a region defined by the size of the drop. (**b**) Small drops follow trajectories as illustrated, while big drop moves under external forces. The chances of collision are smaller in trajectory model. (Adapted from ref. [8]).

5.2.2 Collision efficiency based on trajectory model

In the context of rainfall, coalescence is a key process, required for drops to grow to the sizes that can descend to earth as rain, and the key ideas about the efficiency of drop as collector were detailed by Langmuir [44]. Langmuir recognized that his model was limited to drops following Stokes' law only, and later this problem has been revisited by several researchers [5, 13, 54-57]. The first task in the study of coalescence of drops involves understanding the fact that if a drop of size a_2 approaches a bigger drop of size a_1 horizontally, the small drop is captured only if the vertical offset of the drop is within a critical distance, y_c from the horizontal axis passing through the bigger drop, as shown in Figure 5.3 The ratio, y_c/a_1 is called linear collision efficiency and provides a dimensionless measure of tendency of collision. The more commonly used measure in atmospheric physics is called collision efficiency, E, which is the ratio of collision cross section, πy_c^2 to the geometric cross section defined by $\pi(a_1+a_2)^2$. Since a small sphere follows the trajectory as shown in Figure 5.3, the collision efficiency, E is always $E < 1$, which has been found by various groups as illustrated in the Figure 5.3. Even when the collision does occur, not every collision leads to coalescence. In atmospheric physics, the success of collisions is defined in terms of the collection efficiency, which decreases as the size of drops becomes similar.

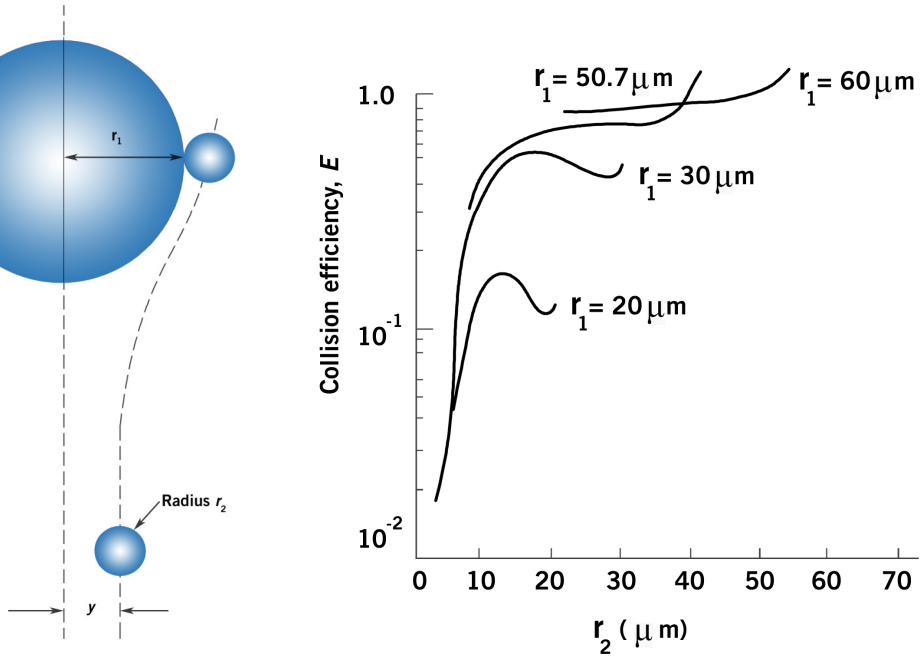

Figure 5.3 A schematic showing collision of drops and a typical plot of collision efficiency of water drops, showing how the efficiency of collision is extremely low for drops under 10 μm. (Adapted from ref. [58]).

While the coalescence efficiency of drops is low, the formation of rain drops requires growth of the drops by coalescence between droplets, which is brought about by growth of few drops that are large enough to act as collector drops. Figure 5.4 shows a schematic of how the collector drop collides with smaller drops that are formed primarily from a condensation growth mechanism. As the collector travels under influence of gravity, the small drops that encounter it, can slide past the drop without colliding or tend to bounce off. The bounce of drops or jets (mentioned earlier) is contributes to low collection efficiency. The overall coalescence rate is controlled by a combination of collision and collector efficiency, and if the typical numbers from atmospheric physics studies are used [5], drops that are 10 μm or lower, not only have low collision efficiency but also have low collection efficiency.

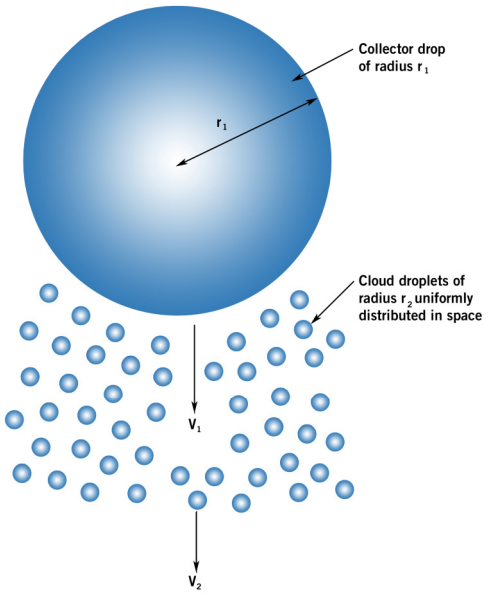

Figure 5.4 A large collector drop falls under gravity with velocity v_1 while smaller drops move with a lower sedimentation velocity, v_2. The collection efficiency describes how effectively small drops coalesce with the large drop. (Adapted from ref. [58]).

5.2.3 Rebound of colliding small drops

When drops approach each other head-on, the probability of collision is high. The collision of drops in air can result in a bounce if the pressure in the intervening film deforms the drop surfaces. In such a case, the kinetic energy of the drops is converted into their deformation energy, and if the non-hydrodynamic interaction forces do not succeed in bringing drops together, the deformed drops slow down and release the energy as if connected a by a hypothetical spring which relaxes back as soon as forces pushing the drops together are overcome. Such collisions have been studied for a range of gas pressures, velocities and drop sizes by a number of researchers [5, 12], including the recent study Gopinath and Koch [59]. The authors discussed the rebound process under various conditions, and the comparison here is carried out for the conditions that are typical for the breath figure templated assembly.

For a drop-vapor interface with interfacial tension σ, the parameters that influence the collision process are described in Table 5.1 using the dimensionless parameters identified by Gopinath and Koch [59]. For water drops with density, ρ the relevant parameters for drop include Weber number, We_d, capillary number, Ca_d based on drop velocity, and Reynolds number, Re_d based on drop properties. The Weber number is the ratio of inertial force to the surface force, whereas the Capillary number is the ratio of flow-based shear force to the surface force. These are quantified for the range of drop sizes and possible drop velocities likely to be encountered in the breath figure templated assembly process. The collision dynamics is influenced by the intervening vapor phase as well, and the corresponding parameters for the vapor phase are Weber number based on vapor density, capillary number based on vapor viscosity and the corresponding Reynolds number. The drop inertia is characterized by Stokes number, St, which is the ratio of the time over which the drops move a distance comparable to their size to the viscous relaxation time that depends upon the force exerted by the surrounding gas.

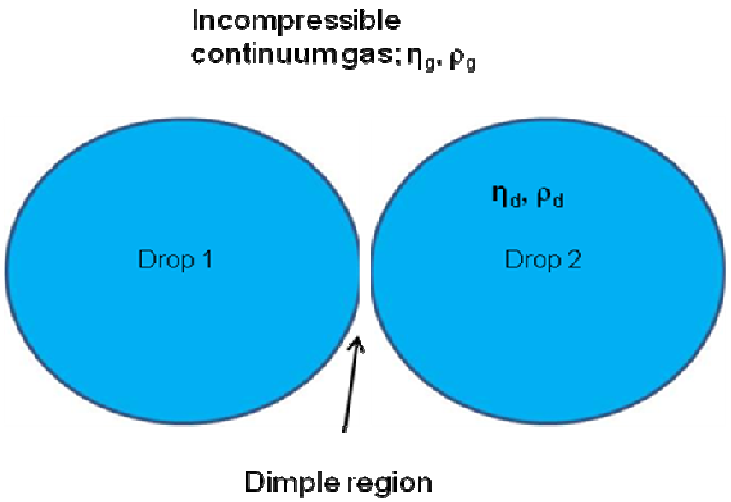

Figure 5.5 Collision of small drops in a gas shown schematically, (adapted from ref. [59]).

Table 5.1 Dimensionless parameters relevant to the collisions of water drops formed in typical conditions during breath figure templated assembly.

Quantity	Symbol	Definition	Drop size dependence	Drop velocity dependence
Radius	R		0.01-10 μm	1
Ambient pressure	P		1 atm	
Velocities	U		1 cm/s	0.001-100 cm/s
Gas Capillary number	Ca_g	$\eta_g U/\sigma$	2.5×10^{-6}	$O(10^{-9}\text{-}10^{-4})$
Gas Weber number	We_g	$\rho_g U^2 r_d/\sigma$	$O(10^{-11}\text{-}10^{-8})$	$O(10^{-13}\text{-}10^{-3})$
Stokes number	St	$2We_d/9Ca_g$ $= 2\rho_d U r_d/9\eta_d$	0.0013 - 1.3	.00013-13
Drop Capillary number	Ca_d	$\eta_d U/\sigma$	1.2×10^{-4}	$O(10^{-7}\text{-}10^{-2})$
Drop Weber number	We_d	$\rho_d U^2 r_d/\sigma$	$O(10^{-8}\text{-}10^{-5})$	$O(10^{-12}\text{-}10^{-2})$
Drop Reynolds number	Re_d	$\rho_d U r_d/\eta_d$	$O(10^{-4}\text{-}10^{-1})$	$O(10^{-5}\text{-}1)$
Gas Reynolds number	Re_g	$\rho_g U r_d/\eta_g$	$O(10^{-5}\text{-}10^{-2})$	$O(10^{-6}\text{-}10^{-1})$

The rebound of the drops occurs when the following conditions are met: 1) $Ca_g \ll 1$, 2) $St \sim O(1)$, 3) $Re_d \gg We_d^{0.5}$ and $We_d \ll 1$. Thus rebound of the drops is likely when the drop velocities are reasonably small, so that the surface forces dominate over the inertial effect (or kinetic energy of colliding drops) as well as over the shear effect generated within the drop. Table 5.1 lists the values for water drops involved in the breath-figure-templated assembly process, and it is apparent that the likelihood of rebound for water drops is large for the range of velocities and drop sizes typically

encountered in the process. The estimate for velocities is made from both the air flow velocities typically used in the experiments and from the velocities of drops tracked in movies collected by Lulu Song, which is described in the next section. Thus while the low collision probability itself leads to low fraction of drops encountering each other, even when they collide with the greatest kinetic energy possible for the system, nearly elastic rebounds make the water drops display the observed noncoalescence behavior.

5.3 Drops near the interface

The crux of our arguments so far can be summarized as follows: water drops nucleate and grow in air and are eventually captured by the polymer solution. There are several unexplored questions about where the drops grow, when they contact and sink into the solution if they levitate, and about the parameters that control the behavior of drops near the interface.

In the studies by Jayarante and Mason [54], drops of water of diameters 120-400 μm were made to collide with air-water interface and their bouncing was observed as a function of incidence angle. Further, in the early experiments in atmospheric physics (see the text by Mason [13], for example) that used polymer solutions to trap water drops formed in a condensation experiment mimicking cloud or fog formation, it was determined that the size distribution of captured drops is biased towards the larger size drops. Indeed, if the drops follow the trajectory directed by air flow, the smallest size drops are likely to be carried away by air flow, in a fashion quite similar to their low collision efficiency with spherical collectors (larger drops), as argued earlier. The problem of impaction of small particles or drops with collectors of different shapes and

sizes is itself a widely studied problem in the field of filtration, colloids and of course, in atmospheric physics [13]. For now, let us leave the impaction problem as an open question and focus on the drops that do become integrated in the substrate, and determine what factors assist or resist their capture.

Dell'Aversena et al [26] carried out experiments with a drop of fluid brought into close contact with the bath of same fluid such that the fluid bath spins slowly, creating an airflow over the fluid, that delays the coalescence with the drop, even when the temperature difference between the drop and the bath goes to zero. In a number of recent experiments, the levitation of drops was observed over a vibrated bath, where the bouncing of drops creates a continuously replenished film of vapor that prevents the drop from coalescing with the bath [60-63] and if a population of drops is used, they self-organize into a hexagonally packed array [63]. Similarly levitation of drops over hot surfaces can be observed in any kitchen by sprinkling a few drops on a hot plate, and this phenomenon, called Leidenfrost effect since 1756, relies on drop weight being balanced by vapor that is replenished by evaporation from the droplet itself [64].

5.3.1 Normal force for a drop moving parallel to interface

For an isothermal case with a stationary drop placed close to a moving liquid bath, or alternatively a drop set in relative motion parallel to the surface, the flow in the film that separates the substrate and the drop can be described using the textbook examples [65] of lubrication flows first described by Reynolds in 1886 [66]. For the sake of argument, the shape of the region between the drop surface and the substrate can be approximated by an inclined plate and a flat surface undergoing a relative motion with

respect to each other with a velocity, U. By treating the flow within this region by the lubrication approximation (described below), i.e. by considering the nearly unidirectional, viscous flow in the narrow gap with $v_x = v_x(x,z)$, and pressure, $P = P(x)$ only, the Navier-Stokes equations [67] reduces to:

$$\frac{\partial^2 v_x}{\partial z^2} = \frac{1}{\eta}\frac{dP}{dx} \tag{5.2}$$

The requirements for lubrication approximation to be valid [65] for a narrow channel amount to saying that P is approximately a function of x only, velocity in z direction, V is small (using continuity equation, the scaling is $V/U(\sim h^*/d)$ <<1 and the flow is such that Re << 1, for drop or plate of size d, with maximum and minimum heights of inclined plate as h_1 and h_2 and $h^*=(h_1+h_2)/2$, the normal force for plate with length, L and width, W can be derived easily and is given by Batchelor [68] to be

$$F_1 = \frac{6\eta_a U L^2 W}{(h_1 - h_2)^2}\left[\log\frac{h_1}{h_2} - 2\frac{h_1 - h_2}{h_1 + h_2}\right] \tag{5.3}$$

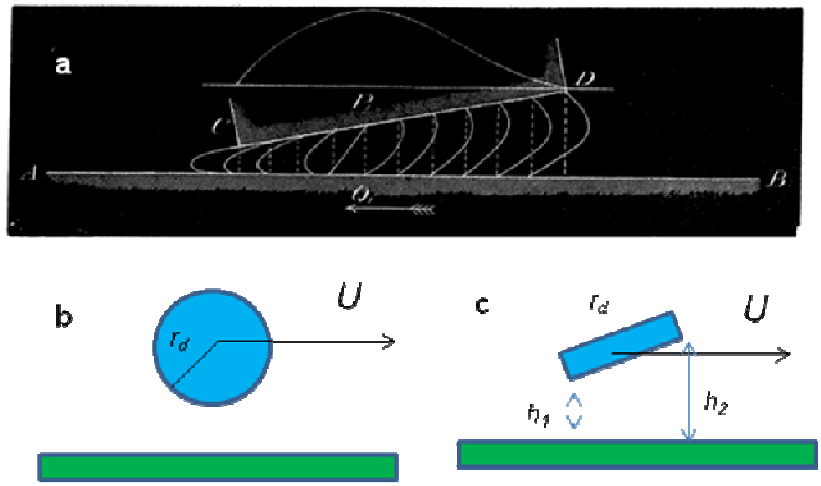

Figure 5.6 Normal force generated by Lubrication flows (**a**) The sketch of lubrication flow from Reynolds (**b**) Drop moving parallel to the interface (c) An inclined plate moving with the same velocity as the sphere.

The velocity of the drops can be determined from the experimental data (collected by Lulu Song) by tracking the motion of drops. A representative plot of the mean square displacement of drops with respect to displacements from an origin defined to be the location at $t = 0$, is shown in Figure 5.7. The drop velocity, U, is at most a few 100 μm/s.

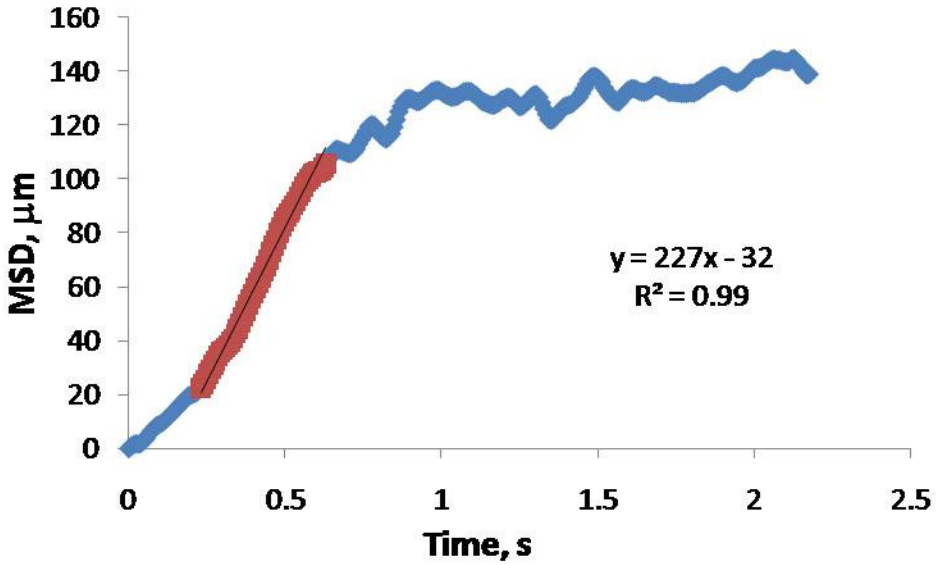

Figure 5.7 Root mean square displacement of a drop of water tracked as it moves in the direction parallel to the plane of the substrate consisting of hexo-PPE in CS_2 (obtained from unpublished experiments/movies from Lulu Song). The fit is for the indicated linear region of the graph.

For a drop with micron size, travelling at a distance of 1 micron from the substrate (this height is much larger than the typical distance at which van der Waals forces become relevant), the normal force can be estimated using $L = W = d = r_d$ to be $F_1 \sim 10^{-14}$ N using the equation 5.3 while the weight of the drop,

$$W_d = (4/3)\rho_d g \pi r_d^3 \qquad (5.4)$$

itself is ~ 0.4 x 10^{-14} N, which can certainly be balanced by the normal force generated by the lubrication flows. Since both $F_1 \sim r_d^3$ and $W_d \sim r_d^3$ depend upon the volume, for the given growing drop, the normal force will continue to balance the drop as long as the

velocity and height of the drop do not change appreciably. It must be added that since $F_1 \sim (h_1-h_2)^{-2}$ or the normal force scales with the inverse square of the drop height over the substrate. So while the effect of decrease in drop velocity is to decrease the normal force, the decrease in drop height makes it increase or stay higher than weight for some time.

5.3.2 Normal force created by the flux of evaporating solvent

In the case of drops moving over an evaporating polymer solution, there is a constant flux of solvent vapor that depends upon the rate of evaporation of the solvent. The fractional rate of mass loss was computed in Chapter 3 for different solvents and the corresponding rate of mass loss per unit area, $\dot{J}$, can hence be considered as a known quantity. If the relative motion between the drop and the substrate is zero, the normal force, F_1, computed above goes to zero. But in the case of evaporation, the region between the drop and the substrate will have a flow due to the vapor flux. In the experiments on magnetic levitation of Helium drops, Weilhert et al [69] reported that such a vapor flux can form a stable film between drops preventing them from coalescing. For two drops next to each other such that r is distance from the center of contact and z is the distance of approach between the two (flattened) drop, Weilhert et al [69] note that the gradient in pressure term is

$$\frac{dP}{dr} = -\frac{2\pi r^2 \dot{J}}{\rho_{gas}} \frac{3\eta_{gas}}{8\pi r z^3} \tag{5.5}$$

Considering the gradient in pressure in x-direction in the Navier-Stokes equation for lubrication equations, and again approximating the drop over interface as an inclined plate, the normal force that is exerted by the flow resulting from solvent vapor flux

(ignoring all other flows, motion of drop itself and the temperature gradients) is derived and it turns out to be,

$$F_2 \sim \frac{3\eta_{gas}\dot{J}r_d^{\,3}}{\rho_{gas}(h_1-h_2)^2}\left[\log\frac{h_1}{h_2}-\frac{h_1-h_2}{h_1}\right] \tag{5.6}$$

The normal force turns out to be quite similar to the force computed for relative motion of plate over a substrate, the only difference being in the magnitude of effective velocity, U_E which in this case is proportional to $\dot{J}/\rho_{gas}$. The magnitude of U_E varies during the experiment in a fashion dictated by the rate of mass loss, which was described in Chapter 3. The simplification of treating both drop surface and substrate as solids and flat, and neglect of the changes in ambient temperature conditions imply that the estimate is quite approximate. It is important here to realize that the effective normal force generated by this evaporation term turns out to be significantly larger than drop weight for initial phase, where the rate of solvent evaporation is at its highest value. A typical estimate for CS_2 evaporation implies the normal force up to ten times the weight of the drop is easily generated, by computing $\dot{J}/\rho_{gas}$ using the results from experimental and theoretical results described in Chapter 3. In reality, the normal force decreases as a square of distance, though for drop height greater than drop size, the lubrication approximation itself breaks down. Further, the rate of evaporation depends critically on the choice of solvent, and it turns out that not only the nucleation and growth of drops is affected by the solvent vapor flux, the ability of drops to grow in levitated state also depends upon it. Hence the choice of solvent is crucial as it sets the timescales for various dynamic and kinetic processes.

5.3.3 Normal force due to thermocapillary flows

It has been argued by Srinivasarao et al [25] that growing drops could be levitating above the solution surface, and the possible cause of levitation is a thermocapillary flow established by the difference in the temperature of growing drops and the polymer solution. The possibility of levitating a drop or a bubble by Marangoni stress (or thermocapillarity) was first realized by Young et al in 1959 [70]. The flows due to temperature gradient that occur within and outside a drop immersed in a fluid have been utilized for drop transport by many researchers [71], including the author [72] who studied flows and chaotic mixing within a drop moving under a temperature gradient. But in the context of breath figure templated assembly, it was only recently that Fisher and Golovin [40] carried out theoretical investigation of the problem, illustrating that the temperature gradient induced in this process, could in principle create Marangoni effects that allow drops to levitate at a steady-state separation distance. The authors assume constant solvent vapor flux and constant temperature gradient and consider thermocapillary forces that act on substrate gas interface and the droplet phase. According to Fisher and Golovin [40], the balance of two thermocapillary flows in drop and in substrate causes the flows within the gas film that act to move the drop away from or towards the interface respectively. In the absence of flows in the substrate, Marangoni effect and gravity effects on the drop can still balance each other, making drop levitate at a certain distance *d* above the interface. According to Fisher and Golovin [40], "Without thermocapillary flow at the drop surface, there is no mechanism for levitation at all."

In a different study on Marangoni floatation of drops by Savino, Paterna and Lappa [73], levitation was observed experimentally for a case where the drop was cooler

than the substrate (and drops were ~ 1 mm or over in size), interface was deformed and the flow at drop gas interface was negligible. In this case, it was found that Marangoni flows keep the drop afloat for a long period of time, and the pressure built up within the curved interface supports the drop. Fisher and Golovin [40] estimated that the substrate keeps a planar interface irrespective of presence of the drop, and compute a radius of curvature, δ_{FG} as $\delta_{FG} / \mathrm{r_d} \sim \sigma / \left(\rho g r_d^{\,2}\right)$. Curiously they cite Savino et al [73] for formulating this argument, though Savino et al [73] calculate a "deformation factor" for substrate,

$$\delta_s \sim W_d / \sigma_s d \sim \left(\rho g d^2\right) / \sigma_s \tag{5.7}$$

and another for drop as

$$\delta_d \sim (W_d / d^2) / (2\sigma_w / d) \sim \left(\rho g d^2\right) / 2\sigma_w \tag{5.8}$$

and say that the ratio $\delta_d / \delta_s \sim \sigma_s / 2\sigma_w \sim$ O(0.1) for their case shows that drop is quasi-spherical. The radius of curvature computed by Fisher and Golovin [40] is actually inversely proportional to drop weight (unlike the factor of Savino et al [73]) and has dimension of length, so is different argument than from the paper they cite.

The right procedure for calculating substrate deformation involves calculation of the curvature (shown in Figure 5.8) using constraint that the weight of the drop, W_d and the weight of substrate fluid below $H(r)$ are equilibrated by the hydrostatic pressure at the bottom and the surface tension cost at the interface. This procedure can be adopted to determine the profile $H(r)$ and to find h_∞ as described by Savino et al [73]. Since the lubrication flows considered herewith certainly show that alternative mechanisms of levitation are plausible, and since the study by Fisher and Golovin [40] treats a hypothetical case with constant vapor and temperature gradients, their claim about

thermocapillarity as the only mechanism is somewhat overstated, as is the argument that the substrate undergoes negligible or no deformation.

A

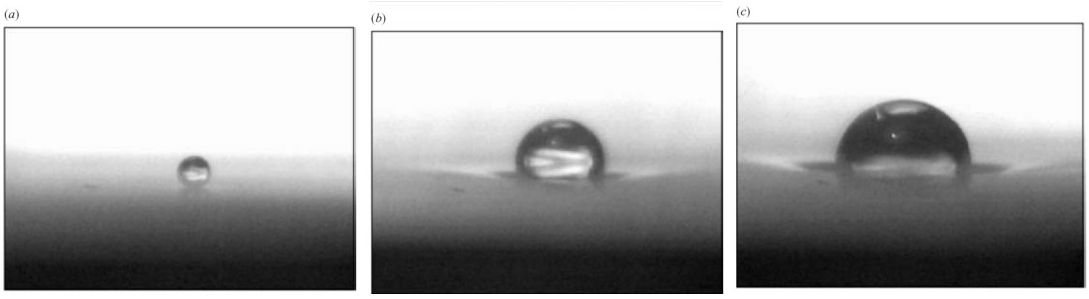

B

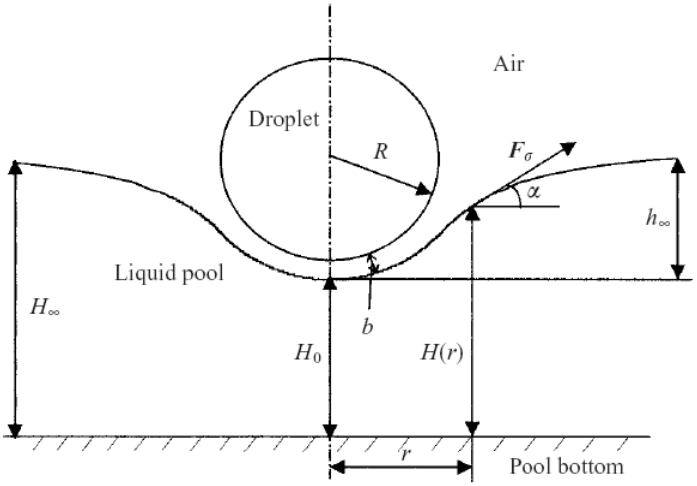

Figure 5.8 Floating drops as visualized by Savino et al [73] A. Marangoni levitation of a drop over the pool of the same liquid. B. Schematic for the meniscus deformation in pool.

While a true test of thermocapillary forces balancing the drop over the substrate and calculation of substrate deformation is not attempted in the present work, in what follows the phenomenological argument of Savino, Paterna and Lappa [73] about pressure build-up is applied to a case where the only flow allowed is a thermocapillary flow within the drop. Thus unlike Savino el al [73], who use Marangoni flow and temperature gradient in the substrate for their analysis, we use the relevant Marangoni

flow for the water drop. The pressure generated by the Marangoni flow can be approximated by using the following formula (deduced from the computation given in ref. [73])

$$\Delta p = \frac{\eta_a V_M}{b^2} r_d = \frac{\eta_a \sigma_T}{\eta_{subs} b^2} r_d^{\,2} \frac{(T_{subs} - T_{air})}{\delta_{BL}} \tag{5.9}$$

While the equation 5.9 is based on the corresponding analysis by Savino, Paterna and Lappa [73], the velocity in our case corresponds to the Marangoni velocity for the drop. The Marangoni flow is computed under a temperature gradient of $(T_{subs} - T_{air})/\delta_{BL}$ (~20 ^{o}C/1mm) where substrate temperature is set by evaporative cooling, boundary layer thickness by air flow velocity through Reynolds number and the term σ_T is the coefficient of surface tension variation with temperature (10^{-4} $Nm^{-1}K^{-1}$ for water). This temperature gradient is only approximate, and provides the upper limit for the estimate of Marangoni velocity in the drop. The normal force estimate turns out to be $F_3 = \Delta p r_d^2$ ~ 1.25 x 10^{-14} N for $b \sim r_d \sim 1$ μm, which is definitely comparable to or greater than weight, W_d ~ 0.4 x 10^{-14} N. As the distance between the drop and interface decreases, the pressure increases by the inverse square law described by equation 5.9. Eventually the temperature gradient itself decreases and so the contribution of thermocapillary flows becomes negligible. Another way of making this estimate is to use $U = V_M$ in the formula for F_1, and since V_M ~ 100 μm/s, the normal force generated can sustain the weight of small drops. In either case, the temperature gradient depends upon the difference between the substrate temperature and the temperature of the air flow. The temporal variation of the substrate temperature, modeled in the chapter 3, can be used to compute the temporal variation in normal force for a drop of given size at a certain fixed height. In reality, the condensation

or evaporation of water affects the temperature gradients as well. Therefore, the packing density as well as local vapor pressure and temperature can vary over the substrate. The only way to describe the effects more accurately would be to divide the area over the substrate into a mesh, and calculate mass and heat transfer, under all different flows, and since it is a multi-body, dynamic problem, the task will be challenging and interesting, and is left for the future researchers.

5.3.4 Observation of levitation

Typical experiments on drops bouncing on a vibrated fluid bath, or Marangoni floatation [73] or observation of thermocapillary flow induced nonwetting [6, 7, 28] between two drops use 1 mm size drops. Thus when the distance between the drop and interface is of the order of few microns, beautiful Newton rings or interference fringes are observed [28, 60, 62]. These have been utilized in studies on bouncing drops as well as drops brought in contact to calibrate and observe the presence of thin film that separates the two fluids. In a typical experiment in breath figure templated assembly, the drop sizes are of the order of a few microns at most, and the largest drops are present only in the last stage of the assembly process. The nucleation and growth of drops depends upon the state of supersaturation set by solvent evaporation and air flow conditions. In an earlier chapter, an evaporation model was described, where the rate of mass loss was related to diffusion limited mass transfer of solvent to air flow from a film with a constant surface area. As long as polymer is present, the contact line of the substrate is fixed and the model from Chapter 2 is applicable. But for a pure solvent, the evaporation is accompanied by movement of contact line, and the conditions are such that much larger

drops of water form in shorter time. In Figure 5.9, a number of such drops are captured, 0.32s after the start of the process, and most drops appear to have Newton rings within them, and some of these drops appear to be over twenty microns in size. The frame is taken from a series of movies that were collected by Lulu Song, though these results were never reported by her, and no such images are found in published literature for breath figure templated assembly. In spite of the fuzziness of the image (drops translate quite fast compared to the capture rate), the image indicates that the drops must be levitating!

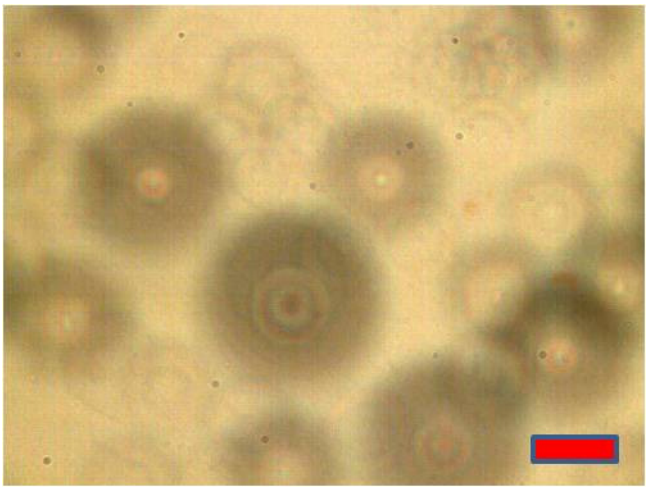

Figure 5.9 Optical micrograph of water drops, levitating over evaporating pure CS_2 seen after 0.32 s. The interference fringes cannot be seen after the first second. (Extracted from Lulu Song's experimental data).

In essence, it is possible for the normal forces that act on the drop, due to relative motion of the drop with respect to the interface, due to flux of evaporating solvent and due to the thermocapillary flow inside the drop can balance the drop weight. The estimates in this section are at best approximate, since each case involved the stated, simplified assumptions. In reality, all three normal forces act together against the weight of the drop (though apart from weight, possibly other forces act to bring the drop closer to the interface). The key point made here is that the drops that are nucleated in air, will

grow to a certain size, before entering the substrate, and their levitation or lingering is possible under well known natural laws. While scaling arguments presented here capture the essential physics, a more quantitative approach is required to determine the time period for which drop is levitating, and for determining the precise size at which drops sink into the substrate.

5.4 Non-coalescing floating drops immersed in concentrated polymer solution

In breath figures formed in pre-cooled, non-volatile liquids, the delayed coalescence of drops, which allows for their assembly into rafts, is attributed to the draining time required for the solvent to move out which scales linearly with viscosity. Further it was found that water drops can grow without coalescence as long as the fractional area occupied by them is small (< 0.4). These non-coalescent drops were found to be stable for tens of seconds [74]. In the case of polymer solution, the same drops will need to drain out a fluid with much higher viscosity. As the polymer solutions progress from a dilute to semi-dilute state, the associated viscosity increases by approximately three orders of magnitude or higher [75]. Thus in the late stages, where droplets are closely packed and lie within the polymer solution, the draining time for the increasingly viscous polymer solution will be three to four orders of magnitude larger than that of the pure solvent. This simple estimate is for the case when draining time is considered to be a linear function of the viscosity of the intervening fluid. Since the whole experiment is over in a span of 100s or so, the kinetic barrier or time scale involved is longer than required for the drops to coalesce.

As drops approach each other, the kinetic energy of drops needs to be damped by utilizing it in forcing the draining film out, and the maximum viscous dissipation happens as drops approach each other. As the intervening fluid is driven out, the resulting stresses can cause a local deformation of drops [10]. Quite like what happens in the drops colliding in air, the deformation of drops from their equilibrium spherical shape creates a bending moment that makes the drops repel each other, which to a naked eye would appear to be an elastic collision (as often noticed in collision of water drops in breath figure templated assembly). The elasticity of deformable drops is observed and studied for emulsions, where surface tension term is usually not as strong as it is for water drops. The repulsion interaction for water drops is derived in the next chapter. But the detailed discussion of velocity of approach of deformable drops, bending energy and of the effect of interaction forces that become relevant after a critical distance is crossed can be found in the text by Kralchevsky and Nagayama [10] (and the references therein).

The viscosity of the polymer solution depends upon the molecular weight, concentration and the architecture of polymer. The choice of initial concentration of polymer, as well as the type and molecular weight of the polymer then affect the viscosity and surface tension of the solution at any given instant during the self-assembly of water drops. For drops to grow and self-assemble, the viscosity needs to vary at a rate that allows drops the mobility to evolve into these closed-packed arrays. The highly ordered pores are typically produced for initially dilute polymer solutions (0.1% - 5%). Higher pore size is found for lower concentration solutions. Differences in the assembly and pore size observed for polymer-solvent systems observed for varied architecture, molecular weight and concentration, (in Table 2.1) keeping the other parameters constant, are

possibly due to the difference in the rate of the change of viscosity of the underlying fluid substrate.

The coalescence behavior of drops in another liquid phase has been studied in detail by many researchers [53, 76, 77], who typically treat film drainage as a problem with drops constrained to move with either a constant force [77] or a constant relative velocity [53] to each other, and this force could be result of van der Waals interaction at small distances (for example), buoyancy force or just Brownian forces. Yang et al [21] point out using experiments and theory that except for the head on collisions, real drops cannot collide as if a constant force was pushing them together, and that drop pairs rotate as a pair, relative to an axis fixed in the external flow. If and only if the drainage time for flow under time dependent force is shorter than the duration of the collision, the off-axis collisions result in coalescence. An intuitive argument could be made to explain inefficiency of most collisions: the shear stress generated by flow of draining film is able to make drops glide across each other. This gliding motion and apparent slip of drops against each other allows these drops to not only pack together, but also exhibit local dynamics till very late stage, where the singular or collective motion of drops reduces the disorder in the two dimensional array of drops. The aspects related to assembly will be presented and discussed in the next chapter.

5.5 Conclusions and suggestions for future work

Breath-figure-templated assembly involves nucleation, growth and packing of water drops over an evaporating polymer solution. The drops are able to grow to a nearly monodisperse size and form a close packed, hexagonally symmetric array because of

their noncoalescence among each other. In the present contribution, the noncoalescence of water drops is assessed by accounting for collision efficiency, draining time and coalescence timescale for water drops as they first form and grow in air and later, when they lie in packed array, embedded in the polymer solution. Collision efficiency refers to the probability of drops encountering each other, and this was shown to be low for the case when drop number density and drop sizes are small. The efficiency was assessed using both diffusion and trajectory models, and the reason for their stability turns out to be quite similar to why fog drops are stable and do not coalesce and fall down easily. Using the wealth of studies in atmospheric physics, the noncoalescence scenarios were mapped out, and it was found that the drop size and mobility make even the head-on collisions of drops ineffective, for in this case, the kinetic energy of the approaching drops and pressure created in draining film cause drops to deform slightly. The deformation of the drops coverts their kinetic energy to elastic energy, and if the pressure in the air film is high enough, the drops bounce back as if they hit an invisible wall.

The initial nucleation and growth of drops occurs in air and eventually these drops formed ordered (or disordered) packed arrays in the substrate. In this chapter, the existence and magnitude of normal forces that can balance the weight of the drops and cause them to be levitated over the polymer solution substrate was considered. The normal force generated by relative motion of drop with respect to the substrate was calculated using lubrication approximation and was found to be comparable to the weight of micron size drops. Similarly normal force created by the evaporation flux of solvent was approximated and it turns out to be upto hundred times the weight of drop. A third contribution to normal force was calculated in terms of the thermocapillary convection

that is driven by the temperature gradient that exists around the water drop, and this appears to be comparable to the weight of a micron size drop as well. The evaporation rate and temperature of the substrate vary with time, thus the normal force decreases as bulk of the solvent evaporates away. Similarly the velocity dependent lubrication force is applicable only when drops have sufficient mobility. Since all the three normal forces act simultaneously on the drop, the drops are likely to levitate for major part of their growth regime. Further, experimental evidence was presented for drops levitating over pure solvent, where Newton rings appear within the drops after 0.32 s of the start of the experiment. Since these drops grow to ~20 microns in size, the levitation lasts for only less than two seconds in this case. The noncoalescence observed in the last stages of the process, where drops are close packed, was attributed to the long time required for removing the intervening drainage film. Since the viscosity of the substrate fluid depends upon the initial concentration, molecular weight and architecture of the polymer, the choice of these is important factor in creating conditions for non-coalescence.

In this chapter, the problem of noncoalescence was addressed and was shown to be a multipart problem, involving collisions of drops in air, drop-substrate collisions and levitation of drops, and noncoalescence of drops immersed in polymer solution substrate. Each of these problems has a long history of studies in the field of atmospheric physics, colloids, filtration, polymer blends and emulsions and accurate results for these require elaborate application of fluid mechanics. Since the current analysis was limited to scaling arguments, it would be useful to compute the contribution of various factors listed in this chapter more exactly. For example, a rigorous argument about the duration for which drops can be levitated requires a model that combines the effect of normal forces

generated by drop (or substrate) motion, thermocapillarity and solvent flux. To accomplish this with greatest accuracy requires calculation of all the forces, under the continuously changing substrate and drop properties and by including the heat and mass transfer involved at each stage of the process.

5.6 References

1. Vivekananda, *The Complete Works of Swami Vivekananda*. 2003: Vedanta Pr.

2. Brandt, E.H., *Levitation in physics.* Science, 1989. **243**(4889): p. 349-355.

3. Davis, E.J., *A history of single aerosol particle levitation.* Aerosol Science and Technology, 1997. **26**(3): p. 212-254.

4. Frohn, A. and N. Roth, *Dynamics of drops*. 2000, Berlin: Springer Velag.

5. Pruppacher, H.R. and J.D. Klett, *Microphysics of Clouds and Precipitation*. 2nd ed. 1996: Springer.

6. Dell'Aversana, P. and G.P. Neitzel, *When liquids stay dry.* Physics Today, 1998. **51**(1): p. 38-41.

7. Neitzel, G.P. and P. Dell'Aversana, *Noncoalescence and nonwetting behavior of liquids.* Annual Review of Fluid Mechanics, 2002. **34**: p. 267-289.

8. Lappa, M., *Coalescence and Non-coalescence Phenomenon in Multi-material Problems and Dispersed Multiphase Flows: Part 1, A Critical Review of Theories.* Fluid Dynamics Material Processing, 2005. **1**(3): p. 201-211.

9. Lappa, M., *Coalescence and Non-coalescence Phenomenon in Multi-material Problems and Dispersed Multiphase Flows: Part 2, A Critical Review of CFD Approaches.* Fluid Dynamics Material Processing, 2005. **1**(3): p. 213-234.

10. Kralchevsky, P.A. and K. Nagayama, *Particles at fluid interfaces and membranes*. Studies in interface science, ed. D. Mobius and R. Miller. 2001, Amsterdam: Elsevier Science B. V.

11. Leal, L.G., *Flow induced coalescence of drops in a viscous fluid.* Physics of Fluids, 2004. **16**(6): p. 1833-1851.

12. Orme, M., *Experiments on droplet collisions, bounce, coalescence and disruption.* Progress in Energy and Combustion Science, 1997. **23**(1): p. 65-79.

13. Mason, B.J., *The Physics of Clouds, 2nd ed.* 1971, London: Oxford University Press.

14. Russel, W.B., D.A. Saville, and W.R. Schowalter, *Colloidal Dispersions*. 1989, Cambridge: Cambridge University Press.

15. Robin, T. and D. Ramakrishna, *Coalescence of charged droplets in agitated liquid-liquid dispersions.* AIChE Journal, 1992. **38**(8): p. 1199-1205.

16. Jeelani, S.A.K., R. Hosig, and E.J. Windhad, *Kinetics of low Reynolds number creaming and coalescence in droplet dispersions.* AIChE Journal, 2005. **51**(1): p. 149-161.

17. Dickinson, E., B.S. Murray, and G. Stainsby, *Coalescence stability of emulsion sized droplets at a planar oil water interface and the relationship to protein film surface rheology.* Journal of the Chemical Society-Faraday Transactions I, 1988. **84**: p. 871-883.

18. Ivanov, I.B., K.D. Danov, and P.A. Kralchevsky, *Flocculation and coalescence of micron-size emulsion droplets.* Colloids and Surfaces a-Physicochemical and Engineering Aspects, 1999. **152**(1-2): p. 161-182.

19. Berg, S., E.A. Adelizzi, and S.M. Troian, *Experimental study of entrainment and drainage flows in microscale soap films.* Langmuir, 2005. **21**(9): p. 3867-3876.

20. Weaire, D.L. and S. Hutzler, *The physics of foams*. 1999, Oxford: Oxford University Press.

21. Yang, H., et al., *The coalescence of two equal-sized drops in a two-dimensional linear flow.* Physics of Fluids, 2001. **13**(5): p. 1087-1106.

22. Ha, J.W. and L.G. Leal, *An experimental study of drop deformation and breakup in extensional flow at high capillary number.* Physics of Fluids, 2001. **13**(6): p. 1568-1576.

23. Ha, J.W., Y. Yoon, and L.G. Leal, *The effect of compatibilizer on the coalescence of two drops in flow.* Physics of Fluids, 2003. **15**(4): p. 849-867.

24. Lyu, S., F.S. Bates, and C.W. Macosko, *Modeling of coalescence in polymer blends.* AIChE Journal, 2002. **48**(1): p. 7-14.

25. Srinivasarao, M., et al., *Three-dimensionally ordered array of air bubbles in a polymer film.* Science, 2001. **292**(5514): p. 79-83.

26. DellAversana, P., J.R. Banavar, and J. Koplik, *Suppression of coalescence by shear and temperature gradients.* Physics of Fluids, 1996. **8**(1): p. 15-28.

27. Dell'Aversana, P. and G.P. Neitzel, *Behavior of noncoalescing and nonwetting drops in stable and marginally stable states.* Experiments in Fluids, 2004. **36**(2): p. 299-308.

28. DellAversana, P., V. Tontodonato, and L. Carotenuto, *Suppression of coalescence and of wetting: The shape of the interstitial film.* Physics of Fluids, 1997. **9**(9): p. 2475-2485.

29. Pitois, O. and B. Francois, *Formation of ordered micro-porous membranes.* European Physical Journal B, 1999. **8**(2): p. 225-231.

30. Peng, J., et al., *Formation of regular hole pattern in polymer films.* Macromolecular Chemistry and Physics, 2003. **204**(1): p. 125-130.

31. Haupt, M., et al., *Breath figures: Self-organizing masks for the fabrication of photonic crystals and dichroic filters.* Journal of Applied Physics, 2004. **96**(6): p. 3065-3069.

32. Hao, X.J., et al., *Molecular composite materials formed from block copolymers containing a side-chain liquid crystalline segment and an amorphous styrene/maleic anhydride segment.* Polymer, 2004. **45**(22): p. 7401-7415.

33. Stenzel, M.H., C. Barner-Kowollik, and T.P. Davis, *Formation of honeycomb-structured, porous films via breath figures with different polymer architectures.* Journal of Polymer Science Part a-Polymer Chemistry, 2006. **44**(8): p. 2363-2375.

34. Bunz, U.H.F., *Breath figures as a dynamic templating method for polymers and nanomaterials.* Advanced Materials, 2006. **18**(8): p. 973-989.

35. Jenekhe, S.A. and X.L. Chen, *Self-assembly of ordered microporous materials from rod-coil block copolymers.* Science, 1999. **283**(5400): p. 372-375.

36. Hayakawa, T. and H. Yokoyama, *Fabrication of self-organized chemically and topologically heterogeneous patterns on the surface of polystyrene-b-oligothiophene block copolymer films.* Langmuir, 2005. **21**(23): p. 10288-10291.

37. Deepak, V.D. and S.K. Asha, *Self-organization-induced three-dimensional honeycomb pattern in structure-controlled bulky methacrylate polymers: Synthesis, morphology, and mechanism of pore formation.* Journal of Physical Chemistry B, 2006. **110**(43): p. 21450-21459.

38. Tung, P.H., et al., *Regular honeycomb porous polymer films based on amphiphilic block copolymer.* Desalination, 2006. **200**(1-3): p. 55-57.

39. Ishizu, K., Y. Tokuno, and M. Makino, *Microporous films from diblock copolymer micelles based on solvent-induced mechanism by temperature control of casting solution.* Macromolecules, 2007. **40**(3): p. 763-765.

40. Fisher, L.S. and A.A. Golovin, *Motion of a droplet near an evaporating liquid-gas interface.* Physics of Fluids, 2007. **19**(3).

41. von Smoluchowski, M., *Outline of the coagulation kinetics of colloidal solutions.* Kolloid-Zeitschrift, 1917. **21**(3): p. 98-104.

42. Chandrasekhar, S., *Stochatic Problems in Physics and Astronomy.* Reviews of Modern Physics, 1943. **15**(1): p. 1-89.

43. van de ven, T.G.M., *Colloidal Hydrodynamics*. 1989, London: Academic Press Inc.

44. Langmuir, I., *The production of rain by a chain reaction in cumulus clouds at temperatures above freezing.* Journal of Meteorology, 1948. **5**(5): p. 175-192.

45. Rayleigh, L., *Further Observations upon Liquid Jets, in Continuation of Those Recorded in the Royal Society's 'Proceedings' for March and May, 1879.* Proceedings of the Royal Society of London 1882. **34**: p. 130-145.

46. Rayleigh, L., *On the Capillary Phenomenon of Jets.* Proceedings of the Royal Society of London, 1879. **29**: p. 71-97.

47. Israelachvili, J., *Intermolecular and Surface Forces*. 2nd ed. 1992, San Diego: Academic Press.

48. Rayleigh, L., *Investigations into capillarity.* Philosophical Magazine, 1899. **36**: p. 321.

49. Eggers, J., J.R. Lister, and H.A. Stone, *Coalescence of liquid drops.* Journal of Fluid Mechanics, 1999. **401**: p. 293-310.

50. Rogers, R.R. and M.K. Yau, *Short Course in Cloud Physics, Third Edition*. 3 ed. 1989: Butterworth-Heinemann.

51. Cates, M.E. and M.R. Evans, *Soft and Fragile Matter*. 2000, Bristol: Institue of Physics Publishing.

52. Fuchs, N.A., *The mechanics of aerosols*. 1964, New York: The Macmillan Company.

53. Davis, R.H., J.A. Schonberg, and J.M. Rallison, *The lubrication force between two viscous drops.* Physics of Fluids a-Fluid Dynamics, 1989. **1**(1): p. 77-81.

54. Jayaratne, O.W. and B.J. Mason, *Coalescence and bouncing of water drops at air/water interface.* Proceedings of the Royal Society of London Series a-Mathematical and Physical Sciences, 1964. **280**(138): p. 545-&.

55. Beard, K.V., H.T. Ochs, and S. Liu, *Collisions between small precipitation drops. Part III: Laboratory measurements at reduced pressure.* Journal of the Atmospheric Sciences, 2001. **58**(11): p. 1395-1408.

56. Beard, K.V. and H.T. Ochs, *Collisions between small precipitation drops. 2. Formulas for coalescence, temporary coalescence, and satellites.* Journal of the Atmospheric Sciences, 1995. **52**(22): p. 3977-3996.

57. Ochs, H.T., et al., *Collisions between small precipitation drops. 1. Laoratory measurements of bounce, coalescence, and temporary coalescence.* Journal of the Atmospheric Sciences, 1995. **52**(12): p. 2258-2275.

58. Wallace, J.M. and P.V. Hobbs, *Atmospheric science: an introductory survey*. 2nd ed. 2006, Amsterdam: Elsevier.

59. Gopinath, A. and D.L. Koch, *Collision and rebound of small droplets in an incompressible continuum gas.* Journal of Fluid Mechanics, 2002. **454**: p. 145-201.

60. Couder, Y., et al., *From bouncing to floating: Noncoalescence of drops on a fluid bath.* Physical Review Letters, 2005. **94**(17).

61. Couder, Y., et al., *Dynamical phenomena - Walking and orbiting droplets.* Nature, 2005. **437**(7056): p. 208-208.

62. Terwagne, D., N. Vandewalle, and S. Dorbolo, *Lifetime of a bouncing droplet.* Physical Review E, 2007. **76**(5).

63. Lieber, S.I., et al., *Self-organization of bouncing oil drops: Two-dimensional lattices and spinning clusters.* Physical Review E, 2007. **75**(5).

64. Biance, A.L., C. Clanet, and D. Quere, *Leidenfrost drops.* Physics of Fluids, 2003. **15**(6): p. 1632-1637.

65. Deen, W.M., *Analysis of Transport Phenomena*. Topics in Chemical Engineering, ed. K.E. Gubbins. 1998, New York: Oxford University Press.

66. Reynolds, O., *On the theory of lubrication and its application to Mr. Beauchamp Tower's experiments, including an experimental determination of the viscosity of olive oil.* Philosophical Transactions of the Royal Society London (Part A), 1886. **177**: p. 157-234.

67. Bird, R.B., W.E. Stewart, and E.N. Lightfoot, *Transport Phenomenon*. 1960, Singapore: John Wiley and Sons.

68. Batchelor, G.K., *An Introduction to Fluid Mechanics*. 1967, Cambridge: Cambridge University Press.

69. Weilert, M.A., et al., *Magnetic levitation and noncoalescence of liquid helium.* Physical Review Letters, 1996. **77**(23): p. 4840-4843.

70. Young, N.O., J.S. Goldstein, and M.J. Block, *The motion of bubbles in a vertical temperature gradient.* Journal of Fluid Mechanics, 1959. **6**(3): p. 350-356.

71. Subramanian, R.S. and R. Balasubramaniam, *The Motion of Bubbles and Drops in Reduced Gravity*. 2001, Cambridge: Cambridge University Press.

72. Grigoriev, R.O., M.F. Schatz, and V. Sharma, *Chaotic mixing in microdroplets.* Lab on a Chip, 2006. **6**(10): p. 1369-1372.

73. Savino, R., D. Paterna, and M. Lappa, *Marangoni flotation of liquid droplets.* Journal of Fluid Mechanics, 2003. **479**: p. 307-326.

74. Steyer, A., et al., *Two-dimensional ordering during droplet growth on a liquid surface.* Physical Review B, 1990. **42**(1): p. 1086-1089.

75. Doi, M. and S.F. Edwards, *The Theory of Polymer Dynamics*. 1986, Oxford: Oxford University Press.

76. Wang, H. and R.H. Davis, *Droplet growth due to Brownian, gravitational, or thermocapillary motion and coalescence in dilute dispersions.* Journal of Colloid and Interface Science, 1993. **159**(1): p. 108-118.

77. Saboni, A., C. Gourdon, and A.K. Chesters, *Drainage and Rupture of Partially Mobile Films during Coalescence in Liquid-Liquid Systems under a Constant Interaction Force* Journal of Colloid and Interface Science, 1995. **175**(1): p. 27-35.

CHAPTER 6

THE PURSUIT OF PERFECT PACKING BY NONCOALESCENT WATER DROPS

One of the most deeply interesting aspects of a crystal […] concerns the mysterious process of its growth from a solution […]. The story of the elucidation, as far as it has yet been accomplished, of the nature of crystallization from solution in water is one of the most romantic which the whole history of science can furnish.
A. E. H. Tutton, *The Natural History of Crystals, 1924*
(as quoted in *The Physics of Foams* by D. Wearie and S. Hutzler [1]).

The breath figure templated assembly of holey films involves the *crystallization of non-coalescent water drops*. The physics that governs the nucleation, growth and non-coalescence of water drops was described and discussed in the previous chapters. The growing water droplets that appear over evaporating organic liquids or polymer solutions, organize into clusters or rafts, which later assemble forming a close packed array of nearly monodisperse drops [2-8]. This packed array of drops progressively transforms itself into a highly ordered, hexagonal array in two dimensions and in certain cases, forms a three-dimensional crystal of non-coalescent water drops. The question about how and why drops organize into a highly ordered structure in two dimension are addressed in this chapter.

6.1 Two-dimensional assembly of non-coalescent water drops

The development of ordered structure from initially randomly distributed drops or clusters of drops is easily observed under a microscope, as can be seen in Figure 6.1. The various images in the figure represent the stages of growth and assembly for water drops that are formed in this case over a hexo-PPE/CS_2 solution, exposed to airflow of 1 m/s.

While these images (as well all the other frames mentioned in this chapter) are extracted from the movies recorded by Lulu Song, the aspects related to assembly described here, were not reported or discussed by her.

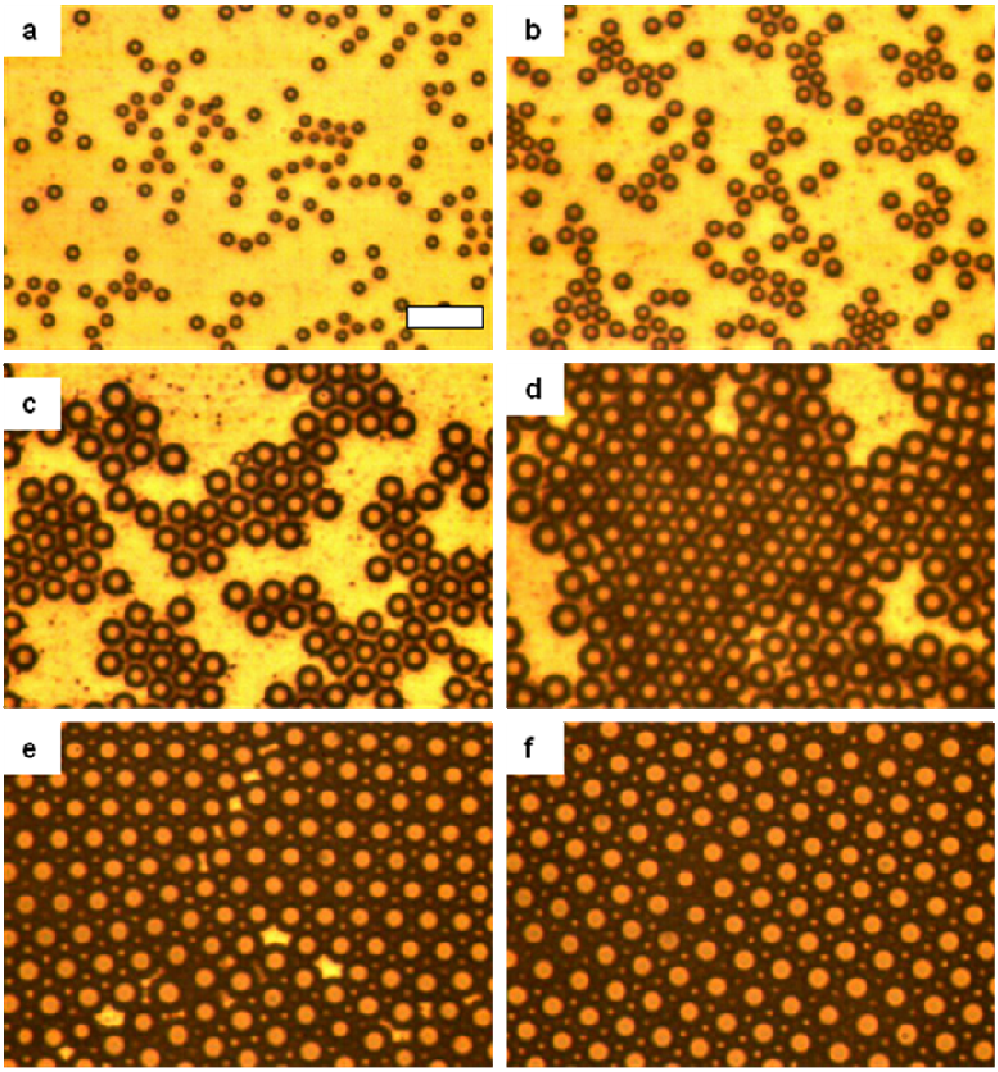

Figure 6.1 Stages of growth and assembly over 0.3% PPE in CS_2 solution, with air flow of 1 m/s. (a) Individual drops as well as doublets and chains visible 0.64s after recording started. (b) Drops grow in size and start to form rafts after 4.5 s. (**c**) Drops locally organize within the rafts after 15.6 s. The size of drops is larger and the average size of rafts is larger. Few drops are seen to be organized as hexagons (d) Rafts start to assemble, while range of drop sizes visible, after 24.8 s. (e) Assembly of drops with stacking faults, vacancies and grain boundaries, after 43.2 s. (f) Ordered array of nearly monodisperse drops, image after 53.4 s.

The initial stage involves formation of drops that grow individually. There is no perceptible size variation among the drops in Figure 6.1 (a). Thereafter as the water drops grow in size, they start to attract each other and form aggregates or rafts. In Figure 6.1 (b), several doublets or larger aggregates are visible. In some experiments, the drops seems to form chains, before they start to aggregate into larger rafts as seen in Figure 6.1 (c). While the drops continue to grow, dispersion in size can be perceived between the drops that lie within the rafts, as opposed to the ones that lie on the edge of the rafts (see Figure 6.1 (d)). Local variations in supersaturation will affect the rate at which drops are growing. As the drops continue to grow, the rafts begin to aggregate further, and when two rafts come together, their local positional order is not commensurate with that of adjoining rafts. This leads to stacking faults or grain boundaries. The drops continue to rearrange themselves till they form the ordered array of drops visible in Figure 6.1 (f), and by this time the size distribution of the drops has become narrower.

Another example of assembly of water drops is extracted from a movie that was captured on PS/CS_2 substrate. The number of drops activated in this case is much larger, and the first few frames images already contain disordered rafts of drops as seen in Figure 6.2 (a). The aggregation and growth of drops makes these rafts connect together forming a nearly percolated network, as seen in Figure 6.2 (b). Like in the case of hexo-PPE/CS_2, the drops at the edge of rafts seem larger in Figure 6.2 (c) and in the next stage, while the rafts have packed tightly, the dispersion in size and stacking faults lead to a very inhomogeneous, disordered structure of Figure 6.2 (d). In the last two frames, the drop sizes continue to grow, size distribution narrows, and by series of rearrangements, the assembly is able to arrive at a reasonably ordered structure. The few dark spots seen

in Figure 6.2 (f) are water drops that are pushed underneath the ordered layer, and their formation will be discussed later.

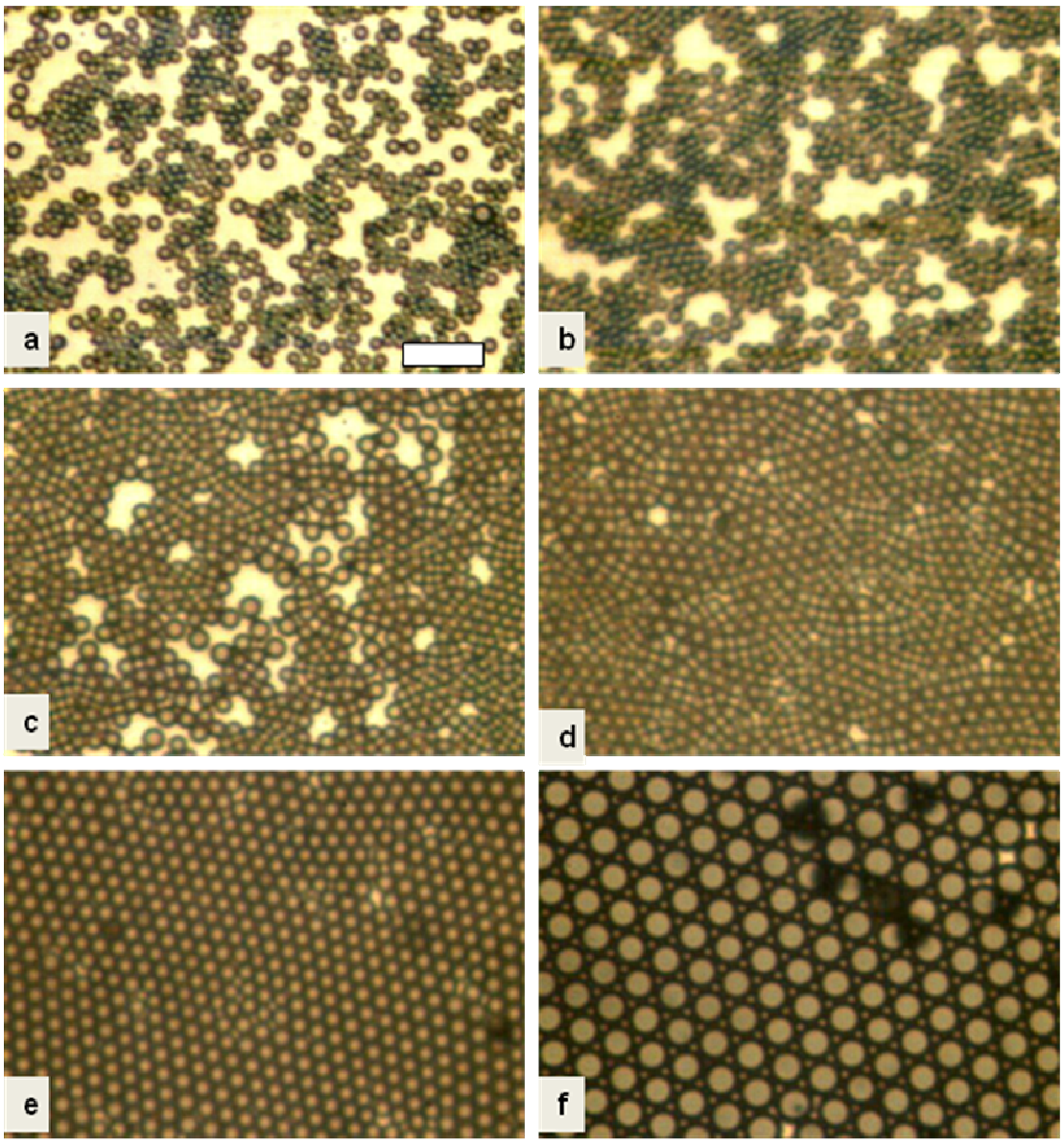

Figure 6.2 Stages of growth and assembly over 1% PS-COOH in CS_2, with air flow of 1 m/s. (**a**) Rafts of water droplets visible after 1 s. (**b**) Both the drops rafts grow in size, forming a percolated network, after 3.6 s. (**c**) As size of drops continues to increase, the area occupied by rafts also increases, after 8.8 s. Notice that drops near the boundary of rafts are slightly larger in size. (**d**) A disordered array of drops, where vacancies and size difference between drops abound, after 10.4 s. (**e**) The size of drops is larger, and most of the vanacies have disappeared. The assembly resembles a multigrain crystal, after 21.8 s. (**f**) Ordered array of nearly monodisperse drops formed after 69.4 s.

In breath figures formed on pre-cooled, nonvolatile liquid substrates [9, 10], the growing water drops form locally ordered rafts that provide an intermediate hexatic phase, and form fat fractals. But the hexatic phase persists only for tens of seconds, before coalescence of water drops sets in. The final assembly in this case consists of drops of many different sizes, which is quite similar to the breath figures formed on solids or dew. The most spectacular difference between breath figures formed on pre-cooled, nonvolatile liquids and the ordered arrays formed on evaporating solutions is the presence of high degree of order in late stage, and size uniformity which are brought about by the sustained noncoalescence of water drops. Limaye et al [7] and Srinivasarao et al [3] suggested that evaporative cooling can induce convection currents within the sample which in conjunction with the airflow across the surface, drive the ordering of the water droplets. Other mechanisms proposed included polymer bag mechanism of Pitios and Francois [7], micelle formation by Jenekhe and Chen [11], and evaporation driven assembly near the contact line proposed by Shimomura and coworkers [12, 13]: all of which were critiqued in the chapter 2. In the present study, the focus is on establishing the mechanistic aspects related to the formation of ordered arrays. This requires an understanding of both the intermediate stages in formation of such arrays, as well as a study of forces that act on the drops to direct them into a hexagonally ordered pattern. Both of these are described in next two sections of this chapter.

6.2 From disorder to order

One of the most fascinating aspects of breath figure templated assembly is also in the fact it involves close packing of noncoalescent water drops, which are themselves

growing as they assemble through the process. Even if the number of drops remains the same through the growth process, the increase in size of drops, say by two times, amounts to increase in area occupied by four times, and thus phase transition from disordered gas or liquid or glass like phase to a crystalline phase will occur due to a simple increase in density, as observed for hard spheres that are used to model the behavior of atoms or molecules. In their assembly process, the noncoalescent water drops seem to behave like colloidal crystals and bubble rafts, are at least three orders of magnitude larger than real atoms or molecules, and interact by forces relevant to the length scale corresponding to the drop size.

In a remarkable study published by Bragg and Nye in 1947 [14], the crystal structure of metals was represented by the structures formed within bubble rafts. The effects 'like grain boundaries, dislocations and other types of fault, slip, recrystallization, annealing and strains due to foreign atoms' were identified and observed in assembly of nearly mm size bubbles. Three more papers [15-17] followed from the same group in the fifties. The opening statements of the paper by Bragg and Nye [14] are: "Models of crystal structure have been described from time to time in which the atoms are represented by small floating or suspended magnets, or by circular disks floating on a water surface and held together by the forces of capillary attraction. These models have certain disadvantages; for instance, in the case of floating objects in contact, frictional forces impede their free relative movement. A more serious disadvantage is that the number of components is limited, for a large number of components is required in order to approach the state of affairs in a real crystal." Bragg and Nye went on to demonstrate that since the bubble rafts contain large number of components, they are good models for

studying the response of atoms present in metals. The study of bubble rafts has been a staple diet of beer drinkers, who pay attention to the order, stability and strength of foam head. The bubble rafts are also a good analogue to granular media and their properties help to explain the industrially and scientifically important questions related to foams and emulsions [1, 18-20]. The formation of ordered arrays of drops is a fine example of formation of two dimensional crystals.

Starting from the studies of Pieranski [21-23], the assembly of colloidal (spherical) particles [21-46], has been of great interest to researchers in the last twenty-five years. The colloidal 'atoms' or 'molecules' have been used to investigate fundamental problems in crystallization [44, 45] and glass transition [47-50]. These include studies on packing of spheres [21-23, 51], nucleation and growth in crystallization [43], as well as melting and pre-melting transitions . Further, the use of colloidal crystallization allows production of close packed assemblies of nanoparticles [24, 25, 28-30, 32, 35, 36, 41, 46, 52, 53], where the physical properties of nanoparticles can be utilized through a well-defined superstructure. The aspects related to assembly of nanoparticles will be reviewed and discussed in chapter 10, in context of self-assembly of colloidal gold nanorods.

The main ideas that emerge from studies on colloidal crystallization of spherical particles can be summarized as follows. The colloids that behave as hard spheres exhibit maximum packing volume fraction of ~64% for disordered spheres, and nearly 74% for hexagonal close packed (HCP) or face center cubic (FCC) crystal lattice in three dimensional systems. Typically above a critical concentration (58% for hard spheres), the spheres get trapped by their neighbors, and form a glassy phase. In two dimensions, the

colloids arrange into hexagonal order at the highest densities, and as the crystal melts, hexatic phases can form. The exact nature of phase transitions depends upon the long range and short range attractive and repulsive forces that act on the particles. For example, the hexatic phase does not occur for systems with extremely short ranged repulsions. While a large amount of literature is devoted to the study of bubble rafts and colloidal crystals, the corresponding assembly, as well as formation and dynamics of water drops, described here has received little attention. Given a microscope, a spoonful of volatile solvent containing < 5 % polymer spread on a glass slide, and some moist air blown from your mouth, is all it takes to construct this dynamic model for crystallization and assembly.

Figures 6.3 (a) and (b) show typical grain boundaries observed in the assembly of water drops. Earlier Figures 6.1 (f) and 6.2 (f) illustrated the late stage, where drops are organized in nearly perfect hexagonal order. Grain boundaries exist as a result of stacking faults. Individual rafts of water drops may have local order, but when these rafts are brought together the rows of drops in different domains are misaligned with respect to each other. Two lines in the Figure 6.3 (a) illustrate the mismatch between two domains. Such grain boundaries were reported by Bragg, Nye and Lomer [14-17] for bubble rafts, and have been identified and studied for foams, colloidal crystals, among others. The presence of grain boundaries affects the overall strength of materials and is studied by material scientists to achieve desired electrical, mechanical and optical properties of the material. Further the presence of grain boundaries limits the number of drops that can be packed in a given area. While the formation of crystals and liquid crystals is typically described in terms of the entropic and enthalpic costs of involved in placing the involved

moieties in a certain positional and orientational order, the essential arguments can be reduced to the question: What is the most efficient way to pack the moieties under given constraints? The problem of packing a given number of spheres or polygons in a given volume or area is key to understanding a number of physical problems, as is described in detail in the book by Aste and Weaire [19], which has also inspired the title of this chapter. The interaction potentials at work will be discussed a little later as well, but let us for now focus only on the geometric arguments.

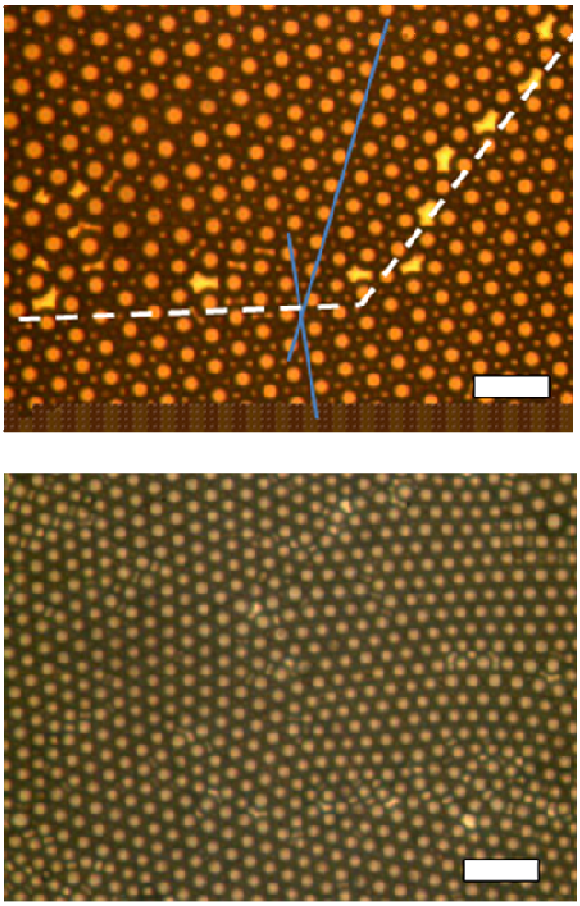

Figure 6.3 Optical micrographs showing polycrystalline arrays of drops. (**a**) Water drops assembled over PPE/CS_2. Notice that the orientation of rows of drops in two regions is different, as marked by solid lines. The dashed line approximately demarcates the grain boundary. (**b**) Water drops assembled over PS/CS_2. The polycrystalline nature of the image is the reason why rows of drops change direction at grain boundaries.

Apart from stacking faults, that create grain boundaries, the water droplets also exhibit typical defects expected for packed spheres. In Figure 6.4 (a), two such point defects are shown. Point defects are created when an atom is missing or a larger or smaller foreign atom is inducted into the aggregate, and their presence disrupts the perfect arrangement of surrounding atoms. The defect denoted by **A** represents a vacancy, for insertion of a drop will complete the local structure of the lattice. The defect **B** mimics the effect of introducing an extra foreign atom, and is usually called a substitutional defect.

In a polydisperse sample, as shown in Figure 6.4 (b), the formation of a disordered, dense phase occurs. This can be simulated by using a collection of pennies, quarters and nickels, and spreading them evenly and randomly on a surface, such that each is in contact with as many nearest neighbors as possible. The tendency for disorder is greater when the difference between the drop sizes is over 25 % or when a few large drops are mixed with small drops [19]. While grain boundaries show how two lattices of adjoining areas are misaligned, the Figure 6.4 (c) illustrates a dislocation, which is also a kind of stacking fault, where a row of drops ends within the matrix, creating a kind of step, and deforming the adjoining rows. The presence of each of these defects creates a local strain, and affects the “mechanical properties” of the whole assembled structure, thus simulating the effect of defects and dislocations on properties of metals.

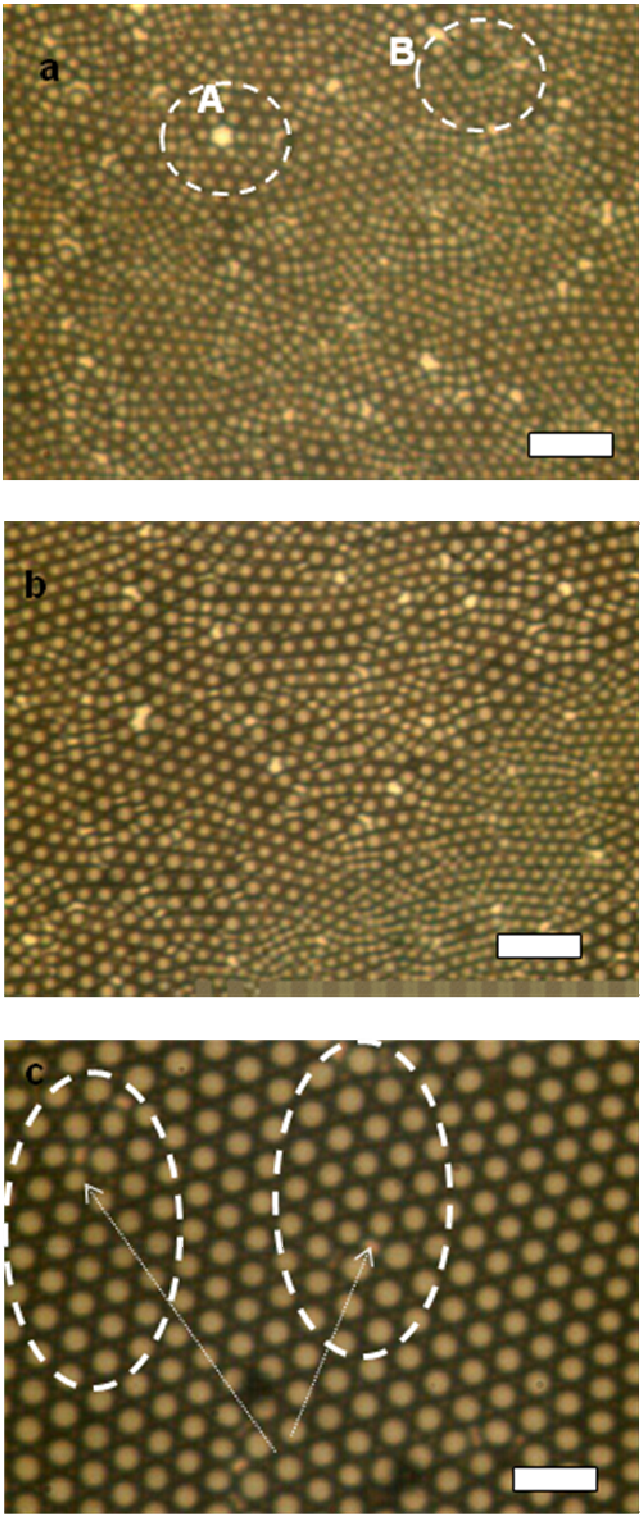

Figure 6.4 (**a**) Point defects: **A** shows a vacancy in the structure formed by water drops on PS/CS_2 sample; **B** shows a 'foreign atom', which disrupts the local packing. (**b**) Polydisperse water drops exhibit disordered close packing over a PS/CS_2 sample. (**c**) Noncoalescent water drops show rows that end at the points shown.

The local rearrangements of drops can be studied using a Voronoi construction as shown in Figure 6.5. The Voronoi cell (or Dirichlet region) is the smallest convex polygon surrounding a point, whose sides are perpendicular bisectors of lines between the point and its neighbors. While the Voronoi diagram consists of polygons that represent the region closest to the point, it allows one to construct Delaunay (or Dolone) tessellation, where non-overlapping simplexes (say triangles on a plane) tessellate the space [54]. Voronoi analysis is a versatile method for pattern recognition and for modeling the properties of spatial structures [54]. The centroids of drops were mapped using Image Pro. This data was used to construct Voronoi polygons using Matlab codes. The presence of drops that are surrounded by five or seven drops is illustrated by colored cells, and increase in order is reflected in increase in the number of hexagonal cells as shown in Figure 6.5. Notice that the pentagon and heptagons typically occur as a pair, or form a chain. The chain is seen to form at the place where grain boundary occurs.

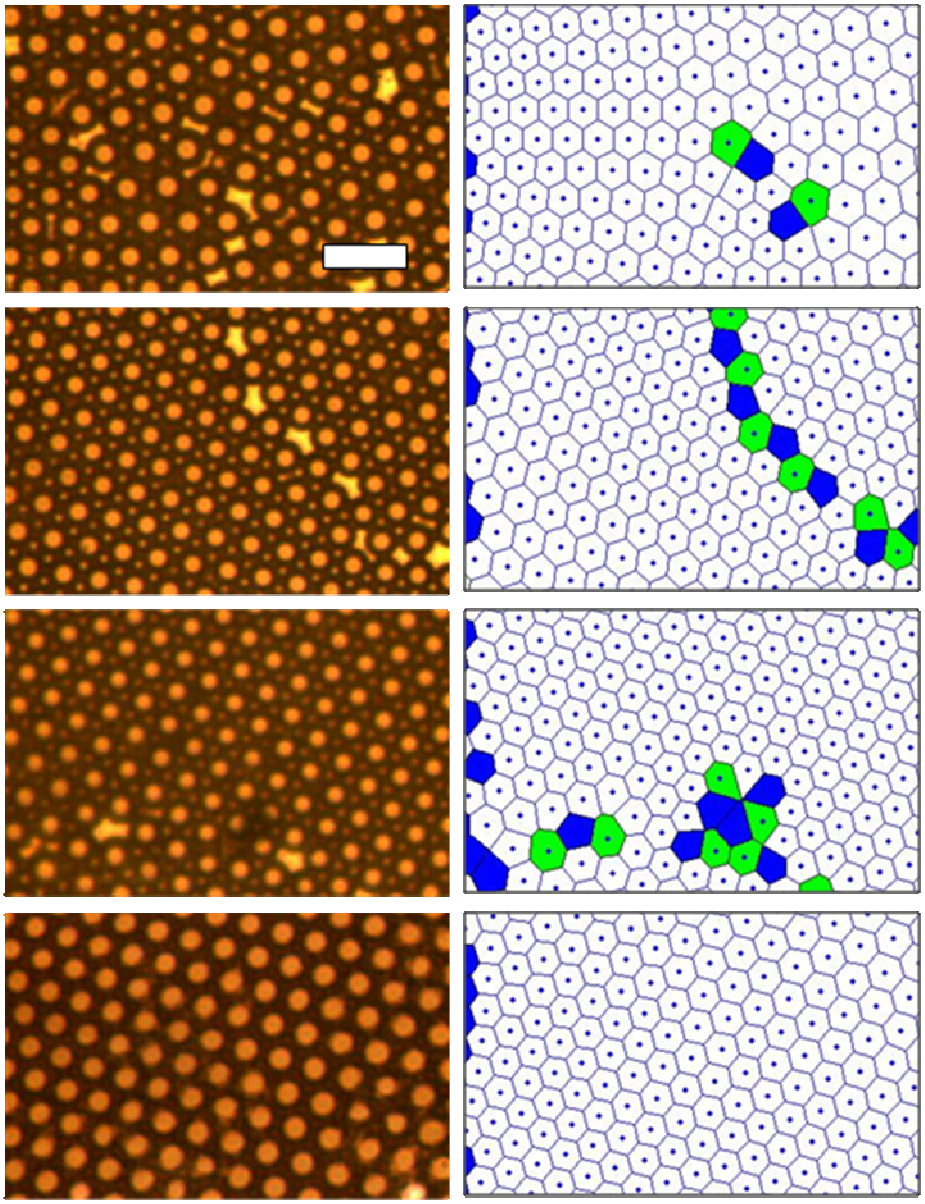

Figure 6.5 Evolution of hexagonally packed array of water drops occurs by corresponding increase in number of hexagons in the Voronoi diagram. Pentagons are colored blue, while heptagons are colored red. Each successive row is 4 s apart. The assembly of water drops occurs over hexo-PPE/CS_2 solution.

Figure 6.6 illustrates how a row of droplets slips over another row of droplets by a distance equal to the distance between the neighboring drops. Notice that the two rows of drops involved in this case are aligned parallel to each other and so there is no grain boundary between them. The slip occurs here because of the presence of what Bragg and

Nye [14] call a “dislocation” – one of the rows has one less drop next to it or there is a vacancy (which is a type of point defect) present, and this slip is able to remove it. Such slips and dislocations are characteristics of both metals and foam. In principle, the amount of stress required to move the drops must be reached before this slip can occur, and in all probability the stress here comes from the need to occupy the available space efficiently.

The changes in local packing (or coordination number) for these drops are followed using Voronoi analysis of the respective frames as shown in Figure 6.7. As the two rows slip over each other, the coordination number of drops changes, as seen by increased number of pentagons and heptagons in frames corresponding to images (d)-(i). The shape and size of Voronoi cells along the slip plane changes considerably during this time.

In certain cases, the slip motion is seen to create droplet coalescence as well as a curious phenomenon captured in Figure 6.8. As the two rows of drops slide over each other, a drop can be noticed to dive under the plane of other drops, and after the process is complete, this drop returns to the plane of drops. In fact, Song [8] has pointed out in her studies that the pursuit of perfect order in one plane can force water drops underneath even in the case of carbon disulfide as a solvent, where density of water is less than the density of carbon disulfide. Such drops are visible in Figure 6.2 (f), and these drops illustrate that the drops experience strong repulsive forces when pushed close to each other, and these forces will be described in the next section.

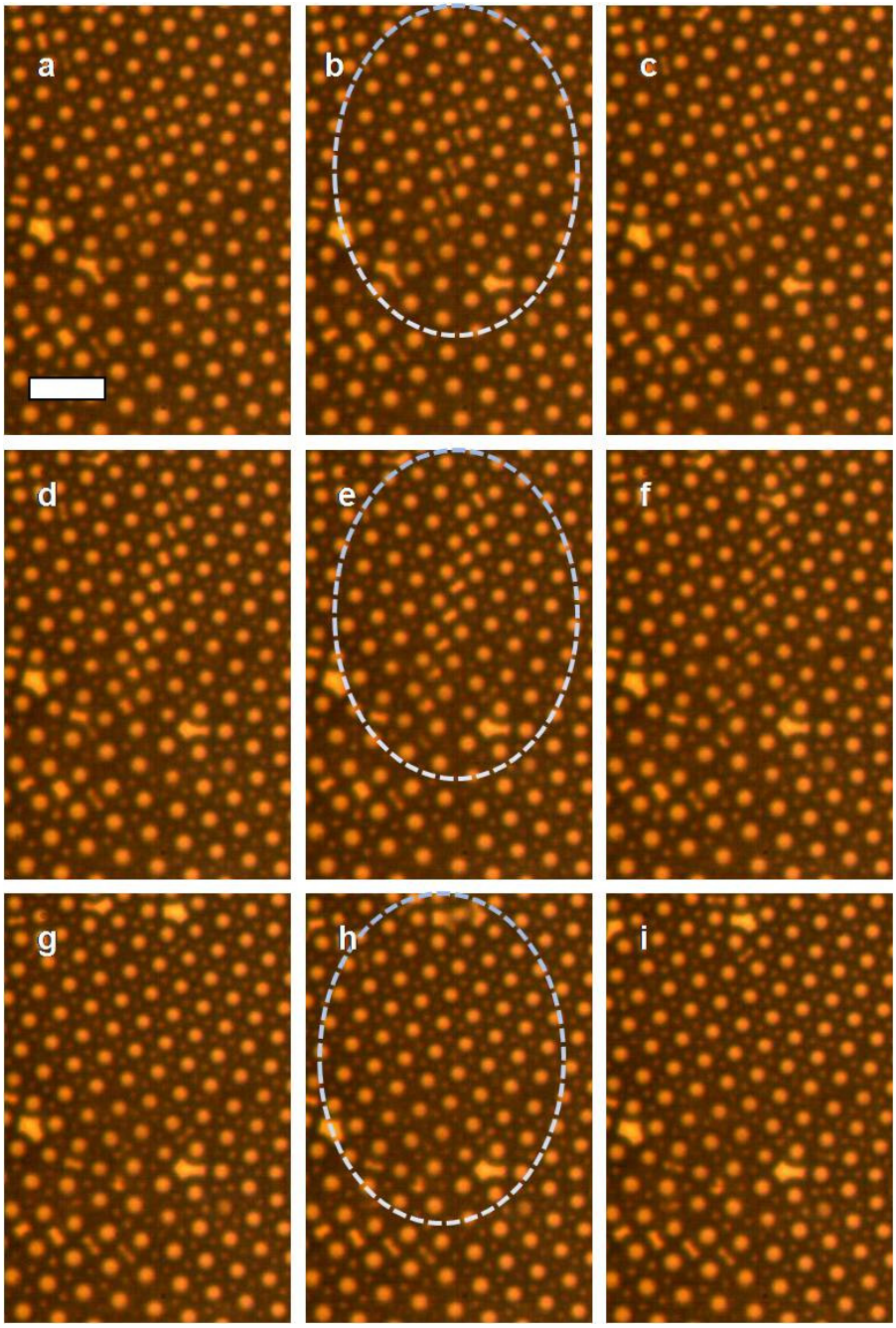

Figure 6.6 Collective dynamics to eliminate stacking faults. A row of drops slips over another row, by exactly one unit. (**a**) Time 0 ms; rows start to slip, where each drop only moves the distance that is a fraction of its diameter. The next seven frames are at (**b**) 32 ms, (**c**) 64 ms, (**d**) 88 ms, (**e**) 96 ms, (**f**) 104 ms, (**g**) 128 ms, (**h**) 144 ms and (**i**) 168 ms.

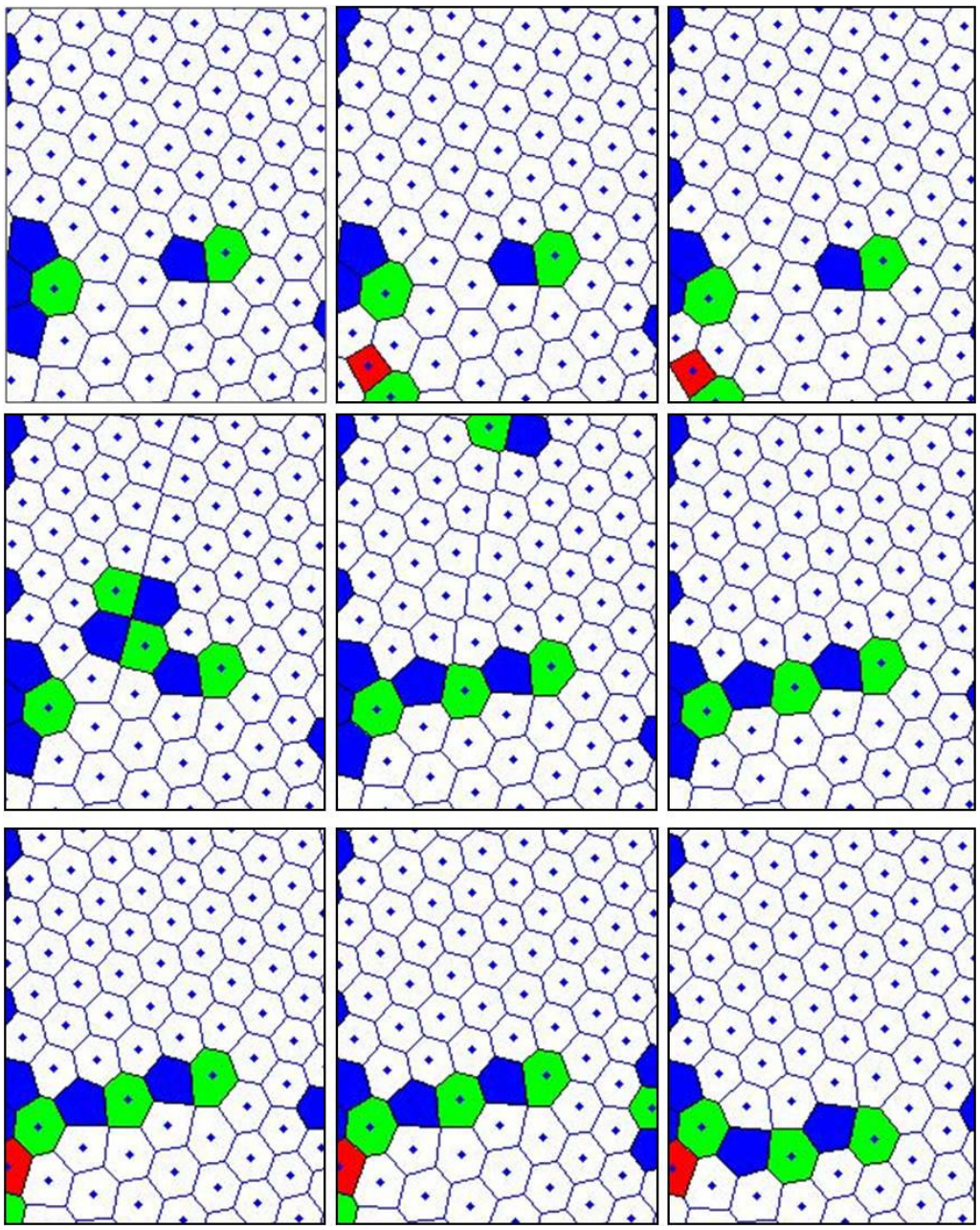

Figure 6.7 Voronoi analysis of the drops undergoing rearrangement. The frames are at (**a**) 0ms (**b**) 32 ms, (**c**) 64 ms, (**d**) 88 ms, (**e**) 96 ms, (**f**) 104 ms, (**g**) 128 ms, (**h**) 144 ms and (**i**) 168 ms. Notice that frame (d) and (e) have hexagons along the slip direction but the hexagons are not regular polygons, and there area is larger than the other hexagons in the frame.

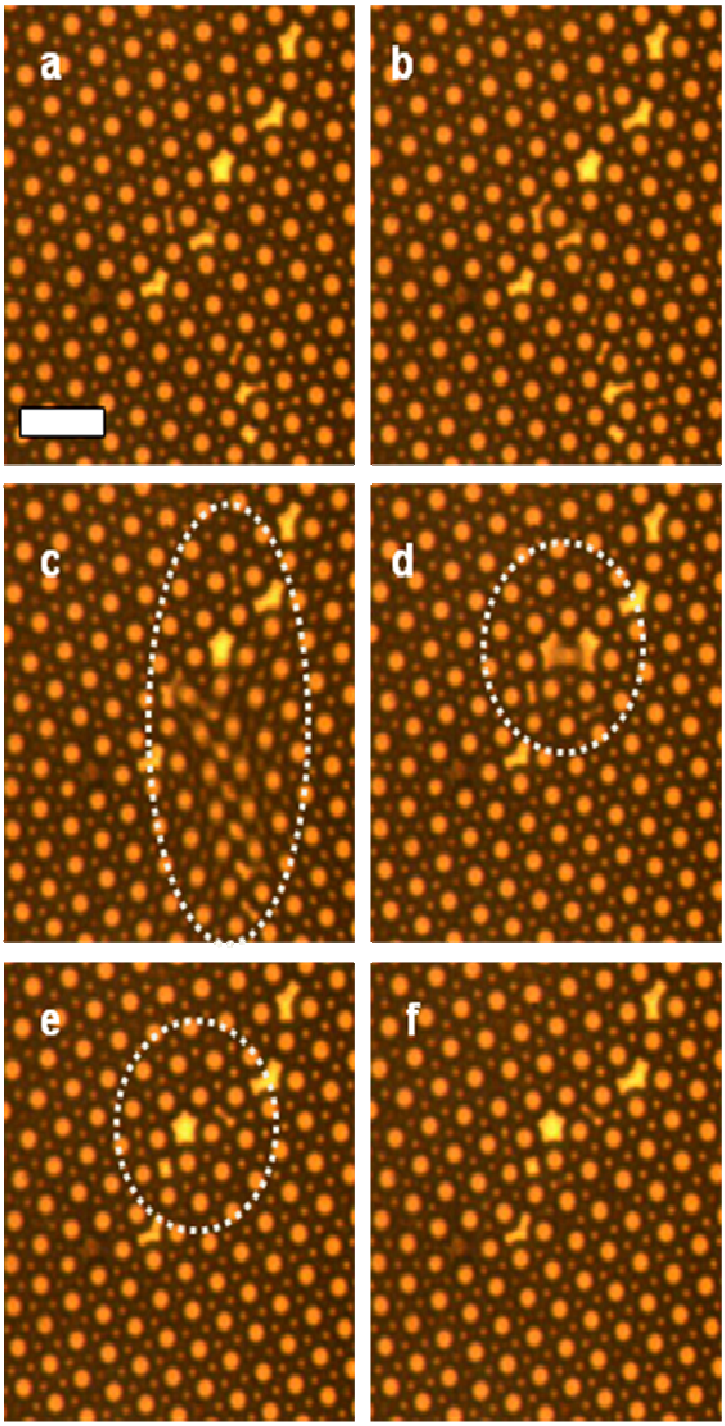

Figure 6.8 Diving drop observed in the assembly of water drops over hexo-PPE/CS_2 solution. Frames are 8ms apart from each other. The two rows that slip past each other are visible in frame (**c**) and the diving drop appears out of focus in the frame (**d**). The diving drop returns to the plane of other drops by frame (**e**), and the slip motion is completed by frame (**f**).

6.3 What forces act on the drops?

Bulk forces that act between two particles or surfaces are usually described as van der Waals forces, which arise due to the orientation dependence of the interaction energy of dipoles or induced dipoles of molecules of particles or surface in question. The net result is that the van der Waals pair potential is of the form w(r) = $-C/r^6$. For this potential, the interaction between two bodies, W, with N_1 and N_2 number of atoms per unit volume, is obtained using Hamaker constant $A = \pi^2 C N_1 N_2$ by summing or integrating the energies of all the atoms of the two bodies [55]. The typical value of Hamaker constant, A, is 10^{-19} J for interactions across vacuum (or air) [55]. The expression for two spheres, separated by distance r, (or center to center distance is $r+(r_1+r_2)$, i.e. r + the sum of the radius of two spheres) is as follows [55]:

$$W = -\frac{A}{r}\frac{r_1 r_2}{r_1 + r_2} \tag{6.1}$$

For two water droplets in air, the van der Waals forces are always active, but because of $1/r^6$ dependence for drops that have $r >> r_1$, they are of importance only below 100 nm (or when equation 6.1 is applicable). The Hamaker constant of water is 3.7 x 10^{-20} J in air [55], and for two drops of water that are 1 μm each in size, at contact with distance r =1 nm, their adhesion force turns out to be $F_{vdW} = Ar_d/12r^2$ ~ 3 nN. Increasing distance between the particles by a factor of 30, makes the force fall to 3 pN, while for 1 nm distance the increase in size by 10 times increases the force only by an order of magnitude. The corresponding interaction energy turns out to be $W = Ar_d/12r \sim 10^4\ k_BT$, which falls to $10k_BT$ when $r \sim r_d$. Since the corresponding Hamaker constant for water interacting across hydrocarbon interface are an order of magnitude smaller, [55] the corresponding force or interaction energy is also an order of magnitude smaller.

Typical forces that act on the colloidal particles include van der Waals forces, thermal forces, O (k_BT/r_d), viscous forces on moving particles, O(~ηr_d), screened electrostatic forces, and steric forces that come into play when polymers are added to a colloidal dispersion. These are described in various texts, and their relevance is discussed in context of the colloidal gold particles in chapter 8. The van der Waals forces were just described. The screened electrostatic forces are quite important for emulsions and colloidal dispersions that contain particles or drops that are stabilized by repulsive forces created by the presence of charge on the particles. The magnitude of interaction is controlled by the dielectric constant of the intervening fluid and by the distribution of ions over the particles as well as in the matrix. In their review on non-coalescence of liquid-liquid interfaces, Neitzel and Dell'Aversana [56] made a passing comment about breath figure templated assembly, saying the noncoalescence and assembly of water drops might be the result of electrostatics.

In this context, the study by Leunissen et al [57] on stability and order in charge stabilized, additive-free emulsions of water in cyclohexyl bromide (CHB) and CHB/decalin is worth mentioning. In this study, 5% water mixed with CHB and CHB/decalin respectively was sonicated for 2 minutes and the water-in-oil dispersion formed was found be ordered as shown in Figure 6.9 and the dispersion was stable for months! Further, the authors investigated a range of solvents to determine the role played by choice of oil on formation and stability of such arrays. Stable drop arrays were found to form only for oils with dielectric constant, ε_{oil}, satisfying $4 < \varepsilon_{oil} < 10$. While cholorform ($\varepsilon_{oil} \sim 4.7$) satisfies this criterion, the corresponding dielectric constant of other commonly used solvents (carbon disulfide, toluene, benzene) is < 3. Similarly the

dielectric constant the polymers is also < 3. Thus, while the electrostatic force or interaction can create repulsive forces capable of creating ordered arrays under certain circumstances, its role in ordering the drops is limited in context of the breath figure templated assembly for solvents like carbon disulfide.

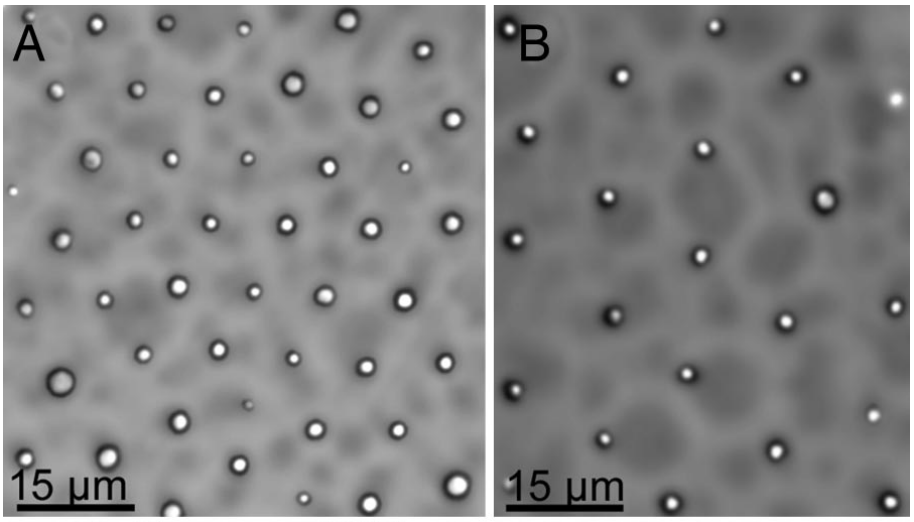

Figure 6.9 Crystalline arrays of noncoalescent water drops formed by sonication of 5% water in (**A**) cyclohexyl bromide (CHB) and in (**B**) CHB/decalin, respectively. The drops are organized in a three dimensional crystalline phase. No emulsifiers were added to the mixture (adapted from ref. [57]).

Srinivasarao et al [3] suggested that the drops that exist on polymer solution/air interface stay afloat as long as the solvent has higher density than water. In effect while Srinivasarao et al [3] stated that water drops will sink and form three dimensional patterns in the case of solvents with density lower than water, say benzene, while carbon disulfide will always form a two dimensional assembly only as CS_2 has a higher specific gravity. Bolognesi et al [58] pointed out that the drops at solution-air interface can be stabilized there by a surface tension term that can allow drops of water to be afloat even in the cases when the density of the solvent is lower than that of water. Bolognesi et al [58] carried out a simple analysis for spherical drops at the interface by neglecting the

weight of water drops and taking only surface tension into account. In fact, both gravitational (or buoyancy) and surface tension effects come into play at the interface, and affect the stability of drops (or particles) at the interface [42, 46].

The presence of a particle at the liquid-air interface can induce a deformation of meniscus around it (determined by balance of interfacial and gravitational contributions). The deformation can be due to the deformation of the interface by presence of a heavy floating particle, as shown in Figure 6.10 (a). Perturbation of the interface can also arise due to the wetting properties of a partially immersed bodies or particles, as shown in Figure 6.10 (b). For two spheres separated by distance r, such that r_1 and r_2 are the radius of the three phase contact line, and satisfy $r_1 << r$, $r_2 << r$, the approximate force between two drops is given [42] by:

$$F = -2\pi\sigma Q_1 Q_2 K_1(qr)\left[1 + O(q^2 r_{d\,1,2})\right]$$

Here σ is the liquid-liquid interfacial energy, $Q_{1,2} = r_{1,2}\sin\Psi_{1,2}$, are effective capillary charges, q is the inverse of capillary length, and K_1 is the Bessel function of the first kind. This attractive force is quite similar to the one quoted by Bragg [16] (credited to Nicolson) for attractive force between bubbles. Both forces differ as the capillary charge contribution is different for both cases, and for $r_{d1,2} \sim r_d$, and $r_{1,2} << r << q^{-1}$, the force for both cases [42] is:

$$F \sim \frac{r_d^{\,6}}{\sigma} K_1(qr) \qquad (6.2\text{ a})$$

$$F \sim r_d^{\,2} K_1(qr) \qquad (6.2\text{ b})$$

The energy of interaction between floating particles, with 5-10 μm size is negligible compared to $k_B T$, whereas the immersion forces are active even for particles of

a few nm in size [42, 46]. Floatation forces can also arise for small particles if these particles are not smooth, for then contact line around them is perturbed. When present, these lateral capillary forces help in aggregating particles. But in the present stage, capillary forces for floating droplets are of no consequence as the water drops are small, are spherical and have a relatively low density to cause significant meniscus deformation required for the lateral capillary forces to become effective.

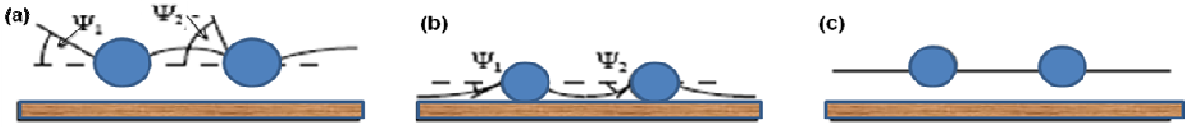

Figure 6.10 Capillary forces between particles. (**a**) Floatation forces, between particles that are large or heavy enough to deform the interface. (**b**) Immersion forces, between particles that interact due to perturbed meniscus as result of wetting behavior. (**c**) Small particles (radius < 5 μm) floating on an interface, with no deformation of interface, and no capillary forces. (Adapted from ref. [42]).

The mechanism postulated by Shimomura group [12, 13], (see chapter 2 for discussion) is based on the idea of colloidal crystallization proposed by Denkov et al [40, 42], as shown in the Figure 6.11. In this scenario, the shape of the interface between partially immersed particles is as shown, and as the evaporation of fluid occurs, a large capillary pressure is created which supplies the solvent to the region between the particles. As pointed out before, the mechanism is a direct contradiction of the experimental observations, for water drops seem to organize into rafts all over the substrate, and their order is poorest near the edges of the polymer solution substrate. Furthermore, experiments show that when a water drop is sunk into the solution or if the water drop comes in close vicinity of the glass substrate, the water drop instantaneously

spreads on glass, under the oil. A simple experiment can be conducted before partaking bread (in an Italian restaurant!): if a few drops of vinegar are poured over olive oil, the drops typically float about. Their coalescence is delayed because of intervening olive oil draining film, but eventually if one of the drop turns out to be large enough, it contacts the saucer and spreads, exactly as water spreads under a carbon disulfide based polymer solution.

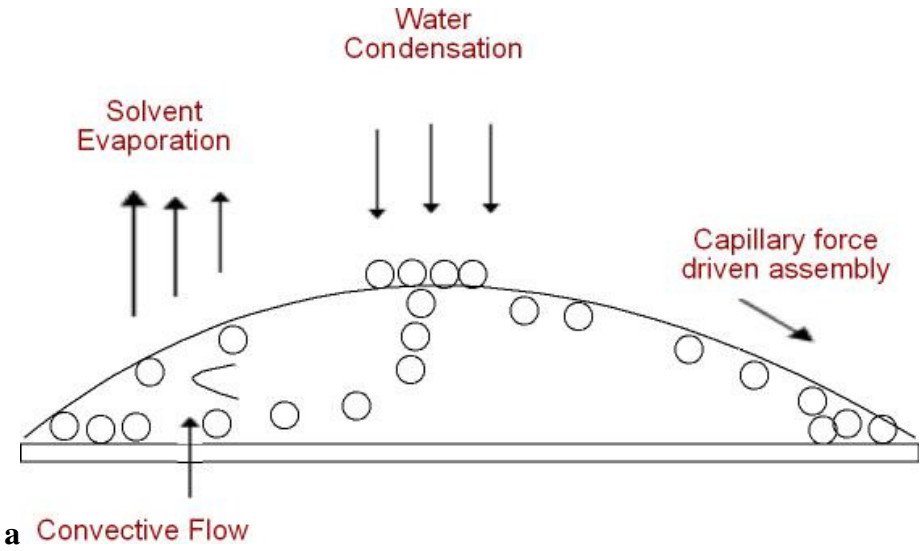

a

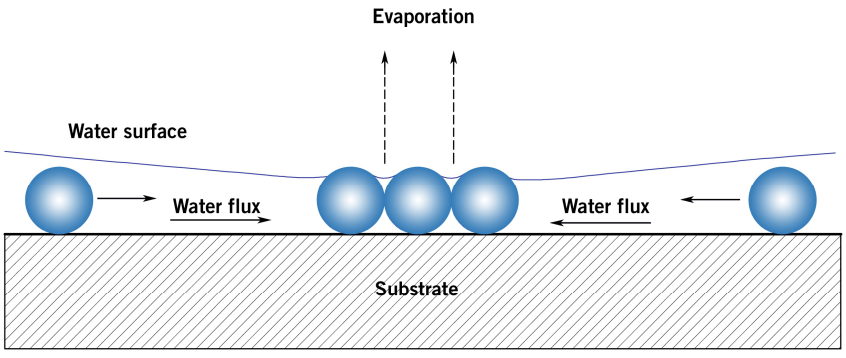

b

Figure 6.11 (a) Capillary force driven assembly at contact line, (adapted from [12, 13]). (**b**) Mechanism for two-dimensional crystallization (adapted from [40]).

In the previous chapter, the noncoalescence of water drops to the polymer solution was attributed to the presence of lubricating film formed by both air entrained by thermocapillary convection, and by the solvent vapor flux. It was argued that the drops in the vicinity of the solution substrate can be levitated due to aforementioned factors, and in such a case, the underlying substrate is deformed. If the deformation of interface does occur, the drops will start to self-assemble over the evaporating solution in a mechanism somewhat reminiscent of the self-assembly of bouncing drops. So while the generation of immersion or floatation forces generated by water drops trapped *at* the liquid-air interface is unlikely, the deformation of meniscus by water drops levitated *over* the substrate might create capillary charges that assemble into a two-dimensional array. The precise determination of such forces requires a computation of the meniscus deformation, which is left as an open problem for now.

The repulsion between the drops can be understood to be a consequence of the forces that prevent the drops from coming close to each other. In the previous chapter, the bounce off of drops colliding in air was attributed to the fact that when two drops are brought together, the pressure generated in lubricating film or drainage film that separates them, creates a small deformation of the drops. This deformation converts the kinetic energy of the drops into an elastic energy, and once the drops come to a halt (due to pressure build up as well as due to viscous resistance), they bounce back by relaxing this energy. The idea of deformation of drops creating a repulsive force is already present in the classical work by Bragg and collaborators [14-17], who studied bubble rafts. Similar repulsion has been computed for emulsions (reviewed in [42]), and in the present case, only main ideas are described. The deviation of the drop from the spherical shape leads to

an increase in the surface area of the droplet, which incurs a surface energy contribution proportional to change in area as well as to the surface tension of the drop. When drop deformation is small compared with the size of the drop or for $r_c << r_d$, the total energy of surface dilation (for small drops) is given [42] by

$$W_{dil} \approx -\frac{\pi}{4}\sigma_d \frac{r_c^{\,4}}{r_d^{\,2}} \tag{6.3}$$

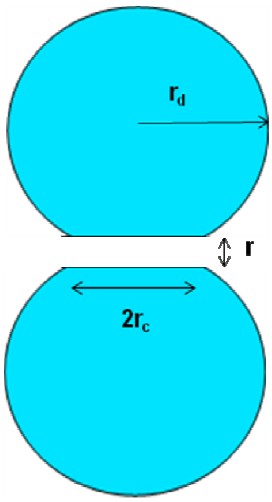

Figure 6.12 Deformation of interacting droplets. The radius of the contact line at film is r_c, and the distance of nearest approach of drops is r as shown. The lengths are not to scale, and r_c is made much larger to illustrate droplet deformation.

Using this formula, the repulsion potential between the drops can be computed as follows. The magnitude of this interaction energy is comparable to k_BT for a micron size drops with $r_c = 0.01 r_d$, and for 10 micron drops the corresponding repulsion energy is $100 k_BT$. In typical scenarios for emulsions [42], another contribution is calculated for the effect of interfacial bending energy, $W_{ben} \approx -2\pi r_c^{\,2} B_0 / r_d$, which depends upon bending moment B_0 (typical value ~ 10^{-11} N), and determines the propensity of drop to flatten. For the case discussed above, the contribution, W_{ben} is at least an order of magnitude weaker (if no consideration is made for presence of polymer), and for water in oil emulsions, it is

typically said to favor flattening. In the case when drops are immersed in polymer solution, any change in shape of water drops must generate a corresponding stress in the polymer solution draining film, which in turn must depend upon the modulus of the polymer solution at that concentration. The kinetic effect of slow drainage was related in previous chapter to high viscosity of polymer solutions. Similarly, the corresponding contribution to repulsion potential by presence of polymer solution must occur, but the magnitude of such contribution and how it can be computed, are still open questions. The present study forms the first step in elucidation of interaction potentials that operate on these noncoalescent water drops, and hopefully provides a starting point for subsequent studies that will be able to elucidate the range of factors that influence the interaction and hence the assembly of water drops. Before concluding this discussion, another fascinating phenomenon that was discovered in certain movies recorded by Lulu Song (though never reported or discussed by her or as far as we know anyone else in the literature on breath figure templated assembly) is described in the next section.

6.4 Liquid Bridges and capillary condensation

The arrays of water drops formed over evaporating polymer solutions are typically composed of drops that are a few microns in size, and the inter-drop distances are typically so small that in close packed arrays, the drops appear to be touching each other. According to Song [8], the drops in PS solutions are always more close packed than in the case of PPE. But since the molecular weights, concentrations and other physical properties of the solutions were not controlled, a quantitative argument cannot be made about how the choice of polymer and polymer properties changes the inter-drop

distances. At the same time, of all the movies recorded by Lulu Song, one movie contains water drops that are reasonably far apart as shown in Figure 6.12, and during the course of experiment, these drops appear to develop bridges that appear and disappear over the course of a few seconds. The formation and break-up of bridges seem to occur randomly among the drops present in the frame.

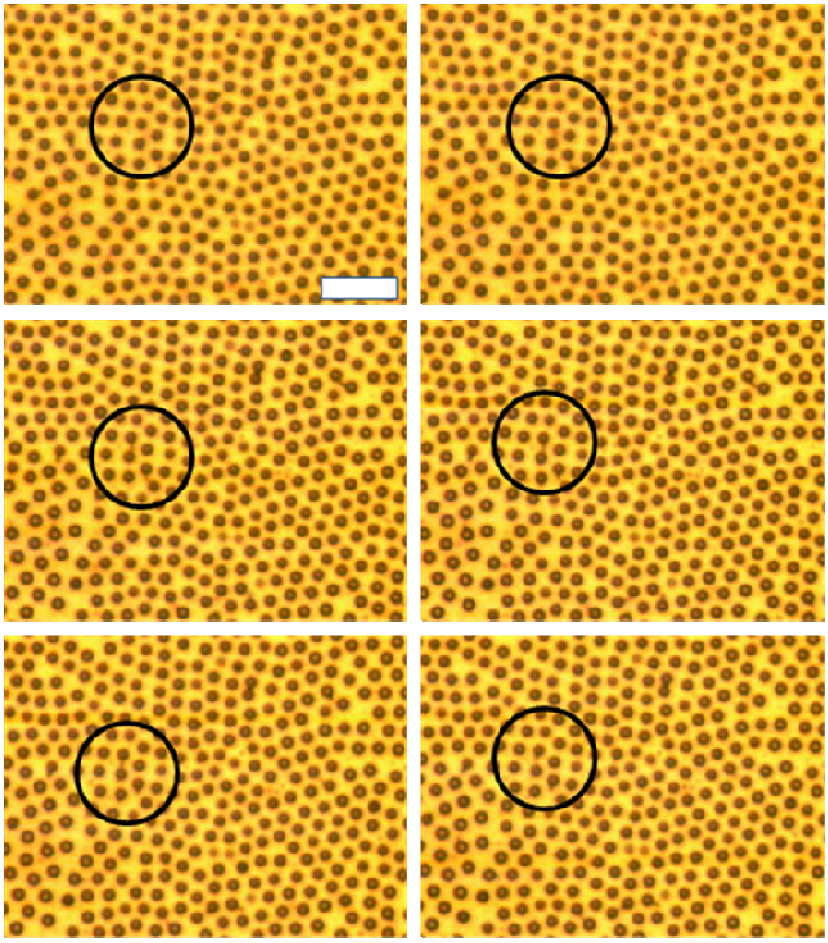

Figure 6.13 Formation and break-up of the capillary bridges, captured over hexo-PPE/ CS_2 solutions. The respective frames are 80 ms apart. The first frame shows the two drops before the formation of the bridge. The middle row shows drops are connected by a bridge, but the relative position of drops does not change. The bridge starts to rupture in the last frame. Liquid bridges can be seen at several locations in the frame, and the region that is circled was chosen to illustrate the life cycle of the bridge. While the drops do not move from their x-y locations on the frame, they do seem to jiggle at their locations. The bridges seem to move from one pair to next, almost like handing over of batons in a relay race.

The formation of capillary bridges [42, 59-61] plays a crucial role in the consolidation of soil, wetting of granular media [62], sticking of dust and powder to surfaces, evaporation rate from porous media as well as in bridging in the atomic force microscopy measurements. While typical examples of capillary bridges involve two solid phases, the formation of capillary bridges between two fluid phases has been studied in the context of antifoaming by dispersed oil drops [42]. The formation of capillary bridges occurs in humid atmosphere by a process of nucleation and growth of a water bridge between two hydrophilic surfaces [42, 59]. The nucleation of water drops over the surface is quite similar to the nucleation events described earlier in the context of cloud condensation nuclei, where the local equilibrium between the water on a surface and water vapor around it is established. The coalescence of water formed on two hydrophobic surfaces that are close to each other leads to formation of the bridge, which is stable in unsaturated atmosphere. The decreased pressure inside the liquid bridge, along with surface tension force acting at the locus of contact line of water on particles typically generates an attractive force between the particles.

The total force generated by capillary bridge, F_{CB}, can be written in terms of these two contributions [42] to be

$$F_{CB} = -\pi\left(2r_{CB0}\sigma - {r_{CB0}}^2 P_{CB}\right) \tag{6.4}$$

Here P_{CB} represents the pressure difference between the bridge and the vapor outside it and r_{CB} is the thickness of the bridge at the center along the axis r, as shown in the Figure 6.14. The negative F_{CB} represents attraction whereas a positive F_{CB} represents repulsion between the two bodies connected by the bridge. The total force due to capillary bridge

remains the same irrespective of what cross-section is used in the computation (see derivation and discussion in Chapter 11 in text by Kralchevsky and Nagayama [42], for example).

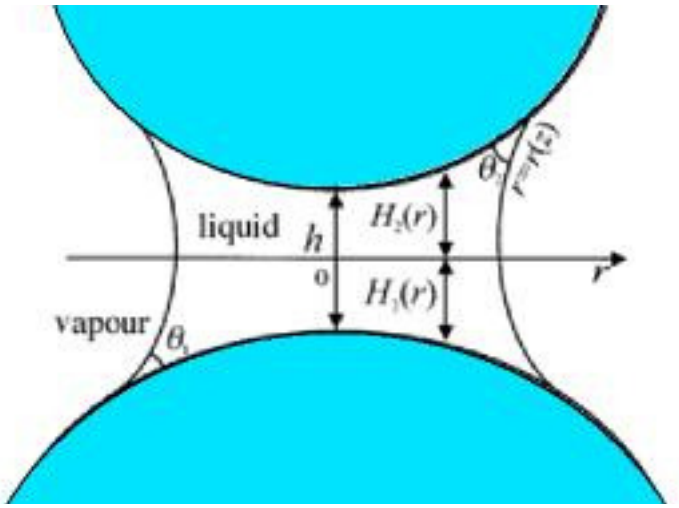

Figure 6.14 Liquid bridge formed between two spheres that have different radius and size. The profile of the meniscus, r (z), depends upon the contact angles of the liquid on the two surfaces.

The stability of capillary bridge under equilibrium conditions is related to the vapor pressure in vicinity of surfaces, and in this case, the radius, r_K, of the bridge is determined by Kelvin's pressure argument. In the stages (A) and (B) in Figure 6.14, the liquid bridge is in equilibrium with the vapor. The transition from (A) to (B) is likely to occur through non-equilibrium process, where the decrease in the distance between two surfaces allows forces, like van der Waals forces, to become significant to make the coalescence event occur. At equilibrium, the length of the capillary bridge, H, is related to the Kelvin radius, r_K, by H=2 r_K cosθ, where θ is the contact angle [59]. As the distance between the surfaces is increased, the liquid bridge becomes unstable and can break by Rayleigh instability. During the course of frames described earlier, in Figure 6.12, the water drops immersed over hexo-PPE/CS_2 solution form such bridges in the late

stages of assembly process when the drops locally encounter an undersaturated mixture. The subsequent formation and snap-off of the liquid bridges must be connected to change in the ambient humidity brought about by falling saturation ratio, while the temperature of substrate begins to rise. The capillary bridges generate an attractive force in this case which can act over distances much larger than the size of drops, as well as the range of van der Waals forces discussed earlier.

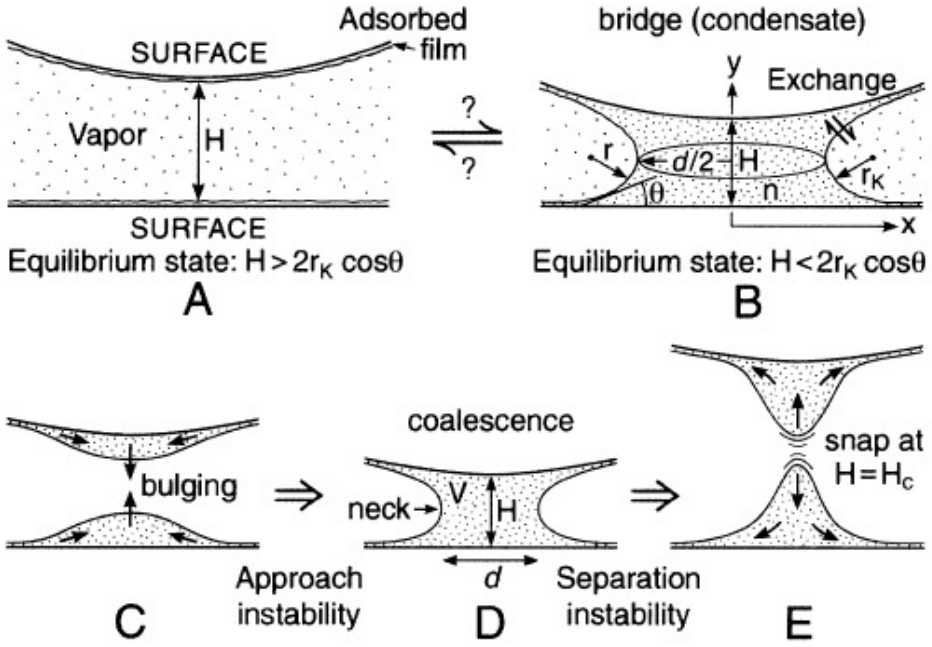

Figure 6.15 The formation and break-up of liquid bridges. (**A**) Adsorbed film of water formed on hydrophilic surfaces. (**B**) Liquid bridge formed between two surfaces. (**C**) As surfaces approach each other, van der Waals forces (for example) cause the adsorbed film to bulge and eventually coalesce as in (**D**). The liquid bridge snaps off (E) under instabilities described in text. (Adapted from ref. [59]).

6.5 Summary

The pursuit of perfect packing by noncoalescent water droplets was described, using the language of crystallization. The water droplets behave like atoms or colloidal particles or bubble rafts, and produce a range of defects and dislocations associated with two dimensional crystals. These include vacancies, defects due to presence of foreign

atoms, stacking faults and grain boundaries. Further, the drops were found to exhibit local and collective dynamics that included slip of two rows of drops to remove a dislocation, and healing of grain boundaries. The efficiency of noncoalescence was revealed also by drops that seemed to dive below the plane. These observations are reported in the context of breath-figure-templated assembly for the first time.

Crystallization of particles is usually described in terms of the repulsive and attractive forces that act on the particles. In this chapter, the various interaction forces acting between water droplets were described. The van der Waals forces are attractive and short ranged, and their magnitude depends upon the choice of solvent as well as size of drops, and distance between the drops. When drops approach each other, the pressure generated in the fluid film that separates them can cause drops to deform from their spherical shape, which generates an effective repulsion between the drops. The attractive and repulsive interaction potentials were computed for water drops that form the breath figure templated assembly.

Further, it was shown that even though lateral capillary forces generated by deformation of meniscus due to floating particles, or immersed particles play limited or insignificant role in assembly process, capillary bridges can form between drops and provide an additional attraction between the drops. The present contribution provides only a preliminary study of interaction potentials that act on drops, and of how drops proceed from disorder to order. The nature and magnitude of interactions, as well as dynamical processes by which water drops form a hexagonal packed array present an exciting area for anyone interested in understanding the statistical thermodynamics and dynamics of crystallization.

6.6 References

1. Weaire, D.L. and S. Hutzler, *The Physics of Foams*. 1999, Oxford: Oxford University Press.

2. Limaye, A.V., et al., *Evidence for convective effects in breath figure formation on volatile fluid surfaces.* Physical Review Letters, 1996. **76**(20): p. 3762-3765.

3. Pitois, O. and B. Francois, *Formation of ordered micro-porous membranes.* European Physical Journal B, 1999. **8**(2): p. 225-231.

4. Pitois, O. and B. Francois, *Crystallization of condensation droplets on a liquid surface.* Colloid and Polymer Science, 1999. **277**(6): p. 574-578.

5. Karthaus, O., et al., *Water-assisted formation of micrometer-size honeycomb patterns of polymers.* Langmuir, 2000. **16**(15): p. 6071-6076.

6. Barrow, M.S., et al., *Physical characterisation of microporous and nanoporous polymer films by atomic force microscopy, scanning electron microscopy and high speed video microphotography.* Spectroscopy-an International Journal, 2004. **18**(4): p. 577-585.

7. Srinivasarao, M., et al., *Three-dimensionally ordered array of air bubbles in a polymer film.* Science, 2001. **292**(5514): p. 79-83.

8. Song, L., *Study of ordered macroporous polymer films by templating breath figures*, in *School of Polymer, Textile and Fiber Engineering*. 2005, Georgia Institute of Technology: Atlanta. p. 193.

9. Steyer, A., P. Guenoun, and D. Beysens, *Hexatic and fat fractal structures for water droplets condensing on oil.* Physical Review E, 1993. **48**(1): p. 428-431.

10. Steyer, A., et al., *Two-dimensional ordering during droplet growth on a liquid surface.* Physical Review B, 1990. **42**(1): p. 1086-1089.

11. Jenekhe, S.A. and X.L. Chen, *Self-assembly of ordered microporous materials from rod-coil block copolymers.* Science, 1999. **283**(5400): p. 372-375.

12. Shimomura, M. and T. Sawadaishi, *Bottom-up strategy of materials fabrication: a new trend in nanotechnology of soft materials.* Current Opinion in Colloid & Interface Science, 2001. **6**(1): p. 11-16.

13. Maruyama, N., et al., *Mesoscopic patterns of molecular aggregates on solid substrates.* Thin Solid Films, 1998. **329**: p. 854-856.

14. Bragg, L. and J.F. Nye, *A dynamical model of a crystal structure.* Proceedings of the Royal Society of London Series a-Mathematical and Physical Sciences, 1947. **190**(1023): p. 474-&.

15. Lomer, W.M., *A dynamical model of a crystal structure. III.* Proceedings of the Royal Society of London Series a-Mathematical and Physical Sciences, 1949. **196**(1045): p. 182-194.

16. Bragg, L. and W.M. Lomer, *A dynamical model of a crystal structure. II.* Proceedings of the Royal Society of London Series a-Mathematical and Physical Sciences, 1949. **196**(1045): p. 171-181.

17. Lomer, W.M. and J.F. Nye, *A dynamical model of a crystal structure IV. Grain boundaries.* Proceedings of the Royal Society of London Series a-Mathematical and Physical Sciences, 1952. **212**(1111): p. 576-584.

18. Weaire, D. and W. Drenckhan, *Structure and dynamics of confined foams: A review of recent progress.* Advances in Colloid and Interface Science, 2008. **137**(1): p. 20-26.

19. Aste, T. and D.L. Weaire, *The Pursuit of Perfect Packing*. 2000, London: Institute of Physics Publishing.

20. Glazier, J.A. and D. Weaire, *The kinetics of cellular patterns.* Journal of Physics-Condensed Matter, 1992. **4**(8): p. 1867-1894.

21. Pieranski, P., *Two dimensional interfacial colloidal crystals.* Physical Review Letters, 1980. **45**(7): p. 569-572.

22. Pieranski, P., *Colloidal crystals.* Contemporary Physics, 1983. **24**(1): p. 25-73.

23. Pieranski, P., L. Strzelecki, and B. Pansu, *Thin colloidal crystals.* Physical Review Letters, 1983. **50**(12): p. 900-903.

24. Murray, C.B., C.R. Kagan, and M.G. Bawendi, *Synthesis and characterization of monodisperse nanocrystals and close-packed nanocrystal assemblies.* Annual Review of Materials Science, 2000. **30**: p. 545-610.

25. Puntes, V.F., K.M. Krishnan, and A.P. Alivisatos, *Colloidal nanocrystal shape and size control: The case of cobalt.* Science, 2001. **291**(5511): p. 2115-2117.

26. Horsch, M.A., Z. Zhang, and S.C. Glotzer, *Self-assembly of laterally-tethered nanorods.* Nano Letters, 2006. **6**(11): p. 2406-2413.

27. Tang, Z.Y., et al., *Self-assembly of CdTe nanocrystals into free-floating sheets.* Science, 2006. **314**(5797): p. 274-278.

28. Glotzer, S.C., et al., *Self-assembly of anisotropic tethered nanoparticle shape amphiphiles.* Current Opinion in Colloid & Interface Science, 2005. **10**(5-6): p. 287-295.

29. Glotzer, S.C., M.J. Solomon, and N.A. Kotov, *Self-assembly: From nanoscale to microscale colloids.* Aiche Journal, 2004. **50**(12): p. 2978-2985.

30. Daniel, M.C. and D. Astruc, *Gold nanoparticles: Assembly, supramolecular chemistry, quantum-size-related properties, and applications toward biology, catalysis, and nanotechnology.* Chemical Reviews, 2004. **104**(1): p. 293-346.

31. Rabani, E., et al., *Drying-mediated self-assembly of nanoparticles.* Nature, 2003. **426**(6964): p. 271-274.

32. Xia, Y.N., et al., *Monodispersed colloidal spheres: Old materials with new applications.* Advanced Materials, 2000. **12**(10): p. 693-713.

33. vanBlaaderen, A., R. Ruel, and P. Wiltzius, *Template-directed colloidal crystallization.* Nature, 1997. **385**(6614): p. 321-324.

34. Sun, S.H. and C.B. Murray, *Synthesis of monodisperse cobalt nanocrystals and their assembly into magnetic superlattices (invited).* Journal of Applied Physics, 1999. **85**(8): p. 4325-4330.

35. Pileni, M.P., *Nanosized particles made in colloidal assemblies.* Langmuir, 1997. **13**(13): p. 3266-3276.

36. Velev, O.D. and E.W. Kaler, *Structured porous materials via colloidal crystal templating: From inorganic oxides to metals.* Advanced Materials, 2000. **12**(7): p. 531-534.

37. Aizenberg, J., P.V. Braun, and P. Wiltzius, *Patterned colloidal deposition controlled by electrostatic and capillary forces.* Physical Review Letters, 2000. **84**(13): p. 2997-3000.

38. Norris, D.J., et al., *Opaline photonic crystals: How does self-assembly work?* Advanced Materials, 2004. **16**(16): p. 1393-1399.

39. Denkov, N.D., et al., *Mechanism of formation of 2-dimensional crystals from latex particles on substrates.* Langmuir, 1992. **8**(12): p. 3183-3190.

40. Denkov, N.D., et al., *2-Dimensional crystallization.* Nature, 1993. **361**(6407): p. 26-26.

41. Murray, C.B., C.R. Kagan, and M.G. Bawendi, *Self-organization of CdSe nanocrystallites into three dimensional quantum dot superlattices.* Science, 1995. **270**(5240): p. 1335-1338.

42. Kralchevsky, P.A. and K. Nagayama, *Particles at fluid interfaces and membranes*. Studies in interface science, ed. D. Mobius and R. Miller. 2001, Amsterdam: Elsevier Science B. V.

43. Gasser, U., et al., *Real-space imaging of nucleation and growth in colloidal crystallization.* Science, 2001. **292**(5515): p. 258-262.

44. Habdas, P. and E.R. Weeks, *Video microscopy of colloidal suspensions and colloidal crystals.* Current Opinion in Colloid & Interface Science, 2002. **7**(3-4): p. 196-203.

45. Anderson, V.J. and H.N.W. Lekkerkerker, *Insights into phase transition kinetics from colloid science.* Nature, 2002. **416**(6883): p. 811-815.

46. Binks, B.P. and T.S. Horozov, eds. *Colloidal particles at liquid interfaces*. 2006, Cambridge University Press: Cambridge.

47. Weeks, E.R. and D.A. Weitz, *Properties of cage rearrangements observed near the colloidal glass transition.* Physical Review Letters, 2002. **89**(9).

48. Weeks, E.R., et al., *Three-dimensional direct imaging of structural relaxation near the colloidal glass transition.* Science, 2000. **287**(5453): p. 627-631.

49. Kegel, W.K. and A. van Blaaderen, *Direct observation of dynamical heterogeneities in colloidal hard-sphere suspensions.* Science, 2000. **287**(5451): p. 290-293.

50. Vanblaaderen, A. and P. Wiltzius, *Real space structure of colloidal hard sphere glasses.* Science, 1995. **270**(5239): p. 1177-1179.

51. Pusey, P.N. and W. Vanmegen, *Phase behavior of concentrated suspensions of nearly hard colloidal sphers.* Nature, 1986. **320**(6060): p. 340-342.

52. Freeman, R.G., et al., *Self-assembled metal colloid monolayers - an approach to SERS substrates.* Science, 1995. **267**(5204): p. 1629-1632.

53. Velev, O.D. and A.M. Lenhoff, *Colloidal crystals as templates for porous materials.* Current Opinion in Colloid & Interface Science, 2000. **5**(1-2): p. 56-63.

54. Okabe, A., et al., *Spatial Tessellations: Concepts and applications of Voronoi diagrams*. 2000, New York: John Wiley & sons, Inc.

55. Israelachvili, J., *Intermolecular and Surface Forces*. 2nd ed. 1992, San Diego: Academic Press.

56. Neitzel, G.P. and P. Dell'Aversana, *Noncoalescence and nonwetting behavior of liquids.* Annual Review of Fluid Mechanics, 2002. **34**: p. 267-289.

57. Leunissen, M.E., et al., *Electrostatics at the oil-water interface, stability, and order in emulsions and colloids.* Proceedings of the National Academy of Sciences of the United States of America, 2007. **104**(8): p. 2585-2590.

58. Bolognesi, A., et al., *Self-organization of polystyrenes into ordered microstructured films and their replication by soft lithography.* Langmuir, 2005. **21**(8): p. 3480-3485.

59. Maeda, N., J.N. Israelachvili, and M.M. Kohonen, *Evaporation and instabilities of microscopic capillary bridges.* Proceedings of the National Academy of Sciences of the United States of America, 2003. **100**(3): p. 803-808.

60. Willett, C.D., et al., *Capillary bridges between two spherical bodies.* Langmuir, 2000. **16**(24): p. 9396-9405.

61. Kralchevsky, P.A. and N.D. Denkov, *Capillary forces and structuring in layers of colloid particles.* Current Opinion in Colloid & Interface Science, 2001. **6**(4): p. 383-401.

62. Herminghaus, S., *Dynamics of wet granular matter.* Advances in Physics, 2005. **54**(3): p. 221-261.

CHAPTER 7

UNUSUAL WETTING AND DRYING BEHAVIOR OF EVAPORATING WATER DROPS

But the pressure was too great. He would have to find something to make good the equilibrium. Something must come with him into the hollow void of death in his soul, fill it up, and so equalize the pressure within to the pressure without. For day by day he felt more like a bubble […]
D. H. Lawrence*, Women in Love* [1]

Water drops that nucleate, grow and organize into ordered arrays over evaporating polymer solution exposed to a current of moist air, eventually evaporate away. While the incoming moist air is undersaturated, the mixing of moist air flow with solvent vapor flux creates supersaturation over the substrate. The temporal variation of supersaturation, and hence the growth of drops, depends upon the rate and extent of evaporative cooling. When the bulk of the solvent evaporates away, condensation of water vapor is not favored, and water evaporates away leaving interconnected holes in the polymer films [2]. So far in this thesis, the mechanistic aspects related to the formation of ordered arrays of noncoalescent drops were described and related to the physical properties of solvent and the air flow velocity and humidity. Most of the studies in the field so far (see Table 2.1 in Chapter 2 for an exhaustive list) have concerned themselves with the characteristics and properties of the final structure only. Before this study, only a few studies were aimed at the elucidation of the aspects related to the growth of drops, issue of noncoalescence and the formation of ordered arrays [2-4]. Before the final porous structure is formed, the ordered arrays of water drops must evaporate away, which must involve heat and mass transfer as well as dewetting/drying mechanism affected by

surface tension. The dynamic processes underlying the evolution of arrays of holes or air bubbles in polymer films from the ordered or disordered arrays of water drops, which was neither studied nor reported by researchers before, will be elucidated in this chapter.

In this chapter, an unusual wetting-dewetting behavior is reported to occur in the stage before water drops evaporate out. Briefly, the water drops that lie immersed in the concentrated polymer solution eventually pop out, and start to coalesce with adjacent drops (as will be demonstrated and discussed later). While the underlying structure persists due to high viscosity of the concentrated polymer solution, the merger of drops creates sessile, interconnected drops over the substrate. Thus, the water does not evaporate from an assembly of cap-like protrusions of immersed drops. This phenomenon was observed by the author first during crude experiments involving blowing air over polymer solution and looking at drop formation and growth on a computer screen, attached to a camera on the microscope. Later, the author located similar late stage effects in the movies made by Lulu Song (though it is never mentioned in her thesis [4] or papers [5, 6]). The experimental data presented in this chapter is extracted from Song's movies. The phenomena described in this chapter illustrate how the capillary forces come into play before the holey films are realized. The holey films themselves have been shown to be superhydrophobic [4] and it is fascinating that *water drops template a structure that is water repellent*. In the following sections, a brief introduction to wetting of hydrophobic and superhydrophobic surfaces is provided. This is followed by the description of the events that remove water drops from the substrate, leaving a holey film. Thereafter the implications of the observations are discussed in context of the science of wetting, but

more importantly, the implications of these observations for the mechanism of the breath figure templated assembly are outlined.

7.1 Wetting of hydrophobic and superhydrophobic surfaces

Wetting refers to the study of spreading of a liquid deposited on a solid or a liquid substrate. Understanding of the wetting behavior is crucial for several scientific and technological areas, including paints, printing, insecticides, anti-frost glass, rise of sap in plants, moisture content of soil, locomotion of insects on water, etc. The detailed survey of these can be found in various textbooks [7-11] and many excellent review articles [12-17]. The book by Rowlinson [7] and a review article by Good [13] retrace the history of wetting and capillarity, and both provide a historically rich introduction to the ideas, as well as controversies of the field. In this section, only the basic aspects relevant to our study are discussed.

A liquid in contact with surface typically: 1) spreads on it, forming a thin film, where the three phase (liquid-air-surface) contact line advances spreading the liquid completely over the surface; or 2) forms a sessile drop, such that the drop contact line expands to a certain radius and the shape of the drop is a section of a sphere with contact angle, θ_Y given by Young's equation [7-11] as:

$$\gamma_{la}\cos\theta_Y = \gamma_{sa} - \gamma_{sl} \tag{7.1}$$

Here γ_{ij} represents the interfacial energy between phases i and j, i.e. air, liquid and solid. While Young's result of 1804 describes an equilibrium contact angle expected for, say a drop placed on a substrate, Laplace in 1805, determined that surface tension creates a pressure difference across a surface [7-11] given by

$$\Delta p = \gamma\left(\frac{1}{R_1}+\frac{1}{R_2}\right) \tag{7.2}$$

Here R_1 and R_2 are the radius of curvature of the surface [7, 8]. For a spherical drop, R_1= R_2= r_d and hence the relationship reduces to

$$\Delta p = \frac{2\gamma}{r_d} \tag{7.3}$$

The pressure is greater inside the drops than outside, and since smaller drops have higher Laplace pressure, fluid typically flows from a small drop or a bubble to a larger drop or bubble if they are connected by a small channel.

A drop of water placed on very clean glass surface spreads completely, whereas a drop placed on a nonstick pan, or for that matter, any plastic surface, forms a stationary puddle or spherical cap as seen in Figure 7.1. When the volume of the fluid is small, the partially wetting drops exist as spherical caps only, but when drop size increases, gravitation force becomes significant and flattens the drop, giving it a shape of a pancake. The length scale beyond which gravity forces show an effect is set by comparing the Laplace pressure to hydrostatic pressure, and is expressed in terms of capillary length, κ^{-1}, [7-11] defined as

$$\kappa^{-1} = \sqrt{\gamma / \rho g} \tag{7.4}$$

The capillary length for water is 2.7 mm. The ability of the drop to wet the surface or to spread over the surface is quantified using spreading parameter [7-11],

$$S = \gamma_{sa} - \left(\gamma_{sl} + \gamma_{la}\right) \tag{7.5}$$

where $S > 0$ for total wetting and $S < 0$ for partial wetting. Figure 7.1 also shows how surface tension terms act at the contact line to move the fluid [17]. In the vicinity of

this three phase contact line, the thickness of the fluid diminishes, and the surface forces or disjoining pressure assumes importance, typically implying that the actual contact of the drop at three phase contact line may not be as sharp as seen macroscopically [9]. The detailed discussion of wetting [8-10] is outside the scope of this work, but it must be mentioned that on most real surfaces, the contact angle observed is different from that obtained by the equilibrium considerations described so far.

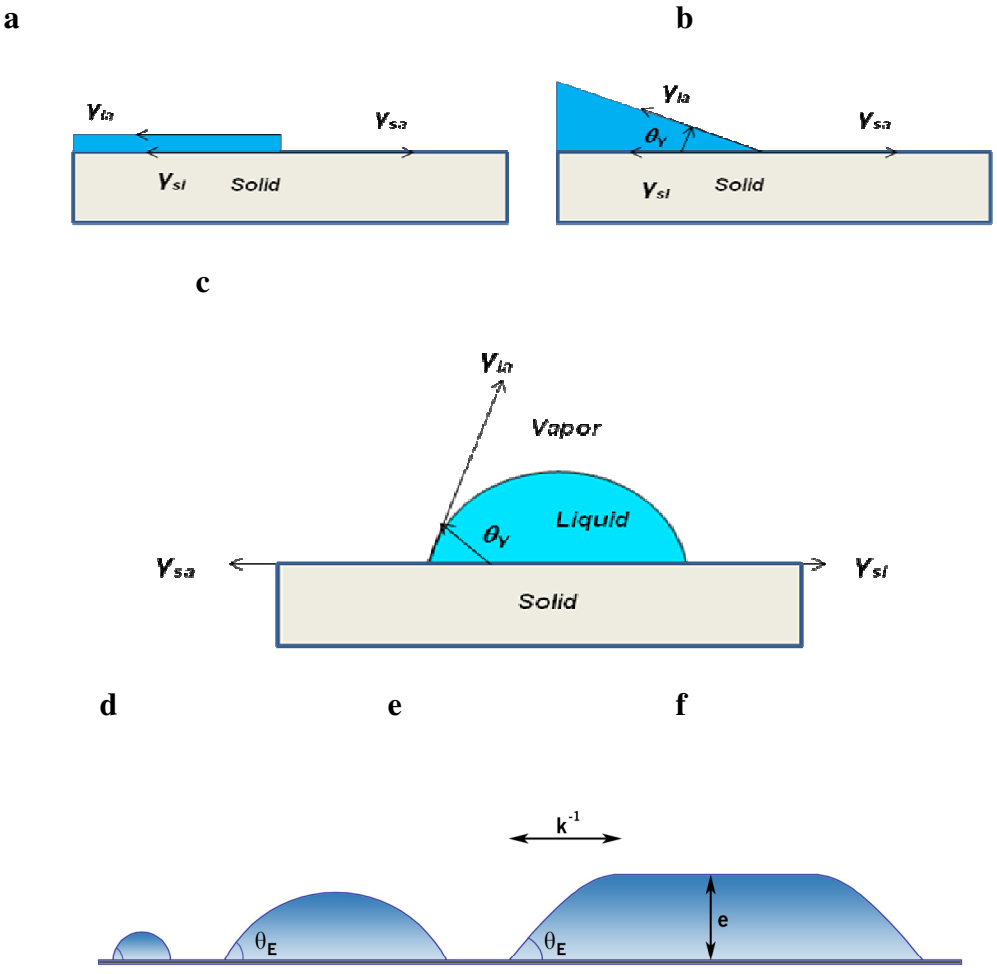

Figure 7.1 (**a**) Complete wetting: liquid film, dragged by surface forces, spreads completely over the substrate. (**b**) Partial wetting: balance of interfacial energy or surface tension determines the contact angle. (**c**) Contact angle for a sessile drop. (**d**)-(**f**) Increasing size of drop beyond capillary length, flattens the drop into a pancake (as described in the text).

Essentially, drops do not exhibit a unique contact angle θ_Y but a can admit a range of values such that $\theta_r < \theta_Y < \theta_a$, where θ_r and θ_a are the receding and advancing contact angles respectively [8, 9]. The difference between the extreme two values is termed as the contact angle hysteresis. The implication of the definition can be illustrated through Figure 7.2, where liquid can be added or removed from the drop by pumping it through the hole at the center. The radius of the base of the drop remains constant as long as the static contact angle remains within the limits set by the advancing and contact angles respectively. Further theoretical and experimental considerations have been reported which assert that the drop is static only when $\theta = \theta_Y$, while the drop undergoes a slow motion for $\theta_r < \theta < \theta_a$, which becomes a macroscopic motion as soon as the contact angle is outside this range. The dynamics of wetting and spreading has received widespread attention in past few decades and approaches of the different schools of thought are critically spelt out in papers [12, 13, 18] as well as books [8, 9].

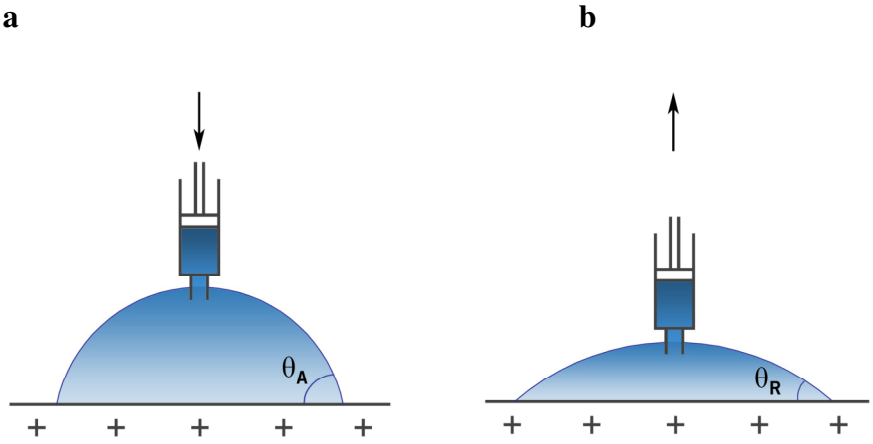

Figure 7.2 For a liquid placed on a surface, multiple states or contact angles exist, $\theta_r < \theta < \theta_a$. (**a**) If liquid is pumped into the drop, its contact angle can be as high as set by advancing contact angle $\theta_a (>\theta_Y)$ and (**b**) if the liquid is pumped out of the drop, the receding contact angle is $\theta_r (< \theta_Y)$. (Adapted from ref. [8]).

In the case of wetting of surfaces with roughness or structural features on them, the observed wetting behavior is affected not only by the surface chemistry, but also by the size and topography of the pattern or roughness [8, 16, 17]. The characterization of surface roughness can be accomplished by optical methods using microscopy, as detailed in the review by Srinivasarao and Park [19]. For the drops placed over patterns or rough surfaces with feature size small compared to the drop size, there are two distinct possibilities, as were identified by Wenzel [20, 21] and Cassie [22-24] respectively. In the Cassie state, the drops are balanced over the roughness feature, with air trapped underneath, whereas if the liquid penetrates the features, as shown in the Figure 7.3, the drop are said to be in Wenzel state.

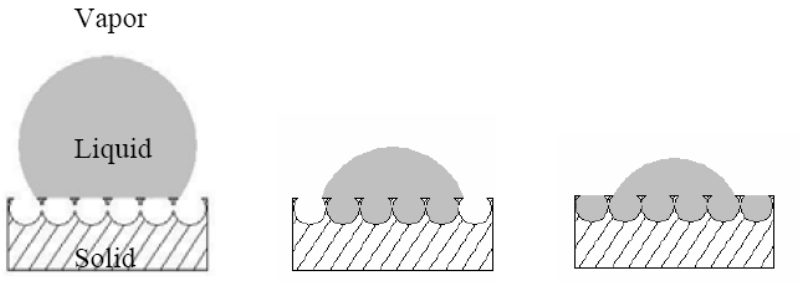

Figure 7.3 (**a**) Cassie state: drops rest on the top of the features, with air trapped underneath. (**b**) Wenzel state: drops rest on feature, with liquid inside (**c**) Film: Drop on a hydrophobic surface rests on features which are full of water. (Adapted from ref. [4]).

For a rough or patterned surface, if *r* is the ratio between the actual area and its apparent (or projected) area, a small displacement *dx* of contact line (in direction parallel to the surface) causes the surface energies per unit length of contact line to change [8] by:

$$dE = r\left(\gamma_{sl} - \gamma_{sv}\right)dx + \gamma_{lv}dx\cos\theta^{*} \qquad (7.4)$$

The minimum in *E* defines the equilibrium, and in this case, it gives the Wenzel's relation [8]:

$$\cos\theta^* = r\cos\theta_Y \tag{7.5}$$

This implies that surface roughness increases the effective hydrophilic or hydrophobic nature of the surface. On the other hand, if small displacement dx is considered for a surface that constitutes of two different species of material, with a fractional area of f_1 and f_2 and contact angle of θ_1 and θ_2 respectively, the energy variation caused turns out to be [8]:

$$dE = f_1\left(\gamma_{sl} - \gamma_{sv}\right)_1 dx + f_2\left(\gamma_{sl} - \gamma_{sv}\right)_2 dx + \gamma_{lv} dx\cos\theta^* \tag{7.6}$$

The minimization of E leads to the Cassie-Baxter relation [8]:

$$\cos\theta^* = f_1\cos\theta_{Y1} + f_2\cos\theta_{Y2} \tag{7.7}$$

The wetting behavior of patterned surfaces is of scientific and technological interest in many realms. For example, superhydrophobic surfaces that exhibit high contact angle and low water roll off angles are ideal for use in microfluidics and other fluid flow applications. These are properties that are quite similar to the lotus leaf and other plant microstructures in nature [25-27], where the drops roll off and in the process also act to clean the surface. Many insects have structural features on their bodies with patterns that help them to stay relatively dry [28, 29], keep their surfaces clean (as for geckos [30]) or assist them in locomotion [31-33] (e. g. strider insects). While most beetles have a waxy layer on their elytra that keeps them dry, there are beetles in Namib desert that have bumpy backs, with alternating hydrophilic and hydrophobic surfaces that allow the beetle to collect water from fog [34]. While there is an increasing demand for materials with controlled wettability, and to some extent this is determined by the choice of material itself, the possibility of changing contact angle simply by making a patterned surface allows more design possibilities. Like the biological structures, the field of

textiles has a long history of wetting studies on hydrophobic surfaces as well as patterned surfaces, and many initial attempts at understanding wetting of textured materials, including by Cassie, were accomplished on fibrous structures or fabrics. In their recent report about the replication of a 1945 patent to make superhydrophobic surfaces, Gao and McCarthy [35] pointed out that a wealth of information is buried in over sixty year old textile and other literature (references in [35] for example). The fiber mat formed by electrospinning is both microporous and microtextured, and leads to superhydrophobic surfaces, which were modified in a recent study to give contact angles > 150^{o} with organic fluids, forming superoleophobic surfaces [36].

When the contact angle is varied using surface roughness, the obvious question that must be addressed is whether the surface will show Wenzel- or Cassie- like behavior. For a drop deposited from outside on a textured or rough hydrophobic surface, the Cassie relation is noted to give good estimate of the contact angles. But when water is deposited on the same surface using condensation [37, 38] or pressure is exerted over the drop laid on the surface [39], the liquid can invade the asperities leading to metastable Wenzel state. Since the lotus leaf effect as well as many applications of patterned surfaces require a crucial understand of how drops or fluid would behave on these, several investigators have addressed this problem both experimentally and theoretically [15, 16, 27, 29, 40-53], though the validity of Cassie and Wenzel equation is itself heavily debated in literature [49-53]. According to Gao and McCarthy [52], the topological nature of roughness – the geometry and fraction of features under the contact line – determines the extent of superhydrophobicity (in terms of contact angles and hysteresis) and the classical or prevalent use of roughness based on area under the drops can lead to erroneous results.

7.2 What happens after water drops assemble over polymer solution?

7.2.1 Jamming and emergence of "sessile" drops

The water drops condensed on the evaporating polymer solutions self-organize forming a close packed two dimensional array. In the late stage of their assembly process, the water drops continue to drift. The drops exhibit singular or collective dynamics to remove the defects and disclinations, thereby reaching the high amount of two-dimensional order observed in many holey films. This pursuit of perfect packing was described in the previous chapter. It was shown that the order in arrays of drops can be related to increase in number fraction of drops that have coordination number of six. This state of collective dynamics is followed by a visible jamming of the whole self-assembled structure.

Once the jamming happens, the water drops become static. Let the positions occupied by drops at this instant be called **cells**. For the rest of the experiment or the process, during which these water drops dry out, the 'x-y' locations of these cells do not change. For example, Figure 7.4 (a) shows nearly close packed water drops in the intermediary state where they can display local or collective dynamics, as described in the previous chapter. The series of changes described in Figure 7.4 are captured for a polystyrene-carbon disulfide solution. In the published literature on formation of holey films, only the states up to Figure 7.4 (a) are described, followed by a description of the properties of microporous, dried films. The stages described hereafter are reported and discussed here for the first time.

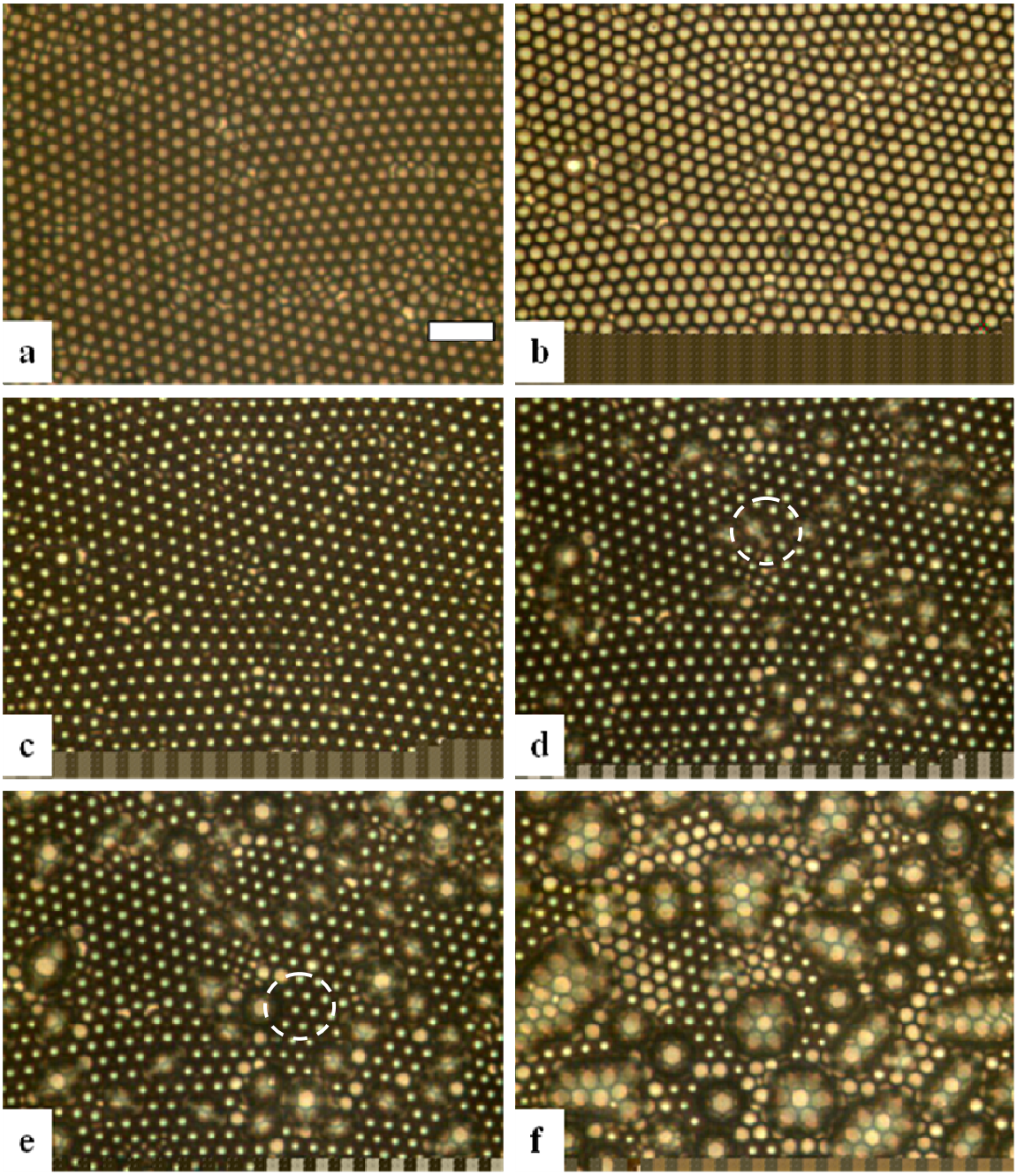

Figure 7.4 Images from a movie showing the late stage in breath figure templated assembly over PS/CS_2 substrate. (**a**) Close packed water drops, with regions of high amount of order. The drops are still mobile, t(a) = 0 s (**b**) Drops are jammed, t(b) = 4 s (**c**) Drops act like lenses, and focus light to their respective centers, t(c) = 7 s (**d**) Water drops that pop-out coalesce with two or three adjoining drops and form 'scars', t(d) = 15 s (**e**) By coalescence and growth, several symmetric drops emerge, with bright central drop, and six surrounding ones, designated as 'flowers', t(e)= 17 s, (**f**) Some coalesced sessile drops have circular circumference, and compared to (e), most lens-like cells have dried up and appear as empty cells rather than dots, t(f) ~ 43 s. Scale bar is 20 µm.

Figure 7.4 (b) denotes the state of drops right after jamming, and these drops appear to be bright, with narrow dark circles for their circumference. These cells then transform to the structure seen in Figure 7.4 (c). While the water drops have not shifted in x-y plane, displacement in z direction may have occurred. The water in each cells appear to contain **dots**. Water drops that are now immersed in polymer solution focus the light that enters the drop. The width of incident cone of light is dictated by the Cassegerian ray optics of the microscope. In the next step, the water from adjoining cells is seen to pop-up and coalesces between three to four drops, forming the "**scars**" noticed at several locations in Figure 7.4 (d). These are termed scars and not blisters, for the edges of the cells beneath are visible.

The growth of these scars continues till some of these scars transform into highly symmetric drops, where a central bright spot and its six nearest neighbors lie under a large water drop. These symmetric drops seen in figure 7.4 (e) are termed as "**flowers**", and these co-exist with a number of scars that either transform to flowers or form large symmetrical or asymmetrical drops visible in Figure 7.4 (f). While scars and flowers form from the nearest neighbors, in the Figure 7.4 (f), the sessile drops that have more than seven cells beneath them are formed by coalescence of neighboring flowers and scars.

Similar effects can be seen on hexo-PPE/CS_2 solution, where the frame in Figure 7.5 (a) represents the close packed drops. These drops move collectively, and continue to remove the defect sites in array till the motion completely stops, or drops become jammed. The next frame, Figure 7.5 (b) is captured after the drops become jammed, and again we refer to their locations as cells. Each cell comprises of drops that have moved

out of focus, suggesting a movement in the z-direction (perpendicular to the plane of the image). The next stage in the case of PPE appears to differ from PS, for here a few cells turn extremely bright or turn into "**lamps**". The dynamic process that follows is like switching random lamps on (one by one) from a large number of lamps arranged in a two dimensional array. While the number of bright cells increases with time, the remaining drops show presence of a focusing effect as observed before for polystyrene solutions, and so a population of dots emerges in Figure 7.5 (d). When the water drops start to pop-out or grow out of the sunken cells, in Figure 7.5 (e), the sessile drop lies on a single cell, surrounded symmetrically by six bright cells. Four such drops of different size are visible in the image, representing stages of their growth. In the next stage, i.e. in Figure 7.5 (f), these two sessile drops invade their nearest neighbors, and they still have a sharp circular contact line. Another sessile drop appears on the right side, which shows a bright central cell. This drop is largest in size, as is clear from the size of the area occupied by it. The scar to flower transition is described in next section.

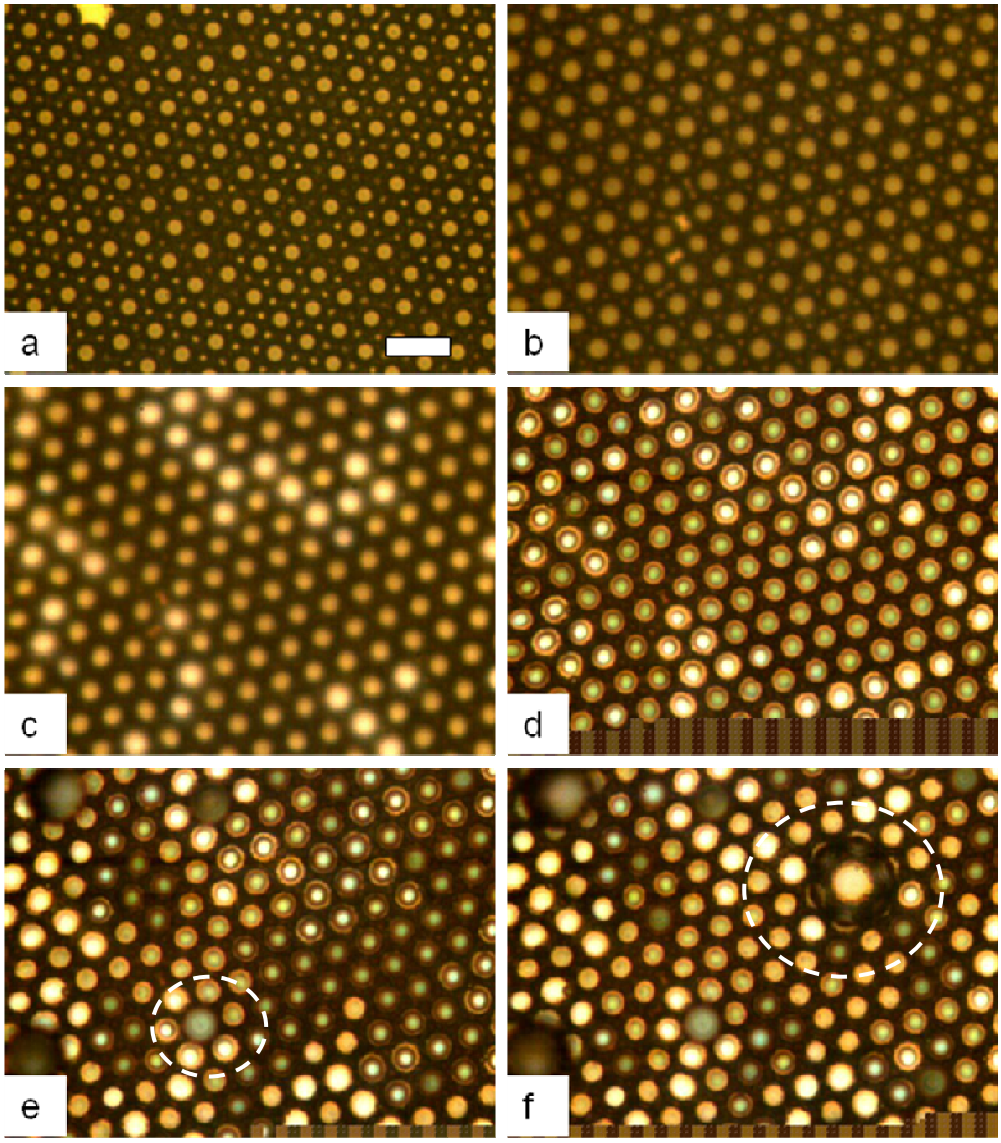

Figure 7.5 Images obtained for hexo-PPE/CS_2 solution, 0.3% polymer, air flow of 0.5 m/s. (**a**) Close packed water drops, with regions of high amount of order. The drops are still mobile, t(a) = 0 s. (**b**) Drops are jammed, t(b) = 8 s. (**c**) Drops seem to go out of focus, followed by appearance of brighter drops that emerge one by one, t(c) = 9 s. (**d**) Two populations of drops visible: one with dot like centers, and a series of brighter drops, t(d) = 10 s. (**e**) Larger sessile drops emerge, t(e)= 12 s. (**f**) Symmetric drop, "flower" appears, t(f) ~ 16 s. Scale bar is 20 µm.

7.2.2 Scars to flowers transition

The transition from 'scars' to 'flowers' is examined in Figure 7.6, where a growing sessile drop that occupies two cells can be observed in Figure 7.6 (a). Typically,

the formation of such a sessile drop involves three to four adjoining cells, and Figure 7.6 (b) shows such sessile drops, where boundaries of cells underneath are visible. These sessile drops, that we call scars grow in size and number, and in Figure 7.6 (c)-(e), we can make out scars comprised of drop over two, three and four cells. Thereafter, as these scars continue to evolve, they transform into flowers. In a flower, the sessile drop lies over a bright central cell, and the surrounding six cells are directly under the contact line of this flower. Images (g)-(h) illustrate that as the number of scars diminishes, first the number of flower rises and eventually compound, large sessile drops occupy the space. The whole set of transitions takes about 15-20 seconds.

Similar scar to flower transitions occur in the hexo-PPE sample as well. In the case of PPE/CS_2 though, all the cells in Figure 7.7 appear to be in nearly perfect hexagonal order, and so unlike PS/CS_2 case, where the nucleation of such events can happen at a cell close to a defect, here the images (a)-(i) show the stages of growth of a sessile drop, over an ordered, hexagonal array of cells. The cells in PS-rich matrix (in Figure 7.6) are not arrayed in perfect hexagonal order. The metamorphosis of a sessile drop in this case happens at much faster rate than in case of PS-rich sample. The contact line of the polygonal drops advances over a row of cells almost instantaneously, i.e. a side of the polygonal contact line jumps over a discrete distance within a frame, or within 8 ms. The growing contact line seems to zip across.

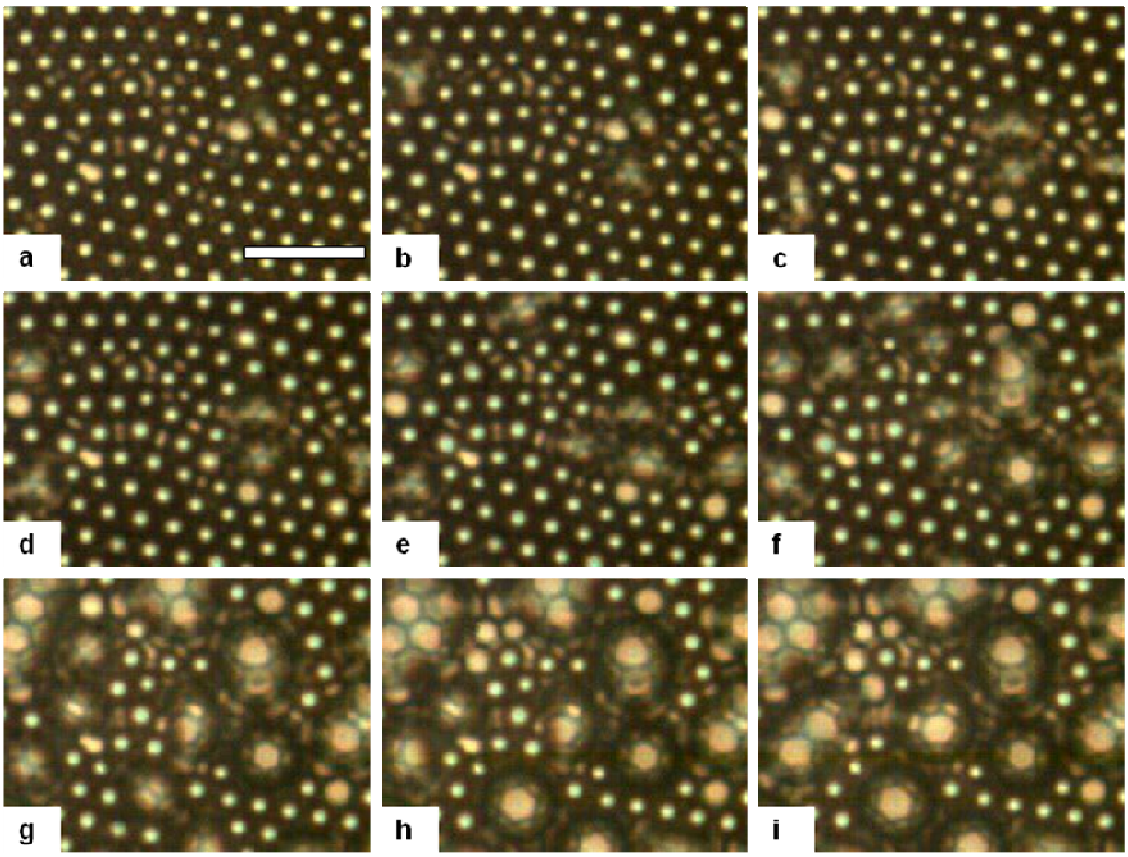

Figure 7.6 Images for PS/CS_2 solution (**a**) Formation of a doublet sessile drop or 'scar' at time = 0 s. (**b**) Two scars with triplet of cells underneath appear at 1.6 s. (**c**) Sessile drops lying over two, three and four cells appear, and the boundary between the cells is visible at 3.2 s (**d**) The doublet converts into a triplet, 4.8 s. (**e**) More scars appear, 6.4 s. (**f**) Flower appears, with a bright cell at the center and drop itself lies on a seven cells, 8.0 s. (**g**) Number of scars rises, 11.2 s. (**h**) More flowers and compound drops appear as scars are gobbled up by coalescence with nearby drops or transition into flowers, 14.4 s. (**i**) Coalesce removes more drops, and compound drops illuminate the multiple cells, 17.6 s. Scale bar is 20 µm, and ~ 62 s elapsed before frame (a).

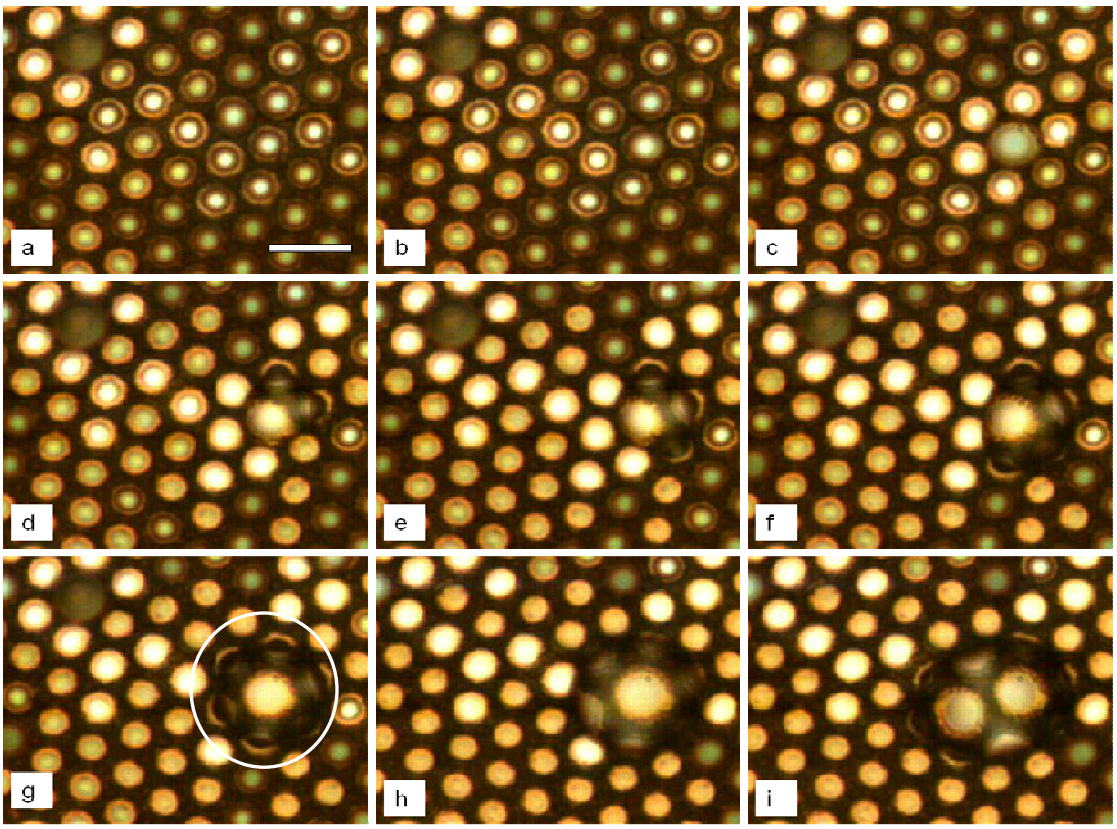

Figure 7.7 Metamorphosis of a sessile drop, from close packed array of water drops immersed in a hexo-PPE/CS_2 matrix. (**a**) The encircled region contains seven cells, and each cell appears to be focusing light differently, at 0 s. (**b**) The dot in the central cell grows larger than dot in six cells around it, at 0.216 s. (**c**) The six cells in neighborhood of the central cell turn into bright cells or lamps; the central cell overflows at 0.240 s. (**d**) Two neighboring cells are invaded by the central cell, forming a scar. The contact line lies on a triplet, and the boundary between cells can be seen under the scar. 0.280 s. (**e**) The scar grows as another adjoining cell is invaded, 0.336 s (**f**) Scar grows further, with five cells beneath it, 1.208 s. (**g**) Formation of flower occurs by the scar invading two cells simultaneously, 1.376 s. (**h**) The flower grows in size, the contact line has greater girth and central is magnified to a size greater than in previous stage, ~3.106 s. (**i**) The sessile drop invades a row of cells, thus occupying ten cells in all, 3.224 s. Scale bar is 20 µm.

7.3 Why do the drops pop out?

The condensation of water drops over evaporating polymer solutions occurs as long as the water drops encounter a supersaturated mixture of air around them. The extent of supersaturation depends upon the temperature and moisture content of the mixture,

which was shown to depend on the mass flux of the evaporating solvent. Now if the drops are semi-immersed in a highly viscous fluid, they can be thought to behave like drops trapped in bowl-shaped asperities, each of which is a few microns in size. If the condensation is still favored, the cap of the drop that project out of the asperities spread out, till it contacts a similar cap from adjoining cell and coalesces with it. Thereafter the cascade of coalescences with more cells occurs as the compound drop needs to occupy an area that encroaches upon the next drop.

The coalescence of water drops arranged in two dimensional pattern was studied by Gau and Herminghaus [54] for both ordered and disordered arrays. In a clever experiment, they generated a two dimensional pattern of wettable patches of soluble salt (calcium chloride) with hexagonal order and adsorbed water onto these. The growing drops were found to coalesce through a cascade of four-droplets, and when the drops were grown on a pattern with increasing amount of disorder, a three-droplet cascade became predominant. In the case of hexo-PPE/CS_2, the coalescence between adjoining drops is seen to occur after one of the drops appears to have excess water that causes the cap that projects over the substrate to spill out and touch the nearest neighbor, as observed in Figure 7.7. If the contact between drops is deemed to be a consequence of geometric effect of the growing size, the coalescence of drops can be considered to be similar to ripening described by Gau and Herminghaus [54]. Since the breath figure templated assembly involves substrate with varying surfaces and the temperature and humidity conditions change continuously, it is likely that other factors come into play in making drops contact with each other and coalesce thereafter. Even though the coalescence of sessile drops is commonly observed for formation of breath figures on

solid surfaces, if the underlying substrate is a smooth surface, drops nucleate and grow randomly, before they encounter each other, and the overall pattern contains several generations of drops, which have different nucleation and growth histories.

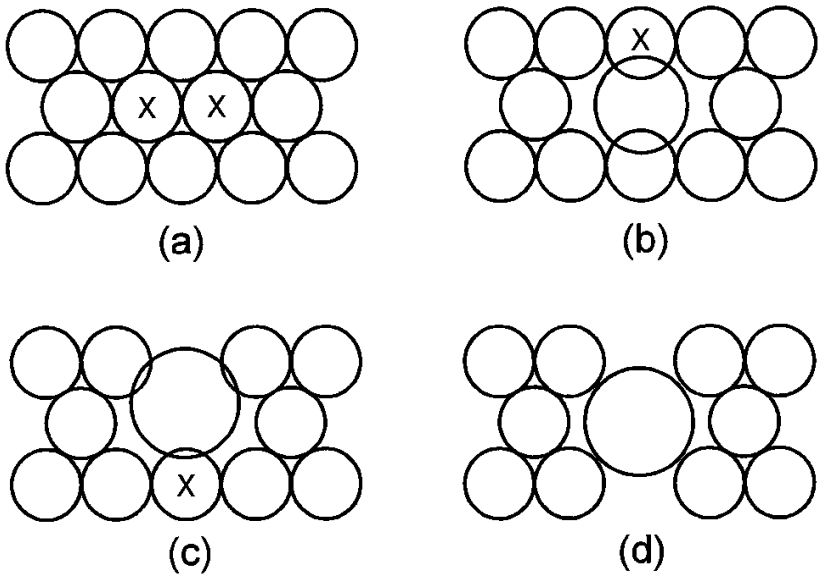

Figure 7.8 (**a**) to (**d**): A model for coalescence cascade due to Gau and Herminghaus [54], for drops arranged in perfect hexagonal order. Conservation of the center of mass of the participating droplets, and of the total mass of the system is assumed. The drops with cross are the drops that will coalesce next. Four-droplet cascades, (d), predominate for hexagonally ordered system whereas three-droplet cascades, sketched in (c), dominate for system with Gaussian disorder.

The drop of water lying immersed in the polymer solution has a high curvature, corresponding to the radius of the sphere. When the drop spills out of spherical pocket, as observed in Figure 7.7 for example, the sessile drop or part of the drop above the substrate, has a lower curvature, implying the Laplace pressure, given by equation 7.2 or 7.3 is lower. When two fluid volumes are brought in contact with each other, the fluid flows from higher pressure to lower pressure. While formation of scars and flowers involves coalescence-growth where drops invade adjoining cells in a fashion similar to

ripening described in Figure 7.8, the experimental evidence presented in earlier sections, or in Figure 7.9 indicates that water is also drawn into sessile drops from the adjoining cells that have no sessile drops over them.

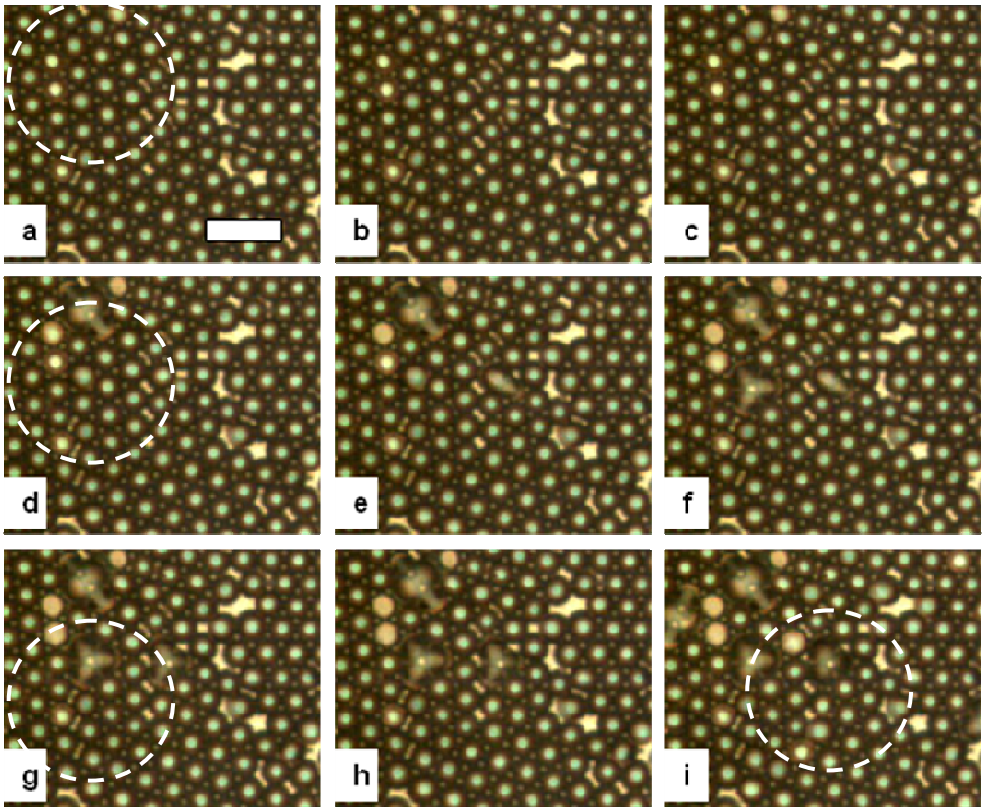

Figure 7.9 Images for the metamorphosis of drops over PS/CS_2 solution. (**a**) Notice two bright cells in the circled region. Each successive image in (a)-(h) is 240 ms apart. (**a**)-(**d**) Formation of a 'scar' is accompanied by change in brightness of an adjoining cell. (**d**)-(**g**) Appearance of second scar within the circled region, makes second bright cell become larger and brighter. The triplet that appears in the periphery of circled region, emerged during this time. (**g**)-(**i**) While sessile drops do not grow, another bright cell appears, which is quite similar in appearance to cells left after all the water drops evaporate out. The last frame is ~4 s after frame (h). Scale bar is 20 µm.

This can be attributed to the capillary suction created by the pressure difference between small, immersed water drop (high Laplace pressure) and low curvature sessile drop (low Laplace pressure). The pressure difference between a water drop with radius 1 µm and the sessile drop, with radius of curvature of 10 µm turns out to be, using

$\Delta p = 2\gamma / r_d$ for each drop, to be 1.3 x 10^5 Pa or 1.3 atm. The pressure difference drives flow from the small drop to the larger drop. In fact, it is likely that the formation of interconnected pores is followed by pressure difference driven flow of water. If one were to consider flow from one cell to another as a Poiseuille flow within a cylindrical pore of radius r_p ~ (1/10)*r_d, and length, l ~ r_d, the flow rate, $Q = \pi r_p^4 \Delta p / 8\eta_w l$, where η_w is viscosity of water, the pore would be emptied in ~ 8 ms. Although the physics involved in creation of bigger drops at the expense of smaller ones is as described, the exact pressure difference and flow rate will depend on factors discussed next.

The equilibrium contact angle over the substrate determines the size of the sessile drop, as well as the pressure within it, where the mobility of contact line depends on both contact angle hysteresis and disjoining pressure. Since the drops now lie on a structured surface, their contact angle must be different from that of pure polymer. Song [4] measured the contact angle on solid, flat polystyrene films at room temperature, and reported that the advancing and receding contact angles as 91^o and 71^o respectively. Figure 7.10 shows how these measurements were made. The measured contact angles for as-cast macroporous films were found to be 132^o and 95^o. The calculated value for such a film with r ~ 3.1 and f_s ~ 0.35 with Cassie drop are 131^o and 122^o, respectively, whereas the corresponding estimates made for Wenzel case give an advancing angle of 93^o. The drops deposited from above on the holey film from above, are in Cassie state, though the receding value is not close to the measured value. Further, Song showed that the drop can be made to transform from Cassie to Wenzel state by heating the drop. It is possible to peel the top layer of the pores, and this increases the superhydrophobic nature of the drops. In the corresponding measurements by Song, for geometric parameters r ~ 1.9 and

f_s ~ 0.09, the measured advancing and receding angles turn out to be 161^o and 116^o respectively. Again, the drops exhibit advancing contact angle close to the value calculated for a Cassie drop (156^o), though the receding contact angle anticipated in this case, 152^o, is again much higher than the measured value of 116^o. The corresponding contact angles for a Wenzel drop are calculated to be 92^o and 52^o respectively.

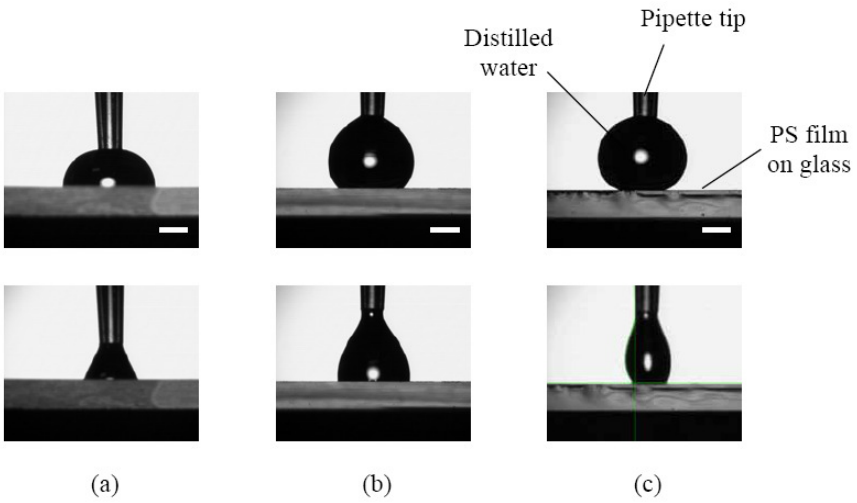

Figure 7.10 Advancing and receding contact angle of polystyrene (mono-carboxyl terminated, M_w= 50,000) films, with different amount of solid fraction. Column (**a**) flat surface; column (**b**) macroporous as-cast holey film and column (**c**) holey film with top peeled off. The top row shows the advancing contact angle measurement. Scale bar: 1 mm (from Song [4]).

The contact angle for water on flat films of PS is much smaller than the corresponding contact angle determined using the Cassie or Wenzel model. Since the sessile drops (as scars or flowers) only occupy a few cells, their size is only two to three times larger than the underlying pattern, while Wenzel and Cassie states describe behavior for drop deposited over substrate with the feature size much smaller than the deposited drop. The nature of the experiment is such that the temperature and vapor pressure over the drop changes continuously, and in essence, the equilibrium

considerations of contact angle, contact line and contact angle hysteresis cannot be applied to quantify the behavior. If we were to assume that water drops are lying on a featureless substrate, the contact line can move as soon as the drop volume increases to the point where the contact angle becomes greater than the advancing contact angle. As two drops coalesce, the combined volume of the drop can lie in any of the metastable states, till the contact angle is exceeded again by incorporation of more fluid, either through condensation or by the capillary driven flow that pulls fluid out of the adjoining cells. Now when the drops lie immersed in the concentrated polymer solution, condensation growth and Laplace pressure difference makes the drop spill out of its cell, till it contacts the next cell, and the coalescence produces a Wenzel-like state. It might be more precise to call it 'film stage', for Wenzel-like state implies that only features below the drop have fluid within them. As the drop grows in size, and after the neighboring cells began to dry out, the sessile water drop seems to lie over pores that have lost water, thus transforming them into Cassie-like state.

The transition from Wenzel to Cassie state was reported by Dorrer and Ruhe [38], when they observed condensation growth of water drops on an ultrahydrophobic substrate formed by creating silicon post structures that were 40 µm tall and the post spacing, *s*, was 8 µm. The posts were square in cross-section and side lengths, *d*, of 4 µm and 8 µm were studied. Besides the controlled roughness, the posts were coated with a hydrophobic fluoropolymer, and the authors observed that for temperature of ~2^{o} C and environment with humidity of ~70%, the condensation growth of water in asperities allowed them to exist in metastable Wenzel state. The drops were observed to transition from Wenzel state to Cassie state, which was observed using microscopy as illustrated in

Figure 7.11. Cassie drops were distinguished from Wenzel drops by the following arguments: (i) Cassie drops are spherical while the Wenzel drops have jagged contact line that follows the post structure; and (ii) since the Cassie drops rest on the top of the posts, they are taller in size and hence they appear blurred if the microscope is focused on the Wenzel drops.

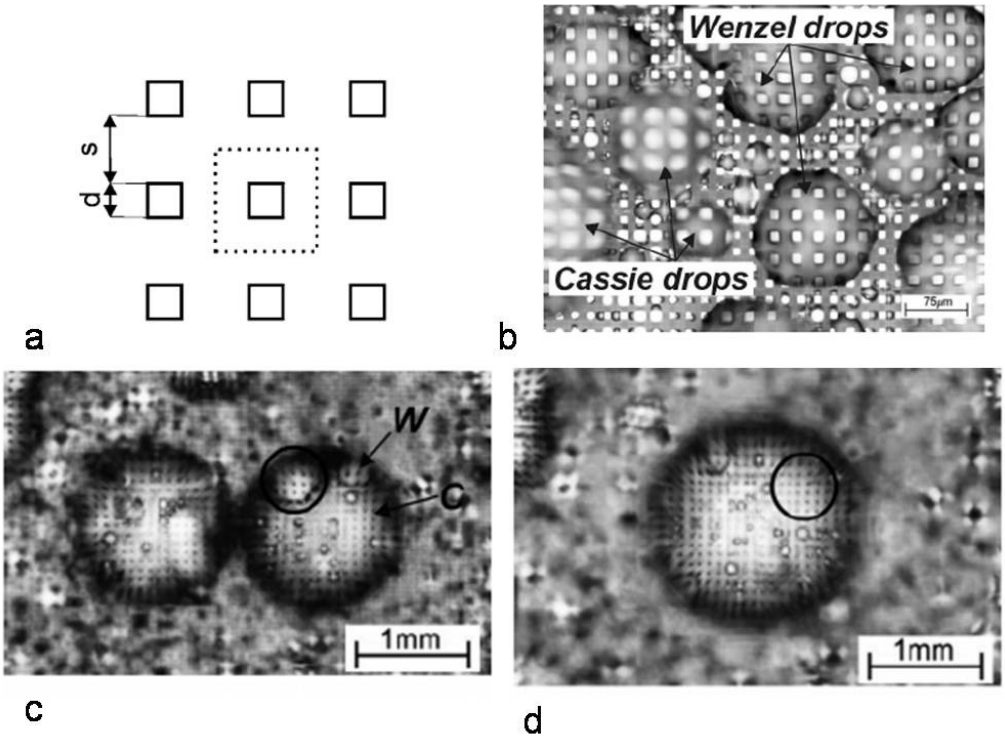

Figure 7.11 (**a**) The pattern consists of silicon posts arrayed as shown. (**b**) Drops in the Cassie and Wenzel states on a post surface (**c**) Before the coalescence event, the black circle and the index W label the Wenzel region in the right drop, while index C shows the Cassie part. (**d**) After coalescence, a region of the drop transitions from the Wenzel state to the Cassie state (Adapted from ref. [38]).

Most of the studies on condensation on microstructures [55-58] with well-defined patterns or roughness were carried out on geometries like the one just described and likewise, involved controlled condensation conditions. Even in the studies involving existing biological structures [37], on e.g. lotus leaf or insects the condensation condition

(temperature and humidity) were controlled externally. Briefly, if a drop is deposited or falls on a superhydrophobic surface, it is not able to enter the capillaries and rolls off. But when condensation occurs on a microstructured substrate, it starts from the crevices and liquid water fills in the cavity, before the drops from different cavities grow to the size where they start to interact and coalesce with each other. Once the drops reach such a size, they are easily drawn into the growing domains that transformation from being the Wenzel type drops to Cassie type occurs. Condensation of water starts in the asperities, and after the liquid fills the asperities, it begins to invade the top surface, where the sessile drop moves with fits and starts, causing a zipping motion [59, 60] and creates a Wenzel state which would not occur if a drop was just deposited on the substrate. The phenomenon is termed as breakdown of superhydrophobicity. Since our system has no prefabricated roughness or structure, and the water drops themselves template the pores that they eventually pop out from, the process cannot be called breakdown of superhydrophobicity, implying that comparison with zipping wetting is only in terms of the contact line mobility.

Lastly, the advancing and receding contact angles over a flat PPE film are 110^{o} and 81^{o} respectively [61], in contrast to PS flat film with 91^{o} and 71^{o} respectively. Thus PPE is intrinsically more hydrophobic than the PS (though the exact values of contact angle will be different for PPE used depending upon the side groups). The time scale during which scars and flowers formed are controlled by the wetting behavior of the solid region in macroporous polymer film and hence, PPE seems to have faster dynamics during formation of sessile drops.

7.4 How does the water evaporate in the last stage of breath figure templated assembly?

Water drops that grow into ordered patterns eventually create the microstructure that consists of hydrophobic polymer, interspersed with air bubbles. The loss of water from the evaporating and drying polymer substrate involves mass transfer to air flow of a given speed and humidity. The sessile drops over the substrate seem to feed on the fluid present in cells around them, perhaps causing the tunnels that connect the holes that are found to exist in the holey film. The stages in drying of water drops are shown in Figure 7.12. As the drop starts drying, while the central drop is seen to shrink and disappear, the drops at the edge of image are first seen to grow, as they feed on the nearby sessile drops.

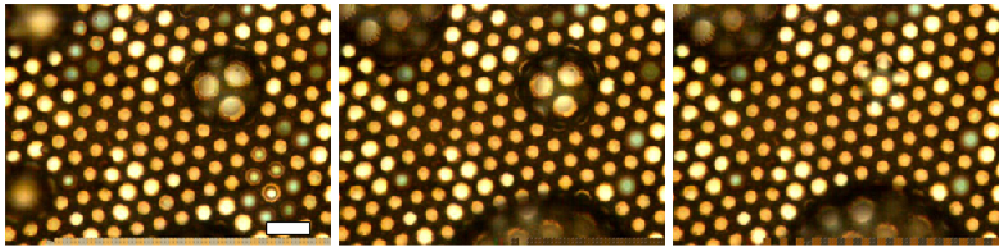

(a) (b) (c)

Figure 7.12 Evolution of sessile drops, (**a**) Drops on the left corner exist over six cells, a central sessile drop shows three cells, that appear larger than their real size due to lensing effect of water. (**b**) The drop at the bottom corner on left has evaporated away, while two large sessile drops have emerged. The central drop has diminished in size, and the cells within it are seen to be in sharper focus. (**c**) The bottom sessile drop has moved towards a rounder shape and increased its size. The central drop is evaporating and only a faint flower like sessile drop is left with edges lying symmetrically in a hexagonal symmetry. Scale bar is 20 µm.

The drying of a drop involves removal of water by evaporation as well as motion of the contact line. The stage, during which sessile drops appear, grow and coalesce, involves drops moving on a composite interface that can consist of water in pores and wet or dry polymer regions. During drying, as the contact line of the drop recedes, it does so in a mechanism reminiscent of dewetting. The curious aspect of the dewetting

behavior is again the presence of discrete jumps that involve one side of polygonal contact line jumping from center of a row of cells to next row, as illustrated in the Figure 7.13. The contact line recedes by nearly 20 µm in about 1 second between images 7.13 (c) and 7.13 (h). The contact line seems to unzip or snap like a taut rubber band, pinned over a set of pegs to form a polygon, let loose by removing one of the pegs.

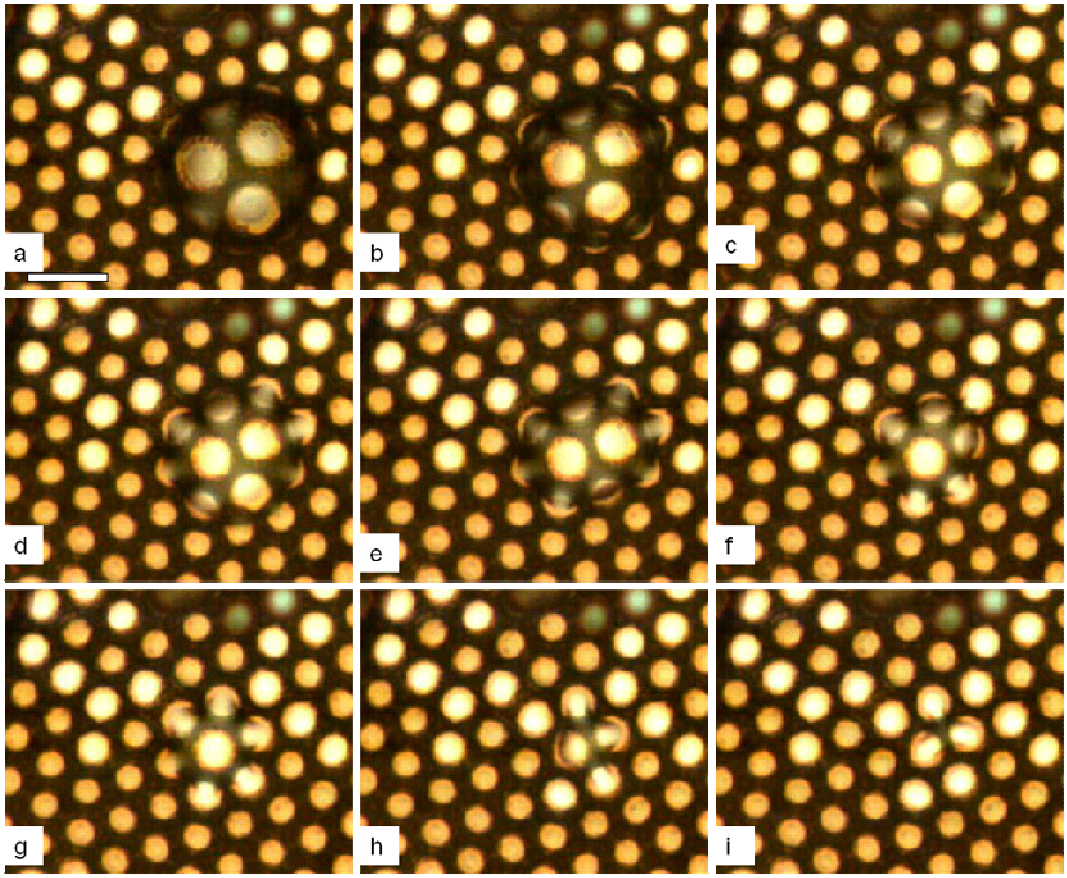

Figure 7.13 Stages of drying, include unzipping dewetting (**a**) Large sessile drop, nearly four times the average cell size, at 0s (**b**) Decrease in size of the drop, makes the lensing effect weaker, and the cells appear smaller in size. The circumference of the drop is smaller, 5 s. (**c**) Drop shrinks further, and also diminishes in height, again the lensing effect shows that curvature of drop decreased, 6 s. (**d**) is 168 ms after stage (c), but the contact line does not seem to move. In (**d**)-(**e**) within two frames that are 8ms apart, the contact line of the drop jumps making the sessile drop even smaller. (**e**)-(**f**) The contact line move to a smaller region in 24 ms. (**g**) The contact line continues to recede, slipping and zipping across rows. While transition from (f)-(g) shows changes that take place in 96 ms, (g)-(h) occurs in 40 ms. (i) Drop shown in its last stage, before it disappears completely. Scale bar is 20 µm.

The most significant aspect of drying behavior described here is that in the context of breath figure templated assembly, the final structure is established somewhat before the water actually dries out, and the drying itself occurs from a thin sessile drop as opposed to the previous belief that it occurs from individual drops buried in a concentrated polymer solution. In most experiments, the formation of final structure is seen to occur within a couple of minutes after spreading the dilute polymer solution, and so unless close attention is paid to the stage after drops are arranged in closed packed array, it is easy to miss these fascinating cascade of events. The evaporation of the sessile drops has been investigated by many researchers (see Hu and Larson [62] and references therein), and the evaporation rate is proportional to the contact line radius, and also depends upon the contact angle. The evaporation behavior of these 'sessile' drops provides an interesting system to study theoretically as well as experimentally. The motion of contact line and contact angle hysteresis here depends not only on the choice of polymer, but also on the microstructure templated by the water droplets.

7.5 Conclusion and open questions

The evaporation of close packed water arrays formed over evaporating polymer solutions was found to exhibit interesting wetting and dewetting dynamics. The phenomenon of drops popping out and growing as sessile drops over polymer rich-substrate is described for the first time. After the drops cease their singular or collective dynamics, that allows the assembly to remove defects and disclinations, the drops get jammed against each other, and their location in the plane of the substrate is fixed, at these cells. Thereafter the drops appear to move in the direction perpendicular to the substrate, and each of these cells focuses light to its center, creating a pattern of bright

dots. Some of these dots transform into sessile water drops that grow in size by either coalescing with the surrounding drops or by hydrodynamic flow from the adjoining cells. The sessile drops that occupy two to four cells, display the underlying cell boundaries, and are designated as scars. These scars eventually grow, such that some of the sessile drops occupy seven cells, where a bright magnified cell is visible at the center and the nearest six cells around it are buried under the contact line, giving the drop appearance of a flower. As more and more scars transform into flowers, the next stage involves growth of compound sessile drops.

These contact line of these drops moves with discrete motions, reminiscent of Zipping wetting, described for patterned superhydrophobic surfaces. In those cases, the condensation of water plugs the asperities and prompts the contact line appears to zip across. Once the drying sets in, the contact line recedes in similar fashion, where the line is seen to jump back or snap from one frame to next (move 2-4 microns in < 8 ms). While wetting behavior of holey film exhibits Cassie state, the observed behavior during the last stage before drops dry out is likely to include Wenzel-like state initially, followed by transformation to a compound Cassie-Wenzel drop. Under equilibrium conditions, a drop can show multiple contact angles in a range defined by advancing and receding contact angles. It is likely that during growth (or drying), the movement of contact line occurs whenever the drop volume increases (or decreases) beyond the point where the drop can be above the advancing contact angle (or below the receding contact angle). The presence of air flow, mass and heat transfer due to condensation or evaporation, and a very heterogeneous interface implies that the wetting behavior visualized here is a result of complex interactions and forces.

In the context of mechanism for the breath figure templated assembly, the most significant points to note are that the wetting-dewetting stages described in the chapter imply that (1) drops are definitely not covered by polymer precipitates or bags (reviewed with the existing mechanisms from literature in Chapter 2), (2) if the drops were to grow inside a viscous polymer solution, they would manifest such spreading and coalescence behavior at an earlier stage, so the nucleation and growth of drops occurs over the substrate, 3) the evaporation of water occurs as thin sessile drops, which is much faster than evaporation from drops buried in polymer solution with only a small cap exposed to the airflow, and 4) pores are interconnected probably due to the forces at work during seeping of water out of cells to feed the growing or drying sessile drops.

The observations recorded in this chapter indicate that the breath figure templated assembly involves not only fascinating aspects related to the growth of monodisperse water drops, but their disappearance itself is full of surprises. Since the wetting-dewetting phenomenon reported here has not received any attention before, the list of unsolved problems is very rich. The problems related to definition and evolution of contact angle and contact line for drops on hydrophobic and superhydrophobic surfaces are fundamental to understanding of wetting as well as to the behavior observed here. What are limits of validity of Cassie or Wenzel relations? The evidence presented here suggests that the coalescence of drops that pop out in the ordered and disordered arrays exhibit different steps or stages. What capillary forces exist within the cells, and how do these depend upon the choice of polymer, solvent and airflow conditions? What causes zipping wetting or unzipping dewetting, and how does that depend upon material or environment as well as the pore dimensions that can be measured for holey films? How does the rate

of evaporation of thin sessile drops compare to the rate of evaporation of the same volume of drops immersed in another fluid with only a small cap exposed to the airflow? In the quest of understanding the mechanism of breath figure templated assembly, the whole field of wetting statics and dynamics, with its questions and understanding, becomes a part of the whole story.

7.6 References

1. Lawrence, D.H., *Women in Love*. 2003, New York: Dover Publications.

2. Srinivasarao, M., et al., *Three-dimensionally ordered array of air bubbles in a polymer film.* Science, 2001. **292**(5514): p. 79-83.

3. Barrow, M.S., et al., *Physical characterisation of microporous and nanoporous polymer films by atomic force microscopy, scanning electron microscopy and high speed video microphotography.* Spectroscopy-an International Journal, 2004. **18**(4): p. 577-585.

4. Song, L., *Study of ordered macroporous polymer films by templating breath figures*, in *School of Polymer, Textile and Fiber Engineering*. 2005, Georgia Institute of Technology: Atlanta. p. 193.

5. Song, L., et al., *Facile microstructuring of organic semiconducting polymers by the breath figure method: Hexagonally ordered bubble arrays in rigid-rod polymers.* Advanced Materials, 2004. **16**(2): p. 115-+.

6. Erdogan, B., et al., *Permanent bubble arrays from a cross-linked poly(para-phenyleneethynylene): Picoliter holes without microfabrication.* Journal of the American Chemical Society, 2004. **126**(12): p. 3678-3679.

7. Rowlinson, J.S., *Cohesion: A Scientific History of Intermolecular Forces*. 2002, Cambridge: Cambridge University Press.

8. de Gennes, P.G., F. Brochard, and D. Quere, *Capillarity and Wetting Phenomena: drops, bubbles, pearls, waves*. 2004, New York: Springer-Verlag.

9. Starov, V.M., M.G. Velarde, and C.J. Radke, *Wetting and Spreading Dynamics*. Surfactant Science Series, ed. A.T. Hubbard. 2007, Boca Raton: Taylor & Francis Group, LLC.

10. Kralchevsky, P.A. and K. Nagayama, *Particles at fluid interfaces and membranes*. Studies in interface science, ed. D. Mobius and R. Miller. 2001, Amsterdam: Elsevier Science B. V.

11. Rowlinson, J.S. and B. Widom, *Molecular Theory of Capillarity*. 2003: Dover Publications.

12. Degennes, P.G., *Wetting -Statics and dynamics.* Reviews of Modern Physics, 1985. **57**(3): p. 827-863.

13. Good, R.J., *Contact angle, wetting and adhesion - a critical review.* Journal of Adhesion Science and Technology, 1992. **6**(12): p. 1269-1302.

14. Leger, L. and J.F. Joanny, *Liquid spreading.* Reports on Progress in Physics, 1992. **55**(4): p. 431-486.

15. Quere, D., *Rough ideas on wetting.* Physica a-Statistical Mechanics and Its Applications, 2002. **313**(1-2): p. 32-46.

16. Herminghaus, S., M. Brinkmann, and R. Seemann, *Wetting and Dewetting of Complex Surface Geometries.* Annual Review of Materials Research, 2008. **38**: p. 101-121.

17. Quere, D., *Wetting and Roughness.* Annual Review of Materials Research, 2008. **38**: p. 71-99.

18. Degennes, P.G., X. Hua, and P. Levinson, *Dynamics of wetting - local contact angles.* Journal of Fluid Mechanics, 1990. **212**: p. 55-63.

19. Srinivasarao, M. and J.O. Park, *Measurement of Surface Roughness of Polymers using Optical Methods*, in *Comprehensive Desk Reference of Polymer Characterization and Analysis*, R.F. Brady, Editor. 2003, Oxford University Press.

20. Wenzel, R.N., *Resistance of solid surfaces to wetting by water.* Industrial and Engineering Chemistry, 1936. **28**: p. 988-994.

21. Wenzel, R.N., *Surface roughness and contact angle.* Journal of Physical and Colloid Chemistry, 1949. **53**(9): p. 1466-1467.

22. Cassie, A.B.D., *Contact angles.* Discussions of the Faraday Society, 1948. **3**: p. 11-16.

23. Cassie, A.B.D., *Contact angles.* Transactions of the Faraday Society, 1948. **44**(3): p. 11-16.

24. Cassie, A.B.D. and S. Baxter, *Large contact angles of plant and animal surfaces.* Nature, 1945. **155**(3923): p. 21-22.

25. Barthlott, W. and C. Neinhuis, *Purity of the sacred lotus, or escape from contamination in biological surfaces.* Planta, 1997. **202**(1): p. 1-8.

26. Neinhuis, C. and W. Barthlott, *Characterization and distribution of water-repellent, self-cleaning plant surfaces.* Annals of Botany, 1997. **79**(6): p. 667-677.

27. Otten, A. and S. Herminghaus, *How plants keep dry: A physicist's point of view.* Langmuir, 2004. **20**(6): p. 2405-2408.

28. Wagner, T., C. Neinhuis, and W. Barthlott, *Wettability and contaminability of insect wings as a function of their surface sculptures.* Acta Zoologica, 1996. **77**(3): p. 213-225.

29. Gu, Z.Z., et al., *Structural color and the lotus effect.* Angewandte Chemie-International Edition, 2003. **42**(8): p. 894-+.

30. Hansen, W.R. and K. Autumn, *Evidence for self-cleaning in gecko setae.* Proceedings of the National Academy of Sciences of the United States of America, 2005. **102**(2): p. 385-389.

31. Bush, J.W.M. and D.L. Hu, *Walking on water: Biolocomotion at the interface.* Annual Review of Fluid Mechanics, 2006. **38**: p. 339-369.

32. Hu, D.L. and J.W.M. Bush, *Meniscus-climbing insects.* Nature, 2005. **437**(7059): p. 733-736.

33. Hu, D.L., B. Chan, and J.W.M. Bush, *The hydrodynamics of water strider locomotion.* Nature, 2003. **424**(6949): p. 663-666.

34. Parker, A.R. and C.R. Lawrence, *Water capture by a desert beetle.* Nature, 2001. **414**(6859): p. 33-34.

35. Gao, L.C. and T.J. McCarthy, *"Artificial lotus leaf" prepared using a 1945 patent and a commercial textile.* Langmuir, 2006. **22**(14): p. 5998-6000.

36. Tuteja, A., et al., *Designing superoleophobic surfaces.* Science, 2007. **318**(5856): p. 1618-1622.

37. Cheng, Y.T. and D.E. Rodak, *Is the lotus leaf superhydrophobic?* Applied Physics Letters, 2005. **86**(14).

38. Dorrer, C. and J. Ruhe, *Condensation and wetting transitions on microstructured ultrahydrophobic surfaces.* Langmuir, 2007. **23**(7): p. 3820-3824.

39. Liu, B. and F.F. Lange, *Pressure induced transition between superhydrophobic states: Configuration diagrams and effect of surface feature size.* Journal of Colloid and Interface Science, 2006. **298**(2): p. 899-909.

40. Patankar, N.A., *Mimicking the lotus effect: Influence of double roughness structures and slender pillars.* Langmuir, 2004. **20**(19): p. 8209-8213.

41. Marmur, A., *Wetting on hydrophobic rough surfaces: To be heterogeneous or not to be?* Langmuir, 2003. **19**(20): p. 8343-8348.

42. Patankar, N.A., *Transition between superhydrophobic states on rough surfaces.* Langmuir, 2004. **20**(17): p. 7097-7102.

43. Quere, D., *Non-sticking drops.* Reports on Progress in Physics, 2005. **68**(11): p. 2495-2532.

44. Bico, J., U. Thiele, and D. Quere, *Wetting of textured surfaces.* Colloids and Surfaces a-Physicochemical and Engineering Aspects, 2002. **206**(1-3): p. 41-46.

45. Bico, J., C. Tordeux, and D. Quere, *Rough wetting.* Europhysics Letters, 2001. **55**(2): p. 214-220.

46. Quere, D. and P. Aussillous, *Non-stick droplets.* Chemical Engineering & Technology, 2002. **25**(9): p. 925-928.

47. Quere, D., A. Lafuma, and J. Bico, *Slippy and sticky microtextured solids.* Nanotechnology, 2003. **14**(10): p. 1109-1112.

48. Quere, D. and M. Reyssat, *Non-adhesive lotus and other hydrophobic materials.* Philosophical Transactions of the Royal Society a-Mathematical Physical and Engineering Sciences, 2008. **366**(1870): p. 1539-1556.

49. Gao, L.C. and T.J. McCarthy, *Contact angle hysteresis explained.* Langmuir, 2006. **22**(14): p. 6234-6237.

50. Gao, L.C. and T.J. McCarthy, *The "lotus effect" explained: Two reasons why two length scales of topography are important.* Langmuir, 2006. **22**(7): p. 2966-2967.

51. Gao, L.C. and T.J. McCarthy, *Reply to "Comment on How Wenzel and Cassie Were Wrong by Gao and McCarthy".* Langmuir, 2007. **23**(26): p. 13243-13243.

52. Gao, L.C. and T.J. McCarthy, *How Wenzel and Cassie were wrong.* Langmuir, 2007. **23**(7): p. 3762-3765.

53. Oner, D. and T.J. McCarthy, *Ultrahydrophobic surfaces. Effects of topography length scales on wettability.* Langmuir, 2000. **16**(20): p. 7777-7782.

54. Gau, H. and S. Herminghaus, *Ripening of ordered breath figures.* Physical Review Letters, 2000. **84**(18): p. 4156-4159.

55. Narhe, R.D. and D.A. Beysens, *Water condensation on a super-hydrophobic spike surface.* Europhysics Letters, 2006. **75**(1): p. 98-104.

56. Narhe, R.D. and D.A. Beysens, *Nucleation and growth on a superhydrophobic grooved surface.* Physical Review Letters, 2004. **93**(7).

57. Jung, Y.C. and B. Bhushan, *Wetting behaviour during evaporation and condensation of water microdroplets on superhydrophobic patterned surfaces.* Journal of Microscopy-Oxford, 2008. **229**(1): p. 127-140.

58. Lafuma, A. and D. Quere, *Superhydrophobic states.* Nature Materials, 2003. **2**(7): p. 457-460.

59. Pirat, C., et al., *Multiple time scale dynamics in the breakdown of superhydrophobicity.* Epl, 2008. **81**(6).

60. Sbragaglia, M., et al., *Spontaneous breakdown of superhydrophobicity.* Physical Review Letters, 2007. **99**(15).

61. Davies, J., et al., *Use of dynamic contact angle profile analysis in studying the kinetics of protein removal from steel, glass, polytetrafluoroethylene, polypropylene, ethylenepropylene rubber, and silicone surfaces.* Journal of Colloid and Interface Science, 1996. **182**(2): p. 437-443.

62. Hu, H. and R.G. Larson, *Evaporation of a sessile droplet on a substrate.* Journal of Physical Chemistry B, 2002. **106**(6): p. 1334-1344.

CHAPTER 8

COLLOIDAL GOLD NANORODS

All that glisters is not gold;
Often have you heard that told:
William Shakespeare*, Merchant of Venice* [1].

8.1 Introduction

Colloidal gold nanoparticles have received widespread attention in recent years [2-17] both due to their unusual properties, and promising applications. Nanoparticles, typically in the size range of 1-100 nm, possess size and shape dependent properties which differ markedly from their bulk behavior [2, 3, 17-19]. For example, spherical colloidal gold particles with a diameter around 10 nm make their aqueous dispersions assume a ruby red color, while increase in their size to nearly 100 nm or change in shape to say a rod-like shape, with aspect ratio of say 3 (length 30 nm, diameter 10 nm) makes the colloidal dispersion appear bluish. It must be remarked that bulk gold has unmistakable yellowish color, and the size dependence at nanometer scale is simply a consequence of how light interacts with matter.

The recent interest in gold nanoparticles is propelled by both the advances in our scientific understanding of their synthesis and physical properties [2-17] as well as the possibility of using them for applications in chemical and biological sensing [3, 5, 7, 11, 20-44], cancer treatment [11, 38, 45-48], catalysis [49, 50], as markers for transmission electron microscopy (TEM) and scanning electron microscopy (SEM) [51] and various specialized photonics and electronic applications [20, 52-56].

The crucial aspect of this chapter is to present the historical background to point out that the physical properties of gold particles *including rodlike particles* were studied

in the early twentieth century and these provided original and ground breaking advances in the field of colloidal matter. Most of the recent studies have overlooked the fundamental experiments summarized here. A glimpse of the work of the early pioneers [57-67] especially Faraday, Zsigmondy, Svedberg, Smoluchowski, Mie, Ostwald and Gans reveals how they delved into the synthesis and physical properties of gold sols primarily to establish the existence of particulate nature of colloidal sols and to explore questions related to the reality of atoms and molecules. Apart from providing with a context for later discussion, their work presents a useful set of experimental and theoretical ideas that can be developed, applied and explored further in modern day research. For example, Zsigmondy's method for visualization of gold particles using ultramicroscopy [61] is elucidated here and Svedberg's and Zsigmondy's ideas about how size dispersity can be controlled by controlling nucleation and growth is presented. A modified version of Svedberg's ultracentrifugation analysis and technique [59] can be used for shape separation of nanorods, as described in the next chapter.

The parameters that affect colloidal stability of gold dispersions as well as the physics that determines the optical properties and color of the rod-like nanoparticles are described, albeit briefly, next. The next chapter elucidates how rodlike particles can be separated from nanospheres (and particles of other shapes) that are the typical byproducts of seed mediated synthesis. The self-assembly of colloidal gold nanorods, identifying the means and methodology to study their phase transition to liquid crystallinity is presented in the chapter 10. Only the concepts relevant to the shape separation and self assembly are included here, and a longer historical perspective as well as description and discussion about the synthesis and the optical properties was recently included in a

review by Sharma, Park and Srinivasarao [68]. The seed mediated synthesis method used for making the rod-like particles is described briefly and related with the results from nucleation and growth of water drops as relevant to breath figure templated assembly to provide a basis for synthesis of more monodisperse dispersions.

8.2 Historical perspective on colloidal gold sols

The use of colloidal gold as a colorant can be traced back at the least to 5th B. C. for its use in making ruby glass and providing reddish tinge to ceramics. According to Ostwald [57], "This colloidal gold was prepared even in the days of the alchemists by the reduction of gold salts by all kinds of organic substances, including urine." Similar concoctions were used by the Hindu chemists for Ayurveda, the ancient system of Indian medicine [69]. In what follows, we outline the representative significant contributions from the giants of early colloidal chemistry and physics.

8.2.1 Synthesis and color of ruby gold

The definitive study on the nature of gold particles in hydrosols – their synthesis by reduction of dilute gold chloride using phosphorus, size dependent optical properties and coagulation behavior – was carried out by Faraday as presented in his 1857 article titled: "The Bakerian Lecture: Experimental relations of Gold (and other metals) to Light" [66]. Faraday determined that the ruby glass was colored so, because of the presence of finely dispersed gold particles, and carried out reactions to ascertain that purple of Cassius could be obtained by adding tin chloride to gold sol. In the context of

his experiments, he attempted to study the optical properties as well as remarked on the aggregation and sedimentation [66].

For nearly forty years, Faraday's work remained unnoticed [66], and even the scientists who worked on the ruby glass and purple of Cassius were not aware of it [62]. Thereafter Zsigmondy began his investigations into the color of ruby glass and formulated a method for preparing colloidal gold by reducing dilute, slightly alkaline solution of gold chloride with boiling formaldehyde. After becoming aware of Faraday's method, he combined both the synthesis techniques to arrive at a two step synthesis method, which in recent literature is referred to as the seed-mediated method, while it was referred to as nuclear method in the early days. Svedberg played a central role in early studies of gold sols and he pioneered the use of electrochemical methods for the synthesis of gold particles. In his text [58], he reports the use of every conceivable reducing agent of available at his time to produce colloidal gold from hydrochloroauric acid [58].

The role of supersaturation in determining the nucleation and growth of gold particles, both in condensation growth from solution and in vapor deposition, was also discussed by Sevdberg [58, 60] and Zsigmondy [61, 62] in their pioneering studies. In his 1921 text [58], Svedberg contends: "The degree of dispersion of gold colloids formed by reduction of $HAuCl_4$ without adding of condensation nuclei is, according to Zsigmondy, (Kolloidchemie, p. 143 (1918)) dependent on two factors, viz: 1) The spontaneous production of nuclei (s.p.n.) 2) The velocity of the growth of the particles (v.g.p.)." He continues: "The spontaneous production of gold nuclei is a kind of coagulation and is therefore accelerated by coagulating electrolytes in small quantities. Higher

concentrations drive the coagulation of the particles too far. Weak reducing agents, e. g. potassium thiocyanate, potassium citrate, congo red, etc., added before the reduction give rise to small gold particles that act as nuclei. Protective electrolytes, e.g., NH_3, $K_4Fe(CN)_6$, $K_3Fe(CN)_6$, retard production of nuclei. Protective colloids do not retard the s.p.n., their particles being too coarse for these very small gold particles. The growth of the particles is also a kind of coagulation. It is retarded by protective colloids and accelerated by coagulating colloids." It must be pointed out that the critical dependence of nucleation and growth on supersaturation can be used in the so called seed mediated method to generate particles with lower polydispersity. While the mechanism that drives the growth is different here from the breath figure templated assembly, qualitatively the size distribution can be made narrow here as well by controlling the conditions, which is perhaps not as well studied or understood as is the growth in case of cloud physics.

8.2.2 Size and shape dependent color of gold sols

In his text [62], Zsigmondy notes: "The color of colloidal gold solutions in transmitted light may be red, violet, or blue, and occasionally yellowish brown, or brown. The ultramicrons of red solutions are green; those of blue solutions are yellow to reddish brown; violet solutions contain both. We have to do with green, yellow, or brown ultramicrons." He also points out: "With regard to the brown color of very small particles a large number of experimental facts point to the assumption that the ultramicrons are not composed of massive gold. The assumption that the particles are spherical in form is made solely for the purposes of calculation, and a number of facts would seem to discredit the hypothesis. The very great independence of the color on the diameter makes

it seem plausible that ultramicrons in red hydrosols are not necessarily spherical when the size is 40 μμ and under." The nm is old days was thus represented as μμ.

The dependence of optical properties on their shape was thus apparent to researchers including Zsigmondy whose text describes difference in color observed by using polarized light parallel and perpendicular to the anisotropic particles oriented by spreading out on a gelatin film [62]. Zsigmondy invented the ultramicroscope [61] which allowed Siedentopf and Zsigmondy to visualize the colloidal gold particles (i.e. nanoparticles), showing that colloidal matter consisted of dispersion of particles of measurable size, and was able to make some of the first particle tracking studies to determine the diffusion behavior of the nanoparticles.

In this respect, the text by Svedberg [60] also describes a few other experiments used to determine size and size - or shape - dependent properties, including Scherrer's determination of particle size using X-ray scattering, and Sevdberg's attempts to determine particle size using particle tracking and Brownian motion as well as measurement of size using osmotic pressure and ultrafiltration. His text [60] mentions that Scherrer and Björnståhl demonstrated that the gold sols have same X-ray diagram as gold wires. Björnståhl (see Svedberg's text [60]) also measured the double refraction of gold sols in presence of external electric, magnetic and flow fields, and found that shape anisotropy as well as coagulation of particles can be studied using these. Though most of these techniques have not been fashionable for the studies on gold (and other metal) nanoparticles, they incorporate concepts and applications that must be reassessed.

8.2.3 Scattering and absorption: Mie theory for spherical, and Gans theory for ellipsoidal particles

Exactly hundred years back in 1908, Mie wrote a seminal paper [65] to theoretically describe the absorption and scattering by metal particles, and his motivation was to explain the color of gold sols. His classic paper "Beiterage zur Optik truber Medien, speziell kolloidaler Metallosungen" which translates to "Contributions on the optics of turbid media, particularly colloidal metal solutions" include calculation of absorption spectrum for gold sols in water, and he plots the absorption and scattering spectra as a function of particle size for spherical gold particles. Mie's theory is applicable to only spherical particles. So when Mie compared his theoretical predictions to the experiments results of his student (Walter Steubing), Mie attributed the deviation to nonspherical particles in certain cases. Mie closed his seminal paper with a statement: "*To complete the theory it is absolutely necessary to study the behavior of ellipsoidal particles*." Gans [64] extended the theory to consider the spheroid particles, showing how smaller aspherical particles can show absorbance at longer wavelengths than spherical particles of comparable size. The physical basis for the size and shape dependent absorbance of colloidal gold sols is described briefly, for the UV-Vis spectroscopy is one of the primary tools used for characterizing optical properties of colloidal gold nanoparticles.

8.2.4 Shape effects on Brownian motion: sedimentation, diffusion and viscosity

The properties of colloids depend, to a large extent, on the movement of particles and this movement consists of translational and rotational Brownian motion. The

advances in theoretical understanding of Brownian motion were brought about by Einstein [70-72], Smoluchowski [73-75] and Langevin [76] (also see Chandrasekhar's review [77] and recent perspectives [78-81]) in the beginning of twentieth century. These provided the requisite understanding to describe the continuous motion of particles observed in ultramicroscope as well to understand the size dependence of their stability and sedimentation behavior.

Einstein (1905) [70, 71] reasoned that suspended particles behave quite like solute molecules and therefore an osmotic pressure should be ascribed to the suspended particles. By applying van't Hoff's law to suspensions and by assuming that dissipative force described by Stokes law balances a force due to osmotic pressure, Einstein was able to describe Brownian motion as a diffusion process. Further by formulating the statistical analysis for Brownian motion, he laid a basis for testing the reality of molecular kinetic theory of matter which became accepted only after Perrin's experiments [82-84]. Einstein showed that mean squared displacement of particles scales linearly with time and postulated that these results could be used to determine molecular dimensions [70-72].

Meanwhile, Smoluchowski (1906) [73] who independently derived the time dependence of distance covered by a Brownian particle, determined that the number of suspended particles as a function of height shows exponential dependence in sedimentation equilibrium, which is akin to variation of atmospheric pressure with height. This sedimentation equilibrium can be reached between osmotic pressure or diffusion and an effective gravitational force [60], such that the number density of particles, $\rho(h)$ at height, h is given by the Boltzmann distribution and follow the barometric profile, i.e. $\rho(h) \sim \exp(-mgh/k_BT)$, where m is the mass of particle, g is

gravitational constant, T is the temperature and k_B is the Boltzmann's constant. Smoluchowski's studies on Brownian motion led him to develop theory of kinetics of coagulation [75, 77] as well as to explanation of how fluctuations lead to critical opalescence [83, 85]. Finally Langevin [76] outlined a simpler derivation for the time dependence of the displacement of Brownian particles by introducing a fluctuating random force and counteracting it with Stokesian drag, and the modern treatment of Brownian motion is typically based on it [77].

Perrin [60, 83, 84] carried out meticulous experiments to count the number of particles as a function of height present in the sedimentation equilibrium. Further he used the distribution function thus obtained to calculate Avogadro's number and establish the equivalence between a colloidal particle and a molecule as required by the molecular kinetic theory. Svedberg's texts [58-60] contain reference to similar initial experiments on gold sols [59, 60]. He notes [60]: "Westgern in his studies of the sedimentation equilibrium of gold and selenium sols also determined the Avogadro constant and actually obtained lower values than Perrin." Perrin's experiments in 1909 gave a value of 6.8×10^{23}, while Westgern got 6.05×10^{23} [60]. Further, Perrin determined that the displacements or velocities of the Brownian particles show a Maxwellian distribution and these calculations, as well as experiments on Brownian motion, were inspired partly by his friend, Langevin [83]. Perrin's careful experiments on translational and rotational Brownian motion not only led support to the theories of Brownian motion but also established the reality of molecules and established the statistical nature of thermodynamics.

Brownian motion and thermal forces set the rules for structure, dynamics and function of soft matter [86-89] (polymers, liquid crystals, emulsions, and colloidal dispersions), and the analysis or theories of Brownian motion apply to stochastic problems in systems ranging from single cells to financial markets to galaxies [77, 90]. The role of Brownian motion in determining colloidal stability, together with the role of interaction forces, is discussed in the next section of this chapter. The discussion also includes the how the diffusion, aggregation and sedimentation behavior of rod-like particles is qualitatively and quantitatively very different from that of spherical nanoparticles. For example, rods experience difference in mobility parallel and perpendicular to their major axis, and their aggregation can result in the formation of a liquid crystalline phase. Since high purity, nearly monodisperse gold (and other inorganic) nanorods have been synthesized only recently, several predictions regarding their behavior remain untested.

Svedberg invented the ultracentrifuge, allowing Rinde and Svedberg [58-60] to size separate particles and to investigate the role of shape and size on the sedimentation equilibria. The basis of the size separation in the spherical particles is simply understood in terms of the Brownian motion of colloidal particle under an external field, where the equilibrium sedimentation velocity is related to the size dependent drag that opposes the downward centrifugal force. The synthesis and physical behavior, including hydrodynamics of gold particles was central to the studies of Svedberg, who later earned the Nobel Prize for "his work on disperse systems." The next chapter describes how this theoretical and experimental protocol was extended and developed to use the shape dependent drag or hydrodynamics during centrifugation to separate rodlike particles from

a mixture containing spheres and cubes. The sedimentation velocity normalized by the centrifugal acceleration is called Svedberg's coefficient and commonly used unit for comparing it is called Svedberg. The details of this mechanism and its usefulness for separating gold nanorods from a collection of particles of other shapes will be discussed in the next chapter.

8.3 Colloidal nature of gold

Typically, a substance is called a colloidal dispersion if it consists of particles within a typical size range of 1 nm - 10 micron [87, 88]. The dispersion may consist of inorganic particles (say gold or silver nanoparticles), emulsions (milk, mayonnaise), macromolecules (in jellies, gels, bio-fluids), micelles (of surfactant) or clay slurries (mud or toothpaste) or drops (fog, mist). The most distinguishing feature of colloidal dispersions is their ability to keep the dispersed phase suspended by virtue of thermal motion or Brownian motion. In equilibrium, colloidal suspensions occur in the phase with the lowest free energy, and their behavior is governed by the laws of statistical physics. It was noted earlier how Perrin and Westgern had looked at the barometric height distribution of particles in gravitation [60, 77].

$$\rho(h) \sim \exp(-mgh/kT) \tag{8.1}$$

They counted the number of particles distributed due to the diffusion-sedimentation equilibrium for calculating Avogadro's number and verifying the statistical predictions of the theory of Einstein [70-72] and Smoluchowski [73, 77].

From this relation, it follows that the average height of a colloidal particle above the surface is equal to

$$\langle h \rangle = kT/mg \tag{8.2}$$

The colloidal regime is best delimited by requiring that the average height, $\langle h \rangle$ is greater than the particle size, which is indeed saying that to be colloidal, a dispersion must display characteristics of Brownian dynamics [88]. For a spherical particle of dimension a, and effective mass density, ρ_{eff}, (after subtracting of density of the fluid displaced by the particle, to account for buoyancy), the criteria yields

$$a = \left(6 k_B T / \pi g \rho_{eff}\right)^{1/4} \tag{8.4}$$

For a particle with ρ_{eff} of 1 g/cc, the above criteria is satisfied for a ~ 1 μm, whereas for metallic nanoparticles, say gold, where the ρ_{eff} is nearly an order of magnitude larger (ρ is 19.3 g/cc for gold, the corresponding estimate tells us that particles above diameter of 0.5 μm cannot be kept dispersed as Brownian particles in a solvent with density comparable with water, under the influence of earth's gravitational field. Further, even though a particle could be stabilized or kept afloat by either using a density matched fluid or by placing it in low gravity environment, the particles can display the characteristics of a colloidal particle only if it observes Brownian motion.

As Frenkel notes in his lecture on colloidal systems [88], both the length scale and time scale of this motion are important. To move a distance comparable to its size, a, the time scale required for a Brownian particles is:

$$\tau = a^2 / D \tag{8.4}$$

where the diffusion coefficient, D, of the particle is given by Stokes-Einstein relation

$$D = k_B T / \zeta \tag{8.5}$$

For spherically symmetric or spherically isotropic bodies, the friction coefficient, $\zeta \sim \eta a$ where η is the viscosity of the solvent or the medium. For the sphere, the exact

relation as derived by Stokes is $\zeta=3\pi\eta a$. While a brick could be kept afloat for example, the time required for it to diffuse a distance comparable to its size is of the order of million years [83, 88], where the timescale for a typical colloidal particle turns out to be a second or less. The understanding of Brownian motion is key to appreciating the sedimentation behavior of gold sols, and is essential for designing separation techniques that can exploit the difference in hydrodynamics of rods and spheres, which will be discussed in the next chapter.

It has been remarked in literature that in the seed mediated method, "for reasons not presently understood" [4], the gold nanorods can grow no more than length of 600 nm, diameter 20-30 nm. *We contend that this is probably due to the fact that these particles are no longer Brownian.* Depending upon the effective density of the particles, beyond a certain physical size, particles cease to display the characteristic physical properties of colloids. Simple back of the envelope estimate shows gold particles would behave as colloids in all respects as long as their size is below a few hundred nm. While the role of thermal motion in determining the colloidal behavior was already mentioned, the overall stability and phase behavior of the submicron particles depends upon the interplay of the attractive or repulsive interparticle forces with the random Brownian forces. These interparticle forces include electrostatic repulsion, attraction due to dispersion forces, attraction and repulsion caused by soluble polymers, and hydrodynamic effects that arise due to relative motion between particles and the liquid [87, 88, 91].

Table 8.1 provides an order of magnitude estimate of the relative importance of forces relevant for gold nanospheres of diameter, a, dispersed in medium with dielectric

constant, ε. The contribution of Brownian forces is of the order of O(kT/a); with k_B being the Boltzmann's constant, and T is the temperature. The dispersion force, which has the contribution from London – van der Waals interaction, is O(A_{eff}/a), where A_{eff} is the Hamaker constant, that depends upon the nature of the particles and the intervening fluid, and the value used (~1.9 eV) here is for gold-gold attractions through dodecane [92]. Coulomb's law, $\varepsilon\varepsilon_0\zeta_{EP}^{\ 2}$, gives an estimate of electrostatic forces between two particles (though they are actually moderated by ions in the intervening fluid); here ε_0 is the permittivity of free space (8.85 x 10^{-12} C/V m), and ζ_{EP} is the electrostatic potential of the particles. The viscous forces for particles moving with velocity U can be estimated by Stokes law to be O (ηaU), which depends upon viscosity of the material, η, while the inertial forces are O ($a^2\rho U^2$). For a typical particle dispersed in a medium, with density difference $\Delta\rho$ between the particle and the medium, the effective gravitational force (taking buoyancy into account) is O ($a^3\Delta\rho g$). While the estimates are made for spherical particles, the corresponding values for rodlike nanoparticles would not be too different.

The absolute magnitude of the interparticle forces depends upon the distance between them. While the screened electrostatic repulsion between two flat surfaces decays exponentially with distance, r, the dispersion forces scales as $1/r^3$. The attractive dispersion forces might dominate the repulsion forces when particles are separated by shorter distances. But as particles try to move into a closer contact, they encounter separation dependent viscous forces, that are required to drain away the intervening fluid layer, and this force diverges as the distance goes to zero.

The sedimentation or gravitational force is insignificant as compared to Brownian forces, though as particle size grows the gravitational forces start to dominate behavior as

discussed before. But if the particles are placed in a centrifugal field, where effective gravitation is two to three orders of magnitudes higher, the gravitational forces become comparable or larger than Brownian forces. Change in solvent implies a different viscosity, which affects viscous forces and also a different dielectric constant, which changes magnitude of repulsive electrostatic and attractive dispersion forces. Adding a salt or an electrolyte can promote particle aggregation precisely because it changes the magnitude of the dispersion force. Lastly, the presence of soluble polymers or polymers adsorbed to particles or proteins or surfactant molecules also affects the interparticle forces, and the contributions typically arise from the strong dependence of local osmotic pressure on concentration and distribution of adsorbed or attached species. A comprehensive list of these (and other) forces and their origin can be found in the text by Evans and Wennerstrom [91].

Table 8.1 Magnitude of the characteristic forces; a = 20 nm, $\eta = 10^{-3}$ kg/ms, U = 1 μm/s, $\rho = 20 \times 10^3$ kg/m^3, $\Delta\rho/\rho$ =20, g = 10 ms^{-2}, $A_{eff} = 10^{-20}$ Nm, ζ_{EP}= 47 mV, $\varepsilon = 10^2$.

$\frac{electric\ \ force}{Brownian\ \ force} = \frac{a\varepsilon\varepsilon_0\zeta_{EP}^{\ 2}}{kT} \approx 10$
$\frac{attractive\ \ force}{Brownian\ \ force} = \frac{A_{eff}}{kT} \approx 10$
$\frac{viscous\ \ force}{Brownian\ \ force} = \frac{\eta U a^2}{kT} \approx 0.01$
$\frac{gravitational\ \ force}{Brownian\ \ force} = \frac{a^3\Delta\rho g}{kT} \approx 0.001$
$\frac{gravitational\ \ force}{viscous\ force} = \frac{a^3\Delta\rho g}{\eta U a} \approx 0.1$
$\frac{inertial\ \ force}{viscous\ \ force} = \frac{\rho a^2 U^2}{\eta U a} \approx 10^{-4}$

The role of some of these interparticle forces is mentioned in the course of the discussion on sedimentation behavior during gravitation and centrifugation and in context of self-assembly. The exact nature of interparticle forces relevant for gold sols depends upon the solvent used, surfactant and salts present, particle shape, among others. While interparticle forces capture the contributions to thermodynamic stability of the colloidal dispersions, their overall stability depends kinetic considerations as well, for the inter-particle dynamics is modulated by hydrodynamic interactions which become important during the study of dynamic properties of the colloids. Several colloidal textbooks [87, 88, 91] can be consulted for detailed discussion on the nature and aspects of the interaction forces and hydrodynamic interaction. At the same time, it must be emphasized that while the focus is on the behavior of gold nanorods, these are mostly stabilized by the use of amphiphilic surfactant molecules, that can aggregate to form micelles spontaneously, and their aggregate size and shape influences growth and stability behavior of particles. The aggregate size and shape of micelles depends upon the solution conditions, including pH, temperature, salt, etc., [91] and in studying any effect of these on stability or response of dispersed gold nanoparticles, one must bear the response of surfactants in mind.

8.4 Optical Properties of Gold Nanoparticles

8.4.1 Genesis of Extinction Spectrum

The interaction of light with matter containing particles invariably involves scattering and absorption, both of which cause attenuation in the intensity of beam passing through the medium [93, 94]. Scattering is caused by heterogeneity in the system,

which could be caused simply by density or concentration fluctuations, or by presence of particles or drops as dispersed phase. For particles dispersed in a fluid or a gas, typically the scattering by fluctuations in the media is much lower than by the particles and can be neglected for practical purposes. The blue color of sky is a result of scattering [95], and the attenuation of light passing through turbid media like fog is also due to scattering. Scattering is often accompanied by absorption, whereby depending upon the material in question, certain frequencies are absorbed and dissipated either as heat or for other internal processes in the molecules or particles. The color of black smoke or of Indian ink dispersed in water is due to absorption.

A light beam passing through a colloidal dispersion of metal nanoparticles gets attenuated by the combined contribution of absorption and scattering, as given by

$$I(z) = I_0 \exp(-n_0 C_{ext} z) \tag{8.6}$$

Here I_0 is the intensity of the incident beam, $I(z)$ is the intensity of the beam after travelling path length, z within the sample, n_0 is the number density of particles and C_{ext} ($= C_{abs} + C_{sca}$) is the extinction cross section of a single particle; and is the sum total of the absorption and scattering cross sections respectively. The product $n_0 C_{ext}$ is often termed as the extinction coefficient, γ and it has units of reciprocal length. The absorption spectrum determined by UV-Visible Spectroscopy is in fact a measure of attenuation caused by a dispersion of gold nanoparticles, and is thus related to the absorption cross section. In what follows, the relationship of the size of gold nanoparticles to extinction cross sections is established, thus establishing the physical basis for their optical response.

The optical properties of noble metal particles originate from localized surface plasmons. These phenomena occur when electromagnetic field interacts with conduction band electrons and induces the coherent oscillation of electrons. As a result, a strong absorption band appears in some region of the electromagnetic spectrum depending on the size of the particle (described in more detail in the next sub-section). This plasmon absorption is a small particle effect. They are absent in the individual atoms as well as in the bulk. Even for thin films, at the interface between a metal and a dielectric, the electromagnetic field can couple to the oscillations of conduction electron plasma creating surface plasmon polaritons. These surface plasmon polaritons are *dispersive, propagating* electromagnetic excitations on the interface that are evanescently confined in perpendicular direction. The detailed derivation and discussion of applications of surface plasmon polaritons is presented in texts like Maier [56], and is outside the scope of this chapter.

But when a metal nanoparticle is exposed to such a field, *non-propagating* excitations of conduction electrons create size dependent localized surface plasmons that arise simply when we consider the absorption and scattering by gold (or other metallic) nanoparticles. When a conductor or metal is placed in an oscillating field of incoming radiation, the electrons cloud is driven into oscillations. In the case of a sub-wavelength conductive nanoparticle, the curved surface of the particle exerts an effective restoring force on these driven electrons (analogy with a damped, driven harmonic oscillator). Like any driven oscillator system, in nanoparticle case, a resonance can arise leading to the field amplification both inside and outside the particle. This resonance for gold and silver particles lies in the visible region of the electromagnetic radiation which is responsible

for their bright colors in both transmitted and reflected light. The reason for field amplification as well as optical response of gold nanoparticles will perhaps become more clear when we approach this problem using electrostatics.

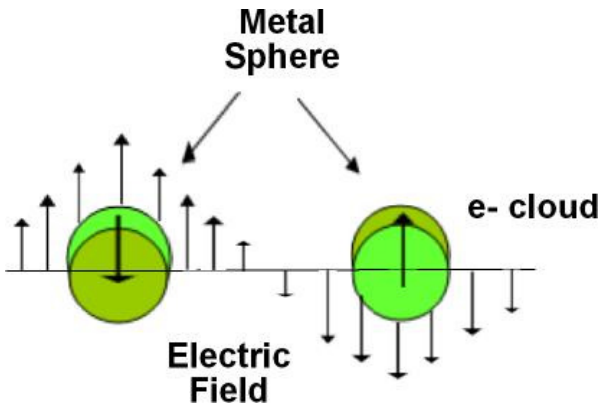

Figure 8.1 Size dependent localized plasmon resonance in metal spheres.

Mie [65] first explained this phenomenon theoretically by solving Maxwell's equations for a radiation field interacting with a spherical metal particle under the appropriate boundary conditions. He applied an exact electromagnetic theory for spherical particles using electrodynamics, and this describes the extinction (absorption + scattering) of spherical particles of any given size. In this section, we will first describe the basis for plasmon resonance, illustrating the underlying quantum effect by discussing the basis for the absorbance by spherical and non-spherical metal particles. The theoretical background presented is essential for understanding the color of gold sols as well as for appreciating how and why localized field enhancements can occur for these particles, leading to their utility as sensors. The reader may wish to refer to textbooks by Bohren and Huffman [93], van de Hulst [94], Kerker [96] and Jackson [97] for more detailed derivations of absorption and scattering. We must suggest the excellent, recent text by Maier [56] that focuses on the fundamentals and applications of plasmonics, and

indispensible articles [2-16, 39, 98-105] that focus on the optical properties of gold nanoparticles.

8.4.2 Localized Surface Plasmon resonance for spherical particles

In the plasma model, the free electrons in a metal can be considered to be like a gas of number density n_0 moving against the fixed background of positive ion cores. The dielectric function of the metal, $\varepsilon(\omega)$ is related to the refractive index, n and the absorption coefficient, k by the following relations:

$$\varepsilon(\omega) = \varepsilon_1(\omega) + i\varepsilon_2(\omega) \tag{8.7a}$$

$$\varepsilon_1 = n^2 - k^2 \;\&\; \varepsilon_2 = 2nk \tag{8.7b}$$

$$n^2 = \frac{1}{2}\varepsilon_1 + \frac{1}{2}\sqrt{\varepsilon_1^2 + \varepsilon_2^2}\;;\; k = \frac{\varepsilon_2}{2n} \tag{8.7c}$$

In what follows, we proceed from Maxwell's equations to describe a much simpler electrostatics computation of interaction of a nanoparticle of size, a, with an electromagnetic radiation of wavelength λ such that $a << \lambda$. Let us first consider a homogeneous, isotropic sphere with dielectric function $\varepsilon(\omega)$, radius, a, placed in the electric field $\boldsymbol{E}$ placed in a medium with the dielectric constant of the medium as ε_m, we can arrive at the resulting electric field as described in textbook examples in say Jackson [97]. This leads to a polarization of the sphere given by

$$\vec{P} = 4\pi\varepsilon_0\varepsilon_m a^3\left[\frac{\varepsilon - \varepsilon_m}{\varepsilon + 2\varepsilon_m}\right]\vec{E}_0 \tag{8.8}$$

implying simply that the applied field introduces a dipole moment inside the sphere.

Since the dielectric function of the gold is frequency dependent, the resonant condition occurs when the extrema of the polarizability is reached. This occurs when the denominator is a minimum, i.e. $|\varepsilon + 2\varepsilon_m|$ is a minimum, which for the case of small or slowly varying Im[ε] around the resonance condition simplifies to $\mathrm{Re}[\varepsilon(\omega)] = -2\varepsilon_m$, called the Fröhlich condition. The associated mode is called the dipole surface Plasmon of the nanoparticle, and for a given metal, depends on the dielectric constant of the medium. This implies that the change in the absorption peak of a given metal nanoparticle can sense the local changes in refractive field, and can be used as a marker for following the changes in refractive index [35]. Note that the magnitude of the polarizability at the resonance condition is well-defined, because even though the Fröhlich condition is satisfied, the Im [ε] is non-vanishing.

In the plasma model, when the electrons oscillate in response to the applied electromagnetic field, their motion is damped via collisions that occur with the frequency of $1/\gamma_D$, where γ_D is a damping constant. The size dependence of damping constant makes dielectric constant and hence the resonance condition function of radius, a of the particles. This resonantly enhanced polarization enhances the efficiency of scattering and absorption of light by metal nanoparticles. This is evident if one examines the corresponding cross sections for scattering and absorption [93]:

$$C_{sca} = \frac{k^4 \alpha^2}{6\pi} = \frac{8\pi}{3} k^4 a^6 \left[\frac{\varepsilon - \varepsilon_m}{\varepsilon + 2\varepsilon_m} \right]^2 \tag{8.9a}$$

$$C_{abs} = k\,\mathrm{Im}[\alpha] = 4\pi k a^3\,\mathrm{Im}\left[\frac{\varepsilon - \varepsilon_m}{\varepsilon + 2\varepsilon_m} \right] \tag{8.9b}$$

It is very difficult to distinguish smaller particles from the background of large scatterers because of the a^6 dependence of scattering cross section. But for small particles with $a << \lambda$, absorbance scales with volume and the scattering with (volume)^2, so absorbance dominates over scattering. Hence when we refer to the extinction measured experimentally, we are typically seeing absorbance spectrum, and the expression for extinction for spherical particles can be written as:

$$\frac{\gamma}{N_p V} = \frac{18\pi\varepsilon_m^{3/2}}{\lambda} \frac{\varepsilon_2}{(\varepsilon_1 + 2\varepsilon_m)^2 + \varepsilon_2^{\,2}} \tag{8.10}$$

The plasmon resonance for rodlike particles is discussed in next chapter, but this background on the spherical particles is necessary to appreciate the optical properties of gold nanoparticles in general as well as for understanding behavior of nanorods.

8.5 The Ultramicroscope

In recent literature, the size and shape of gold particles is often characterized by transmission electron microscopy (TEM) and such measurements allow direct visualization of nanoparticles deposited and dried onto a copper grid. In the context of our studies too, morphology and mean size of NPs were examined by TEM (JEOL100 at 100 KV). It is widely recognized that broad plasmon resonance peaks observed in UV-Visible absorption spectroscopy can arise due to either polydispersity or difference in shape and size of constituent particles and hence a directly visualization provides necessary and complimentary information. While TEM images are almost indispensible sources of size and shape, a simpler technique for direct visualization of particles exists in ultramicroscopy and has been completely ignored by the community. In what follows,

the basis of ultramicroscopy and its demonstrated ability to show size and optical response of nanometer size particles is explained. A discussion about how particles can self-assemble, size or shape separate on TEM grids in the last section of assembly and liquid crystallinity of rods will be carried out in a subsequent chapter. There is a merit in looking at particles in their dispersed phase, and hence we describe ultramicroscopy for stressing why it could be revived for studies on colloidal dispersions of gold and other noble metal particles.

When a narrow beam of sunlight enters a dark room, the scattering from dust particles makes them visible. If there were no dust particles, the medium will behave as optically void, and if the particles are decidedly small in size, the beam of light acquires a bluish tinge. This phenomenon is called Tyndall effect and is indicative of presence of suspended particles. Hence all colloidal suspensions exhibit this phenomenon in proper illumination. In his seminal paper [66], Faraday looked at gold sols under such illumination and noted that the gold particles scatter light. Zsigmondy placed a microscope to visualize the Faraday-Tyndall cone of light, and was able to establish that gold sols consist of nanometer size particles [61]. (Of course, as remarked before, he never called the particles nanoparticles and never referred to the dimensions in nm units, rather used the term ultramicrons and called particles ultramicroscopic.)

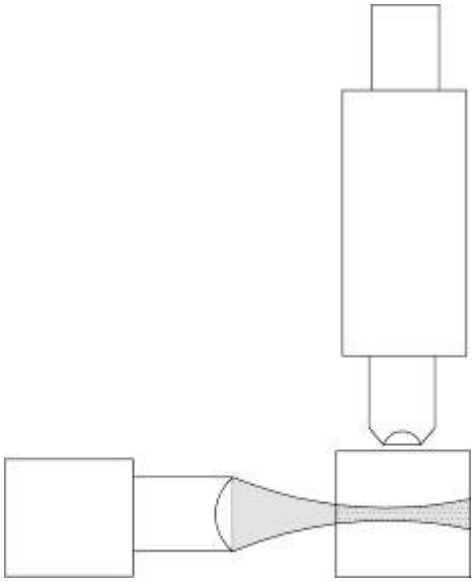

Figure 8.2 A simple schematic of Siedentopf-Zsigmondy ultramicroscope, where particles in Faraday-Tyndall cone are visualized using a microscope.

Abbe's diffraction theory tells us that the resolution of the microscope depends upon the wavelength λ of light, and the numerical aperture, NA ($n \sin\alpha$), of the objective of the microscope, where n is the refractive index of the immersion medium. This implies that we can distinguish points that are at a distance larger than $d \sim \lambda/\text{NA}$. Under the best conditions, by using highest numerical aperture objective and by using oil immersion to extend the resolution, we see that the minimum distances resolved by an optical microscope tend to be ~0.2 μm. The reader can refer to any standard text [106-109] for more detailed discussion on image formation and resolution of microscopes. While it is commonly believed that particles smaller than this size cannot be resolved by a microscope, the real limit is set by our ability to detect the light reflected or emitted by particles of sub-microscopic or as Zsigmondy called them ultramicroscopic size. Any particle that can be made to emit enough light can be seen if it is not too close to another particle, and this condition can be satisfied by taking a dilute colloidal suspension. The

next step is to illuminate the particles with a strong source of light and to observe them with an optical system that collects maximum possible light emitted by the particles. The smallest size reported to be seen by Zsigmondy was 1.7 nm! [67] Colloidal solutions of gold and other metals are particularly conducive for ultramicroscopy due to the marked difference between the optical constants of the dispersed phase and the disperse media.

8.6 Recipe for nanorod synthesis using seed-mediated method and role of supersaturation

In this study, the experimental results are based on the nanords synthesized by Kyounweon Park using the seed mediated method of Nikoobakht et al [110]. First the seed solution was prepared by mixing hexadecyltrimethylammonium bromide (CTAB) solution (5.0 mL, 0.20 M) with 5.0 mL of 0.00050 M $HAuCl_4$. 0.60 mL of ice-cold 0.010 M $NaBH_4$ was added to the stirred solution, and this resulted in the formation of a brownish yellow solution. Vigorous stirring of the seed solution was continued for 2 min. After the solution was stirred, it was kept at 25 °C. Thereafter, the growth solution was prepared by mixing 5 mL of the solution at a known concentration of surfactant (CTAB, hexadecyltrimethylammonium chloride(CTAC), BDAC) to 5 mL of 0.001M $HAuCl_4$ solution. 200 µl of 0.0040 M $AgNO_3$ solution was added to the solution at 25 °C. After gentle mixing of the solution, a known amount of 0.10M ascorbic acid was added to the test tube. The color of the growth solution changed from dark yellow to colorless. The final step was the addition of 10 µl of the seed solution to the growth solution. The color of the solution changed over the period of time depending on the final size of the NRs. The surfactants, CTAB and BDAC, were purchased from TCI America and all the other

chemicals ($HAuCl_4$, $AgNO_3$, $NaBH_4$, potassium bromide, hexadecyltrimethylammonium chloride, and L-(+)-ascorbic acid) were purchased from Sigma-Aldrich. All chemicals were of analytical grade (purity > 98%) and were used without further purification. Deionized water (18 MΩ) was used in all the experiments.

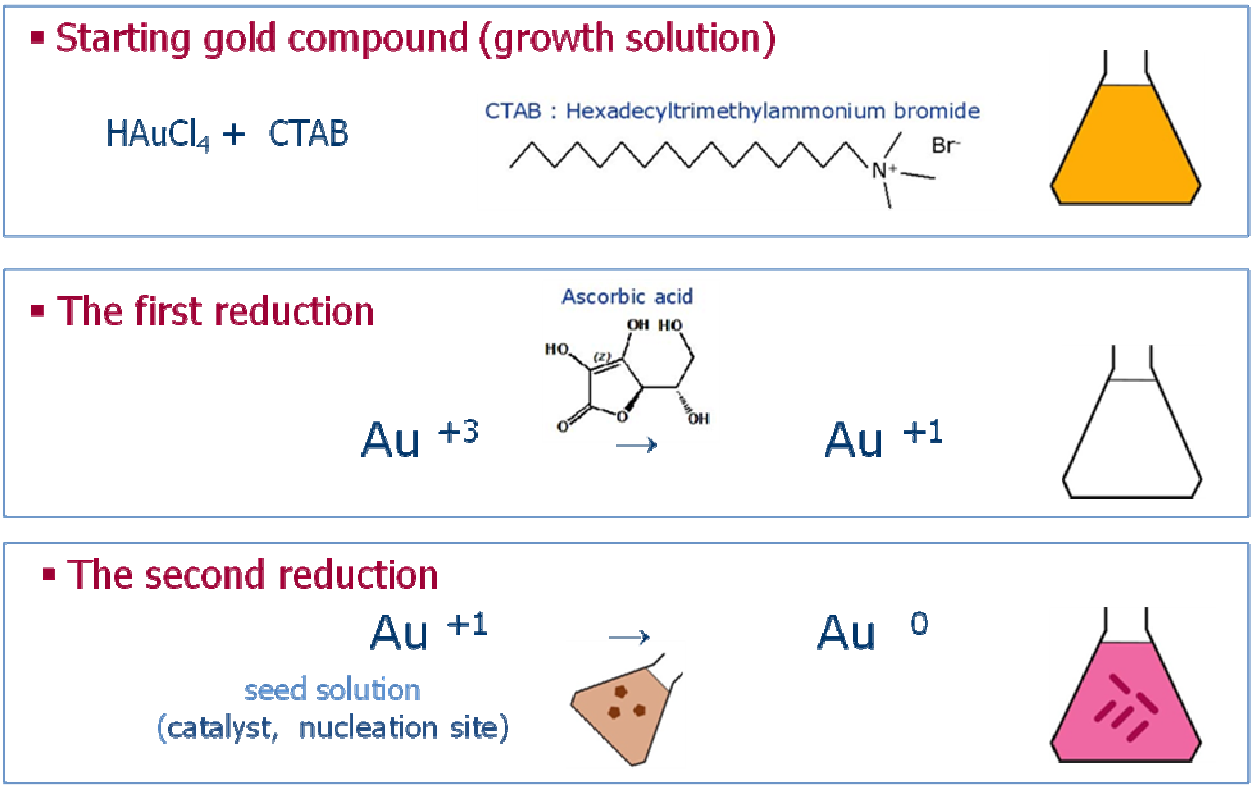

Figure 8.3 Schematic of seed-mediated method with CTAB as surfactant and ascorbic acid as the reducing agent (see text for details).

Before ending the discussion of seed mediated synthesis, lets remark on how and why the control of supersaturation, through control of reactant concentrations, can not only separate the nucleation and growth steps, but thereby provide a means of controlling size dispersity in the as-made nanoparticle dispersion. The argument at present is qualitative, but is known to produce monodisperse sols in a variety of colloidal dispersions [91] and in other condensation growth processes, such as formation of drops

in the atmosphere [111] and formation of monodisperse population of drops as described in the chapter 4 of this thesis.

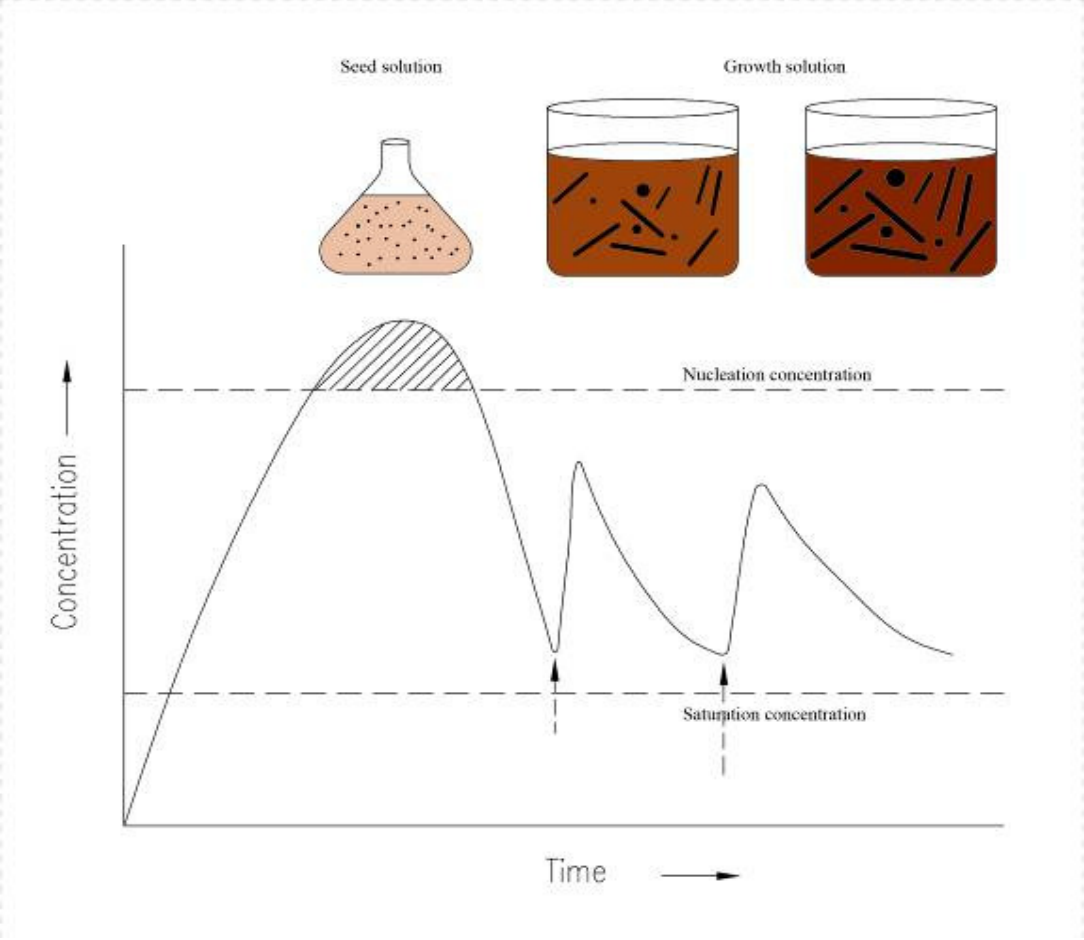

Figure 8.4 Nucleation and growth during seed-mediated method. The threshold concentrations for nucleation and saturation are shown with dotted lines. Nucleation (dashed region) creates seed solution. Growth is carried out in separate steps by controlled addition of reactants.

The nucleation of particles in a solution requires a certain critical concentration or solubility product to be exceeded, before it becomes thermodynamically favorable for the nuclei to appear. In the seed mediated method, this is accomplished in the first bath, where the addition of reactants creates the required concentration, such that nuclei are formed in a single burst, and this causes the concentration to drop below the critical

value. In the second bath, the growth of nanoparticles can be accomplished by providing just enough reactants such that growth of existing particles is favored, where new nuclei cannot be formed. As long as concentration is kept within these limits, and Ostwald ripening and coalescence are ruled out, the condensation growth can proceed to give monodisperse sols. The determination of solubility product in a reaction bath consisting of seed solution, binary surfactant, reducing agents and other additives is thus the crucial ingredient in progressing towards controlled synthesis. The parameters including pH, temperature and ionic content affect colloidal stability and phase behavior of surfactants as well, and thus their role in controlling morphology and polydispersity of as-produced particles is a realm of endless possibilities. Since current methods produce dispersions that are relatively polydisperse in shape and size, the theoretical basis of the use of centrifugation assisted separation as well as experimental demonstration of its effectiveness is discussed in the next chapter.

8.6 Summary

Colloidal gold dispersions played a crucial role in development of the science and technology of colloidal matter and of soft condensed matter. The recent interest in colloidal gold nanoparticles is motivated by the possibility of using their physical properties for various applications, especially in chemical and biological sensing. While a large number of researchers have focused on the synthesis and characterization of gold nanorods in recent two decades, a wealth of information was buried in the studies of the early giants of colloidal science, like Faraday, Svedberg, Ostwald, Zsigmondy and Mie. This chapter provides a glimpse of their observations, noting how the seed mediated

synthesis as well as the physical properties dependent of anisotropic shape of gold nanorods were known and studied by these esteemed scientists. The description of several methods used to determine size of colloidal particles, especially ultramicroscopy is made with an attempt to provide the background necessary for widespread use of these techniques. The basis for colloidal stability, for Brownian motion and the forces acting on colloidal particles were assessed and described, for these determine the usefulness of any dispersion, as well as explain why only rods below a certain size are stable towards sedimentation under gravity. The chapter also introduces concepts related to optical properties and dynamics of colloidal gold, which form a background to the results and discussion in latter chapters.

8.7 References

1. Shakespeare, W., *Merchant of Venice*. Unabridged ed. 1992, New York: Washington Square Press.

2. El-Sayed, M.A., *Some interesting properties of metals confined in time and nanometer space of different shapes.* Accounts of Chemical Research, 2001. **34**(4): p. 257-264.

3. Daniel, M.C. and D. Astruc, *Gold nanoparticles: Assembly, supramolecular chemistry, quantum-size-related properties, and applications toward biology, catalysis, and nanotechnology.* Chemical Reviews, 2004. **104**(1): p. 293-346.

4. Murphy, C.J., et al., *Anisotropic metal nanoparticles: Synthesis, assembly, and optical applications.* Journal of Physical Chemistry B, 2005. **109**(29): p. 13857-13870.

5. Perez-Juste, J., et al., *Gold nanorods: Synthesis, characterization and applications.* Coordination Chemistry Reviews, 2005. **249**(17-18): p. 1870-1901.

6. Alekseeva, A.V., et al., *Gold nanorods: Synthesis and optical properties.* Colloid Journal, 2006. **68**(6): p. 661-678.

7. Dykman, L.A. and V.A. Bogatyrev, *Gold nanoparticles: Preparation, functionalisation, applications in biochemistry and immunochemistry.* Uspekhi Khimii, 2007. **76**(2): p. 199-213.

8. Jiang, X.C. and M.P. Pileni, *Gold nanorods: Influence of various parameters as seeds, solvent, surfactant on shape control.* Colloids and Surfaces a-Physicochemical and Engineering Aspects, 2007. **295**(1-3): p. 228-232.

9. Eustis, S. and M.A. El-Sayed, *Why gold nanoparticles are more precious than pretty gold: Noble metal surface plasmon resonance and its enhancement of the radiative and nonradiative properties of nanocrystals of different shapes.* Chemical Society Reviews, 2006. **35**(3): p. 209-217.

10. Jain, P.K., et al., *Review of some interesting surface plasmon resonance-enhanced properties of noble metal nanoparticles and their applications to biosystems.* Plasmonics, 2007. **2**(3): p. 107-118.

11. Huang, X.H., et al., *Gold nanoparticles: interesting optical properties and recent applications in cancer diagnostic and therapy.* Nanomedicine, 2007. **2**(5): p. 681-693.

12. Song, J.H., et al., *Crystal overgrowth on gold nanorods: Tuning the shape, facet, aspect ratio, and composition of the nanorods.* Chemistry-a European Journal, 2005. **11**(3): p. 910-916.

13. Kelly, K.L., et al., *The optical properties of metal nanoparticles: The influence of size, shape, and dielectric environment.* Journal of Physical Chemistry B, 2003. **107**(3): p. 668-677.

14. Link, S. and M.A. El-Sayed, *Spectral properties and relaxation dynamics of surface plasmon electronic oscillations in gold and silver nanodots and nanorods.* Journal of Physical Chemistry B, 1999. **103**(40): p. 8410-8426.

15. Link, S. and M.A. El-Sayed, *Size and temperature dependence of the plasmon absorption of colloidal gold nanoparticles.* Journal of Physical Chemistry B, 1999. **103**(21): p. 4212-4217.

16. Link, S. and M.A. El-Sayed, *Shape and size dependence of radiative, non-radiative and photothermal properties of gold nanocrystals.* International Reviews in Physical Chemistry, 2000. **19**(3): p. 409-453.

17. Burda, C., et al., *Chemistry and properties of nanocrystals of different shapes.* Chemical Reviews, 2005. **105**(4): p. 1025-1102.

18. El-Sayed, M.A., *Small is different: Shape-, size-, and composition-dependent properties of some colloidal semiconductor nanocrystals.* Accounts of Chemical Research, 2004. **37**(5): p. 326-333.

19. Alivisatos, A.P., *Perspectives on the physical chemistry of semiconductor nanocrystals.* Journal of Physical Chemistry, 1996. **100**(31): p. 13226-13239.

20. Maier, S.A. and H.A. Atwater, *Plasmonics: Localization and guiding of electromagnetic energy in metal/dielectric structures.* Journal of Applied Physics, 2005. **98**(1).

21. Willets, K.A. and R.P. Van Duyne, *Localized surface plasmon resonance spectroscopy and sensing.* Annual Review of Physical Chemistry, 2007. **58**: p. 267-297.

22. Hutter, E. and J.H. Fendler, *Exploitation of localized surface plasmon resonance.* Advanced Materials, 2004. **16**(19): p. 1685-1706.

23. Li, C.Z., et al., *Fluorescence properties of gold nanorods and their application for DNA biosensing.* Chemical Communications, 2005(31): p. 3924-3926.

24. Elghanian, R., et al., *Selective colorimetric detection of polynucleotides based on the distance-dependent optical properties of gold nanoparticles.* Science, 1997. **277**(5329): p. 1078-1081.

25. Hu, M., et al., *Gold nanostructures: engineering their plasmonic properties for biomedical applications.* Chemical Society Reviews, 2006. **35**(11): p. 1084-1094.

26. Yu, C.X. and J. Irudayaraj, *Multiplex biosensor using gold nanorods.* Analytical Chemistry, 2007. **79**(2): p. 572-579.

27. Cheng, S.F. and L.K. Chau, *Colloidal gold-modified optical fiber for chemical and biochemical sensing.* Analytical Chemistry, 2003. **75**(1): p. 16-21.

28. Aslan, K., et al., *Saccharide sensing using gold and silver nanoparticles - A review.* Journal of Fluorescence, 2004. **14**(4): p. 391-400.

29. Li, Z.P., et al., *Chemiluminescent detection of DNA hybridization using gold nanoparticles as labels.* Analytical and Bioanalytical Chemistry, 2007. **387**(2): p. 613-618.

30. Sonnichsen, C. and A.P. Alivisatos, *Gold nanorods as novel non-bleaching plasmon based orientation sensors.* Biophysical Journal, 2005. **88**(1): p. 364A-365A.

31. Orendorff, C.J., et al., *Light scattering from gold nanorods: tracking material deformation.* Nanotechnology, 2005. **16**(11): p. 2601-2605.

32. Murphy, C.J., et al., *Chemical sensing and imaging with metallic nanorods.* Chemical Communications, 2008(5): p. 544-557.

33. Haes, A.J., et al., *Nanoscale optical biosensor: Short range distance dependence of the localized surface plasmon resonance of noble metal nanoparticles.* Journal of Physical Chemistry B, 2004. **108**(22): p. 6961-6968.

34. Haes, A.J., et al., *Plasmonic materials for surface-enhanced sensing and spectroscopy.* Mrs Bulletin, 2005. **30**(5): p. 368-375.

35. Rashid, M.H., R.R. Bhattacharjee, and T.K. Mandal, *Organic ligand-mediated synthesis of shape-tunable gold nanoparticles: An application of their thin film as refractive index sensors.* Journal of Physical Chemistry C, 2007. **111**(27): p. 9684-9693.

36. Templeton, A.C., et al., *Solvent refractive index and core charge influences on the surface plasmon absorbance of alkanethiolate monolayer-protected gold clusters.* Journal of Physical Chemistry B, 2000. **104**(3): p. 564-570.

37. Kneipp, K., et al., *Surface-enhanced Raman Spectroscopy in single living cells using gold nanoparticles.* Applied Spectroscopy, 2002. **56**(2): p. 150-154.

38. Schultz, D.A., *Plasmon resonant particles for biological detection.* Current Opinion in Biotechnology, 2003. **14**(1): p. 13-22.

39. Jain, P.K., et al., *Calculated absorption and scattering properties of gold nanoparticles of different size, shape, and composition: Applications in biological imaging and biomedicine.* Journal of Physical Chemistry B, 2006. **110**(14): p. 7238-7248.

40. Jain, P.K. and M.A. El-Sayed, *Universal scaling of plasmon coupling in metal nanostructures: Extension from particle pairs to nanoshells.* Nano Letters, 2007. **7**(9): p. 2854-2858.

41. Jain, P.K., S. Eustis, and M.A. El-Sayed, *Plasmon coupling in nanorod assemblies: Optical absorption, discrete dipole approximation simulation, and exciton-coupling model.* Journal of Physical Chemistry B, 2006. **110**(37): p. 18243-18253.

42. Storhoff, J.J., et al., *What controls the optical properties of DNA-linked gold nanoparticle assemblies?* Journal of the American Chemical Society, 2000. **122**(19): p. 4640-4650.

43. Haes, A.J., et al., *A nanoscale optical biosensor: The long range distance dependence of the localized surface plasmon resonance of noble metal nanoparticles.* Journal of Physical Chemistry B, 2004. **108**(1): p. 109-116.

44. Chen, J.Y., et al., *Gold nanocages: Engineering their structure for biomedical applications.* Advanced Materials, 2005. **17**(18): p. 2255-2261.

45. Huang, W.Y., et al., *Effect of the lattice crystallinity on the electron-phonon relaxation rates in gold nanoparticles.* Journal of Physical Chemistry C, 2007. **111**(29): p. 10751-10757.

46. Huang, X.H., et al., *Cancer cells assemble and align gold nanorods conjugated to antibodies to produce highly enhanced, sharp, and polarized surface Raman spectra: A potential cancer diagnostic marker.* Nano Letters, 2007. **7**(6): p. 1591-1597.

47. Huang, X.H., et al., *Cancer cell imaging and photothermal therapy in the near-infrared region by using gold nanorods.* Journal of the American Chemical Society, 2006. **128**(6): p. 2115-2120.

48. Jain, P.K., I.H. El-Sayed, and M.A. El-Sayed, *Au nanoparticles target cancer.* Nano Today, 2007. **2**(1): p. 18-29.

49. Narayanan, R. and M.A. El-Sayed, *Catalysis by metallic nanoparticles: the good and the bad.* Chimica Oggi-Chemistry Today, 2007. **25**(1): p. 84-86.

50. Ipe, B.I., et al., *Photoinduced charge separation in a fluorophore-gold nanoassembly.* Journal of Physical Chemistry B, 2002. **106**(1): p. 18-21.

51. Horisberger, M. and J. Rosset, *Colloidal Gold, A useful marker for transmission and scanning electron microscopy.* Journal of Histochemistry & Cytochemistry, 1977. **25**(4): p. 295-305.

52. Caseri, W., *Nanocomposites of polymers and metals or semiconductors: Historical background and optical properties.* Macromolecular Rapid Communications, 2000. **21**(11): p. 705-722.

53. AlRawashdeh, N. and C.A. Foss, *UV/visible and infrared spectra of polyethylene/nanoscopic gold rod composite films: Effects of gold particle size, shape and orientation.* Nanostructured Materials, 1997. **9**(1-8): p. 383-386.

54. Al-Rawashdeh, N.A.F., et al., *Visible region polarization spectroscopic studies of template-synthesized gold nanoparticles oriented in polyethylene.* Journal of Physical Chemistry B, 1998. **102**(2): p. 361-371.

55. Maier, S.A., *Plasmonics - Towards subwavelength optical devices.* Current Nanoscience, 2005. **1**(1): p. 17-23.

56. Maier, S.A., *Plasmonics: Fundamentals and Applications*. 2007, Bath: Springer.

57. Ostwald, W., *An Introduction to Theoretical and Applied Colloid Chemistry*. 1917, New York: John Wiley & Sons, Inc.

58. Svedberg, T., *The Formation of Colloids*. 1921, New York: D. Van Nostrand Company.

59. Svedberg, T. and K.O. Pedersen, *The Ultracentrifuge*. 1940, Oxford: Oxford University Press.

60. Svedberg, T. and A. Tiselius, *Colloid Chemistry*. Second ed. 1928, New York: The Chemical Catalog Company, Inc.

61. Zsigmondy, R., *Colloids and the ultramicroscope*. 1909, New York: John Wiley & Sons, Inc.

62. Zsigmondy, R., *The Chemistry of Colloids*. 1917, New York: John Wiley & Sons, Inc.

63. Zsigmondy, R. and E. Huckel, *The reduction rate and the growth of smaller gold particles in the creation of a colloid gold solution.* Zeitschrift Fur Physikalische Chemie--Stochiometrie Und Verwandtschaftslehre, 1925. **116**(3/4): p. 291-303.

64. Gans, R., *The shape of ultra microscopic gold particles.* Annalen Der Physik, 1912. **37**(5): p. 881-900.

65. Mie, G., *Articles on the optical characteristics of turbid tubes, especially colloidal metal solutions.* Annalen Der Physik, 1908. **25**(3): p. 377-445.

66. Faraday, M., *The Bakerian Lecture: Experimental Relations of gold (and other metals) to light.* Philosophical Transactions of the Royal Society of London, 1857. **147**: p. 36.

67. Bancroft, W.D., *Applied Colloid Chemistry*. 1921, New York: McGraw-Hill Book Company, Inc.

68. Sharma, V., K. Park, and M. Srinivasarao, *Colloidal dispersion of gold nanorods: Historical background, optical properties, seed mediated synthesis, shape separation and self-assembly.* submitted to Materials Science & Engineering R-Reports, 2008.

69. Ray, P.C., *History of Hindu Chemistry*. 1903, Calcutta: The Bengal Chemical and Pharmaceutical Works, Limited.

70. Einstein, A., *The motion of elements suspended in static liquids as claimed in the molecular kinetic theory of heat.* Annalen Der Physik, 1905. **17**(8): p. 549-560.

71. Einstein, A., *Investigation on the theory of Brownian movement*. 1956, New York: Dover Publications.

72. Einstein, A., *The theory of the Brownian Motion.* Annalen Der Physik, 1906. **19**(2): p. 371-381.

73. von Smoluchowski, M., *The kinetic theory of Brownian molecular motion and suspensions.* Annalen Der Physik, 1906. **21**(14): p. 756-780.

74. von Smoluchowski, M., *Three presentations on diffusion, molecular movement according to Brown and coagulation of colloid particles.* Physikalische Zeitschrift, 1916. **17**: p. 557-571.

75. von Smoluchowski, M., *Three lectures on diffusion, Brown's molecular movements and the coagulation of colloid parts.* Physikalische Zeitschrift, 1916. **17**: p. 585-599.

76. Langevin, P., *The theory of brownian movement.* Comptes Rendus Hebdomadaires Des Seances De L Academie Des Sciences, 1908. **146**: p. 530-533.

77. Chandrasekhar, S., *Stochatic Problems in Physics and Astronomy.* Reviews of Modern Physics, 1943. **15**(1): p. 1-89.

78. Haw, M.D., *Colloidal suspensions, Brownian motion, molecular reality: a short history.* Journal of Physics-Condensed Matter, 2002. **14**(33): p. 7769-7779.

79. Newburgh, R., J. Peidle, and W. Rueckner, *Einstein, Perrin, and the reality of atoms: 1905 revisited.* American Journal of Physics, 2006. **74**(6): p. 478-481.

80. Dhont, J.K.G. *Translational Brownian motion*. in *Physics meets biology: From Soft Matter to Cell Biology, 35th Spring School of the Institut fur Festkorperforschung*. 2004. Julich: Forschungszentrum.

81. Dhont, J.K.G. *Rotational Brownian motion of colloidal rods*. in *Soft Matter: Complex Materials on mesoscopic scales, 33rd IFF-Ferienschule*. 2002. Julich: Forschungszentrum Julich GmbH.

82. Perrin, J., *Brownian motion and molecular reality.* Annales De Chimie Et De Physique, 1909. **18**: p. 5-114.

83. Perrin, J., *Atoms*. 2nd ed. 1923, London: Constable & Company Ltd.

84. Nye, M.J., *The Question of the Atom*. The History of Modern Physics, 1800-1950. Vol. IV. 1984, Los Angeles: Tomash Publishers.

85. von Smoluchowski, M., *Molecular-kinetic theory of the opalescence of gases in a critical state, as well as several related occurrences.* Annalen Der Physik, 1908. **25**(2): p. 205-226.

86. Doi, M. and S.F. Edwards, *The Theory of Polymer Dynamics*. 1986, Oxford: Oxford University Press.

87. Russel, W.B., D.A. Saville, and W.R. Schowalter, *Colloidal Dispersions*. 1989, Cambridge: Cambridge University Press.

88. Cates, M.E. and M.R. Evans, *Soft and Fragile Matter*. 2000, Bristol: Institue of Physics Publishing.

89. Witten, T.A. and P.A. Pincus, *Structured Fluids: Polymers, Colloids, Surfactants*. 2004, New York: Oxford University Press.

90. Berg, H.C., *Random Walks in Biology*. 1983, Princeton: Princeton University Press.

91. Evans, D.F. and H. Wennerstrom, *The Colloidal Domain*. Advances in Interfacial Engineering Series. 1999, New York: Wiley-VCH.

92. Ohara, P.C., et al., *Crystallization of opals from polydisperse nanoparticles.* Physical Review Letters, 1995. **75**(19): p. 3466-3469.

93. Bohren, C.F. and D.R. Huffman, *Absorption and scattering of light by small particles*. 1983, New York: John Wiley & Sons.

94. van de Hulst, H.C., *Light Scattering by Small Particles*. 1981, Mineola: Dover Publications, Inc.

95. Strutt, J.W.L.R., *On the light from the sky, its polarization and colour.* Philosophical Magazine, 1871. **107**: p. 274-279.

96. Kerker, M., *The scattering of light and other electromagnetic radiation*. 1969, New York: Academic Press, Inc.

97. Jackson, J.D., *Classical Electrodynamics*. 1962, New York: John Wiley & Sons, Inc.

98. Link, S., M.B. Mohamed, and M.A. El-Sayed, *Simulation of the optical absorption spectra of gold nanorods as a function of their aspect ratio and the effect of the medium dielectric constant.* Journal of Physical Chemistry B, 1999. **103**(16): p. 3073-3077.

99. Hao, E., et al., *Synthesis and optical properties of "branched" gold nanocrystals.* Nano Letters, 2004. **4**(2): p. 327-330.

100. Hao, E., et al., *Optical properties of metal nanoshells.* Journal of Physical Chemistry B, 2004. **108**(4): p. 1224-1229.

101. Hao, E., G.C. Schatz, and J.T. Hupp, *Synthesis and optical properties of anisotropic metal nanoparticles.* Journal of Fluorescence, 2004. **14**(4): p. 331-341.

102. Hao, F., et al., *Plasmon resonances of a gold nanostar.* Nano Letters, 2007. **7**(3): p. 729-732.

103. Lazarides, A.A., et al., *Optical properties of metal nanoparticles and nanoparticle aggregates important in biosensors.* Journal of Molecular Structure-Theochem, 2000. **529**: p. 59-63.

104. Lazarides, A.A. and G.C. Schatz, *DNA-linked metal nanosphere materials: Structural basis for the optical properties.* Journal of Physical Chemistry B, 2000. **104**(3): p. 460-467.

105. Murphy, C.J., *Biosensors - Plasmons spring into action.* Nature Materials, 2007. **6**(4): p. 259-260.

106. Lipson, S.G., H. Lipson, and D.S. Tannhauser, *Optical Physics*. 1995, Cambridge: Cambridge University Press.

107. Inoue, S. and K.R. Spring, *Video Microscopy: The fundamentals*. 2nd ed. 1997, New York: Springer.

108. Srinivasarao, M. and J.O. Park, *Measurement of Surface Roughness of Polymers using Optical Methods*, in *Comprehensive Desk Reference of Polymer Characterization and Analysis*, R.F. Brady, Editor. 2003, Oxford University Press.

109. Born, M. and E. Wolf, *Principles of Optics: Electromagnetic Theory of Propagation, Interference and Diffraction of Light*. 7th ed. 1999, Cambridge: Cambridge University Press.

110. Nikoobakht, B. and M.A. El-Sayed, *Preparation and growth mechanism of gold nanorods (NRs) using seed-mediated growth method.* Chemistry of Materials, 2003. **15**(10): p. 1957-1962.

111. Sedunov, Y.S., *Physics of Drop Formation in the Atmosphere*. 1974, New York: Wiley. 234.

CHAPTER 9

SHAPE SEPARATION OF GOLD NANORODS

All that is gold does not glitter,
Not all those who wander are lost;
J. R. R. Tolkein*, Lord of the Rings* [1]

Nanoparticle synthesis, by typical methods that involve condensation from a solution, is characterized by a polydispersity in shape and size. The physical and chemical properties as well as the applications of nanoparticles are controlled and limited by their dimensions and shape, which implies that it is highly desirable to produce nanoparticles with well-defined and controlled size and shape. While great strides have been made in optimizing conditions and parameters during synthesis, there is a definite need for shape and size selective separation methods. Conventionally spherical colloidal particles have been separated based on their hydrodynamic behavior using sedimentation, flocculation, electrophoresis or centrifugation [2-4]. Size selective precipitation has been commonly used for nanospheres dispersed in organic solvents [5, 6]. Capillary electrophoresis [7] and column chromatography [8] have been used in the separation of metal nanoparticles. Gold nanorod dispersions synthesized by wet chemical methods inevitably contain spherical particles as a byproduct. Depending on the different methods, the fraction of byproduct can be 10% to almost 90 % [9-11]**.** The use of separation methods mentioned above [5-8] is limited because either they are not applicable to shape separation or they result in partial separation [12]**.** In this report, we provide a comprehensive set of theoretical arguments and experimental evidence showing how we utilized centrifugation to extract nanorods from a mixture of rods and spheres.

While centrifugation assisted sedimentation is routinely used to measure size and separate colloidal particles of different size [3, 4], successful separation based on shape (rods from spheres) is relatively less ubiquitous. Using the centrifugation parameters mentioned in the scattered reports in literature [11, 13, 14], we failed to achieve efficient separation repeatedly and reproducibly. As in literature reports, depending upon case to case basis, seemingly small differences in concentrations, centrifugation parameters and particle dimensions drove rods either to sediment out or remain in solution. Driven by the need and desire to understand these separation phenomena, we set out to identify the physics that drives shape separation in centrifugation. In this chapter, a comprehensive set of theoretical arguments and experimental evidence are provided, showing how nanorods were successfully extracted from a mixture of rods and spheres by using centrifugation. The experimental verification was carried out by Kyoungweon Park, who was also the one to bring this problem to the attention of the author.

By investigating the role of hydrodynamics in the centrifugation of Brownian rods and spheres, the size, shape and concentration dependence of sedimentation coefficients and velocities was determined, and was used to establish conditions that effect shape separation. The arguments advanced here, with described caveats, are applicable to shape and size separation for organic, inorganic and biological particles and molecules. Further, the presented analysis successfully interprets and explains the experimental observations of centrifugation of other groups [11, 13-17]. This is perhaps the first systematic study of shape separation, where central role of hydrodynamics of these particles is elucidated to explain their separation procedure.

The gold nanorods used for experiments described here were synthesized by seed mediated method and the size and shape of nanoparticles is gauzed using transmission electron microscopy (TEM) and UV-Vis-NIR spectroscopy. In UV-visible spectrum, nanoparticles have size dependent plasmon resonance peaks. Spheres have only one surface plasmon peak around 520 nm, while the rods have both a transverse peak (~520 nm) and longitudinal plasmon resonance at higher wavelengths. This peak position shifts to longer wavelength with increasing aspect ratio, and cumulative data from UV-Vis-NIR and TEM is useful in characterizing both the size and shape separation. The genesis of longitudinal plasmon resonance of rodlike particles is described here as well.

9.1 Theoretical aspects of sedimentation of rods and spheres

9.1.1 Sedimentation of a Brownian particle in an external field

Let us begin by considering a simple phenomenological analysis of forces acting on a Brownian particle placed in a centrifuge. The forces acting on the particle include centrifugal force, F_c,

$$F_c = \omega^2 rm \tag{9.1}$$

buoyant force,

$$F_b = -\omega^2 rm_o \tag{9.2}$$

Brownian fluctuating force, F_f, and viscous drag force, F_d,

$$F_d = -\zeta v \tag{9.3}$$

Here ω is the angular velocity, m is mass of particle, m_o mass displaced by the particle, r is the distance from the center to the location of particle, v is the sedimentation velocity and ζ is the friction or drag coefficient. The balance of these forces leads to the Langevin

equation of a particle undergoing Brownian motion under the influence of an external force. At equilibrium,

$$F_{total} = F_d + F_b + F_c + F_f = 0 \tag{9.4}$$

implies $\omega^2 r(m - m_0) - \varsigma v = 0$. This yields the Svedberg coefficient,

$$S = v / \omega^2 r = (m - m_o) / \zeta \tag{9.5}$$

which expresses the sedimentation velocity normalized by the applied angular acceleration. Svedberg coefficient is a measure of sedimentation rate and depends upon the ratio of effective mass, and friction factor [3, 18].

The relative importance of diffusion and flow is judged by a dimensionless number called the Peclet number, *Pe*, which for typical Brownian nanosphere is

$$Pe = va / D_m = (m - m_o)\omega^2 ra / k_B T < 1 \tag{9.6}$$

where a is the radius of the sphere and D_m is the diffusivity, implying that the thermal fluctuations are non-negligible. This distinguishes nanoparticle sedimentation theories from the theories applied to macroscopic falling objects [19].

In the context of the description of the barometric number distribution of colloidal particles with height given earlier (previous chapter), note here that qualitatively the only thing different in this case is the presence of centrifugal field, which essentially acts like a much stronger gravitational field. So the expression for Svedberg coefficient can also be written as

$$S = v / g_{eff} = m_{eff} / \zeta \tag{9.7}$$

This emphasizes that essentially we are still dealing with sedimentation behavior, and the use of centrifugation allows us to overcome the kT forces and distribute particles of effective mass according to effectively a greater "gravitational" force. Since $g_{eff} >> g$, the

centrifugation-assisted sedimentation is much faster, and when the sedimentation-diffusion equilibrium is reached, the average height $<h_{eff}>$ for colloidal particles is of course diminished. Let us for now focus on the determination of Svedberg coefficient (which is simply renormalized sedimentation velocity).

Basically a shape dependent computation of the effective mass, and of friction factor, ζ, is required so that a comparison of sedimentation rates of rods to that for spheres can be made. The expression for friction coefficient depends upon another dimensionless number, the Reynolds number, *Re* and *Re* «1 for the typical sedimentation problems in nanoscale. Reynolds number, *Re* ($=\rho UL/\eta$), where η is the viscosity, ρ is density of the fluid, *U* is characteristic speed, and *L* characteristic length, represents the ratio of characteristic magnitudes of inertial and viscous forces. Being in low Reynolds number regime implies that the inertial effects are negligible and the Stokes or creeping flow equations apply. Drag on a Stokesian sphere is $6\pi\eta aU$, implying a friction coefficient,

$$\zeta = 6\pi\eta a \tag{9.8}$$

and this yields us with a Svedberg coefficient of

$$S^{sph} = 2(\rho - \rho_o)a^2 / 9\eta \tag{9.9}$$

In fact, the friction coefficients are similar for spherically isotropic objects, i.e. all regular polyhedra and bodies derived from them by symmetrically cutting or rounding off the corners, edges and/or faces [20]. Hence the description of dynamics of spheres holds equally well for the cubic, icosahedra and octahedral bodies encountered during synthesis of colloidal particles. Modified Stokes law gives

$$v = K(\rho - \rho_o)a_{eq}{}^2 r\omega^2 / 18\eta \tag{9.10a}$$

$$K = 0.843 \log_{10}(A_{eq} / A * 0.065) \quad (9.10b)$$

where a_{eq} and A_{eq} correspond to diameter and area of the sphere with same volume as the particle. Using the equivalent sphere volume and including a correction factor, K~2-4 for difference in shape, the sedimentation of isotropic shapes is easily mapped from sphere case.

On the other hand, for anisotropic bodies both force and torque balance is required, and typically the coupling of translation and rotation needs to be considered. Translational friction coefficient of a falling single rod depends of the orientation of rod, and friction felt parallel to the rod is ½ that of the transverse falling rods, i.e $\zeta_{\perp} = 2\zeta_{//}$ [2, 20, 21]. Unlike the spherical particles that settle in the direction of gravity, the non-spherical Brownian particles sediment an angle to the direction of effective gravity, which can be up to 19.5 degrees for a thin rods [2]. But the Brownian rods, on an average, are guided in the direction of effective external field [2]. In computing drag for the rods, orientation plays as big a role as the dimensions of the rod itself, one of the reasons that make both theoretical and experimental studies of dynamics of rods a lot more interesting and challenging. If two rods of equal dimensions make multiple rotations due to Brownian motion during the time they sediment a distance comparable to their length, then their velocity relative to each other is zero. In this case, the sedimentation velocity is dependent only on the average friction coefficient. Mathematically this requires [22]

$$L/v_s t_{rot} \sim 12 k_B T / F_c L << 1 \quad (9.11)$$

where v_s is sedimentation velocity and F_c is the centrigfugal force, t_{rot} is the time required for one rotation and this is satisfied for gold nanorods considered here. Using the

expressions of friction coefficient, and mass of the rods, we derive the Svedberg coefficient for rods to be

$$S_o^{rod} = (\rho - \rho_o) D^2 \left[2\ln(L/D) - (\upsilon_\perp + \upsilon_{//})\right] / 24\eta_o \qquad (9.12)$$

where $\upsilon_\perp$ and $\upsilon_{//}$ are the correction factors of the rod perpendicular or parallel to the rods orientation, respectively.

9.1.2 Hydrodynamic interaction for spheres

During the sedimentation of many bodies, the velocity of surrounding particles influences the velocity of a particle. This fluid mediated particle interaction, called hydrodynamic interaction, makes the average sedimentation velocity different from that evaluated for a single sphere. In the presence of hydrodynamic interactions, the sedimentation velocity of sphere corrected up to first order in concentration, ϕ, is given by [4]

$$v^{sph} = v_o (1 - \beta\phi) \qquad (9.13)$$

and value of β depends upon nature of interaction, being 6.5 for hard spheres. While the hydrodynamic interactions decrease the sedimentation velocity for hard spheres (repulsive interactions), the sedimentation velocity for associating or attracting spheres will be greater than that of single sphere. It must be pointed here that the sedimentation of colloids causes an inhomogeneous backflow of solvent, and the velocities we refer to in reality are ensemble averages that take into account the effect of walls, boundaries and other divergences. Additionally the particle undergoing sedimentation is kicked by diffusion or Brownian motion to make the boundaries between differently sized spheres diffuse, but a self sharpening effect which causes the particles that lag behind to have

higher sedimentation speed due to concentration dependence of the drag (for hard spheres), the overall effect is to provide well-defined regions of different size species.

9.1.3 Hydrodynamic interaction of rods

Next the corresponding interaction is examined for rods. Here the computation is non-trivial as both hydrodynamic forces and torques need to be evaluated. Concentration dependence for sedimentation of hard rods was derived recently by Dogic et al [22], and their theory agrees with the only other theoretical result of Peterson's theory [23] up to aspect ratio of 30. In the calculations by Dogic et al [22], hydrodynamic interaction is calculated by assuming that the time scale over which the rod travels distance of the order of L is much larger than the Brownian rotational relaxation time and the alignment of suspension and interactions are negligible. To the first order in concentration, i.e. for dilute solutions, the relationship is

$$v^{rod} = v_o^{rod}(1-\alpha\phi) \tag{9.14}$$

where the coefficient α is given by

$$\alpha = \frac{6.4 + 2L/9D}{2\ln\{L/D\} - (\upsilon_{\perp} + \upsilon_{//})} \frac{L}{D} \tag{9.15a}$$

$$\alpha_{Peterson} = \frac{8(3/8)^{2/3}(L/D)^{1/3}}{2\ln\{L/D\}} \frac{L}{D} \tag{9.15b}$$

Relative sedimentation behavior of colloidal rods and spheres can be described by the ratio of the sedimentation coefficients between rods and spheres. The ratio

$$s_o^{rod} / s_o^{sph} = v_o^{rod} / v_o^{sph} = \lambda_o = 6(D/2a)^2[\ln L/D + ((\upsilon_{\perp} + \upsilon_{//})] \tag{9.16}$$

for single rod and single sphere allows us to see that for this case *the central role in separation is played by the ratio of the squares of diameters of the rod and sphere*. For a

given *L/D*, whether the rods or spheres sediment faster is mainly controlled by the relative diameters of the particles, and since the aspect ratio dependence enters through the logarithmic term, the effect is much less dramatic than the effect of the diameters. While the effective weight of the rod might be more than that of sphere, the overall sedimentation velocity could still be lower.

The physics and use of centrifugation for separating spherical colloidal particles is well documented [2-4, 18, 20, 24-27] and it is easy to see that relative sedimentation velocity of spheres of same material (effective density) is simply equal to the square of ratio of their diameters. Also note that for two rods, with different aspect ratios, again the critical parameter will be the ratio of their diameters, for effect of length or aspect ratio is in logarithmic term.

$$S_{o\ (1)}^{rod} / S_{o\ (2)}^{rod} = (D_{(1)}{}^2 / D_{(2)}{}^2) \times \left[2\ln(L/D)_{(1)} - (\upsilon_{\perp} + \upsilon_{//})\right] / \left[2\ln(L/D)_{(2)} - (\upsilon_{\perp} + \upsilon_{//})\right] \tag{9.17}$$

The above relationships are derived using single rod and single sphere sedimentation behavior. As the concentration of the particles increase, their hydrodynamic behavior starts to get affected by the flow field of each other, and the correction for this appears in form of "hydrodynamic interaction" term [4, 22, 23, 28]. Including the hydrodynamic interaction terms, the ratio becomes

$$\lambda = s^{rod} / s^{sph} = v^{rod} / v^{sph} = \lambda_o (1 - \alpha\phi) / (1 - \beta\phi) \tag{9.18}$$

where $\alpha \geq \beta$ implies a stronger self-sharpening effect for the rods allowing for better separation. There will be hydrodynamic interaction between rods and spheres as well, which was not accounted for in the above discussion, a reasonable assumption for such low concentrations. It must be mentioned however that the sedimentation diffusion

equilibrium was used by early practitioners of ultracentrifugation (Rinde, Westgern, Svedberg) to determine the size and size distribution of gold sols [25], which typically comprised of spherical nanoparticles. A similar determination for rodlike gold particles is expected to be equally useful.

9.1.4 Concentration profiles

In non-equilibrium thermodynamics, the sedimentation during centrifugation can be described using the Brownian motion under an external field using modified Smoluchowski equation [27-31]. In this version, the Brownian motion yields Fickian type diffusion equation, called Lamm differential equation for centrifuge, with flux terms that account for the external field as well as the chemical potential gradients, i. e.

$$\partial_t c(z,t) = \partial_z \left(D_m \partial_z c(z,t) + \kappa c(z,t) F^{ext} \right) \tag{9.19}$$

The concentration profile, written using non-dimensionalized parameters ($C(Z,T) = c(z,t) z_o / c_o$, Z=z/z$_o$, $T = D_o t / z_o^2$ and $\varepsilon = v_s^o z_o / D_o$) is as follows [31]

$$\begin{aligned} C(Z,T) = (4\pi T)^{-1/2} \left[\exp\left\{ -(Z-1)^2 / 4T \right\} + \exp\left\{ -(Z+1)^2 / 4T \right\} \right] \times \\ \exp\left\{ -(\varepsilon(Z-1) + \varepsilon^2 T)/2 \right\} + \frac{\varepsilon}{\pi^{1/2}} \exp\left\{ -\varepsilon Z \right\} \int_{\frac{Z+1-\varepsilon T}{\sqrt{4T}}}^{\infty} dx \exp\left\{ -x^2 \right\} \end{aligned} \tag{9.20}$$

The resulting concentration profile is Gaussian distribution [27, 29-31] such that the peak position of the Gaussian corresponds to the position with the highest number of particles. As the centrifugation proceeds, the peak position shifts, reflecting that the whole distribution of particles is moving in the direction of centrifugal field. The shift in peak position as a function of time is dictated by the average sedimentation velocity of the

particles. Different shapes and sizes result in differently peaked distributions leading to separation.

The long time solution yields barometric concentration profiles. This implies that if centrifugation is carried for very long time, the distribution would be similar to that obtained once equilibrium is reached under gravity, which for 5600g (the acceleration used in experiments described) leads to nearly all particles going to the bottom. Another point to note is that the above consideration is equivalent to the probability distribution function of free particle in one dimension and provides only an expectation rather than an exact theory for multi-particle system. Even for the non-Brownian particles, sedimentation phenomenon is a highly non-equilibrium process and even though the behavior is described by deterministic equations, the dynamics is chaotic with high sensitivity to initial conditions and particles experience diffusive behavior induced by flows originating due to other particles, called hydrodynamic diffusion [19].

The following sections will show how these hydrodynamic arguments about relative sedimentation velocity were employed to obtain nanorods of greater purity, viz. lower size and shape dispersity. The size dispersity is characterized by use of two techniques: UV-Vis spectroscopy, where the size and shape dependent plasmon resonance determines the overall absorbance of the dispersion and by TEM visualization. Before proceeding to the discussion of experiments on centrifuged samples, let's first look how the UV-Vis absorbance is determined by the dimensions and polydispersity of the nanorod dispersions.

9.2 Plasmon Resonance for ellipsoidal nanoparticles

For gold nanorods, the plasmon absorption splits into two bands corresponding to the oscillation of the free electrons along and perpendicular to the long axis of the rods [32]. The transverse mode (transverse surface plasmon peak: TSP) shows a resonance at about 520 nm, while the resonance of the longitudinal mode (longitudinal surface plasmon peak: LSP) strongly depends on the aspect ratio of nanorods. As aspect ratio is increased, the longitudinal peak is red-shifted. To account for the optical properties of nanorods, it has been common to treat them as ellipsoids, which allows the Gans formula (extension of Mie theory) to be applied. A geometrical factor P_j was introduced to calculate the absorbance of light by ellipsoids.

Gans' formula [33] for randomly oriented elongated ellipsoids in the dipole approximation can be written as

$$\frac{\gamma}{N_p V} = \frac{2\pi {\varepsilon_m}^{3/2}}{3\lambda} \sum_{j=A}^{C} \frac{\left(\frac{1}{{P_j}^2}\right)\varepsilon^2}{\left[\varepsilon_1 + \left(\frac{1-P_j}{P_j}\right)\varepsilon_m\right]^2 + {\varepsilon_2}^2} \tag{9.21}$$

where N_p represents the number concentration of particles, V the single particle volume, λ the wavelength of light in vacuum, and ε_m the dielectric constant of the surrounding medium and ε_1 and ε_2 are the real (n^2 - k^2) and imaginary ($2nk$) parts of the complex dielectric function of the particles. The geometrical factors P_j for elongated ellipsoids along the A and B/C axes are respectively given by

$$P_A = \frac{1-e^2}{e^2}\left[\frac{1}{2e}\ln\left(\frac{1+e}{1-e}\right) - 1\right] \tag{9.22a}$$

$$P_B = P_C = \frac{(1-P_A)}{2} \text{ and } \quad e = \left(\frac{L^2 - d^2}{L^2}\right)^{1/2} \tag{9.22b}$$

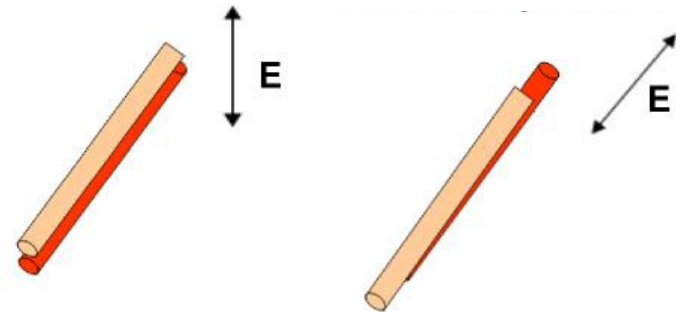

Figure 9.1 Transverse and longitudnal modes of plasmon resonance in rodlike particles.

Figure 9.2 shows the absorbance spectra for gold nanorods with varied aspect ratio calculated using the Gans expressions. The dielectric constants used for bulk gold are taken from the measurements done Johnson and Christy [34], while the refractive index of the medium was assumed to be constant and same as for H_2O (1.333). The maximum of the longitudinal absorbance band shifts to longer wavelengths with increasing aspect ratio. There is the small shift of the transverse resonance maximum to shorter wavelengths with increasing aspect ratio. Electron microscopy reveals that most nanorods are more like cylinders or sphero-capped cylinders than ellipsoids. However, an analytical solution for such shapes is not derived yet, and so while the results are compared to the formula given by ellipsoids, we must remember that such comparisons are approximate.

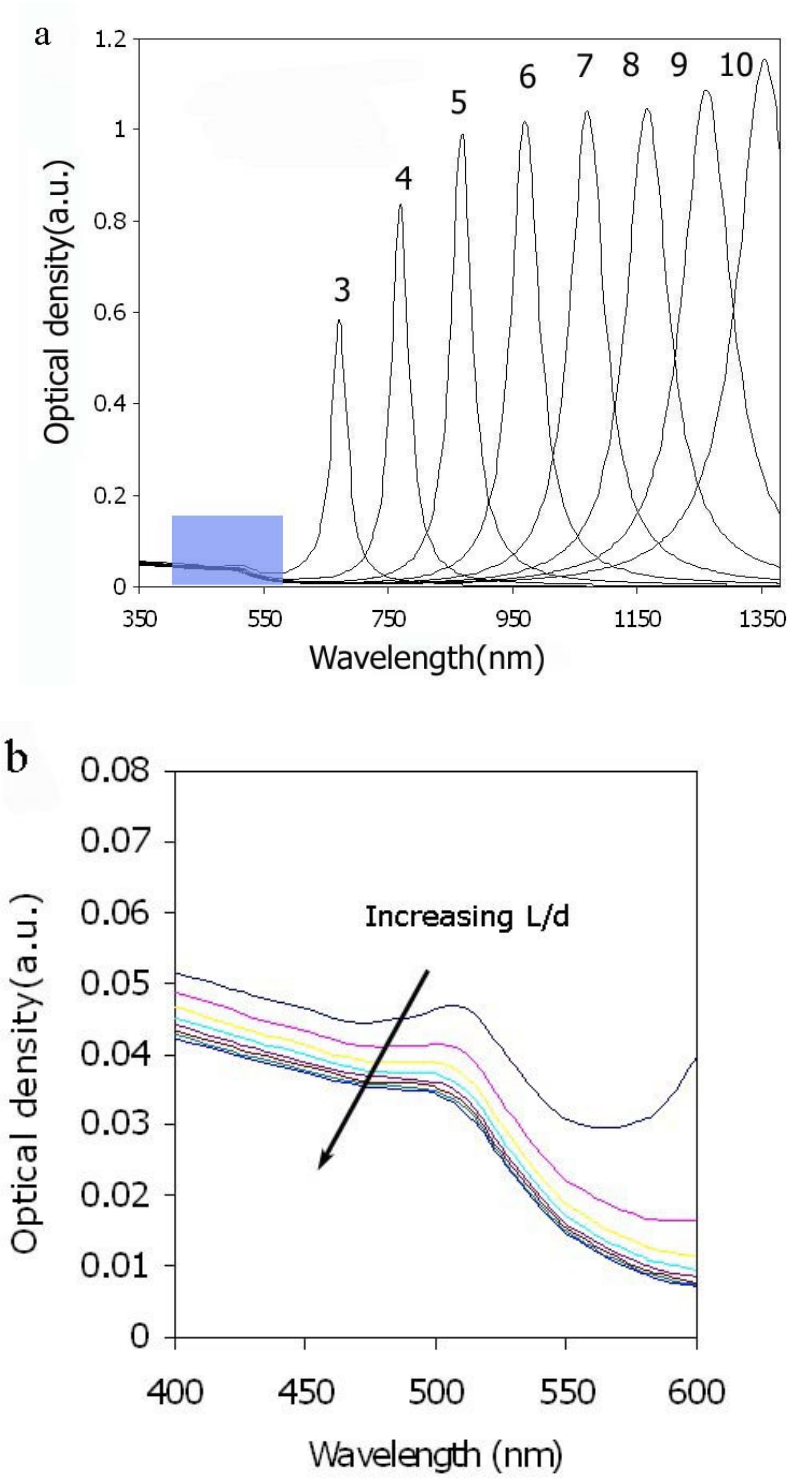

Figure 9.2 Absorbance spectra calculated with the expressions of Gans for elongated ellipsoids using the bulk optical data for gold. (**a**) The numbers on the spectral curves indicate the aspect ratio (*L*/*d*). (**b**) Enlargement of the shaded area of (a) showing slight blue shift of transverse plasmon resonance peak on increasing aspect ratio [35, 36].

9.3 Separation of nanorods from spherical nanoparticles using centrifugation

As-made dispersions of nanorods were centrifuged at 5600 G for 20 to 40 min (Jouan centrifuge MR23i, fixed angle rotor). After centrifugation was stopped, the tube was taken and visibly inspected. Figure 9.3 shows the TEM image taken from the mother dispersion showing the mixture of rods and spherical particles. The average diameter of the spherical particles is 16.59 nm while the average diameter of NRs is 8.06nm. The average length of NR is 58.54 nm. Hence, the aspect ratio is 7.3. The number fraction of spherical particles is less than 10% (counting 700 particles). It can be seen by UV- Vis-NIR spectroscopy, (figure 9.4) that the intensity of transverse plasmon peak is lower as compared to that of the as-made mother solution.

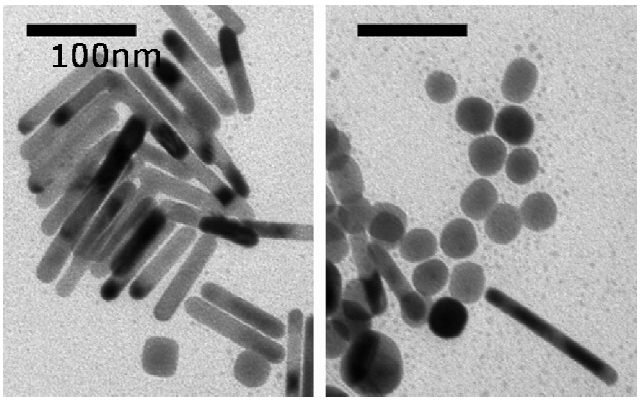

Figure 9.3 TEM image of mother colloidal sol. L/d of gold NRs is 7.3 [35, 36].

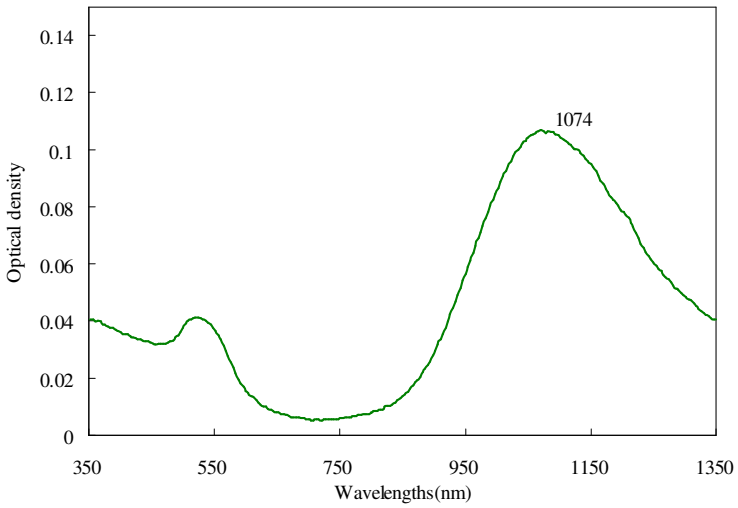

Figure 9.4 UV-Vis –NIR spectrum of mother colloidal sol. L/d of the gold NRs is 7.3 [35, 36].

The centrifuge tube upon centrifugation is schematically illustrated in Figure 9.5. The color of sols taken from the bottom and the side wall of the centrifuge tube is distinctively different indicating that the particles deposited in different sites have different optical properties, and hence are different in the size or shape or both.

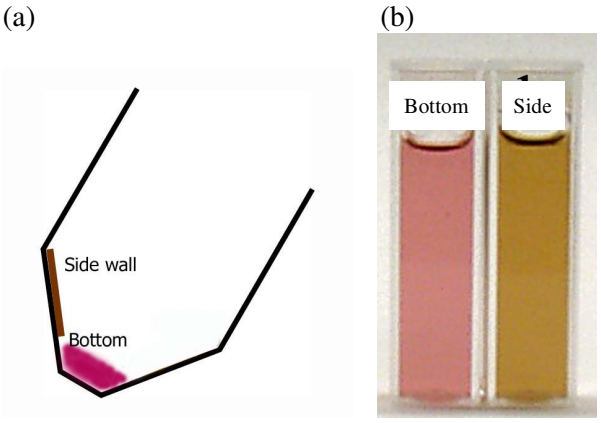

Figure 9.5 (**a**) Schematic drawing of the centrifuge tube after the centrifugation and the color of resulting sols. (**b**) The color of the sols made by redispersing the nanoparticles taken from two different locations shown in (a).

The UV-Vis-NIR spectrum of the sol of the side wall shows intense longitudinal surface plasmon peak red shifted from the mother sol and very tiny transverse plasmon

peak indicating that it contains mostly nanorods and the aspect ratio is larger than that of the mother sol. The spectrum of the sol prepared by redipersing particles from the bottom shows broad transverse plasmon resonance peak with high intensity indicating that it contains spherical particles and nanorods. The longitudinal plasmon peak of this sol is blue shifted from the mother sol indicating that the aspect ratio of nanorods is smaller than those of mother sol.

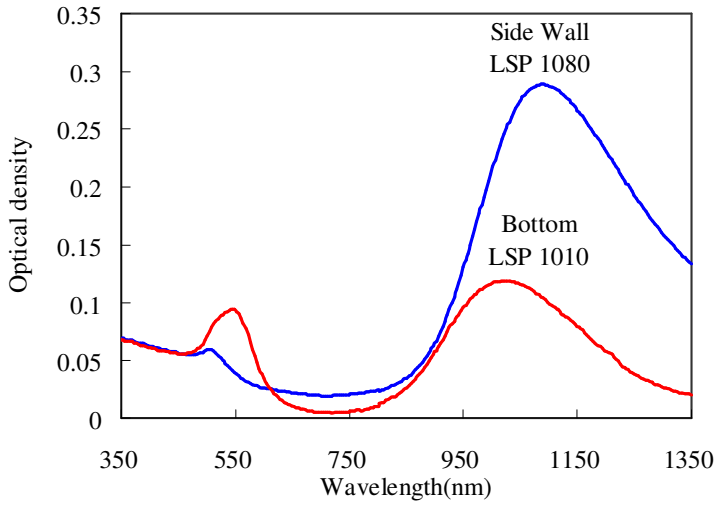

Figure 9.6 UV–Vis-NIR spectrum of separated sols of (**a**) deposit on the side of the tube and (**b**) deposit at the bottom.

The size of the particles in these two sols was measured by TEM (counting 500 particles from each sol). TEM images, (figure 9.7) show that the separation of nanorods was successfully accomplished using the described centrifugation conditions. The dispersion made from the bottom deposit contains lots of spherical particles, while the dispersion from the side wall contains mostly NRs. In the as-made dispersion of colloidal gold, the average diameter of spherical particles was almost twice as large as of the diameter of NRs, implying that the ratio $s_o^{rod} / s_o^{sph} = v_o^{rod} / v_o^{sph} = \lambda_o \langle\langle\ 1$ (average diameter of sphere is 16.6 nm) and therefore, in this case the spherical particles sediment faster

than the nanorods. The nanorods that segregated to the side wall have longer length and smaller diameter (higher aspect ratio) than the mother dispersion. Shorter and fatter NRs were found to dominate in the dispersion made from nanoparticles deposited at the bottom.

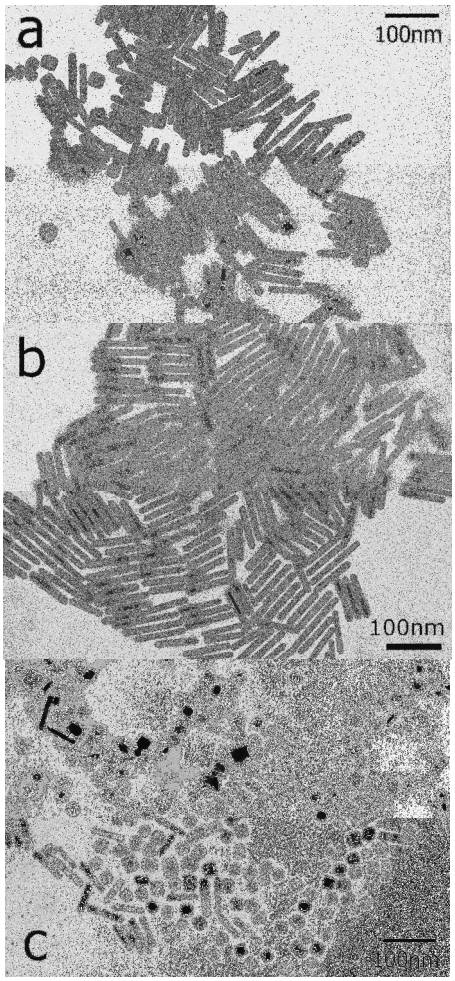

Figure 9.7 TEM images of gold nanoparticles: (**a**) mother sol, (**b**) after centrifugation, nanorods deposited on the side of the tube, and (**c**) after centrifugation, sedimented at the bottom, nanocubes, spheres and nanorods with larger diameter.

Table 9.1 The size of NRs before and after the separation (unit: nm).

	L	D	L/D
Mother	58.54	8.06	7.30
Separated	65.73	7.87	8.35

Yield of nanorods can be calculated based on the amount of the sol and the intensity of the UV-Vis-NIR absorption peak. Through a single centrifugation, the yield was 20 to 60 percent depending on the property of as made sol such as the fraction of nanospheres and the relative dimensions of the dispersed particles. The yield can be increased up to 70 to 80 percent by repeated centrifugation of the supernatant sol. But more than 3 times of centrifugation resulted in the irreversible precipitation of nanorods [35].

9.4 Separation of nanorods with different aspect ratio

Dispersion of nearly pure nanorods was centrifuged. The centrifuge was stopped every 10 minute and the deposit at the bottom was taken. Figure 9.8 shows the UV-Vis-NIR spectra of the centrifuged sample as a function of time. By the red-shift of longitudinal plasmon peak (as well as blue-shift of the transverse peak), it is apparent that the aspect ratio of the nanorods obtained at different times becomes longer as a function of time indicating longer nanorods sediment later then the shorter nanorods. Also the shape of peak due to transverse plasmon resonance changes as a function of time. The sol obtained earlier has a broad shoulder and it becomes suppressed towards the later stage.

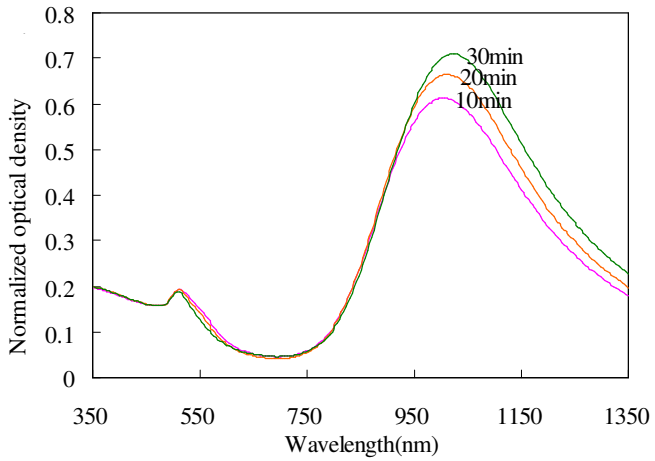

Figure 9.8 The UV-Vis-NIR spectra of the centrifuged sample as a function of time [35, 36].

In the synthesis by Park **[35]**, generally longer nanorods have smaller diameter, as shown in Figure 9.9. The result that nanorods having larger diameter, sediment faster than nanorods with thinner diameter (albeit a large aspect ratio) agrees with the theoretical prediction that the sedimentation behavior of nanorods depends more strongly on the diameter of nanorods than on their total weight or aspect ratio. Again the key factor for the sedimentation is the ratio of Svedberg coefficients of the nanorods.

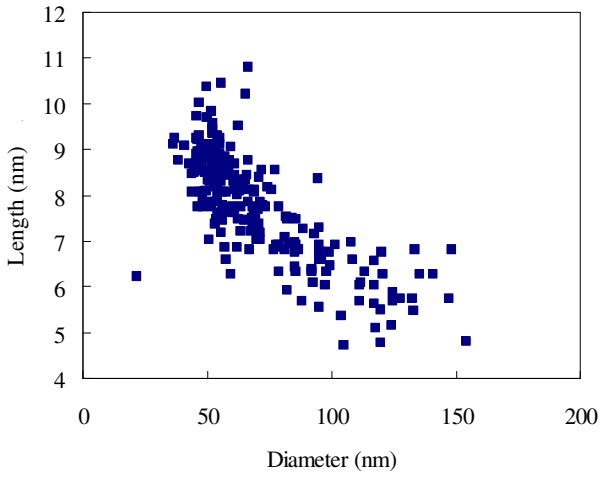

Figure 9.9 The plot of diameter and length of the nanorods [35, 36].

In literature, it has been often quoted that the long rods settle down preferentially at the bottom as they are heavier [11, 15] or due to so called surfactant assisted self assembly [14]. In the present example (figure 9.7), the weight of nanorods is greater than that of spheres and yet it is the spheres that settle to the bottom. Similarly, shorter and fatter rods segregated to bottom, rather than the rods with longer length and comparable or higher effective weight. As explained in the theoretical considerations, one needs to remember that the dynamics of nanoparticles in this system are controlled by the ratio of their effective mass and friction coefficient. As the calculation of the ratio of velocities of rods and spheres illustrate, the relative ease of separation of these particles is mainly controlled by the relative diameters of the particles. This explains why spheres with larger diameter and fatter rods settle to the bottom in our case.

The separations reported in the literature [11, 13-17] conform to the analysis presented, which is based solely on hydrodynamics. Like in the presented case, Chang et al [16] observed spheres formed bulk of sediments in their first centrifugation. The prediction that rods and spheres with similar diameters are hard to shape separate is also borne by reports in literature [11, 13, 14]. Repeated centrifugation followed by dissolution of sedimentation particles in a surfactant solution [11, 13, 14] is equivalent to selecting bigger particles in each run and by dilution, rods tend to sediment faster than they can in a more concentrated solution as described above.

In this context, the protocol reported by Jana [14] as “surfactant assisted separation of nanorods” from a concentrated dispersion was repeated. Jana emphasizes that nanorods preferentially precipitated by the formation of liquid crystalline phase.

While it is plausible that increasing surfactant concentration can induce phase separation in a mixture of rods and spheres, the typical as made dispersions, as well as the denser dispersions obtained after centrifugation have extremely low volume fraction of rods, thus precluding the formation of liquid crystalline phase. The increase in surfactant concentration was found to increase the yield of nanorods in the shape separation affected by centrifugation [35]. This is perhaps related to the effect of changing ionic content that is known to affect the sedimentation behavior of colloidal dispersions containing charged or interacting particles [37-40]. The effect of dissolved surfactant and of particle shape and size can be critically examined only by conducting a thorough study of how interparticle forces act together with Brownian motion in determining sedimentation equilibrium, electrophoretic mobility and coagulation behavior. The phase behavior of nanorods is richer than spherical particles for concentrated dispersions of rods can transition to liquid crystalline phases. The theoretical and experimental aspects of the formation of liquid crystalline phase will be discussed in the next chapter.

The arguments advanced in this chapter are strictly applicable in dilute regime only; the thermodynamic considerations that come into play at higher concentrations may be part of the reason why rods assemble with a considerably high purity on the sidewall in described experiments. The concentration of the nanoparticles in the solutions used lies in the dilute range, as the average distance between particles, $\phi^{-1/3}$ is much larger than L or $\phi << L^{-3}$. Here L is the size of the particles and ϕ denotes the number of particles per unit volume. The sedimentation cell used has these nanoparticles suspended uniformly to begin with, and since the standard cell for the centrifugation is used, effects of heating, convection in fluid, etc are minimized. The physics of centrifugation is modified both at

higher concentrations of particles and in highly charged systems. Dogic et al [22] reported that in the highly concentrated solutions, nematic phase formation causes the faster sedimentation of rods in the denser LC phases, but since the rods were observed to assemble on the side-wall, and concentration of as-made solution is very low, the formation of LC phase cannot occur in this case. The solution needs to be concentrated by over 1000 times to reach the required concentration for phase transition from isotropic to nematic phase, and thus the probability of this happening in dispersed phase or particles aggregating is negligible.

9.5 Absorption Spectrum of colloidal dispersions of gold nanorods

It is made evident in previous sections that the longitudinal and transverse plasmon resonance can be computed as a function of aspect ratio either by using analytical expression put forth by Gans in 1912 [33] or by using one of numerical techniques [41, 42]. We now describe the how the absorption spectrum measured experimentally compares to the results from Gans theory [33] and DDA simulations [41, 43]. Even though optical properties of pure water were used for calculating the spectrum, the peak resonance measured experimentally show a remarkable agreement with theoretical and simulation results. Several groups have observed similar trends [32, 44], though we assert that the best comparisons can be made only with samples with lowest possible polydispersity. It must be pointed out here that the nanorods used in our research were not only synthesized in a controlled manner to produce lower size dispersity, but they were also separated more efficiently from nanospheres using our understanding of what controls shape separation during centrifugation.

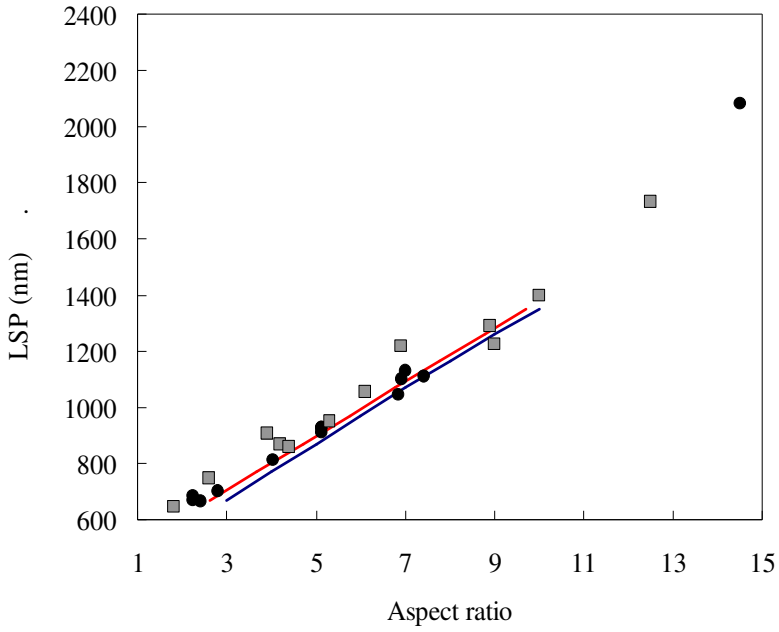

Figure 9.10 Longitudinal surface plasmon peak (nm) versus the aspect ratio of nanorods. Simulation results using the DDA method [41, 43] and the corresponding fit (red straightline) and Gans' calculation (blue straight line). Experimental data from the work of van der Zande et al [45] (gray squares). Experimental data from our study (black circles) [35, 36].

The visible light region consists of a spectrum of wavelengths, which range from approximately 700 nm to 400 nm. For the nanorods, the transverse plasmon resonance peak is not quite as sensitive to the change of aspect ratio, as the longitudinal peak, which shows noticeable shifts in the aspect ratio as seen in Figure 9.11 which shows the UV-Vis-NIR spectrum of gold nanorods dispersions. As predicted by theory, the transverse peak blue shifts with an increasing aspect ratio. This result requires a dispersion of nanorods of extremely high purity, and to the best of our knowledge has not been reported before. The relatively intensity of transverse peaks shows that mostly nanorods are present. This testifies that the synthesis method developed by Park [35] and the separation technique described here can be used for making nanorod dispersions with high monodispersity.

a)

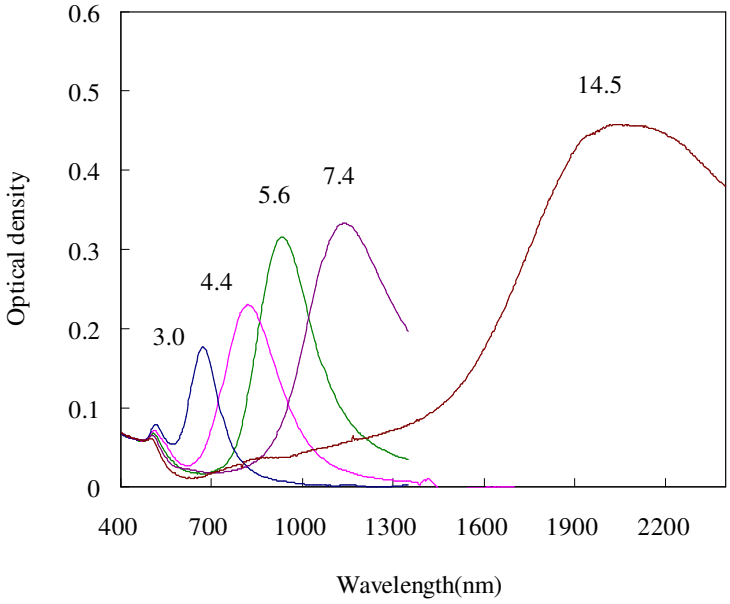

b)

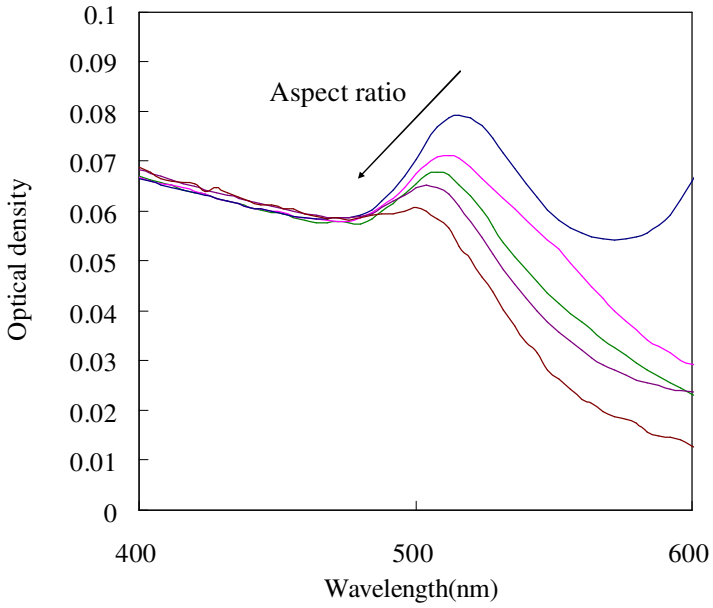

Figure 9.11 (**a**) UV-Vis-NIR spectra of dispersions containing gold nanorods with different aspect ratios. (**b**) Blow up of the transverse peak shows the blue shift as the aspect ratio of rods increases [35, 36].

9.6 Summary

The conditions, under which, centrifugation leads to shape separation of nanoparticles, were elucidated by analyzing the hydrodynamics of rods and spheres. The ratio of the sedimentation velocities of Brownian rods and spheres undergoing centrifugation primarily depends upon the ratio of the square of their diameters. The sedimentation velocity of a particle depends upon the ratio of the effective mass of the particle and the drag experienced by it. The drag itself depends upon the shape of the particle, and for particles of same weight with different shapes, it can make particles sediment at very different velocities. The understanding of the parameters and physics that drives separation is a necessary step in widespread use of centrifugation to shape separate particles. It is believed that the arguments presented here will prove beneficial in approaching centrifugation for shape separation of all kinds of particles and provide impetus to research efforts directed towards study of separation techniques, that we believe, is as necessary as efficient synthesis methodology to get nearly monodisperse, shape segregated nanoparticle dispersions. The efficient separation was illustrated by both the TEM images as well as UV-Vis-NIR spectra. The blue shift in transverse plasmon reflection predicted by theory for nanorods with increasing aspect ratio was also observed for the first time, for it requires dispersions with low content of nanospheres. The assemblies and patterns observed on TEM are studied in a greater detail in the following chapter.

9.7 References

1. Tolkein, J.R.R., *The Lord of the Rings*. 1988: Houghton Mifflin.

2. van de ven, T.G.M., *Colloidal Hydrodynamics*. 1989, London: Academic Press Inc.

3. Svedberg, T. and K.O. Pedersen, *The Ultracentrifuge*. 1940, Oxford: Oxford University Press.

4. Russel, W.B., D.A. Saville, and W.R. Schowalter, *Colloidal Dispersions*. 1989, Cambridge: Cambridge University Press.

5. Murray, C.B., D.J. Norris, and M.G. Bawendi, *Synthesis and characterization of nearly monodisperse CdE (E= S, Se, Te) semiconductor nanocrystallites.* Journal of the American Chemical Society, 1993. **115**(19): p. 8706-8715.

6. Whetten, R.L., et al., *Nanocrystal gold molecules.* Advanced Materials, 1996. **8**(5): p. 428-&.

7. Liu, F.K., et al., *Studying the size/shape separation and optical properties of silver nanoparticles by capillary electrophoresis.* Journal of Chromatography A, 2005. **1062**(1): p. 139-145.

8. Wei, G.T., F.K. Liu, and C.R.C. Wang, *Shape separation of nanometer gold particles by size-exclusion chromotography.* Analytical Chemistry, 1999. **71**(11): p. 2085-2091.

9. Nikoobakht, B. and M.A. El-Sayed, *Preparation and growth mechanism of gold nanorods (NRs) using seed-mediated growth method.* Chemistry of Materials, 2003. **15**(10): p. 1957-1962.

10. Yu, Y.Y., et al., *Gold nanorods: Electrochemical synthesis and optical properties.* Journal of Physical Chemistry B, 1997. **101**(34): p. 6661-6664.

11. Jana, N.R., L. Gearheart, and C.J. Murphy, *Wet chemical synthesis of high aspect ratio cylindrical gold nanorods.* Journal of Physical Chemistry B, 2001. **105**(19): p. 4065-4067.

12. Perez-Juste, J., et al., *Gold nanorods: Synthesis, characterization and applications.* Coordination Chemistry Reviews, 2005. **249**(17-18): p. 1870-1901.

13. Jana, N.R., *Shape effect in nanoparticle self-assembly.* Angewandte Chemie-International Edition, 2004. **43**(12): p. 1536-1540.

14. Jana, N.R., *Nanorod shape separation using surfactant assisted self-assembly.* Chemical Communications, 2003(15): p. 1950-1951.

15. Nikoobakht, B., *Synthesis, characterization and self-assembly of gold nanorods on surface-enhanced Raman studies*. 2001, Georgia Institute of Technology: Atlanta.

16. Chang, S.S., et al., *The shape transition of gold nanorods.* Langmuir, 1999. **15**(3): p. 701-709.

17. Kim, F., J.H. Song, and P.D. Yang, *Photochemical synthesis of gold nanorods.* Journal of the American Chemical Society, 2002. **124**(48): p. 14316-14317.

18. Svedberg, T., *The Formation of Colloids*. 1921, New York: D. Van Nostrand Company.

19. Ramaswamy, S., *Issues in the statistical mechanics of steady sedimentation.* Advances in Physics, 2001. **50**(3): p. 297-341.

20. Happel, J. and H. Brenner, *Low Reynolds number hydrodynamics* 2nd ed. 1973, Leyden: Noordhoff International Publishing.

21. Doi, M. and S.F. Edwards, *The Theory of Polymer Dynamics*. 1986, Oxford: Oxford University Press.

22. Dogic, Z., et al., *Concentration-dependent sedimentation of colloidal rods.* Journal of Chemical Physics, 2000. **113**(18): p. 8368-8380.

23. Peterson, J.M., *Hydrodynamic alignment of rodlike macromolecules during ultracentrifugation.* Journal of Chemical Physics, 1964. **40**(9): p. 2680-.

24. Bancroft, W.D., *Applied Colloid Chemistry*. 1921, New York: McGraw-Hill Book Company, Inc.

25. Svedberg, T. and A. Tiselius, *Colloid Chemistry*. Second ed. 1928, New York: The Chemical Catalog Company, Inc.

26. Zsigmondy, R., *The Chemistry of Colloids*. 1917, New York: John Wiley & Sons, Inc.

27. Fujita, H., *Foundations of Ultracentrifugation Analysis*. 1975, New York: John Wiley and Sons.

28. Doi, M. and S.F. Edwards, *The Theory of Polymer Dynamics*. 1988, New York: Oxford University Press. 406.

29. Chandrasekhar, S., *Stochatic Problems in Physics and Astronomy.* Reviews of Modern Physics, 1943. **15**(1): p. 1-89.

30. Dhont, J.K.G. *Rotational Brownian motion of colloidal rods.* in *Soft Matter: Complex Materials on mesoscopic scales, 33rd IFF-Ferienschule*. 2002. Julich: Forschungszentrum Julich GmbH.

31. Dhont, J.K.G. *Translational Brownian motion*. in *Physics meets biology: From Soft Matter to Cell Biology, 35th Spring School of the Institut fur Festkorperforschung*. 2004. Julich: Forschungszentrum.

32. Link, S. and M.A. El-Sayed, *Size and temperature dependence of the plasmon absorption of colloidal gold nanoparticles.* Journal of Physical Chemistry B, 1999. **103**(21): p. 4212-4217.

33. Gans, R., *The shape of ultra microscopic gold particles.* Annalen Der Physik, 1912. **37**(5): p. 881-900.

34. Johnson, P.B. and R.W. Christy, *Optical Constants of the Noble Metals.* Phys. Rev. B, 1972. **6**(12): p. 4370-380.

35. Park, K., *Synthesis, characterization and self-assembly of size tunable gold nanorods*, in *School of Polymer, Textile and Fiber Engineering*. 2006, Georgia Institute of Technology: Atlanta.

36. Sharma, V., K. Park, and M. Srinivasarao, *Colloidal dispersion of gold nanorods: Historical background, optical properties, seed mediated synthesis, shape separation and self-assembly.* submitted to Materials Science & Engineering R-Reports, 2008.

37. Rasa, M., et al., *Macroscopic electric field and osmotic pressure in ultracentrifugal sedimentation-diffusion equilibria of charged colloids.* Journal of Physics-Condensed Matter, 2005. **17**(15): p. 2293-2314.

38. Philipse, A.P., *Remarks on the Donnan condenser in the sedimentation-diffusion equilibrium of charged colloids.* Journal of Physics-Condensed Matter, 2004. **16**(38): p. S4051-S4062.

39. Rasa, M. and A.P. Philipse, *Evidence for a macroscopic electric field in the sedimentation profiles of charged colloids.* Nature, 2004. **429**(6994): p. 857-860.

40. Philipse, A.P. and G.H. Koenderink, *Sedimentation-diffusion profiles and layered sedimentation of charged colloids at low ionic strength.* Advances in Colloid and Interface Science, 2003. **100**: p. 613-639.

41. Kelly, K.L., A.A. Lazarides, and G.C. Schatz, *Computational electromagnetics of metal nanoparticles and their aggregates.* Computing in Science & Engineering, 2001. **3**(4): p. 67-73.

42. Bohren, C.F. and D.R. Huffman, *Absorption and scattering of light by small particles*. 1983, New York: John Wiley & Sons.

43. Kelly, K.L., et al., *The optical properties of metal nanoparticles: The influence of size, shape, and dielectric environment.* Journal of Physical Chemistry B, 2003. **107**(3): p. 668-677.

44. Murphy, C.J., et al., *Anisotropic metal nanoparticles: Synthesis, assembly, and optical applications.* Journal of Physical Chemistry B, 2005. **109**(29): p. 13857-13870.

45. van der Zande, B.M.I., et al., *Colloidal dispersions of gold rods: Synthesis and optical properties.* Langmuir, 2000. **16**(2): p. 451-458.

CHAPTER 10

OCEAN IN A DROP OF GOLD NANORODS

A drop of water has the properties of the sea,
but cannot exhibit a storm.
There is beauty of a concert, as well as of a flute;
strength of a host, as well as of a hero.
Ralph Waldo Emerson*, Swedenborg; or, the mystic* [1]

10.1 Self Assembly of Rodlike Nanoparticles

Self assembly has emerged as one of the most significant paradigms for fabricating devices for applications in nanotechnology [2-6]. The possible sub-micron structures encompasses the whole spectrum of possible morphologies emerging from drying mediated aggregation [7-10], crystallization of colloids [11-25], microphase separation of block copolymers [26-28], self-assembled monolayers [29-31], phase behavior of amphiphilic molecules [32-34], breath figure templated assembly to make holey films [35-37], among others. Additionally rich complexity of non-equilibrium patterns can be derived by interplay of different external fields and inherent phase possibilities [6, 38]. Qualitative understanding of these structures can be guided by our understanding of the analogies derived from various realms of condensed matter physics [6, 38-41]. The process and outcome of self-assembly is controlled by the size and shape of the moieties, their interaction and packing behavior, and surface and hydrodynamic forces they encounter. While self assembly provides a way of bottoms up fabrication, it also presents a range of fundamental scientific problems. Various researchers have explored the realm of self-assembly of spherical or spherically isotropic nanoparticles as a viable means of organizing them into useful lattice structure [10-23, 42-49]. The breath figure templated

assembly described in earlier part of the thesis is a representative example of the pursuit of perfect packing by spherical moieties.

In the present chapter, the self-assembly of rod-like gold nanoparticles is examined in the context of what drives it and how it can be characterized. The first series of questions that motivated this study are as follows: *Can colloidal gold nanorods form a lyotropic liquid crystalline phase? How can such a phase be observed and characterized? What causes nanorods to self-assemble over TEM grids? Can a mixture of rods and spheres phase separate while drying to make samples for characterization over the TEM grid?* Many of these questions were a direct consequence of effort directed to elucidate the efficiency of shape separation, for the size dispersity of rods is characterized by the observation from UV-Vis spectra or by looking at TEM images. In the TEM images collected by Kyoungweon Park and reported in literature [50-56], the nanorods seem to organized into range of patterns, including assemblies of nanorods termed as liquid crystalline [53, 54]. Driven by the idea that such an ordered phase can be characterized in terms of orientational and positional order exhibited by the rods over the TEM grid, the patterns were characterized and contrasted to theoretical predictions. The consequences of shape anisotropy and influence on other factors that control the observed behavior are examined. The drying mediated aggregation and as well as their liquid crystalline behavior prior to drying is the focus of the first part of the chapter.

Besides the assemblies on the TEM grids, drying of drops over glass slides was carried out in collaboration with Kyoungweon Park. As the drop dries out, flows within the drying droplet carry the nanorods to the contact line, where the formation of a liquid crystalline phase was observed. The pattern formation is qualitatively similar to the

formation of coffee stain when the drops of coffee dry up – though in this case, besides the single band of deposit, in certain experiments multiple bands of particles were formed, where concentric rings of the particles were separated by regions with no particles. The questions at hand here are: *What drives the formation of the deposit at the contact line? Does liquid crystalline phase form in the vicinity of the contact line? How is the behavior of rodlike particles distinct from that of spherical particles in a similar circumstance?* These questions are addressed in the latter part of the chapter, after a brief introduction to the liquid crystalline behavior of rodlike particles.

10.2 Lyotropic liquid crystals from inorganic colloidal particles

Rod-like nanoparticles are particularly interesting because anisotropy in shape provides them access to order at lower concentrations. Just like spherical colloids are considered good model systems for comparison with hard sphere fluids [57-59], rod-like nanoparticles can be thought of model systems for comparison with hard rod fluids [60, 61]. The rods are randomly aligned in an isotropic phase, on increasing concentration they demonstrate an increasing amount of long range orientation order, forming a nematic phase. This long range order of the nematic is described by a unit vector ***n***, known as the director. Assuming that the liquid crystal consists of a distribution of cylindrically symmetric rods oriented preferentially along the director, the scalar order parameter, *S*, for a three dimensional system is given by $S = \frac{1}{2}\left\langle 3\cos^2\theta - 1 \right\rangle$. Here θ is the angle between the long axis of rods and the director, ***n***. The angular brackets show that the order parameter is a statistical or ensemble average quantity. The order parameter is 0

for random orientation, and equals 1 for a perfectly parallel alignment, and typically it has a value between these limits.

The distribution function that represents the orientation of the rods in the system and the corresponding order parameter can be measured using various experimental techniques and the related anisotropic physical response measured or calculated using theory and experiments [62-64]. At still higher densities, sometimes rods organize themselves into smectic order, such that rods lie in layers, though layers themselves are no thicker than the rods, and this stratified structure possesses both higher positional and orientational order. The rods can also form a crystalline structure, and the transition from one phase to another is characterized by differences in their physical properties (manifested in textures in microscope, flow viscosity and difference in x-ray scattering, etc.) [62-64]. The approach described for understanding the self assembly of colloidal gold nanorods stems from the marriage of two exciting fields: the assembly of colloidal (spherical) particles [10-23, 42-48] and the physics of lyotropic liquid crystals [60-66].

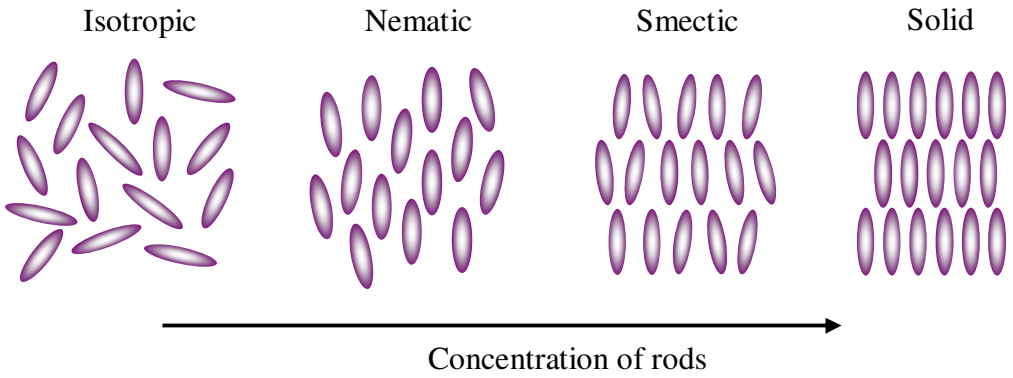

Figure 10.1 Phase transition of lyotropic liquid crystals. The orientational and positional order increases with concentration.

The liquid–crystalline properties of rod-like colloidal suspensions of vanadium pentoxide, V_2O_5, dispersed in water, were first studied by Zocher in 1925 [67, 68], who

also later (1929) discovered anisotropic phase in β-FeOOH. Later, in 1938, Langmuir reported the phase separation of suspensions of bentonite clay platelets showing an isotropic phase (I) in equilibrium with a nematic liquid-crystal phase (N) [69]. Bawden et al [70] found the nematic ordering of suspensions of Tobacco Mosaic Virus (TMV), a rod-like virus, and Onsager [71, 72] laid out a theory for describing phase behavior of hard rods. The reader may refer to recent reviews by Davidson and Gabriel [65, 73] that summarize the advances and history of lyotropic liquid crystals based on inorganic nanoparticles and mineral moieties. The synthesis and assembly of inorganic nanoparticle based liquid crystal assemblies has seen resurgent interest in last few years, mainly through seminal work by Davidson and coworkers [65, 68, 73-83] and from Lekkerkerker and collaborators [84-96]. Ever since the first reports about lyotropic phases formed by tobacco mosaic virus (TMV) appeared in 1936 [70], the major experimental studies on lyotropic liquid crystals have relied on studies with TMV and fd-virus and much of the recent work on phase behavior of viruses and mixtures of rods of different dimension or mixtures of spheres and rods has come from Fraden and coworkers [97-104].

Interestingly, Onsager [71, 72] was trying to explain the formation of anisotropic phases by TMV when he pointed out that beyond a certain concentration of rods, there is a net increase in entropy on transition from isotropic to nematic phase. While the rotational entropy is maximized by having random orientation distribution of rods, the translational entropy is maximized by having smallest free volume or largest translational motion per unit rod. At high enough concentrations, the loss in rotational entropy is more than compensated by a gain in translational entropy, due to the lower excluded volume required in a nematic phase.

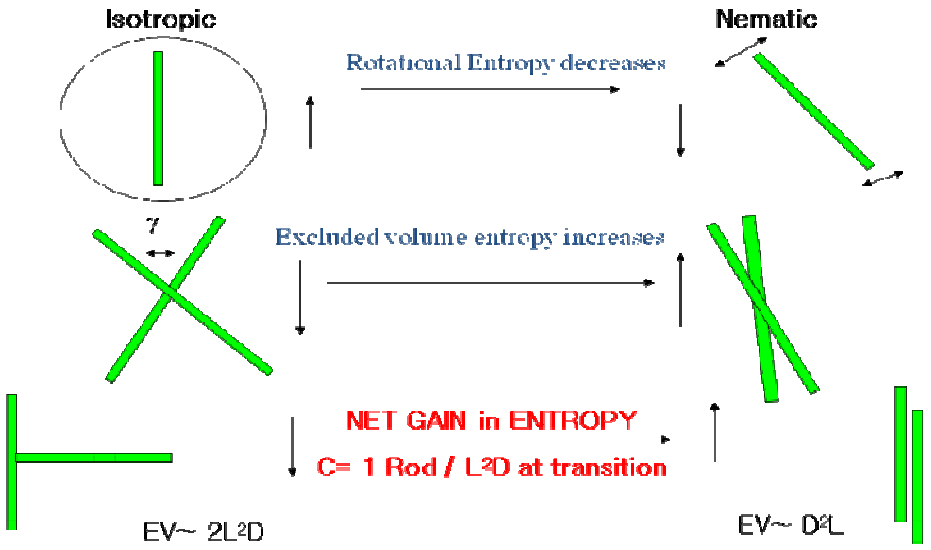

Figure 10.2 Onsager theory [71, 72]: How phase transition is driven by a net gain in entropy.

Since Onsager's theory [71, 72] is based only on two particle interaction, it is exact only for aspect ratios of hundred or higher. For lower aspect ratios generally found in rodlike nanoparticles, one must account for multi-particle interactions, and this requires extension of theory as done by Lee and Meyer [105, 106] or by the use of excellent simulations from Frenkel and coworkers [60, 61, 107-113]. The relevant extensions to Onsager's theory as applied to theoretical and experimental studies on lyotropic phases formed by colloidal particles and rod-like polymers are summarized in reviews (e. g. [66]) and books [62-64]. Suitable theoretical predictions and examples from viruses are included to outline the aspects of self assembly that can be observed and anticipated for rodlike nanoparticles.

10.3 Liquid Crystalline behavior of spherocylinders

In the present study, only the rodlike nanoparticles that can be approximated as spherocylinders are considered. The aspect ratio of spherocylinders is described in terms

of (*L/D*), implying a sphere has *L/D* = 1. Further the examples considered are limited to particles with *L/D* < 20 and *L* ~ 100 nm, ensuring that even for metallic particles, the particles considered are Brownian (see previous chapter for discussion). Most of the nanoparticles are stabilized by the presence of charge or steric hindrance. Presence of charge results in an extra interaction term, which can be accounted for by using an effective diameter, D_{eff}, where D_{eff} is dependent on the Debye screening length, κ^{-1} [66, 71]. Additionally the presence of charge leads to an orientation dependent potential, which acts to misalign the particles and its magnitude is characterized by a twist parameter , $h = \kappa^{-1} / D_{eff}$. If h > 1.33, the nematic phase ceases to exist, or in other words, the behavior of charged rods is richer than that of hard rods, and this must be born in mind, when the experimental results from dispersed gold nanorods are compared to the theoretical results.

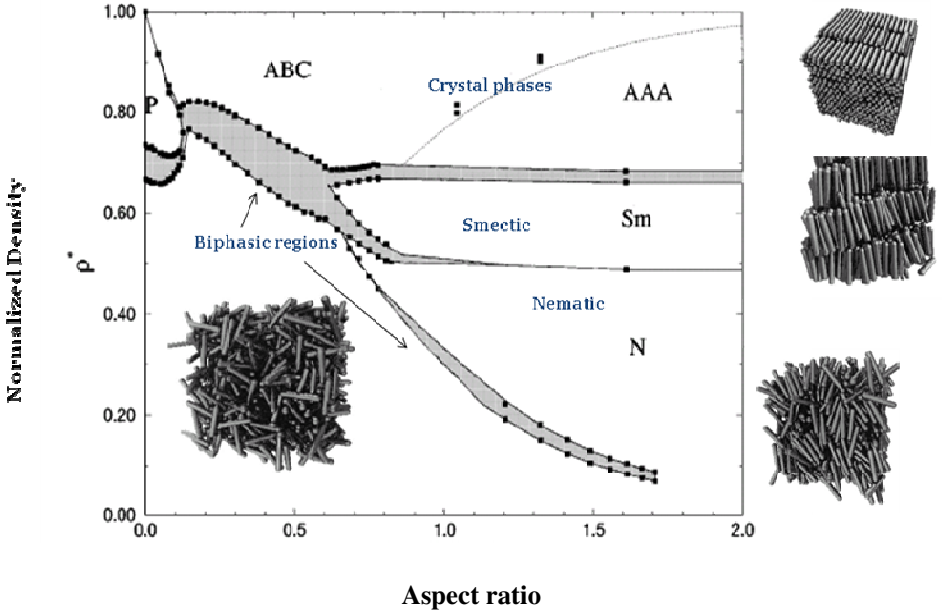

Figure 10.3 Phase diagram for spherocylinders, as computed by Bohlius and Frenkel [112].

For the lower aspect ratios that concern us here, the phase diagram for spherocylinders was obtained by Frenkel and coworkers [60, 61, 107, 110-113] for both two dimensional and three dimensional systems for hard spherocylinders. Bohlius and Frenkel [112] mapped out the phase diagram for the spherocylinders, showing how it depends on the density as well as the aspect ratio of the constituent particles, as shown in Figure 10.3. The density here is normalized in terms of the close packed density, which is given by $\rho_{cp} = 2/(\sqrt{2} + ((L-D)/D)\sqrt{3})$ and depends upon the aspect ratio of the rods. Their computation indicates that while hard ellipsoidal particles do not form a smectic phase, the spherocylinders can form a stable smectic phase for *L/D* ~ 3.1. The subtle difference in particle shape, dimensions and concentrations, apparently translate to different phases, making phase behavior of rods quite different from that of ellipsoids [108] or platelets [84-88].

10.4 Coffee ring-like pattern formation with rodlike particles

The as-made dispersion of gold nanorod produced by seed mediated method is extremely dilute and must be concentrated to observe the liquid crystal phase. We rationalized that the concentrated phase can be reached by evaporating a drop of aqueous dispersion or by emulating the process by which drop of coffee dries to form a ring-like deposit of the dried powder. The mechanism by which coffee ring forms is as an example of colloidal self assembly and has been studied extensively [7-9, 114, 115] for spherical particles, see Figure 10.4 (a) for example. Similar ring forms when a dispersion of gold nanorods is dried over a glass substrate, as observed in Figure 10.4 (b).

a) b)

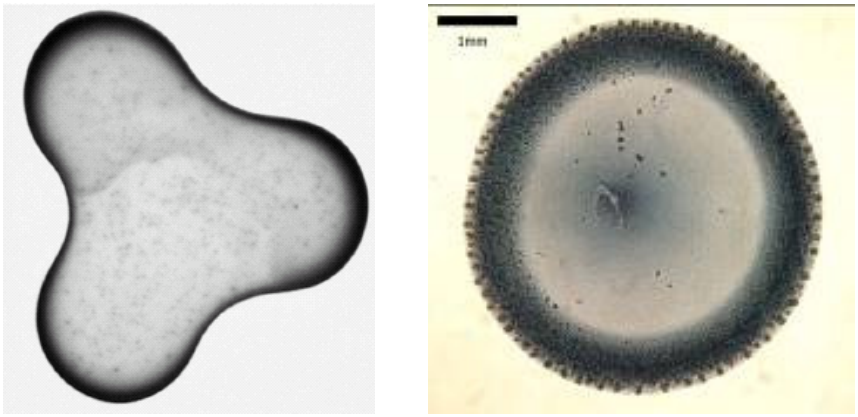

Figure 10.4 (**a**) Coffee stain (2 mm in diameter) [7-9] and (**b**) dried colloidal gold NRs [116, 117], where the scale bar is 1 mm.

According to Deegan et al [7-9], when a drop of coffee starts to evaporate on a solid substrate, the presence of spherical coffee powder particles pins the contact line, and for this geometry, the evaporative flux is highest at the edge as shown in the Figure 10.5. Due to evaporation, the particles in the edge become depleted of the fluid, and their interstices act as capillaries that drive a strong outward, radial flow that carries nearly all the solute to the edge. The velocity of the flow is dictated by evaporation rate, which is diffusion limited, as the evaporated vapor must be removed from the top of the fluid.

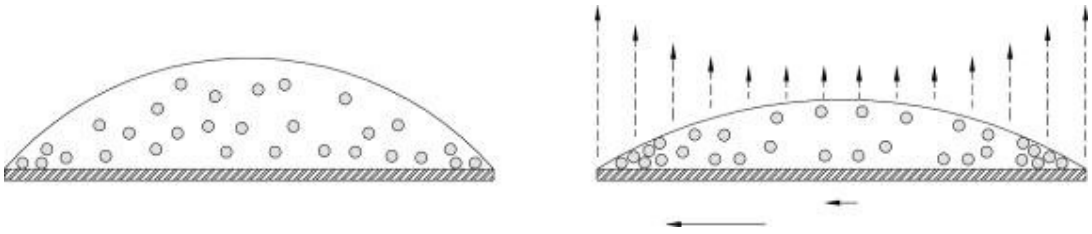

Figure 10.5 Mechanism of coffee ring formation: (**a**) Sessile drop containing homogeneous dispersion of nanoparticles. (**b**) The evaporating drop, with pinned contact line i.e. same drop radius, though height decreases. The evaporation flux (vertical arrows) is maximum at the edges, which drives the flow of particles towards the edge. The flow becomes stronger radially outwards (horizontal arrows). (The particles and drops are not to scale.) (Adapted from ref. [8])

Since the concentration increases as particles approach the edge, and liquid crystal phase forms beyond a certain concentration of rods (that depends upon the aspect ratio, among other things), we determined that the ring formation will be accompanied by formation of liquid crystalline phase. The liquid crystalline phase can be simply observed by using polarized light microscopy, for the liquid crystalline phases are birefringent and exhibit characteristic textures that are used for identifying them (in conjunction with other techniques). The quantitative theory or simulation based on these ideas remains an open question, and for the present, we will describe the experimental results, with phenomenological arguments about their origin.

As a drop of colloidal gold nanorods is dried, formation of a highly birefringent deposit is observed under crossed polarizers on a polarized optical microscope. For a dispersion containing mainly nanorods with the aspect ratio larger than 4, the formation of rings is preceded by appearance of highly birefringent domains that are about about 3-4 μm in size, that appear to move towards the edge as shown in Figure 10.6.

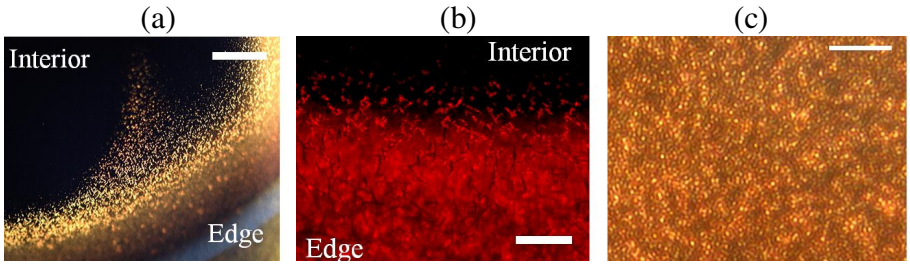

Figure 10.6 The images of a drop of colloidal dispersion of gold nanorods during evaporation under optical microscope with cross polarizers, as described in the text. (**a**) Emerging liquid crystal domain from the interior and moving toward the edge. (**b**) Magnified image showing the individual domain joins the existing structure. (**c**) The assembly of liquid crystal domains. The scale bar is 200 μm for (**a**) and 20 μm for (**b**) and (**c**) [116, 117].

Certainly, the drying and densification drives the system into the bistable region and the spontaneous phase separation creates these domains of liquid crystals. We see

that these domains exhibit the characteristic birefringence and fluidity of liquid crystals drops, and keep sparkling until the drying is completed. The sparkling is a consequence of fluctuations in the director field that are caused simply by the thermal fluctuation within these drops or domains. The domain size can be determined by minimization of free energy, where the surface tension term tries to minimize the surface area while the confinement of rods is opposed by a volume free energy term that has contribution from an elastic term (estimated from Frank's constants, using theory of Lee and Meyer [105, 106]). The minimization of free energy for a spherical shape is quite similar to the calculation of critical nuclei described in the chapter on nucleation and growth of water drops. The typical values of Frank's constants and the estimated surface tensions for these gold nanorods give a domain size of few microns as observed. The domains in this case are non-spherical, called tactoids, and their specific size and shape depends upon the aspect ratio of the constituent nanorods.

The width of this highly birefringent increases inwards as a function of time, as shown in Figure 10.7. A drop of 2 μL takes 11 minutes to evaporate completely. The highly birefringent edge only appears after 3min. The evaporation at the edge drive flow within the drops carrying more and more solute towards the edge. While these processes continue, the supply of fluid to the outer limits of the birefringent band becomes insignificant, and a distinct color change distingues the outer, drier part from the inner region. The presence of fluid lends a different optical path to the observed radiation. The observed color depends upon both the size and the aspect ratio of the rods as well as the dielectric environment around the rods, as was described in the previous chapters.

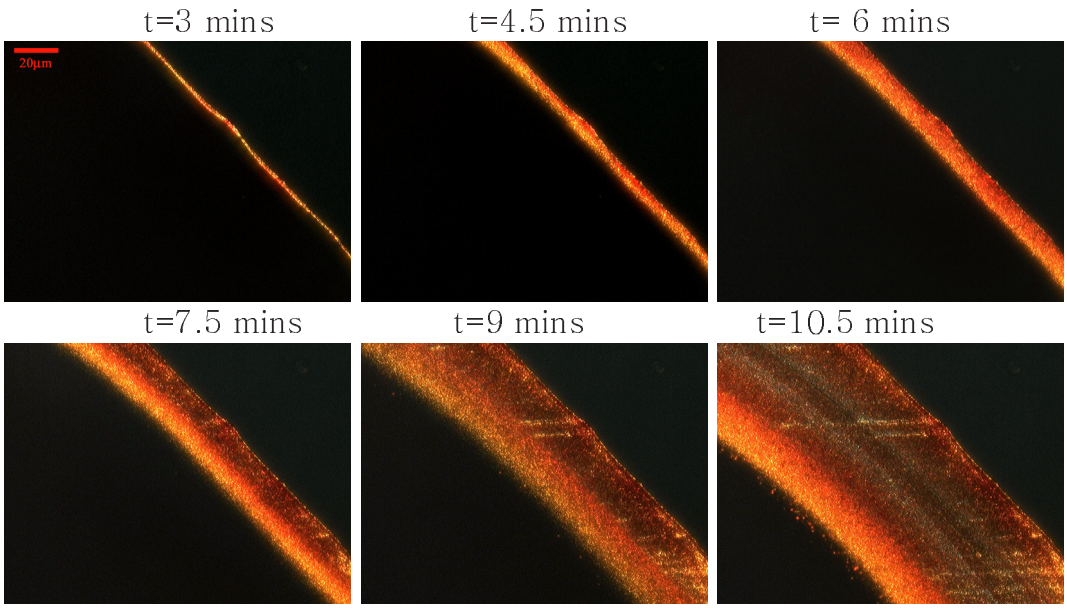

Figure 10.7 The images of the drop of gold NRs sol during evaporation under optical microscope with cross polarizers [116, 117]. In this series of images the center of the drop is in the bottom left corner. The scale bar is 20 µm.

When the a drop containing gold nanorods with aspect ratio less than 4 is evaporated, the ring depositing near the contact line is not birefringent, though the birefringence from the surfactant crystal appears after water evaporates completely, as shown in Figure 10.8. As predicted by the simulations of Bohlius and Frenkel [112], the liquid crystalline phase is expected to form only beyond a certain aspect ratio (~3 from their simulations on hard rods). Since the colloidal dispersion of rods contains a large amount of surfactant, the phase transitions for the gold nanorods may correspond to an effective aspect ratio (where diameter, D_{eff} is different from the real diameter D). But the non-existence of liquid crystalline phase below a certain concentration is qualitatively in agreement with theoretical predictions.

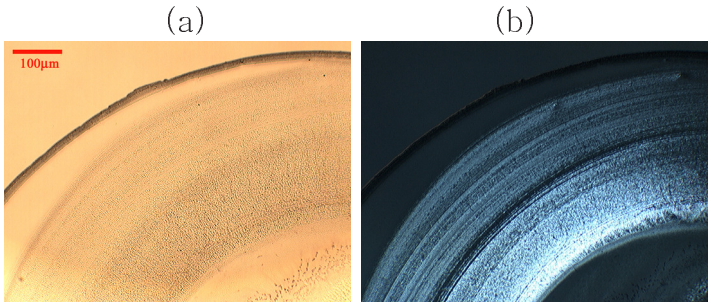

Figure 10.8 (**a**) Bright field image of the drop of gold NR, aspect ratio of 3. Ring formed at the edge of (**b**) image with crossed polarizers. Birefringence is from the surfactant crystals, observed after evaporation is completed [116, 117]. Scale bar is 100 µm.

It was shown in the studies by Deegan [7-9] and Popov [114, 115] that the flow within the drying drop of coffee is a result of the capillary pressure which depends upon the packing fraction (Darcy's law), and hence the shape of the particles. While the qualitative features of ring formation in rods are similar to their coffee stain problem [7-9], since the maximum packing fraction, ρ_{cp} is different for the rods, the capillary pressure and the flux inside the drop must be different from that for spheres. In principle, by using Darcy's law, one can compute the capillary pressure and by computing the diffusion limited evaporation, one can also determine the corresponding flow field within the drop, as well as how the concentration of rods at any location changes as a function of time. The problem is decidedly more complex than the corresponding case of spherical particles, and at this point, is left as a challenge for future work.

10.5 Concentric birefringent bands on glass-slide: Liesegang ring like patterns

Apart from the single birefringent band that appears in certain cases, as described above, we find that certain drops form multiple bands or rings on evaporation. The evaporation conditions and the concentration and aspect ratio of nanorods dispersed in

the droplets was varied to determine the conditions that lead to the formation of these multiple rings. Figure 10.9 shows the deposits resulting from dried drops of different initial volume fraction of gold NRs (aspect ratio 6). For each image, a drop of 2µl gold NR sol was deposited on the glass slide. Drops of size ~ 3mm in diameter formed on the substrate.

The upper row in Figure 10.9 shows the images of dried deposits formed from the slow evaporation, accomplished by keeping the evaporating drop in a closed environment. Under these conditions, it takes 1hr for the drop to be completely dried. Regardless of the volume fraction of the solute in the drop, a single ring/band forms at the contact line, though the width of the band decreases as the volume fraction of nanorods decreases. The bottom row in Figure 10.9 shows the images of dried deposits formed during fast evaporation (about 11mins), accomplished by placing the drop in open environment. In (f) there is a dark ring formed at the edge. As the volume fraction decreases, we observed concentric multiple ring formed interior of this ring while the width of the ring also slightly decreased (g, h and i). Upon decreasing the concentration further, very thin ring was formed without additional rings inside (h).

The higher magnification images of the region near the contact line, taken under cross polarizers, during the evaporation process is shown in Figure 10.10. When the evaporation is carried out in a closed environment, the evaporation proceeds such that the color change representative of complete drying of particles does not start till a thick band of deposit already forms close to the edge. In open environment, where the evaporation is faster and the process is completed in nearly one-sixth of the time, the deposit at the edge seems to dry out quicker, and at the same time, a concentric ring

develops within the drop. This process is observed till a number of rings form in the system.

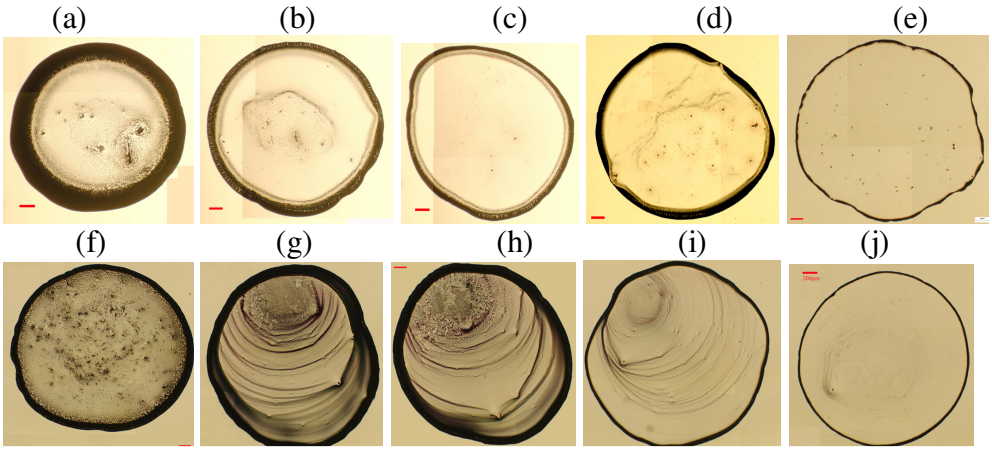

Figure 10.9 "Coffee stain" formed by drying drops of gold NR sol. The images in the upper row show the drying drops from slow evaporation. The volume fraction decreases from left to right (**a**) 1×10^{-5}, (**b**) 5×10^{-6}, (**c**) 3.3×10^{-6} (**d**) 2.5×10^{-6} and (**f**) 1.25×10^{-6}. The images in the bottom row are from fast evaporation. The volume fraction of the drops in the same column is identical. The scale bar is 200µm [116, 117].

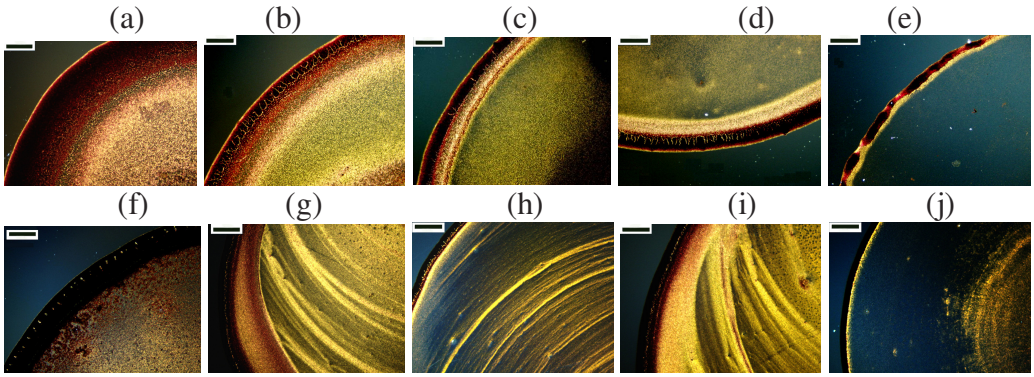

Figure 10.10 The patterns formed by various concentrations and different evaporation condition were visualized by polarized optical microscopy. The figure number used is same for the corresponding image shown in Figure 10.9. The scale bar is 200µm [116, 117].

Other instances where such concentric rings have been reported include formation of the Liesegang rings [118-123], multi-rings for latex particles observed by Stone et al [124], concentric rings obtained by Maeda et al [125] by evaporating collagen solution

droplets, and multi-rings in polymers and polyelectrolytes [126-133]. In the experimental study by Stone et al [124], it was shown that the formation of multi-rings is more likely for dilute sols of latex particles and for large size drops. They rationalized their observations by stating that the contact line can move inwards till it encounters the next pinning sites. The ability to form multi-rings is therefore controlled by the interplay of depinning and pinning of contact line; due to high evaporation rate at the edge the depinning can take place and the contact line moves till it encounters the next set of pinned particles. This is similar to the observations made by Deegan in his experiments [7].

Starting from initial studies of Liesegang from 1896, Liesegang rings have been seen for more than a hundred years in reaction-diffusion systems [119-123], where periodic precipitate form in the wake of a reaction front. Ostwald advanced an explanation for formation of Liesegang rings which are bands or rings formed in a reaction diffusion system, where typically precipitation reaction is introduced into a homogeneous solution or gel, by diffusion of a second species. According to Ostwald, the phenomenon is a result of interplay of discontinuous nucleation and supersaturation affected by local concentration gradients [118]. In the typical systems studied thereafter, one of the reactants is dispersed in a gel, as other reactant is added, it propagates through diffusive flux. The reaction causes a local depletion of reaction, and this leads to concentric rings of precipitates, as shown schematically in Figure 10.11. The spacing and width of Liesegang rings follows simple scaling laws, (for example the position of n^{th} band x_n scales as $t_n^{0.5}$ and the width w_n increases as x_n) and have been described or modeled quite successfully by various researchers in the past [118-123].

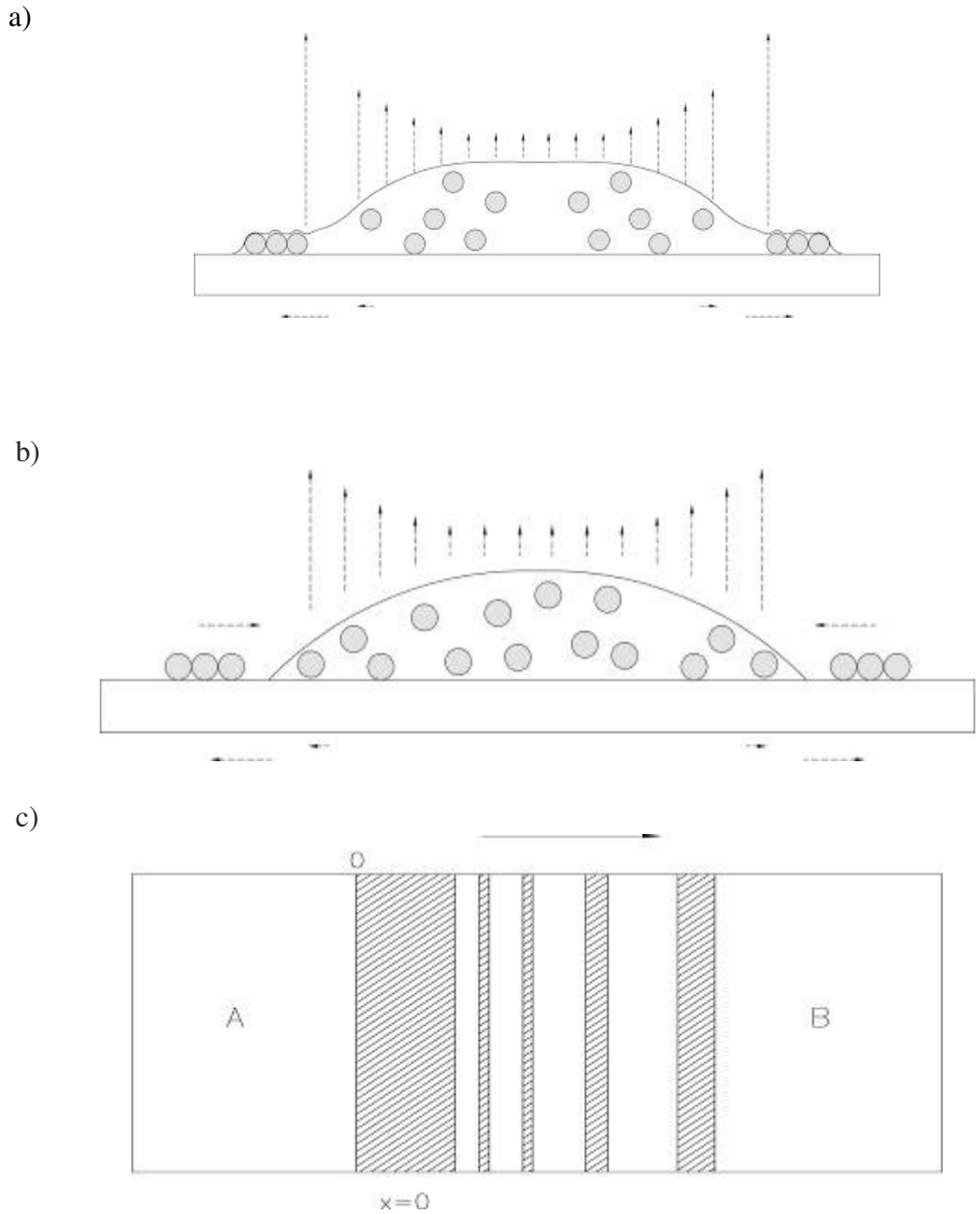

Figure 10.11 (**a**) Schematic illustrating how nanoparticles accumulate at the contact line when the rate of evaporation is slow (akin to coffee ring mechanism). Most of the particles are carried to the edge and form a single dark ring. (**b**) The case of fast evaporation: Contact line recedes, till it encounters next set of pinned particles. (**c**) Schematic illustrating how Liesegang rings form when two species A moves into initially uniform concentration of B, forming dark precipitates with location and width given by characteristic scaling laws (see text for details).

Unlike Liesegang rings, where diffusive flux competes with propagating reaction front and precipitation, the dominant transport in this system is through convective flow. The transition to the liquid crystal can be thought of like the precipitation reaction, and in close analogy, once the concentration levels reach the metastable regime, spontaneous nucleation and growth of liquid crystalline phase occurs. This can lead to local depletion zone and allow a similar formation of concentric bands. But from our preliminary data, the spacing between the bands as well as the width of the bands does not seem to follow the scaling behavior observed in the case of the Liesegang rings. Figure 10.18 shows a well defined concentric multiple ring pattern. The distance between the contact lines as well as the time between pinning and sticking events do not show any periodicity. Therefore the motion of the contact line cannot be described as a simple sinusoidal response [125] or through reaction-diffusion models typically used for Liesegang rings [118-123]. It is believed that with precise control of the drop size, roughness of the substrate and evaporation condition, one might obtain better data to conduct more systematic analysis of the multiple ring patterns.

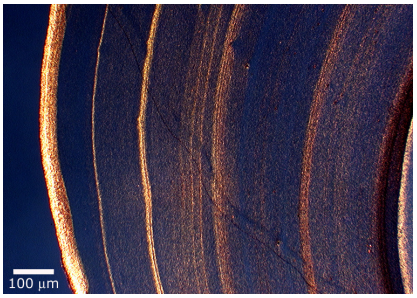

Figure 10.12 The well defined concentric multiple ring pattern formed by evaporation of dilute gold nanorod sol. Image taken under optical microscope with cross polarizers. The scale bar is 100 µm [116, 117].

The question of what really controls the pattern formation and the kinetics of phase transition requires further experimental study and theoretical analysis. So only a

phenomenological explanation is offered here. Essentially, the presence of particles can pin the contact line, and the more the number of particles, i.e. higher the concentration, better the pinning. The capillary action is controlled by the packing fraction. Hence one can expect that the higher initial concentration causes a stronger flow, and results in transfer of all the solute to the contact line. On the other hand, at the lower concentration of solute, the velocity reached is not high enough to ensure that all particles reach the edge before drying complicates the process. If drying weakens the flow, the particles can get pinned at some distance away from the first band. Thus this interplay of capillary flux, diffusive flux towards emerging domains (due to phase transition) and pinning-depinning cause multiple rings to form. The phenomenon will be described and understood better if an elaborate study of the pattern formation for a range of aspect ratios, drop sizes, evaporation rates and surfactant concentration is carried out. The reason why surfactant concentration can play a role is: 1) it alters the surface tension, changing the contact angles and 2) presence of surfactant induces Marangoni stresses that can alter the flow terms [134-136]. Several of the unsolved problems for our research are relevant to the coffee ring type assemblies and multi-ring patterns observed in colloids [7-9], polymers and polyelectrolytes [126-133], collagen [137], porphyrin dyes [138] and have received recent attention, though, as far as we know, corresponding pattern formation has not been studied in a quantitative fashion for rodlike particles. It is hoped that this description of the observations will provide the inspiration for in-depth study of the same.

10.6 Self Assembly on TEM grids

The formation of the ring patterns indicates that this capillary flow driven assembly can self-organize and order the nanorods. While the formation of micron size domains can be observed in an optical microscope, the resolution to the scale of nanorods is not possible. We decided to examine the self-assembled nanorods in transmission electron microscopy (TEM). Since the patterns formed over the glass slides cannot be used in TEM studies, we evaporated drops of 1μl sol of gold nanorods on the carbon coated copper TEM grids. While the self-assembly is still controlled by drying mediated fluxes, the physical properties including surface roughness, contact angle, etc. of the grid are quite different from the surface condition of the glass slide. Yet we can observe the orientational and positional order of the pattern formed on the same TEM grid by characterizing the location and orientation of individual rods. Thus we can contrast the role played by the initial concentration and size of gold nanorods and the influence of different evaporation condition. In the following sub-sections, some such observations are outlined.

10.6.1 Two dimensional phase transitions observed in self assembly on a TEM

When an extremely dilute dispersion of gold nanorods is dried over the TEM grid, the nanorods can deposit a monolayer, within which the position and orientation of each rod can be assessed using image analysis. In what follows, the characteristics of observed patterns are summarized, and then qualitative arguments are advanced to explain their formation. For aspect ratio of 6, at low number density, 2 to 4 NRs form aggregates and are dispersed in an isotropic state, as seen in Figure 10.13. As the number density increases, nanorods start to form a monolayer of nematic-like phase.

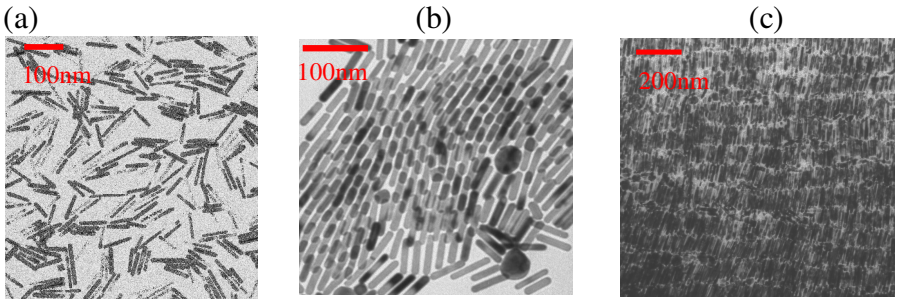

Figure 10.13 TEM images of gold NRs assembly. Aspect ratio is 6. (**a**) isotropic phase (**b**) nematic-like assembly (**c**) smectic-like assembly [116, 117].

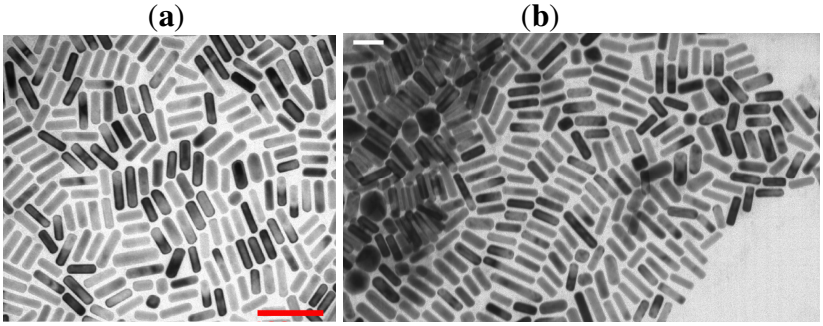

Figure 10.14 TEM images of gold NRs assembly. The aspect ratio is 3. (**a**) isotropic phase (**b**) transition from isotropic to smectic like assembly [116, 117].

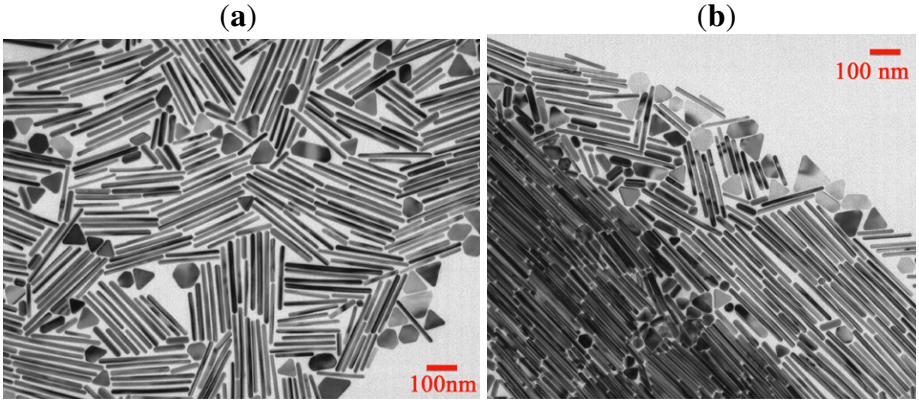

Figure 10.15 TEM images of gold NRs assembly. The aspect ratio is 14. (**a**) isotropic phase (**b**) nematic like assembly [116, 117].

With further increase of number density, nanorods form a multilayer of smectic-like phase. For short nanorods (aspect ratio is 3), the smectic-like assembly showing both orientational and positional order was observed Figure 10.14. The ordered assembly was observed for the very long NRs (aspect ratio is 14), as seen in Figure 10.15. In this case,

even though the suspension contains some of the spherical byproducts, phase transition from isotropic to nematic-like and smectic-like phase can be confirmed by the self assembly of dried suspension, as seen in Figure 10.13.

Several groups have reported such nematic-like and smectic-like assemblies for gold nanorods [51, 52, 54, 139, 140] as well as other rodlike nanoparticles [141-147]. But when only a layer of nanorods is found on the grid, as observed in Figure 10.4-6, the pattern formation, and in this case, possible phase change occurs in a thin region, implying that *the assembly process is two dimensional rather than three dimensional*. The order parameter, as well as phase diagram depends upon the dimensionality of the program. In this case, the angle between the director and the long axis of each rod can be measured and the formula for 2-dimensional order parameter is $S = \langle \cos 2\theta \rangle$. The order parameter for the nematic-like phase in Figure 10.13 (b) is 0.58, while the value obtained for the smectic-like phase is 0.97. The absolute number of particles selected for the calculation changes the order parameter. Likewise, if the order parameter is calculated using TEM images from Kim et al [144] who studied phase behavior of $BaCrO_4$, or from rods of aspect ratio 2 studied by Jana [51], the order parameter for smectic-like phase is over 0.90. Again, the order parameter is dependent on the number of particles included in averaging. Thus, while the visual observation suggests that the phase is ordered, the crucial question that must be asked is, how can one ascertain that ordered arrays of rodlike particles represent a liquid crystalline phase?

Bates and Frenkel [110] studied two-dimensional hard rod fluids consisting of spherocylinders confined to lie in a plane using Monte Carlo simulations. For long rods, a 2D nematic phase is observed at high density and the transition from this phase to the

low density isotropic phase is continuous. For short rods, the nematic phase disappears so that, the solid phase (which is akin to both smectic and crystal phase) undergoes a first order transition directly to an isotropic phase. In this respect, according to Bates and Frenkel [110], the order parameter is dependent on the size of the system, and the characteristic feature of 2-D system is absence of a true long range order. The order parameter depends both on density of rods and on the system size. By determining the order parameter as a function of system size, one can compare it with the prediction that $S \sim N^{-k_B T / 2\pi K}$, where N is the number of particles and K is the Franck's constant of elasticity. [110] Since a realistic comparison will require a system size with nearly 7,000 particles (as was used in simulation), we were not able to compute these statistics, though in future, if extended assembly of nanorods is found, it will be a worthwhile experiment to examine this behavior.

10.6.2 Heterogeneity and polydispersity of the sample

As-made sol is typically a mixture of rodlike and spherical particles. When as-made sol is evaporated 'slowly' on the TEM, shape selective assembly or micro phase separation of different shapes is seen to occur. Nanorods and spherical particles assemblies form separate clusters on the TEM grid, as shown in Figure 10.16. In the case of faster evaporation, the particles of different shape are kinetically trapped into a mixture as seen in Figure 10.16 (b). Such phenomenon is extensively studied theoretically and has also been confirmed by simulations [148].

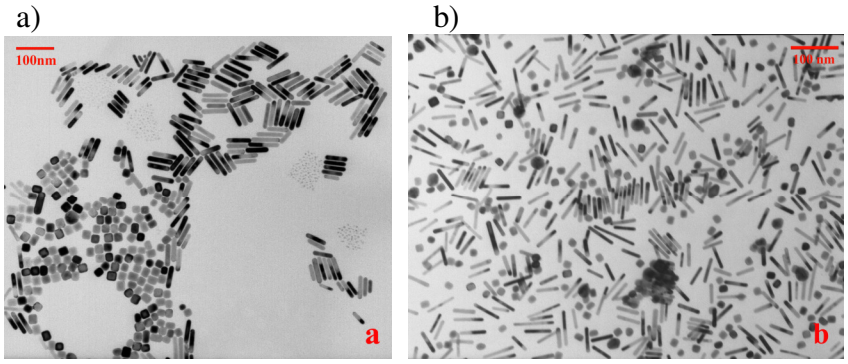

Figure 10.16 TEM image of self assembly of as-made sol with (a) slower evaporation and (b) faster evaporation. The coverage of particle in both images is about 20% [116, 117].

Figure 10.17 shows another example showing micro phase separation of 3 different shapes of nanoparticles (nanorods, nanospheres and nanocubes). The shape separation not only leads to locally purer, low polydispersity samples, but can provide domains with high amount of order. While it is well known that polydispersity prevents long range positional ordering [65], on a TEM grid, the lack of long range order could be a consequence of 2-D liquid crystal phase, as discussed before. Several reports on self assembly of gold nanorods [52, 55, 140] focused on patterns formed in a small domain, and concluded that the concentration and pH of the dispersion determine the properties of self assembly. Given the non-equilibrium nature of assembly on TEM grids, the comparisons with patterns expected from equilibrium cannot explain the range of patterns obtained. For example, even if the dispersion has rods of a given aspect ratio in a known concentration to begin with, factors like whether evaporation is homogeneous and heterogeneous, determine the patterns formed by rods before solvent evaporates away, as described in next section. Nearly a hundred years back, Perrin [149, 150] saw two dimensional packing of spherical colloidal particles and reasoned that capillary forces can make particles organize into a close packed structure. The role of capillary forces [24,

151, 152], quantified as immersion forces for partially submerged particles, and floatation forces for particles on air-solvent interface, is being actively investigated for spherical systems, and was discussed briefly in chapter 6. In principle, the origin of forces will be similar for rods, but the shape anisotropy will change the directional nature of the forces.

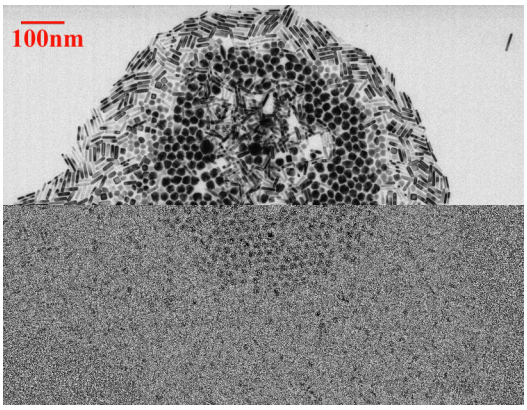

Figure 10.17 TEM image of self assembly of as-made sol showing micro phase separation of 3 different shapes of nanoparticles [116, 117].

Lastly, Bates and Frenkel [111] used Monte Carlo simulations to show that the increasing polydispersity in length of particles destabilizes the smectic phase, making it almost non-existent beyond a polydispersity of 0.18 (as measured by standard deviation in length). The existence of smectic-like phase as well as the uniformity of size constituent rods assembled on the TEM grid indicates that the centrifugation assisted separation helps us to obtain low polydispersity dispersions. Purdy et al [101] have shown that a mixture of thick and thin colloidal rods has a rich phase behavior and Fraden and coworkers [97, 104] have also studied (for three-dimensional case) how the addition of spheres can alter the concentration at which liquid crystalline phase occurs and how it can create a layered smectic phase. While a layered smectic phase (with row of spheres stacked within rows of rods) has not been observed, the phase separation

between particles of different shapes is observed quite often, and might form a good system for comparison with studies on viruses. In any observations made on the TEM, the observation of low polydispersity in the size and "shape" of as-made nanoparticles can sometimes be an effect or artifact of phase separation, rather than due to efficient synthesis method. If one is aware of the phase diagram, one can relate observed patterns to the nanoparticle dimensions, or at least ensure that one is not misguided from observations from one region of the TEM grid.

10.6.3 Patterns formed by evaporation

Rabani, et al [10] modeled the drying mediated self assembly in spherical particles by accounting for pinning, diffusion and solvent assisted aggregation. The equilibrium and non-equilibrium patterns were found to correspond very well to the experimentally observed patterns for spherical CdSe particles. The case of homogeneous evaporation provides patterns expected from coarsening behavior, for example the phase separated domains can exhibit self-similar growth as expected for systems undergoing spinodal decomposition. In heterogeneous evaporation, the local concentration and solvent fluctuations produce patterns that are consequence of both thermodynamic and kinetic effects. The rate of drying and the timescale for particle diffusion become important parameters in determining the outcome for the drying dispersion. Similar patterns have been observed by us in the assemblies on TEM grids for gold nanorods, though in absence of similar simulations or theory for rodlike particles, our inferences about their thermodynamic or kinetic origin are at best intuitive or speculative.

Figure 10.18 shows the patterns taken from the center area of a single TEM grid. The aspect ratio of NRs is 5. At very low coverage (less than 5%) ribbon-like aggregates of nanoparticles dominate the self-assembly (Figure 10.18 (a)). As the coverage increases, Figure 10.9 (b), disk-like aggregates of nanoparticles dominate the self-assembly. At still higher coverage or particle density, the clusters are interconnected. These patterns are quite similar to the aggregates formed by water drops, as described in chapter 5. We observed similar patterns in the nanorod suspensions with aspect ratio 3 to 6. The dynamics of nanoparticle assembly must be modulated here by interparticle attractive forces, phase separation kinetics and by drying induced solvent fluxes, though the role of these factors is unclear for we only see, (if we may say so) the fossil and not the beast, on a TEM grid. Further, the aggregates thus formed could simply result from a diffusion-limited aggregation [41, 153], where the aggregate structure is rather insensitive to interparticle interactions. For example, such aggregates formed by colloidal gold sols (~15 nm spherical particles) have been characterized by describing them as fractals [154-156]. The use of similar structure analysis can be applied to patterns formed here, and it is likely to be useful in describing optical and transport properties of such self-assembled structures. The excellent text by Meakin [41] provides a detailed discussion on fractals, diffusion-limited aggregation and pattern formation.

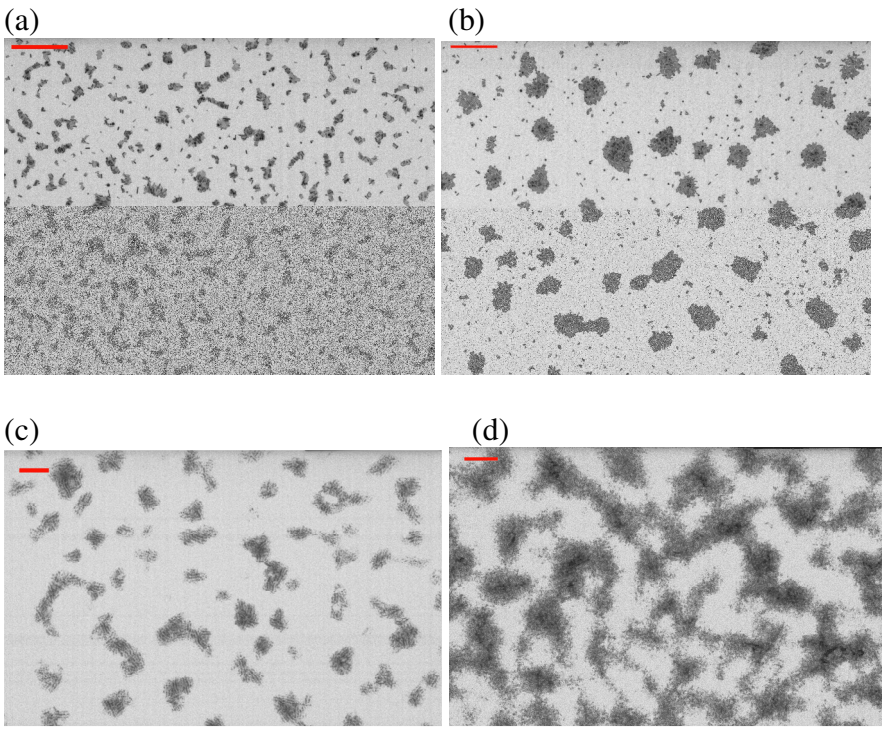

Figure 10.18 The TEM images showing different patterns formed at different coverage ratio of (**a**) 4% (**b**) 10% (**c**) 15% and (**d**) 40%. The aspect ratio is 5 and the scale bar is 1 µm [116, 117].

The drying of gold nanorod suspensions can sometimes yield interesting ring patterns as shown in Figure 10.19. These patterns were observed when the coverage was between 10 to 20% and they occur in the region between the center and the edge of the drop on TEM grid. The ring patterns were formed by various aspect ratio of gold NRs (aspect ratio 4 to 7). The shape of the ring is very close to a perfect circle and the size of the ring ranges from 200nm (the diameter of the hole) to 1µm and does not seem to depend on the aspect ratio of gold nanorods. Interestingly many rings were found to lie in a straight line and are not only similar in size, but also in the distance that separates them.

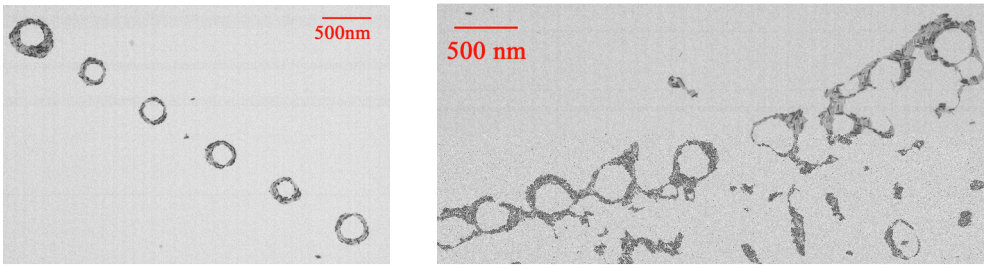

Figure 10.19 Ring-like array observed when the coverage is 10 to 20%. a) Aspect ratio 4, b) Aspect ratio 6 [116, 117].

The formation of such rings on TEM grids has been reported before by Ohara et al [157], for a dispersion of 2.5 nm silver nanoparticles coated with dodecanethiol and dispersed in hexane. The scenario in this case is quite different from the coffee ring mechanism [7-9] that operates in sessile drops, where capillary driven outward flow is said to drive the particles to the edge, as discussed before. In this case [157], the authors postulated that for a wetting fluid, the solvent evaporates as a thin film, and so the hole that opens up pins the contact line, and as the hole advances outwards, it pushes particles outwards. Unlike the case studied by Deegan and coworkers [7-9], here the pinning is not automatic, and it is dependent on the particle-substrate interaction as well as particle size. The theoretical arguments of Ohara et al [157] suggest that the ring sizes should be same for a given concentration of nanoparticles, as observed in Figure 10.19. The efforts to draw any reliable correlations of ring size with particle size or aspect ratio were unsuccessful but it is expected that the role of shape anisotropy and particle-substrate interaction in controlling the pattern formation can be deciphered by conduction controlled experiments, where evaporation rate and saturation conditions around the drop are montinored.

10.7 Conclusions and outlook

The colloidal drop of nanorods can dry to form a single band pattern similar to coffee ring systems studied extensively for spherical nanoparticles. In this case, as the region near the contact line becomes concentrated, a phase transition to liquid crystallinity occurs and micron size, liquid crystalline domains are created near the contact line. Further a multi-ring assembly, containing concentric bands of deposits forms for lower concentration dispersions. The multi-ring assembly was compared to Liesegang ring like patterns and it was determined that the ring locations and widths do not follow algebraic relationships typical for Liesegang rings. The multiple bands appear to form by a pinning-depinning mechanism, which is favored when the number of particles is not large enough to be driven to the periphery.

The self assembly of rodlike particles observed on TEM grids is described as a consequence of drying mediated aggregation, and it is pointed out that the visual appearance of an ordered nematic-like or smectic-like phase may not imply that actual phase transition occurred from an isotropic phase to liquid crystalline phase before the drop was dried. It was pointed out that the phase behavior over a TEM grid should be compared to two dimensional liquid crystalline phases rather than three dimensional phases. Further, a range of examples show that the apparent monodispersity of nanorods or purity of sample observed on TEM grid could be a consequence of phase separation of particles of different shape. At the same time, the existence of transient liquid crystalline domains in drops dried on glass slides indicates that colloidal gold nanorods beyond aspect ratio of four do exhibit the liquid crystalline behavior and the shape separation (and synthesis) provide us rods with low degree of polydispersity. The quantitative

comparisons with phase diagrams for short spherocylinders requires a theory of capillary-driven flow in evaporating drops containing rodlike particles, and experimental and theoretical determination of concentration at which the liquid crystalline domains appear in the drying drops.

10.8 References

1. Emerson, R.W., *Representative Men: Seven Lectures*. 1903, Boston: Houghton, Mifflin and Co.

2. Whitesides, G.M., J.P. Mathias, and C.T. Seto, *Molecular self-assembly and nanochemistry - a chemical strategy for the synthesis of nanostructures.* Science, 1991. **254**(5036): p. 1312-1319.

3. Whitesides, G.M. and B. Grzybowski, *Self-assembly at all scales.* Science, 2002. **295**(5564): p. 2418-2421.

4. Bowden, N., et al., *Self-assembly of mesoscale objects into ordered two-dimensional arrays.* Science, 1997. **276**(5310): p. 233-235.

5. Parviz, B.A., D. Ryan, and G.M. Whitesides, *Using self-assembly for the fabrication of nano-scale electronic and photonic devices.* Ieee Transactions on Advanced Packaging, 2003. **26**(3): p. 233-241.

6. Ball, P., *The Self-Made Tapestry: Pattern Formation in Nature*. 1999, New York.

7. Deegan, R.D., *Pattern formation in drying drops.* Physical Review E, 2000. **61**(1): p. 475-485.

8. Deegan, R.D., et al., *Capillary flow as the cause of ring stains from dried liquid drops.* Nature, 1997. **389**(6653): p. 827-829.

9. Deegan, R.D., et al., *Contact line deposits in an evaporating drop.* Physical Review E, 2000. **62**(1): p. 756-765.

10. Rabani, E., et al., *Drying-mediated self-assembly of nanoparticles.* Nature, 2003. **426**(6964): p. 271-274.

11. Pieranski, P., *Colloidal crystals.* Contemporary Physics, 1983. **24**(1): p. 25-73.

12. Pieranski, P., *Two dimensional interfacial colloidal crystals.* Physical Review Letters, 1980. **45**(7): p. 569-572.

13. Pieranski, P., L. Strzelecki, and B. Pansu, *Thin colloidal crystals.* Physical Review Letters, 1983. **50**(12): p. 900-903.

14. Denkov, N.D., et al., *Mechanism of formation of 2-dimensional crystals from latex particles on substrates.* Langmuir, 1992. **8**(12): p. 3183-3190.

15. Denkov, N.D., et al., *2-Dimensional crystallization.* Nature, 1993. **361**(6407): p. 26-26.

16. Murray, C.B., C.R. Kagan, and M.G. Bawendi, *Self-organization of CdSe nanocrystallites into three dimensional quantum dot superlattices.* Science, 1995. **270**(5240): p. 1335-1338.

17. Murray, C.B., C.R. Kagan, and M.G. Bawendi, *Synthesis and characterization of monodisperse nanocrystals and close-packed nanocrystal assemblies.* Annual Review of Materials Science, 2000. **30**: p. 545-610.

18. Xia, Y.N., et al., *Monodispersed colloidal spheres: Old materials with new applications.* Advanced Materials, 2000. **12**(10): p. 693-713.

19. vanBlaaderen, A., R. Ruel, and P. Wiltzius, *Template-directed colloidal crystallization.* Nature, 1997. **385**(6614): p. 321-324.

20. Sun, S.H. and C.B. Murray, *Synthesis of monodisperse cobalt nanocrystals and their assembly into magnetic superlattices (invited).* Journal of Applied Physics, 1999. **85**(8): p. 4325-4330.

21. Pileni, M.P., *Nanosized particles made in colloidal assemblies.* Langmuir, 1997. **13**(13): p. 3266-3276.

22. Velev, O.D. and E.W. Kaler, *Structured porous materials via colloidal crystal templating: From inorganic oxides to metals.* Advanced Materials, 2000. **12**(7): p. 531-534.

23. Aizenberg, J., P.V. Braun, and P. Wiltzius, *Patterned colloidal deposition controlled by electrostatic and capillary forces.* Physical Review Letters, 2000. **84**(13): p. 2997-3000.

24. Kralchevsky, P.A. and K. Nagayama, *Particles at fluid interfaces and membranes*. Studies in interface science, ed. D. Mobius and R. Miller. 2001, Amsterdam: Elsevier Science B. V.

25. Gasser, U., et al., *Real-space imaging of nucleation and growth in colloidal crystallization.* Science, 2001. **292**(5515): p. 258-262.

26. Bates, F.S., *Polymer polymer phase behavior.* Science, 1991. **251**(4996): p. 898-905.

27. Bates, F.S. and G.H. Fredrickson, *Block copolymers - Designer soft materials.* Physics Today, 1999. **52**(2): p. 32-38.

28. Bates, F.S. and G.H. Fredrickson, *Block copolymer thermodynamics - theory and experiment.* Annual Review of Physical Chemistry, 1990. **41**: p. 525-557.

29. Bain, C.D., et al., *Formation of monolayer films by the spontaneous assembly of organic thiols from solution onto gold.* Journal of the American Chemical Society, 1989. **111**(1): p. 321-335.

30. Kumar, A., H.A. Biebuyck, and G.M. Whitesides, *Patterning self-assembled monolayers - applications in materials science.* Langmuir, 1994. **10**(5): p. 1498-1511.

31. Laibinis, P.E., et al., *Comparison of the structures and wetting properties of self-assembled monolayers of normal-alkanethiols on the coinage metal surfaces, Cu, Ag, Au.* Journal of the American Chemical Society, 1991. **113**(19): p. 7152-7167.

32. Discher, B.M., et al., *Polymersomes: Tough vesicles made from diblock copolymers.* Science, 1999. **284**(5417): p. 1143-1146.

33. Jain, S. and F.S. Bates, *On the origins of morphological complexity in block copolymer surfactants.* Science, 2003. **300**(5618): p. 460-464.

34. Matsen, M.W. and F.S. Bates, *Unifying weak- and strong-segregation block copolymer theories.* Macromolecules, 1996. **29**(4): p. 1091-1098.

35. Barrow, M.S., et al., *Physical characterisation of microporous and nanoporous polymer films by atomic force microscopy, scanning electron microscopy and high speed video microphotography.* Spectroscopy-an International Journal, 2004. **18**(4): p. 577-585.

36. Song, L., et al., *Facile microstructuring of organic semiconducting polymers by the breath figure method: Hexagonally ordered bubble arrays in rigid-rod polymers.* Advanced Materials, 2004. **16**(2): p. 115-+.

37. Srinivasarao, M., et al., *Three-dimensionally ordered array of air bubbles in a polymer film.* Science, 2001. **292**(5514): p. 79-83.

38. Cross, M.C. and P.C. Hohenberg, *Pattern formation outside of equilibrium.* Reviews of Modern Physics, 1993. **65**(3): p. 851-1112.

39. Witten, T.A. and P.A. Pincus, *Structured Fluids: Polymers, Colloids, Surfactants*. 2004, New York: Oxford University Press.

40. Stevens, P.S., *Patterns in Nature*. 1974, Boston: Little, Brown and Company.

41. Meakin, P., *Fractals, scaling and growth far from equilibrium*. 1998, Cambridge: Cambridge University Press.

42. Puntes, V.F., K.M. Krishnan, and A.P. Alivisatos, *Colloidal nanocrystal shape and size control: The case of cobalt.* Science, 2001. **291**(5511): p. 2115-2117.

43. Horsch, M.A., Z. Zhang, and S.C. Glotzer, *Self-assembly of laterally-tethered nanorods.* Nano Letters, 2006. **6**(11): p. 2406-2413.

44. Tang, Z.Y., et al., *Self-assembly of CdTe nanocrystals into free-floating sheets.* Science, 2006. **314**(5797): p. 274-278.

45. Glotzer, S.C., et al., *Self-assembly of anisotropic tethered nanoparticle shape amphiphiles.* Current Opinion in Colloid & Interface Science, 2005. **10**(5-6): p. 287-295.

46. Glotzer, S.C., M.J. Solomon, and N.A. Kotov, *Self-assembly: From nanoscale to microscale colloids.* Aiche Journal, 2004. **50**(12): p. 2978-2985.

47. Daniel, M.C. and D. Astruc, *Gold nanoparticles: Assembly, supramolecular chemistry, quantum-size-related properties, and applications toward biology, catalysis, and nanotechnology.* Chemical Reviews, 2004. **104**(1): p. 293-346.

48. Norris, D.J., et al., *Opaline photonic crystals: How does self-assembly work?* Advanced Materials, 2004. **16**(16): p. 1393-1399.

49. Freeman, R.G., et al., *Self-assembled metal colloid monolayers - an approach to SERS substrates.* Science, 1995. **267**(5204): p. 1629-1632.

50. Jana, N.R., *Nanorod shape separation using surfactant assisted self-assembly.* Chemical Communications, 2003(15): p. 1950-1951.

51. Jana, N.R., *Shape effect in nanoparticle self-assembly.* Angewandte Chemie-International Edition, 2004. **43**(12): p. 1536-1540.

52. Jana, N.R., et al., *Liquid crystalline assemblies of ordered gold nanorods.* Journal of Materials Chemistry, 2002. **12**(10): p. 2909-2912.

53. Murphy, C.J., et al., *Anisotropic metal nanoparticles: Synthesis, assembly, and optical applications.* Journal of Physical Chemistry B, 2005. **109**(29): p. 13857-13870.

54. Nikoobakht, B., Z.L. Wang, and M.A. El-Sayed, *Self-assembly of gold nanorods.* Journal of Physical Chemistry B, 2000. **104**(36): p. 8635-8640.

55. Orendorff, C.J., P.L. Hankins, and C.J. Murphy, *pH-triggered assembly of gold nanorods.* Langmuir, 2005. **21**(5): p. 2022-2026.

56. Perez-Juste, J., et al., *Gold nanorods: Synthesis, characterization and applications.* Coordination Chemistry Reviews, 2005. **249**(17-18): p. 1870-1901.

57. Cates, M.E. and M.R. Evans, *Soft and Fragile Matter*. 2000, Bristol: Institue of Physics Publishing.

58. Frenkel, D., *Colloidal systems - Playing tricks with designer "atoms"*. Science, 2002. **296**(5565): p. 65-66.

59. Anderson, V.J. and H.N.W. Lekkerkerker, *Insights into phase transition kinetics from colloid science.* Nature, 2002. **416**(6883): p. 811-815.

60. Frenkel, D., *Onsager spherocylinders revisited.* Journal of Physical Chemistry, 1987. **91**(19): p. 4912-4916.

61. Frenkel, D., *Structure of hard core models for liquid crystals.* Journal of Physical Chemistry, 1988. **92**(11): p. 3280-3284.

62. Chandrasekhar, S., *Liquid Crystals*. 1977, Cambridge: Cambridge University Press.

63. Kleman, M. and O.D. Lavrentovich, *Soft matter physics: an introduction*. 2003, New York: Springer-Verlag Inc.

64. de Gennes, P.G. and J. Prost, *The Physics of Liquid Crystals*. 2nd ed. International Series of Monographs on Physics. 1995: Oxford University Press, USA.

65. Davidson, P. and J.C.P. Gabriel, *Mineral liquid crystals.* Current Opinion in Colloid & Interface Science, 2005. **9**(6): p. 377-383.

66. Vroege, G.J. and H.N.W. Lekkerkerker, *Phase transitions in lyotropic colloidal and polymer liquid crystals.* Reports on Progress in Physics, 1992. **55**(8): p. 1241-1309.

67. Zocher, H., *On independent structure formation in brine.* Zeitschrift Fur Anorganische Und Allgemeine Chemie, 1925. **147**(1/3): p. 91-U15.

68. Davidson, P., A. Garreau, and J. Livage, *Nematic colloidal suspensions of V2O5 in water or Zocher phases revisited.* Liquid Crystals, 1994. **16**(5): p. 905-910.

69. Langmuir, I., *The role of attractive and repulsive forces in the formation of tactoids, thixotropic gels, protein crystals and coacervates.* Journal of Chemical Physics, 1938. **6**(12): p. 873-896.

70. Bawden, F.C., et al., *Liquid crystalline substances from virusinfected plants.* Nature, 1936. **138**: p. 1051-1052.

71. Onsager, L., *The effects of shape on the interaction of colloidal particles.* Annals of the New York Academy of Sciences, 1949. **51**(4): p. 627-659.

72. Hemmer, P.C., H. Holden, and S.K. Ratkje, *The Collected Works of Lars Onsager: with commentary*. 1996, Singapore: World Scientific.

73. Gabriel, J.C.P. and P. Davidson, *New trends in colloidal liquid crystals based on mineral moieties.* Advanced Materials, 2000. **12**(1): p. 9-+.

74. Lemaire, B.J., et al., *Outstanding magnetic properties of nematic suspensions of goethite (alpha-FeOOH) nanorods.* Physical Review Letters, 2002. **88**(12).

75. Lemaire, B.J., et al., *Physical properties of aqueous suspensions of goethite (alpha-FeOOH) nanorods - Part I: In the isotropic phase.* European Physical Journal E, 2004. **13**(3): p. 291-308.

76. Lemaire, B.J., et al., *The complex phase behaviour of suspensions of goethite (alpha-FeOOH) nanorods in a magnetic field.* Faraday Discussions, 2005. **128**: p. 271-283.

77. Lemaire, B.J., et al., *Magnetic-field-induced nematic-columnar phase transition in aqueous suspensions of goethite (alpha-FeOOH) nanorods.* Physical Review Letters, 2004. **93**(26).

78. Lemaire, B.J., et al., *Physical properties of aqueous suspensions of goethite (alpha-FeOOH) nanorods - Part II: In the nematic phase.* European Physical Journal E, 2004. **13**(3): p. 309-319.

79. Davidson, P., et al., *Mineral liquid crystalline polymers.* Progress in Polymer Science, 1997. **22**(5): p. 913-936.

80. Lamarque-Forget, S., et al., *Electrooptic effects in the nematic and isotropic phases of aqueous V2O5 suspensions.* Advanced Materials, 2000. **12**(17): p. 1267-+.

81. Pelletier, O., et al., *A detailed study of the synthesis of aqueous vanadium pentoxide nematic gels.* Langmuir, 2000. **16**(12): p. 5295-5303.

82. Pelletier, O., et al., *A biaxial nematic gel phase in aqueous vanadium pentoxide suspensions.* European Physical Journal B, 1999. **12**(4): p. 541-546.

83. Pelletier, O., et al., *The effect of attractive interactions on the nematic order of V2O5 gels.* Europhysics Letters, 1999. **48**(1): p. 53-59.

84. van der Kooij, F.M., K. Kassapidou, and H.N.W. Lekkerkerker, *Liquid crystal phase transitions in suspensions of polydisperse plate-like particles.* Nature, 2000. **406**(6798): p. 868-871.

85. van der Kooij, F.M. and H.N.W. Lekkerkerker, *Formation of nematic liquid crystals in suspensions of hard colloidal platelets.* Journal of Physical Chemistry B, 1998. **102**(40): p. 7829-7832.

86. van der Kooij, F.M. and H.N.W. Lekkerkerker, *Liquid-crystal phases formed in mixed suspensions of rod- and platelike colloids.* Langmuir, 2000. **16**(26): p. 10144-10149.

87. van der Kooij, F.M. and H.N.W. Lekkerkerker, *Liquid-crystalline phase behavior of a colloidal rod-plate mixture.* Physical Review Letters, 2000. **84**(4): p. 781-784.

88. van der Kooij, F.M. and H.N.W. Lekkerkerker, *Liquid-crystal phase transitions in suspensions of plate-like particles.* Philosophical Transactions of the Royal Society of London Series a-Mathematical Physical and Engineering Sciences, 2001. **359**(1782): p. 985-995.

89. van der Kooij, F.M., D. van der Beek, and H.N.W. Lekkerkerker, *Isotropic-nematic phase separation in suspensions of polydisperse colloidal platelets.* Journal of Physical Chemistry B, 2001. **105**(9): p. 1696-1700.

90. van der Kooij, F.M., M. Vogel, and H.N.W. Lekkerkerker, *Phase behavior of a mixture of platelike colloids and nonadsorbing polymer.* Physical Review E, 2000. **62**(4): p. 5397-5402.

91. van der Beek, D. and H.N.W. Lekkerkerker, *Nematic ordering vs. gelation in suspensions of charged platelets.* Europhysics Letters, 2003. **61**(5): p. 702-707.

92. van der Beek, D. and H.N.W. Lekkerkerker, *Liquid crystal phases of charged colloidal platelets.* Langmuir, 2004. **20**(20): p. 8582-8586.

93. van der Beek, D., et al., *Evidence of the hexagonal columnar liquid-crystal phase of hard colloidal platelets by high-resolution SAXS.* European Physical Journal E, 2005. **16**(3): p. 253-258.

94. van der Beek, D., T. Schilling, and H.N.W. Lekkerkerker, *Gravity-induced liquid crystal phase transitions of colloidal platelets.* Journal of Chemical Physics, 2004. **121**(11): p. 5423-5426.

95. Buining, P.A. and H.N.W. Lekkerkerker, *Isotropic nematic phase separation of a dispersion of organophilic boehmite rods.* Journal of Physical Chemistry, 1993. **97**(44): p. 11510-11516.

96. Buining, P.A., A.P. Philipse, and H.N.W. Lekkerkerker, *Phase behavior of aqueous dispersions of colloidal boehmite rods.* Langmuir, 1994. **10**(7): p. 2106-2114.

97. Dogic, Z., D. Frenkel, and S. Fraden, *Enhanced stability of layered phases in parallel hard spherocylinders due to addition of hard spheres.* Physical Review E, 2000. **62**(3): p. 3925-3933.

98. Adams, M., et al., *Entropically driven microphase transitions in mixtures of colloidal rods and spheres.* Nature, 1998. **393**(6683): p. 349-352.

99. Adams, M. and S. Fraden, *Phase behavior of mixture's of rods (tobacco mosaic virus) and spheres (polyethylene oxide, bovine serum albumin).* Biophysical Journal, 1998. **74**(1): p. 669-677.

100. Varga, S., et al., *Nematic-nematic phase separation in binary mixtures of thick and thin hard rods: Results from Onsager-like theories.* Physical Review E, 2005. **72**(5).

101. Purdy, K.R., et al., *Nematic phase transitions in mixtures of thin and thick colloidal rods.* Physical Review Letters, 2005. **94**(5).

102. Dogic, Z. and S. Fraden, *Ordered phases of filamentous viruses.* Current Opinion in Colloid & Interface Science, 2006. **11**(1): p. 47-55.

103. Dogic, Z. and S. Fraden, *Smectic phase in a colloidal suspension of semiflexible virus particles.* Physical Review Letters, 1997. **78**(12): p. 2417-2420.

104. Dogic, Z. and S. Fraden, *Development of model colloidal liquid crystals and the kinetics of the isotropic-smectic transition.* Philosophical Transactions of the Royal Society of London Series a-Mathematical Physical and Engineering Sciences, 2001. **359**(1782): p. 997-1014.

105. Lee, S.D. and R.B. Meyer, *Computations of the phase equilibrium, elastic constants, and viscosities of a hard rod nematic liquid crystal.* Journal of Chemical Physics, 1986. **84**(6): p. 3443-3448.

106. Lee, S.D. and R.B. Meyer, *Crossover behavior of the elastic coefficients and viscosities of a polymer nematic liquid crystal.* Physical Review Letters, 1988. **61**(19): p. 2217-2220.

107. Frenkel, D., H.N.W. Lekkerkerker, and A. Stroobants, *Thermodynamic stability of a smectic phase in a system of hard rods.* Nature, 1988. **332**(6167): p. 822-823.

108. Frenkel, D., B.M. Mulder, and J.P. McTague, *Phase diagram of a system of hard ellipsoids.* Physical Review Letters, 1984. **52**(4): p. 287-290.

109. Bolhuis, P. and D. Frenkel, *Numerical study of the phase diagram of a mixture of spherical and rodlike colloids.* Journal of Chemical Physics, 1994. **101**(11): p. 9869-9875.

110. Bates, M.A. and D. Frenkel, *Phase behavior of two-dimensional hard rod fluids.* Journal of Chemical Physics, 2000. **112**(22): p. 10034-10041.

111. Bates, M.A. and D. Frenkel, *Influence of polydispersity on the phase behavior of colloidal liquid crystals: A Monte Carlo simulation study.* Journal of Chemical Physics, 1998. **109**(14): p. 6193-6199.

112. Bolhuis, P. and D. Frenkel, *Tracing the phase boundaries of hard spherocylinders.* Journal of Chemical Physics, 1997. **106**(2): p. 666-687.

113. Bolhuis, P.G., et al., *Numerical study of the phase behavior of rodlike colloids with attractive interactions.* Journal of Chemical Physics, 1997. **107**(5): p. 1551-1564.

114. Popov, Y.O. and T.A. Witten, *Characteristic angles in the wetting of an angular region: Surface shape.* European Physical Journal E, 2001. **6**(3): p. 211-220.

115. Popov, Y.O., *Evaporative deposition patterns: Spatial dimensions of the deposit.* Physical Review E, 2005. **71**(3).

116. Park, K., *Synthesis, characterization and self-assembly of size tunable gold nanorods*, in *School of Polymer, Textile and Fiber Engineering*. 2006, Georgia Institute of Technology: Atlanta.

117. Sharma, V., K. Park, and M. Srinivasarao, *Colloidal dispersion of gold nanorods: Historical background, optical properties, seed mediated synthesis, shape separation and self-assembly.* submitted to Materials Science & Engineering R-Reports, 2008.

118. Ostwald, W., *An Introduction to Theoretical and Applied Colloid Chemistry*. 1917, New York: John Wiley & Sons, Inc.

119. Henisch, H.K., *Periodic Precipitation*. 1991, New York: Permagon Press.

120. Dee, G.T., *Patterns produced by precipitation at a moving reaction front.* Physical Review Letters, 1986. **57**(3): p. 275-278.

121. Prager, S., *Periodic precipitation.* Journal of Chemical Physics, 1956. **25**(2): p. 279-283.

122. Smith, D.A., *On Ostwald supersaturation theory of rhythmic precipitation (Liesegang rings)* Journal of Chemical Physics, 1984. **81**(7): p. 3102-3115.

123. Venzl, G. and J. Ross, *Nucleation and colloidal growth in concentration gradients (Liesegang rings).* Journal of Chemical Physics, 1982. **77**(3): p. 1302-1307.

124. Shmuylovich, L., A.Q. Shen, and H.A. Stone, *Surface morphology of drying latex films: Multiple ring formation.* Langmuir, 2002. **18**(9): p. 3441-3445.

125. Maeda, H., *Observation of spatially rhythmic patterns from evaporating collagen solution droplets.* Langmuir, 2000. **16**(26): p. 9977-9982.

126. Hong, S.W., J.F. Xia, and Z.Q. Lin, *Spontaneous formation of mesoscale polymer patterns in an evaporating bound solution.* Advanced Materials, 2007. **19**(10): p. 1413-+.

127. Hong, S.W., et al., *Mesoscale patterns formed by evaporation of a polymer solution in the proximity of a sphere on a smooth substrate: Molecular weight and curvature effects.* Macromolecules, 2007. **40**(8): p. 2831-2836.

128. Lin, Z.Q. and S. Granick, *Patterns formed by droplet evaporation from a restricted geometry.* Journal of the American Chemical Society, 2005. **127**(9): p. 2816-2817.

129. Byun, M., et al., *Self-assembling semicrystalline polymer into highly ordered, microscopic concentric rings by evaporation.* Langmuir, 2008. **24**(7): p. 3525-3531.

130. Maheshwari, S., et al., *Coupling between precipitation and contact-line dynamics: Multiring stains and stick-slip motion.* Physical Review Letters, 2008. **1**(4).

131. Xu, J., J.F. Xia, and Z.Q. Lin, *Evaporation-induced self-assembly of nanoparticles from a sphere-on-flat geometry.* Angewandte Chemie-International Edition, 2007. **46**(11): p. 1860-1863.

132. Xu, J., et al., *Self-assembly of gradient concentric rings via solvent evaporation from a capillary bridge.* Physical Review Letters, 2006. **96**(6).

133. Zhang, L., et al., *Evaporative self-assembly from complex DNA-colloid suspensions.* Langmuir, 2008. **24**(8): p. 3911-3917.

134. Hu, H. and R.G. Larson, *Marangoni effect reverses coffee-ring depositions.* Journal of Physical Chemistry B, 2006. **110**(14): p. 7090-7094.

135. Hu, H. and R.G. Larson, *Analysis of the microfluid flow in an evaporating sessile droplet.* Langmuir, 2005. **21**(9): p. 3963-3971.

136. Hu, H. and R.G. Larson, *Analysis of the effects of Marangoni stresses on the microflow in an evaporating sessile droplet.* Langmuir, 2005. **21**(9): p. 3972-3980.

137. Maeda, H., *An atomic force microscopy study of ordered molecular assemblies and concentric ring patterns from evaporating droplets of collagen solutions.* Langmuir, 1999. **15**(24): p. 8505-8513.

138. van Hameren, R., et al., *Macroscopic hierarchical surface patterning of porphyrin trimers via self-assembly and dewetting.* Science, 2006. **314**(5804): p. 1433-1436.

139. Mitamura, K., et al., *Fabrication and self-assembly of hydrophobic gold nanorods.* Journal of Physical Chemistry B, 2007. **111**(30): p. 8891-8898.

140. Sau, T.K. and C.J. Murphy, *Self-assembly patterns formed upon solvent evaporation of aqueous cetyltrimethylammonium bromide-coated gold nanoparticles of various shapes.* Langmuir, 2005. **21**(7): p. 2923-2929.

141. Yang, P.D. and F. Kim, *Langmuir-Blodgett assembly of one-dimensional nanostructures.* Chemphyschem, 2002. **3**(6): p. 503-+.

142. Zimnitsky, D., et al., *Domain and network aggregation of CdTe quantum rods within Langmuir-Blodgett monolayers.* Nanotechnology, 2008. **19**(21).

143. Maeda, H. and Y. Maeda, *Atomic force microscopy studies for investigating the smectic structures of colloidal crystals of beta-FeOOH.* Langmuir, 1996. **12**(6): p. 1446-1452.

144. Kim, F., et al., *Langmuir-Blodgett nanorod assembly.* Journal of the American Chemical Society, 2001. **123**(18): p. 4360-4361.

145. Li, L.S. and A.P. Alivisatos, *Semiconductor nanorod liquid crystals and their assembly on a substrate.* Advanced Materials, 2003. **15**(5): p. 408-+.

146. Li, L.S., et al., *Isotropic-liquid crystalline phase diagram of a CdSe nanorod solution.* Journal of Chemical Physics, 2004. **120**(3): p. 1149-1152.

147. Maeda, H. and Y. Maeda, *Liquid crystal formation in suspensions of hard rodlike colloidal particles: Direct observation of particle arrangement and self-ordering behavior.* Physical Review Letters, 2003. **90**(1).

148. Koenderink, G.H., et al., *Depletion-induced crystallization in colloidal rod-sphere mixtures.* Langmuir, 1999. **15**(14): p. 4693-4696.

149. Perrin, J., *Brownian motion and molecular reality.* Annales De Chimie Et De Physique, 1909. **18**: p. 5-114.

150. Perrin, J., *Atoms*. 2nd ed. 1923, London: Constable & Company Ltd.

151. Kralchevsky, P.A. and N.D. Denkov, *Capillary forces and structuring in layers of colloid particles.* Current Opinion in Colloid & Interface Science, 2001. **6**(4): p. 383-401.

152. Kralchevsky, P.A. and K. Nagayama, *Capillary interactions between particles bound to interfaces, liquid films and biomembranes.* Advances in Colloid and Interface Science, 2000. **85**(2-3): p. 145-192.

153. Witten, T.A. and L.M. Sander, *Diffusion-limited aggregation, a kinetic critical phenomenon.* Physical Review Letters, 1981. **47**(19): p. 1400-1403.

154. Dimon, P., et al., *Structure of aggregated gold colloids.* Physical Review Letters, 1986. **57**(5): p. 595-598.

155. Lin, M.Y., et al., *Universality in colloid aggregation.* Nature, 1989. **339**(6223): p. 360-362.

156. Weitz, D.A. and M. Oliveria, *Fractal structures formed by kinetic aggregation of aqueous gold colloids.* Physical Review Letters, 1984. **52**(16): p. 1433-1436.

157. Ohara, P.C., J.R. Heath, and W.M. Gelbart, *Self-assembly of submicrometer rings of particles from solutions of nanoparticles.* Angewandte Chemie-International Edition in English, 1997. **36**(10): p. 1078-&.

CHAPTER 11

IRIDESCENT BEETLE CHRYSINA GLORIOSA

I have my own views about Nature's methods,
though I feel that it is rather like a beetle
giving his opinions upon the Milky Way.
Sir Arthur Conan Doyle, *The Stark Munro Letters* [1].

11.1 Introduction

Iridescent beetles, butterflies, certain sea organisms and many birds derive their color from the interaction of light with the structure or morphology that is imprinted on their exoskeleton or wings [2-6]. The color may have contribution from the pigmentation in the underlying layers. The bright and varied colors of beetles have been of interest not only to scientists [3, 7-9], but they have a long and interesting history as "jewel beetles" which were used in textiles or ornaments [10] in many Asian countries. The study of photonics in nature reveals beautiful and diverse examples of sub-wavelength structural features that create observed colors through thin layered or multilayered interference, diffraction, zero order diffraction and light scattering [2-6]. While the complexity of the patterns is in part determined genetically, and requires understanding of the triggers and the biomolecules that are designed to produce them, their final development and control is related to the conditions during the development of the pattern [11, 12]. The physical and chemical aspects of morphogenesis can be unraveled by studying the patterns in nature and analyzing their analogues in the equilibrium and non-equilibrium patterns formed in condensed matter [13-16]. The quest for miniature optical devices and photonics is most likely to benefit from the study of bioengineered organs and organelles of the biological world. Rational design requires one to understand how basic structural

units interact with light and how they can be fabricated either by self-assembly or a top-down approach. The present chapter is a study of the structural features on the iridescent beetle *Chrysina gloriosa*. Since most of the results presented here were acquired in collaboration with Matija Crne and Dr. Jung Ok Park, the chapter is written in the first person plural.

11.2 Chyrsina gloriosa reflects left circularly polarized light

In this context, we have been examining the structure on the exocuticle of the beetle *Chrysina gloriosa* or *Plusiotis gloriosa* that selectively reflects left-circularly polarized light and possesses a brilliant metallic appearance (see Figure 11.1). If left circularly polarized light is blocked by the use of a quarter wave plate and a polarizer, as shown in Figure 11.1, the beetle 'loses' its characteristic bright green reflection. The ability of certain species of beetles to reflect circularly polarized light has been investigated since Michelson first reported it in 1911 [7]. Recently Goldstein [8] summarized the history of optical measurements made in scarab beetles and performed ellipsometric studies confirming their polarizing behavior. The reflectance of the *P. gloriosa* beetle has a broad halo from 500-600 nm with two peaks at 530 and 580 nm respectively. We must remark here that the ability of certain beetles to selectively reflect circularly polarized light with a preferred handedness has been unexplained in terms of whether it serves any purpose for beetles or other organisms preying on them [3]. Only recently, for the first time a visual system capable of detecting and analyzing circularly polarized light was demonstrated for stomatopod crustaceans [17].

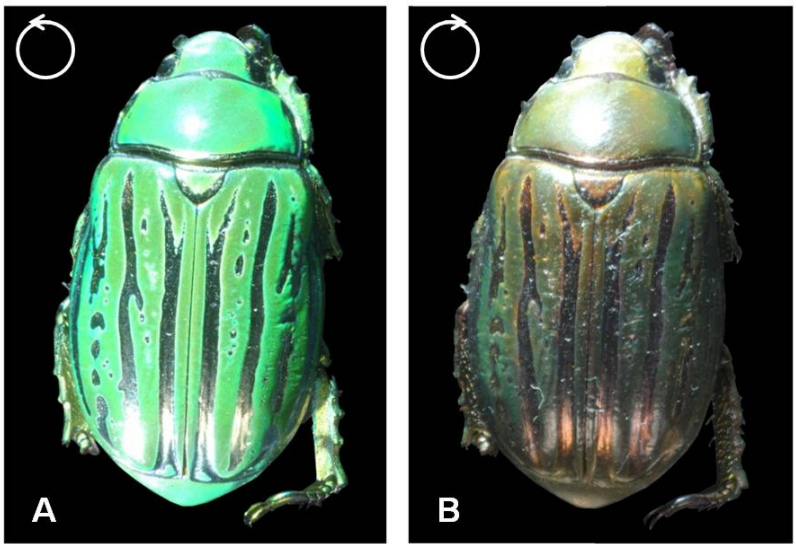

Figure 11.1 Photographs of beetle *Chrysina gloriosa.* (**A**) The bright green color, with silver stripes as seen in the unpolarized light or with a left-circular polarizer. (**B**) The green color is mostly lost when seen with a right-circular polarizer.

11.3 Voronoi analysis of tiles that decorate the beetle exoskeleton

When the exoskeleton of the beetle is observed under an optical microscope, the body appears as a richly decorated mosaic of cusps and color, consisting of a regularly spaced lattice of features that distinguish one species of the beetle from the other. In bright field microscopy (Figure 11.2), the structure of *Chrysina gloriosa* seems to consist of hexagonal cells (~10 μm), where each cell appears to be green with a bright yellow core or nucleus. Before pondering over the question of what produces this pattern and what purpose is served by it, we decided to characterize the extent of hexagonal order in patterns using Voronoi analysis.

A close examination of the Voronoi diagram reveals that while the population of six sided polygons is the highest, there exist a large number of five and seven sided polygons. If we define P_n to represent the fraction of n sided polygons, we find that P_5 decreased from 0.34 at the highly curved head to about 0.19 at the flattest region on the

beetles' back, whereas P_7 is typically close to 0.13 everywhere else. While most of the pentagons and heptagons occur in clusters, there are a finite number of pentagons that occur individually. The number and spatial distribution of polygons characterizes the spatial order. Entropy, $S = - \Sigma P_n \ln P_n$ of the structure was determined for each image. For perfectly ordered hexagons, $P_6 = 1$ and $S = 0$. The value of the entropy on beetle exoskeleton varies between 0.85-0.95 and is higher in the regions of greater curvature, revealing packing issues on curved surfaces.

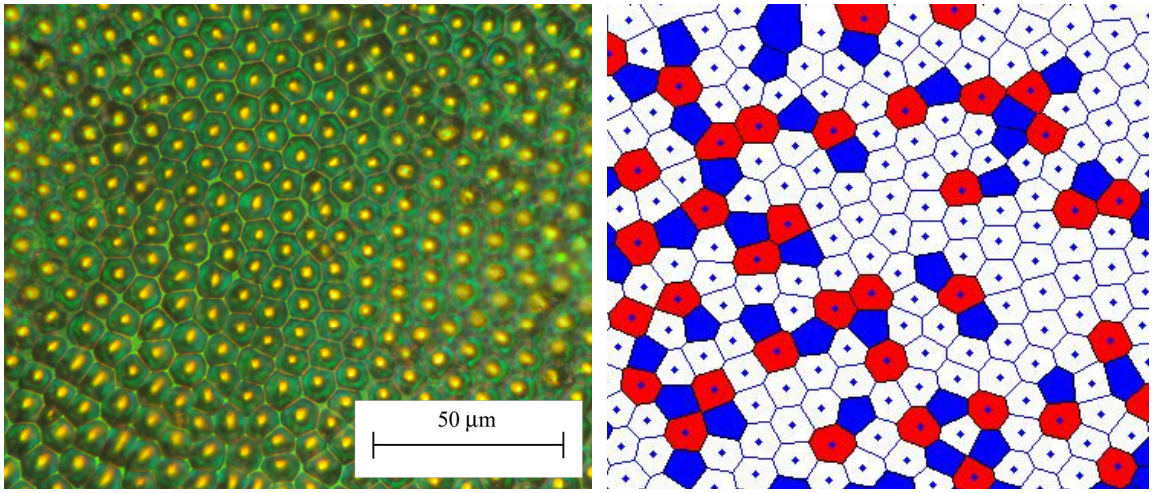

Figure 11.2 (**A**) An optical micrograph of the exoskeleton of beetle *Chrysina gloriosa* showing bright yellow reflections from the core of each cell (~10 µm size), and greenish reflection from the edges. (**B**) Voronoi analysis of a section from the corresponding image. Pentagons are colored blue, heptagons are red and hexagons are white.

It is well established that it is not possible to tile a curved surface with just hexagons [18], and the head, thorax and abdomen of a beetle are all curved. While hexagonal packing provides the most efficient utilization of space on a plane, defects in coordination number are essential for wrapping such tessellations on a sphere. For example, soccer balls and C60 (fullerenes), contain 12 pentagons in addition to the hexagons that template the curved structure. For *N* particles of size a, placed over surface

of size R ($R^2 \sim Na^2$), following Euler's theorem, the number of triangles T, edges E and vertices N are related by $T - E + N = 2$. Thus a triangulation using Delaunay construction with co-ordination number Z_i at every node will have at most 12 five-fold disclinations for an arbitrary number of six-coordinated sites. Since the beetle has a curved body, a certain number of pentagons are expected. The research efforts in spherical crystallography [18-20] illustrate the importance of grain boundaries and defects in creating minimum-energy configurations for the curved substrates. According to Nelson [18], the energetic cost associated with creating these 12 defects scales as YR^2, where Y is the two-dimensional Young's modulus. Since the cost becomes substantial for systems with large R/a, the system seeks ways to reduce this energy. This can be done in two ways. A buckling transition can occur for hollow spherical shells. Conversely, if surface tension limits the buckling out of the local tangent plane, disclinations can emanate grain boundary scars. While such grain boundary scars have been observed for particles packed on a spherical droplet, called colloidosomes [19], the presence of buckling has been used to rationalize the faceted morphology of viruses [18]. The various pattern formation mechanisms that create hexagonally symmetric patterns on planar two-dimensional surfaces can likewise be expected to break the symmetry on curved surface, if the six fold triangulations are not energetically most favored everywhere.

Since Turing's influential paper on reaction-diffusion induced patterning in morphogenesis [13], the patterns on various biological organisms have been attributed to and described using this model [14-16]. While most of the studies considered such effects on planar surfaces, the corresponding patterns are likely to encounter geometric frustration on a curved surface, creating a rich range of topologies, including the ones

with grain scars or faceted surfaces. For example, recently Bowick et al [21] found such defects in bubble rafts assembled on the curved (paraboloidal) surface of a rotating fluid. The formation of the exocuticle involves intricate biochemical reactions [22] of proteins, enzymes and pigments, and usual steps involve crosslinking between polypeptide chains, causing progressive hardening, dehydration and close packing of biopolymers [23]. Cellular patterns can arise in foams, colloidal packing, hydrodynamic instabilities, drying of gels, cracking and in various other instances due to equilibrium or non-equilibrium spatiotemporal effects [12, 14, 15]. Their mere existence does not inform us about the morphogenesis or pattern formation. But given the stunning topology and colors of beetle, we decided to use optics and confocal microscopy to illuminate us!

11.4 What creates the patterns on the beetle exoskeleton?

We examined the beetle exoskeleton using a laser scanning confocal microscope (Leica TCS SP DMR XE), which allows us to construct a three-dimensional map of the underlying structure in fluorescence mode. The inherent fluorescence of the beetle provides the necessary response to visualize it under the excitation of 488nm laser. The relief of the cells, when observed under high magnification, reveals itself to consist of bright and dark, nearly concentric regions. The fluorescence response from the unidentified fluorophore present in the elytra is dependent on the polarization state and intensity of light that excites it. Hence the darker regions could point to either changing fluorophore orientation or to a change in the fluorophore concentration. The 3-D reconstruction of the images shows the existence of a microstructure of nested arcs and the cells seem to have a conical protrusion at the center.

The confocal image (Figure 11.3 B or 11.4 A) has a remarkable similarity to the TEM images of *P. gloriosa* by Pace [24]. Further, the microstructure of the beetle surface has an uncanny resemblance to the AFM image of the focal conic domains that spontaneously arise on the free surface of a siloxan oligomer based cholesteric liquid crystal [25]. The spiral structure (Fig. 3) observed in each cell on the beetle exoskeleton also correlates nicely with the conical form observed by Meister et al [25] using AFM, where with the periodic structure due to the cholesteric pitch is superimposed on a fat cone (height/maximum diameter ~0.01). Likewise the focal conic cholesteric domains are organized in a near hexagonal packing. Furthermore, our SEM image (Fig. 4D) of the beetle exoskeleton bears similarity to the corresponding AFM image (Fig. 4E) obtained for a section microtomed perpendicular to the free surface [25], where the underlying layers can be seen clearly.

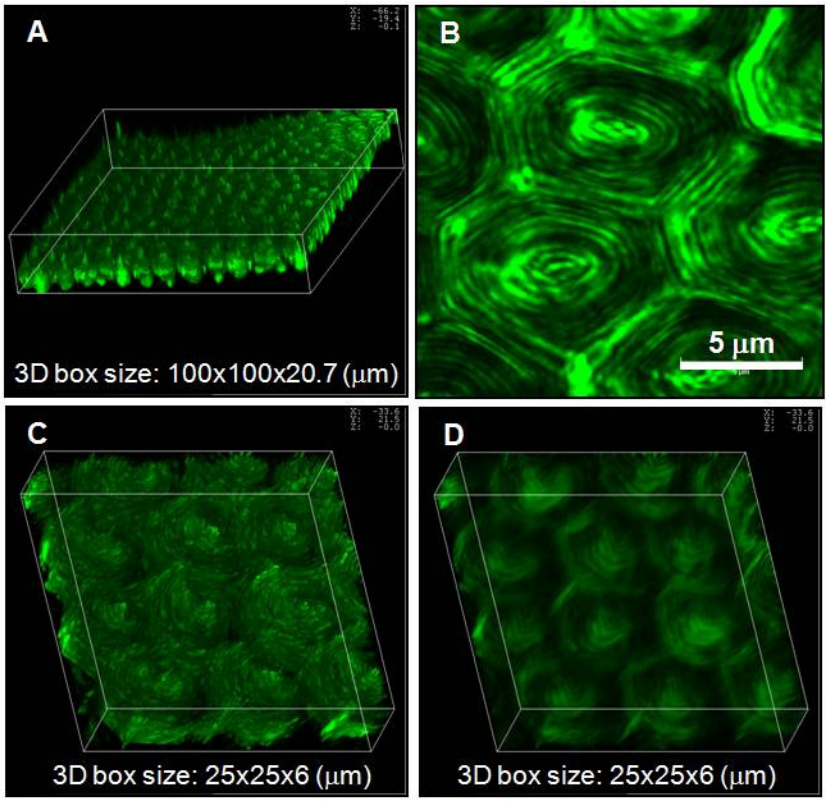

Figure 11.3 Fluorescence confocal microscopy images of the cellular exoskeleton of the beetle *Chrysina gloriosa*, obtained using excitation at 488nm. (**A**) An angled view of three dimensional image at a low magnification reveals upward cones at the center of each cell. (**B**) A typical x-y section, showing a relief feature with concentric rings that is resolved only at a high magnification, and present only near the free surface. (**C**)-(**D**) 3-D images at high magnification for limited thickness range in different viewing modes, which may imply the concentric bright/dark regions are spiraled.

The optical response of exocuticles of many beetles has been noted to be similar to that of cholesteric liquid crystals (for example, see Neville and Caveney [26-28]). Nematic liquid crystals consist of rodlike moieties or molecules that possess long range orientational order, described by a unit vector **n**, known as the director. If the nematic liquid crystal is either composed of chiral mesogenic molecules or has a chiral dopant, the equilibrium director structure becomes a helicoid [29-32] forming a cholesteric liquid crystal. The director advances uniformly tracing a helix of pitch *p* as sketched in Figure 4C. Both possibilities exist for biological systems [32, 33].While the helicoidal structure

has been cited as a possible means of generating such an optical response of the beetles [3, 6, 28], the observed hexagonal pattern remains unexplained, with no attempt made to relate the microstructure to the textures of the cholesteric phase. The only example where morphology was compared to cholesteric liquid crystal comes from Pace's forgotten paper[24] that presented TEM images and noted that the beetle *P. gloriosa* has a liquid crystal-like microstructure (which he called a Bouligand structure). Bouligand [34] had carried out an extensive study on the similarity of textures observed in crabs and other organisms to cholesteric liquid crystals and explored their role in morphogenesis. The surfaces produced by the freeze fracture process can possess a relief due to the anisotropic propagation of fracture and the action of a microtome knife produces a topography that depends upon the texture of the cut material.[25, 34, 35] This is both the boon and bane of the TEM studies and perhaps led to effectively burying Pace's interpretation[24] about the relief of this beetle. But in this study, since we imaged the three dimensional microstructure of the beetle elytra in a non-destructive fashion using a confocal microscope, the similarity to the cholesteric focal conic texture at the free surface is unmistakable.

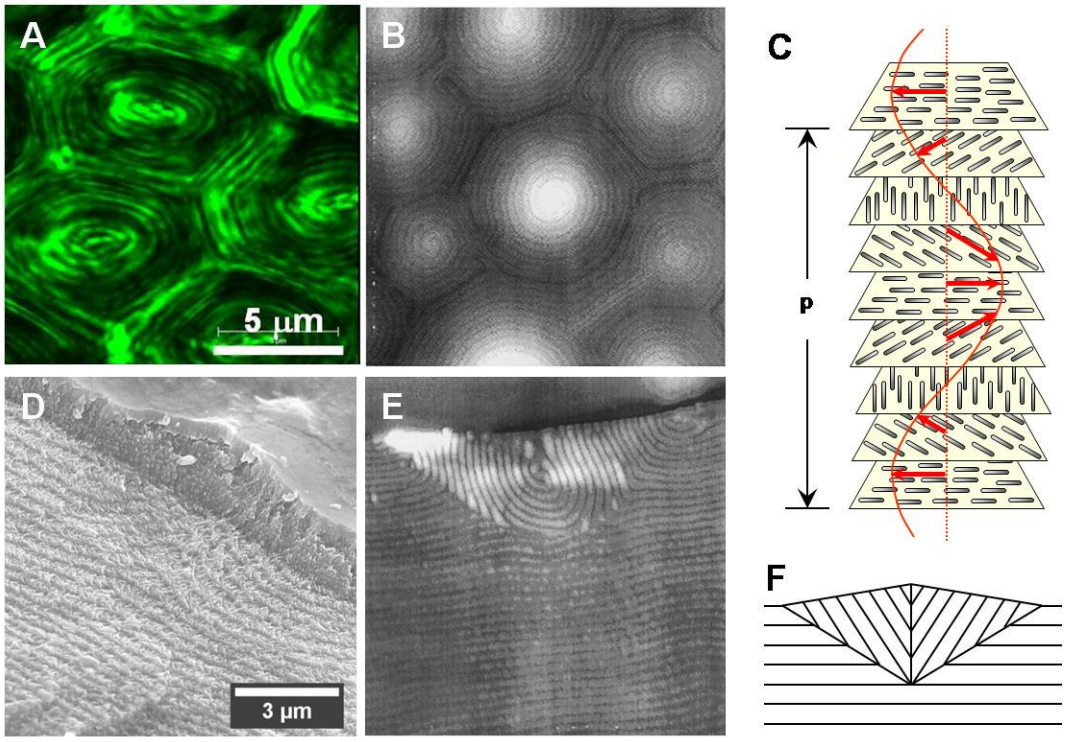

Figure 11.4 (**A**) Confocal image (x-y section) of the microstructure of the beetle. (**B**) An AFM image of the cholesteric focal conic domains at the free surface, showing double spirals that form a shallow cone (from ref. [25]). (**C**) Schematic representation of relative arrangement of chiral mesogens in a cholesteric liquid crystal, stacked in a single twist structure (layers are for illustration purposes only, no lamellar ordering in the z direction). (**D**) SEM image shows the nested arcs and a waxy layer on top (**E**) AFM image of the microtome cut perpendicular to free surface (from ref. [25]). (**F**) Model of focal conic domain adopted from ref. [25], showing a cut along the center of the cone, whereby neglecting the exact structure at the center.

The microstructure or the texture of the cholesteric phase is dictated by the interplay of many factors, including chirality, curvature elasticity, surface anchoring, and coupling to applied fields [29, 31]. The identification of the phase relies on their physical properties as revealed in microscopic and spectroscopic investigation. The selective reflection of the cholesteric phases can be modified by a change in pitch, birefringence, cell thickness, angle of incidence, polarization as well as by the orientation of helical axis [29-31, 36]. This is more important for the multi-domain system observed here. It has been pointed out before that even though the confocal microscope helps in determining

the director configuration in a cholesteric liquid crystal, the light propagation in a birefringent, helical structure is non-trivial to simulate and the image resolution is limited in comparison to the isotropic medium [37]. Since we observed structures at the surface or close to the surface, we expect that the aberrations and defocusing associated with birefringent media will be minimal. Given the complexity and intricate nature of the structure and optics of the beetle elytra, it is quite a challenge to construct a physical system (artificial beetle skin) based on cholesteric phase that could emulate or simulate the behavior. Further, the artificial beetle skin will need to match the structural integrity and support that are intrinsic to manifold functions performed by the exoskeleton. In addition, the exoskeleton of the beetle involves geometric frustration and topological consequences at every scale, from structure of mesogen to the cellular structure with defects. The role of curvature in complex self-assembly require a mathematics and language of shape [38] that is just beginning to evolve, and focal conic textures involve geometrical and topological theories of defects that are still an active area of research [31, 32].

11.5 Color of the beetle

Finally we return to the question of the color reflected off the beetles. Since we infer that the architecture of the beetle exoskeleton is similar to a cholesteric focal conic domain at a free surface (see Figure 11.4), and we have limited knowledge of all the optical and structural parameters necessary for determining response by ray tracing, we can put forward only phenomenological arguments. Due to their chiral and periodic helicoidal structure, the cholesteric phase with a pitch comparable to the wavelength of

visible light, shows Bragg-like reflection for normal incidence, peaked at wavelength, λ_0, given by $\lambda_0 = np$, where n is the average refractive index. The spectral width of the reflection peak for a pure cholesteric phase is related to birefringence ($\Delta n = n_e - n_o$) by $\Delta\lambda = p\Delta n$ [29, 30], where n_o and n_e are the refractive indices for polarizations perpendicular (ordinary) and parallel (extraordinary) to the axis of anisotropy, respectively. For oblique incidence at an angle ϕ, the reflection for a helix oriented at some angle θ with respect to surface normal, the condition is modified to $\lambda = np\cos(\phi - \theta)$. When we look at the beetle structure in the white light in a reflection microscope, the Bragg-like reflection is yellow at the center of the cell and green elsewhere. When the range of incidence angles is increased by increasing the aperture size (Figure 11.5A), the locus of the yellow reflection expands, implying that by increasing the angle of incidence of beams over the beetle, cos (ϕ-θ) becomes smaller and thus a longer wavelength (yellow as opposed to green) satisfies the condition. In the dark field, when only large angles of incidence are possible, the cos (ϕ-θ) term near the center gets even smaller, leading to extinction of color at the center (Figure 11.5C).

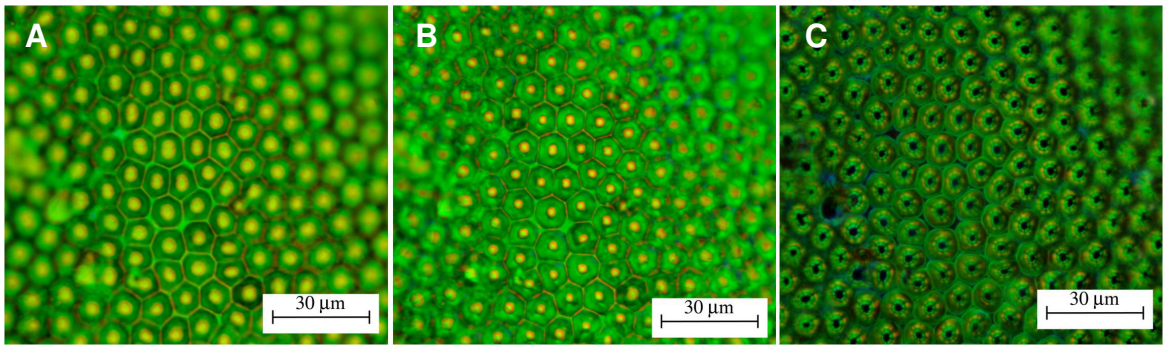

Figure 11.5 Optical micrographs of the exoskeleton of *P. gloriosa*. (**A**) In bright field, with microscope aperture wide open, to allow a bigger cone of white light. (**B**) In bright field, near normal incidence obtained by decreasing the aperture. (**C**) In dark field, where near normal incidence is not present. Since the surfaces are curved, only central part of the image is in focus.

In the optical studies by Jewell et al [39] on *P. boucardi* beetles, similar hexagonal cells are observed to shows dark centers in darkfield and these spots turn yellow in bright field. For both *P. boucardi [39]* and the New Zealand manuka beetle [40], the presence of chiral reflectors with two different pitches satisfying Bragg reflection was cited as responsible for color. Lowery et al [9] simulated their ellipsometric studies on three different species of beetle by using a chirped stack of structurally perturbed chiral resonators. Similarly, Brink et al [41] attributed the reflected spectrum of the red and green scarabaeid beetle *Gymnopleurus virens* to an exocuticle structure which can be simulated using a perturbed cholesteric structure that has an abrupt jump in pitch, and rotation of the cholesteric structure. We propose that the cholesteric focal conic domains created at the free surface of a cholesteric liquid crystal can create the perturbed cholesteric relief that can account for the color and the morphology of the exocuticle of the scarabaeid beetles. While the details of morphogenesis will influence the exact nature of microstructure and observed color for a particular beetle, we infer that each of these mechanisms provides us with inspiration to the design of chiral reflectors. The desired optical response can be achieved by incorporating either a bistable cholesteric phase formed due to free surface, by using controlled anchoring, or by using structures with variable pitch (which can also be accomplished by having a concentration gradient of nematic blended into a cholesteric fluid [42]).

11.6 Conclusions

In this study, we have only scratched the surface of the topologically rich, structurally intricate and colorful realm of beetle photonics. We imaged the cellular structure on the beetle using both confocal and polarizing microscopy in reflectance mode, and applied crystallographic concepts to analyze the topological features. We described how the optical and structural behavior of the beetle elytra is similar to the periodic relief structure observed on the free surface of a cholesteric liquid crystal. In effect, we propose that the observed microstructure results from the formation of cholesteric liquid crystal during the development of elytra. The questions about how morphogenesis (mediated by the formation of liquid crystal phases) is controlled and triggered are intimately coupled to questions about how anchoring, curvature, curvature elasticity, environmental conditions, etc. influence the pattern formation. The ability of nature to design useful devices or organelles spontaneously from a soup of molecules, when emulated, may usher in a revolution in chiral and non-chiral optical devices.

11.7 References

1. Doyle, A.C., *The Stark Munro Letters*. 2006, Charleston: Bibliobazaar.
2. Ghiradella, H., *Light and color on the wing - structural colors in butterflies and moths.* Applied Optics, 1991. **30**(24): p. 3492-3500.
3. Srinivasarao, M., *Nano-optics in the biological world: Beetles, butterflies, birds, and moths.* Chemical Reviews, 1999. **99**(7): p. 1935-1961.
4. Vukusic, P. and J.R. Sambles, *Photonic structures in biology.* Nature, 2003. **424**(6950): p. 852-855.
5. Parker, A.R., *515 million years of structural colour.* Journal of Optics a-Pure and Applied Optics, 2000. **2**(6): p. R15-R28.
6. Bertheier, S., *Iridescences: The Physical Color of Insects*. 2007: Springer.

7. Michelson, A.A., *Studies in Optics*. 1927, Chicago: The University of Chicago Press.

8. Goldstein, D.H., *Polarization properties of Scarabaeidae.* Applied Optics, 2006. **45**(30): p. 7944-7950.

9. Lowrey, S., et al., *Observation and modeling of polarized light from scarab beetles.* Journal of the Optical Society of America a-Optics Image Science and Vision, 2007. **24**(8): p. 2418-2425.

10. Motte-Florac, E. and J.M.C. Thomas, *Les Insectes Dans La Tradition Orale/Insects In Oral Literature And Traditions*. 2004: David Brown.

11. Thompson, D.A., *On Growth and Form*. 1961, Cambridge: Cambridge University Press.

12. Stevens, P.S., *Patterns in Nature*. 1974, Boston: Little, Brown and Company.

13. Turing, A.M., *The Chemical Basis of Morphogenesis.* Philosophical Transactions of the Royal Society (Part B), 1953. **237**: p. 37-72.

14. Ball, P., *The Self-made tapestry: pattern formation in nature*. 1999, Oxford: Oxford University Press.

15. Cross, M.C. and P.C. Hohenberg, *Pattern formation outside of equilibrium.* Reviews of Modern Physics, 1993. **65**(3): p. 851-1112.

16. Koch, A.J. and H. Meinhardt, *Biological pattern formation - from basic mechanisms to complex structures.* Reviews of Modern Physics, 1994. **66**(4): p. 1481-1507.

17. Chiou, T.H., et al., *Circular polarization vision in a stomatopod crustacean.* Current Biology, 2008. **18**(6): p. 429-434.

18. Nelson, D.R. *Spherical Crystallography: Virus Buckling and Grain Boundary Scars*. in *The Physics Of Complex Systems: New Advances And Perspectives: Proceedings of International School of Physics Enrico Fermi*. 2004: IOS Press.

19. Bausch, A.R., et al., *Grain boundary scars and spherical crystallography.* Science, 2003. **299**(5613): p. 1716-1718.

20. Vitelli, V., J.B. Lucks, and D.R. Nelson, *Crystallography on curved surfaces.* Proceedings of the National Academy of Sciences of the United States of America, 2006. **103**(33): p. 12323-12328.

21. Bowick, M.J., et al., *Bubble-raft model for a paraboloidal crystal.* Physical Review E, 2008. **77**(2).

22. Andersen, S.O., *Biochemistry of insect cuticle.* Annual Review of Entomology, 1979. **24**: p. 29-61.

23. Hopkins, T.L. and K.J. Kramer, *Insect cuticle sclerotization.* Annual Review of Entomology, 1992. **37**: p. 273-302.

24. Pace, A., *Cholesteric liquid crystal-like structure of cuticle of Plusiotic gloriosa.* Science, 1972. **176**(4035): p. 678-&.

25. Meister, R., et al., *Structure of the cholesteric focal conic domains at the free surface.* Physical Review E, 1996. **54**(4): p. 3771-3782.

26. Neville, A.C. and S. Caveney, *Sacarabaeid beetle exocuticle as optical analogue of cholesteric liquid crystals.* Biological Reviews of the Cambridge Philosophical Society, 1969. **44**(4): p. 531-&.

27. Caveney, S., *Cuticle reflectivity and optical activity in scarab beetles - role of uric acid.* Proceedings of the Royal Society of London Series B-Biological Sciences, 1971. **178**(1051): p. 205-&.

28. Neville, A.C., *Biology of fibrous composites: Development beyond the cell membrane*. 1993, Cambridge: Cambridge University Press.

29. Chandrasekhar, S., *Liquid Crystals*. 1977, Cambridge: Cambridge University Press.

30. de Gennes, P.G. and J. Prost, *The Physics of Liquid Crystals*. 2nd ed. International Series of Monographs on Physics. 1995: Oxford University Press, USA.

31. Kleman, M. and O.D. Lavrentovich, *Soft matter physics: an introduction*. 2003, New York: Springer-Verlag Inc.

32. Bouligand, Y., *Some geometrical and topological problems in liquid crystals* in *Bifurcation Theory, Mechanics and Physics*, C.P. Bruter, A. Arangol, and A. Lichenrowicz, Editors. 1983, D. Riedel Publishing Company: Dordecht.

33. Srinivasarao, M., *Chirality and polymers.* Current Opinion in Colloid & Interface Science, 1999. **4**(2): p. 147-152.

34. Bouligand, Y., *Liquid crystals and biological morphogenesis: Ancient and new questions.* Comptes Rendus Chimie, 2008. **11**(3): p. 281-296.

35. Berreman, D.W., et al., *Theory and simulation of freeze fracture in cholesteric liquid crystals.* Physical Review Letters, 1986. **57**(14): p. 1737-1740.

36. Stjohn, W.D., et al., *Bragg reflection from cholesteric liquid crystals.* Physical Review E, 1995. **51**(2): p. 1191-1198.

37. Lavrentovich, O.D., et al., eds. *Defects in Liquid Crystals: Computer Simulations, Theory and Experiment*. 2001, Kluwer Academic Publishers, The Netherlands.

38. Hyde, S., et al., *The Language of Shape*. 1997, Amsterdam: Elsevier Science B. V.

39. Jewell, S.A., P. Vukusic, and N.W. Roberts, *Circularly polarized colour reflection from helicoidal structures in the beetle Plusiotis boucardi.* New Journal of Physics, 2007. **9**.

40. De Silva, L., et al., *Natural and nanoengineered chiral reflectors: Structural color of manuka beetles and titania coatings.* Electromagnetics, 2005. **25**(5): p. 391-408.

41. Brink, D.J., et al., *Unusual coloration in scarabaeid beetles.* Journal of Physics D-Applied Physics, 2007. **40**(7): p. 2189-2196.

42. Broer, D.J., J. Lub, and G.N. Mol, *Wide band reflective polarizers from cholesteric polymer networks with a pitch gradient.* Nature, 1995. **378**(6556): p. 467-469.

CHAPTER 12

CONCLUSIONS

How often have I said to you that when you have eliminated the impossible, whatever remains, however improbable, must be the truth?
Sherlock Holmes, in The Sign of Four (Sir Arthur Conan Doyle [1]).

The introduction to this dissertation stated that the motivation for this research can be summed up in three questions. 1) Breathing on cold glass produces patterns called breath figures that consist of drops of many sizes, randomly arranged (surface coverage ~55%), but breathing on evaporating polymer solutions produces water drops that are noncoalescent, monodisperse, and closely packed (surface coverage in two dimensions ~90%), before they evaporate out leaving a polymer film full of ordered arrays of pores: *What is the mechanism for this breath-figure-templated assembly that makes water drops grow and organize without coalescence, and create porous or "holey" film?* 2) *How can you separate colloidal gold nanorods from nanoparticles of other shapes, and how can you ascertain that those were separated efficiently?* 3) *What causes the exoskeleton of the beetle Chrysina Gloriosa to show iridescent colors?* The chapters 2-11 present the literature review, results and discussion aimed at finding answers to these three questions. In this final chapter, the significant results and contributions of this research are summarized, and suggestions for future work are included.

12.1 What is the mechanism for breath-figure-templated assembly that makes water drops grow and organize without coalescence, and create porous or "holey" film?

The formation of water drops over evaporating polymer solutions exposed to moist airflow occurs due to supersaturation created by mixing of moist air with the

solvent vapor flux. The supersaturation that results from warmer moist air encountering colder solvent vapor flux, is similar to formation of breath fog from the mixing of warm, moist breath with cold, ambient air in winter. Likewise, the initial nucleation and growth of water droplets then occurs in air, over the dust particles present in air, which act as the condensation nuclei.

The rate and extent of evaporative cooling is determined by the choice of solvent and air flow velocity, and was modeled using diffusion limited heat and mass transfer from the polymer solution. The effect of air flow was incorporated using mass and heat transfer coefficients for laminar flow in the boundary condition used. The model was shown to correlate with the experimental measurements of the rate of mass loss and temperature drop for carbon disulfide solutions. The temporal variation of supersaturation over the substrate is controlled by the relative fraction of moist air, and solvent vapor flux. Using rate of evaporation and extent of evaporative cooling, the supersaturation was found to depend upon the humidity and the velocity of air flow as well as the physical properties of solvent.

The similarity to breath fog, rather than dew or breath figures, represents a paradigm shift in our understanding of nucleation and growth of water droplets over evaporating polymer solutions. The growth kinetics for the drops formed in breath figure templated assembly is quite different from that followed by drops formed in breath figures. While the drop sizes slightly increase with air flow velocity in breath figures, the increase in air flow velocity leads to decrease in drop sizes. The model predictions are in accord with several experimental observations. Further, it was shown that the

condensation growth mechanism itself is responsible for the observed monodipersity of pores.

Since the initial nucleation and growth of water drops occurs in mixed air, the questions pertaining to the noncoalescence of water drops were addressed for drops interacting in air, drops interacting with substrate and inter-drop interactions when drops are floating in polymer solution. The coalescence of drops typically involves three stages: collision of drops, flow of draining fluid that separates the drops as they approach each other and the actual merger of drops on contact. The collision efficiency for drops was shown to be quite low for drops colliding in air, both due to their low volume fraction and due to their small sizes. Further, the possibility of levitation of drops over evaporating polymer solutions was assessed and it was found that the normal force generated by the flux of solvent vapor (among other factors) can balance the weight of water drops. The noncoalescence of floating drops was attributed to the large time scale involved in the flow of draining film that separates the drops.

The pursuit of perfect packing by water droplets was described, using the language of crystallization. The water droplets behave like atoms or colloidal particles or bubble rafts, and produce a range of defects and dislocations associated with two dimensional crystals. These include vacancies, defects due to presence of foreign atoms, stacking faults and grain boundaries. Further, the drops were found to exhibit local and collective dynamics that included slip of two rows of drops to remove a dislocation, and healing of grain boundaries. The efficiency of noncoalescence was revealed also by drops that seemed to dive below the plane. These observations are reported in context of breath figure templated assembly for the first time. Crystallization of particles is usually

described in terms of the repulsive and attractive forces that act on the particles. In this contribution, the various interaction forces acting between water droplets were described. Further, it was shown that even though lateral capillary forces generated by deformation of meniscus due to floating particles, or immersed particles play limited or insignificant role in assembly process, capillary bridges can form between drops and provide an additional attraction between the drops. The observation of capillary or liquid bridges in the context of breath-figure-templated assembly has not been reported before this work.

The evaporation of close packed water arrays formed over evaporating polymer solutions was found to exhibit interesting wetting and dewetting dynamics. The phenomenon of drops popping out and growing as sessile drops over polymer rich-substrate is described for the first time. After the drops cease their singular or collective dynamics, that allows the assembly to remove defects and disclination, the drops get jammed against each other, and their location in the plane of the substrate is fixed, at these cells. Thereafter the drops appear to move in the direction perpendicular to the substrate, and each of these cells focuses light to its center, creating a pattern of bright dots. Some of these dots transform into sessile water drops that grow in size by either coalescing with the surrounding drops or by hydrodynamic flow from the adjoining cells. The sessile drops that occupy two to four cells, display the underlying cell boundaries, and are designated as scars. These scars eventually grow, such that some of the sessile drops occupy seven cells, where a bright magnified cell is visible at the center and the nearest six cells around it are buried under the contact line, giving the drop appearance of a flower. As more and more scars transform into flowers, the next stage involves growth of compound sessile drops. These drops are seen to move their contact line with discrete

motions, reminiscent of Zipping wetting, described for patterned superhydrophobic surfaces, where condensation of water plugs the asperities and the contact line appears to zip across. Once the drying sets in, the contact line recedes in similar fashion, where the line is seen to jump back or snap from one frame to next (move 2-4 microns in < 8 ms). The Laplace pressure of a drop that is partially immersed in polymer solution is higher than that of a sessile drop, as the latter has a larger radius, and therefore, fluid is transferred from pores into the larger sessile drops. *The most significant aspect of drying behavior described here is that in the context of breath-figure-templated assembly, the final structure is established somewhat before the water actually dries out, and the drying itself occurs from a thin sessile drop as opposed to the previous belief that it occurs from individual drops buried in a concentrated polymer solution*.

The specific questions about mechanism that were addressed during the course of this research are as follows:

- What is effect of changing air speed and humidity on the pore size?

  Change in the air flow velocity affects the rate and extent of evaporative cooling as well as temporal variation of supersaturation. For the typical conditions used in these experiments: higher the air flow velocity, lower is the temperature drop, and lower is the peak value of supersaturation, hence lower is the size of drops. Similarly, the supersaturation is directly proportional to the humidity of moist air; so higher the humidity, larger the drop sizes achieved (keep other conditions the same). The scenario is different from breath figures where increase in air flow velocity leads to slight increase in drop size.

- What is the lowest humidity at which these structures can form?

  The real factor that determines the nucleation and growth of water drops is the local supersaturation that arises due to mixing of humid air with solvent vapor flux. The relative humidity of air only expresses the fraction of vapor present in air at that temperature, with respect to the saturation vapor pressure determined by Clausius-Clapeyron equation. So even if relative humidity of air at higher temperature is 'low', the same volume of air will behave as saturated volume at a lower temperature. For a given air flow velocity and temperature of air, the lowest relative humidity of air that allows condensation growth depends upon the solvent chosen, and for carbon disulfide, even 25% relative humidity of air at 25^{o}C can nucleate and grow the water drops.

- Where, how and why do the drops nucleate?

  The mixing of two unsaturated volumes (solvent flux and moist air flow) of vapor creates a supersaturated mixture and hence allows nucleation and growth of water droplets in air, in fashion similar to the formation of breath fog. The number of nuclei that become active and grow into drops, depends upon the air quality, i.e. on the distribution function of aerosols, and it is related to the peak value and the temporal variation of supersaturation.

- What is the role of solvent?

  The physical properties of the solvent: mass diffusivity, heat diffusivity, latent heat of vaporization, heat conductivity, vapor pressure and density determine the rate and

extent of evaporative cooling as well as the peak value and temporal variation of supersaturation. For the same air flow velocity, the depth and width of curve representing the temperature drop as a function of time is in the following sequence: carbon disulfide > benzene > chloroform > toluene. The peak value of supersaturation as well as size of drops that grow under same air flow conditions also follows this sequence. The framework developed here can be adopted for determining these quantities for any given solvent. Solvent viscosity and surface tension assume importance in context of the drop non-coalescence and assembly.

When drops are floating in polymer solution, the viscosity of the intervening fluid determines the time required for them to contact and merge with each other. Since increase in polymer concentration increases the viscosity of the solution by several orders of magnitude or higher, the effect of solvent viscosity is not as strong as is the effect of polymer architecture and molecular weight. The solvent density and surface tension determine how large drops can be stabilized at the interface, and what forces act on them.

- What is the reason for non-coalescence of water droplets when they assemble on the evaporating polymer solutions?

  The coalescence of drops typically involves three stages: collision of drops, flow of draining fluid that separates the drops as they approach each other and the actual merger of drops on contact. The collision efficiency for drops was shown to be quite low for drops colliding in air, both due to their low volume fraction and due to their small sizes. Further, the drop size and mobility make even the head-on collisions of

drops ineffective, for in this case, the kinetic energy of the approaching drops and pressure created in draining film cause drops to deform slightly. The deformation of the drops coverts their kinetic energy to elastic energy, and if the pressure in the air film is high enough, the drops bounce back as if they hit an invisible wall.

After initial nucleation and growth in air, the drops eventually exist as floating drops in polymer solution substrate. But there is an intermediate regime, where drops can be levitated over the polymer solution. The existence and magnitude of normal forces that can balance the weight of the drops, and cause them to be levitated is described as follows. The normal force generated by a) relative motion of drop with respect to the substrate, calculated using lubrication approximation, b) by the evaporation flux of solvent, and c) by the thermocapillary convection that is driven by the temperature gradient that exists around the water drop. Since the evaporation rate and temperature of the substrate vary with time, thus the normal forces decrease as bulk of the solvent evaporates away.

Further, experimental evidence was presented for drops levitating over pure solvent, where Newton rings appear within the drops after 0.32 s of the start of the experiment. The noncoalescence observed in last stages of the process, where drops are close packed, can be attributed to the large time required for removing the intervening drainage film. Since the viscosity of the substrate fluid depends upon the initial concentration, molecular weight and architecture of the polymer, the choice of these is important factor in creating conditions for non-coalescence for floating drops.

- Is the presence of amphiphilic polymer, surfactant or hydrophilic group necessary for getting an ordered assembly of pores?

  The presence of amphiphilic polymers or surfactants is not required for the ordered arrays of water drops to form. The mechanisms based on the formation of micelles or polymer precipitates around water drops, that require special polymer types or architectures, were shown to be inconsistent with experimental results. Experimentally, the assembly is seen to occur for linear polymers. The experimental evidence as well as theoretical arguments outlined in this thesis indicate that the formation of ordered array of pores is explained best by the mechanism termed as breath-figure-templated assembly. The key is to realize that the nucleation and growth of water drops is more similar to breath fog rather than breath figures. Yet, the growth of the drops occurs simply by condensation mechanism, and the formation of drops occurs as long as the conditions of evaporative cooling, set primarily by choice of solvent, and the supply of water vapor, set by humidity and velocity of air flow are right.

- Is the architecture or molecular weight of the polymer important?

  Since the viscosity of the substrate fluid largely depends upon the initial concentration, molecular weight and architecture of the polymer, the choice of these is important factor in creating the conditions for non-coalescence and for assembly. While the noncoalescence of water drops floating in solution is promoted by the rise in viscosity, the assembly requires drops to have sufficient mobility to pack as efficiently as possible.

- Why are the drops and pores nearly monodisperse in size?

  The rate of growth of water drops under given conditions is brought about by condensation, where the temporal variation of supersaturation is determined by the rate and the extent of evaporative cooling, and the humidity as well as the velocity of moist air. The growth law suggests that smaller drops grow faster, and are able to catch up with larger drops and therefore an initially polydisperse population of drops becomes narrower with time. In absence of coalescence and for the cases when nucleation is limited to a short span of time, condensation growth always produces a narrow particle or drop size.

- What causes the drops to self-assemble?

  Two drops in close vicinity (<100 nm spacing between drops) of each other experience short ranged van der Waals attraction, whereas the repulsion at close range is caused by the energetic cost of deforming two drops from their equilibrium spherical shape. Besides these, meniscus deformation that is likely to occur under levitated drops can create attractive forces between the drops. The meniscus deformation also plays a role in bringing drops together. Apart from the attractive and repulsive forces that act on the drops, the hexagonal close packing of drops occurs as it is the most efficient way of packing a given number of spheres in both two dimensions and three dimensions. In this respect, the change in volume of drops that occurs due to the condensation growth of drops, forces them to close pack like crystalline solids. While the formation of rafts of drops suggests that they do act like

spheres with both repulsive and attractive forces, the need for efficient packing drives the close packed assembly of drops to remove defects, dislocations and grain boundaries.

- What is the mechanism involved in drying of water drops?

  The hexagonally close packed array of water drops (considering only two dimensional case), has drops that are partially immersed into the polymer solution. The experimental evidence provided here (for the first time in literature) reveals that water drops do not dry out from the pores, but are drawn out and grow into these sessile drops. The sessile drops or drops above the substrate have much lower radius of curvature, than the partially immersed drops, and so the Laplace pressure difference between these drops drives the fluid into larger drops. The larger drops then dry out. The growth of these 'sessile' droplets as well as their disappearance during drying involves a very interesting contact line dynamics, which is analogous to zipping wetting (and unzipping dewetting).

12.2 How can you separate colloidal gold nanorods from nanoparticles of other shapes, and how can you ascertain that those were separated efficiently?

The separation of colloidal gold rods from nanoparticles of other shapes can be carried out by using centrifugation-assisted sedimentation. *The ratio of the sedimentation velocities of Brownian rods and spheres undergoing centrifugation primarily depends upon the ratio of the square of their diameters.* The sedimentation velocity is itself dependent upon the ratio of the effective mass of the particle and the drag experienced by

it. The drag itself depends upon the shape of the particle, and for particles of same weight with different shapes, can make particles sediment at very different velocities.

The efficiency of separation can be illustrated by looking at the TEM images as well as UV-Vis-NIR spectra. Increase in aspect ratio of rods leads to a shift in the longitudinal plasmon resonance of the colloidal dispersion. The blue shift in transverse plasmon reflection predicted by theory for nanorods with increasing aspect ratio is also observed, for dispersions with low content of nanospheres. The drying of a drop of colloidal gold nanorods on glass slides creates coffee ring like deposits near the contact line, which is preceded by the formation of a liquid crystalline phase. While the TEM micrographs allow one to count the nanorods and determine their polydispersity, the patterns observed on TEM are a result of equilibrium and non-equilibrium processes that lead to drying mediated aggregation, as well as shape-based phase separation of nanoparticles, and the ordered phases are similar to two dimensional liquid crystals. The formation of liquid crystalline phase is surpressed for a dispersion of rodlike particles with polydispersity higher than 18% and hence the existence of ordered phase provides evidence for better control over the shape and size dispersion of rods.

12.3 What causes the exoskeleton of the beetle *Chrysina gloriosa* to show iridescent colors?

The iridescent, metallic green beetle, *Chrysina gloriosa*, which selectively reflects left circularly polarized light when illuminated with unpolarized light, is observed to possess a nearly hexagonal cellular pattern on its exoskeleton. Using crystallographic concepts and Voronoi analysis of the structure present on the exoskeleton, we determined

that these hexagonal cells (~10 μm each) coexist with pentagons and heptagons, interdispersed typically as clusters, between hexagons. In an optical microscope, each cell appears to contain a bright yellow core, placed in greenish cell that has yellowish borders. Using confocal microscope and the auto-fluorescence of the exoskeleton matrix, these cells were observed to consist of nearly concentric, nested arcs that lie on surface of a shallow cone. *These patterns are analogous to the focal conic domains formed spontaneously on the free surface of a cholesteric liquid crystal.* We propose that these cholesteric textures provide the basis for the formation and structure of tiles that decorate the exoskeleton of *Chrysina gloriosa*, leading to its iridescent color.

12.4 Recommendations for future work

The purpose of the thesis was to address some of the questions described in previous sections. The research provided clues about mechanistic aspects of breath figure templated assembly, shape separation and self-assembly of colloidal gold nanorods, and about the structure that makes the beetle *Chrysina gloriosa* iridescent. The unanswered and open questions were outlined throughout the dissertation, and only some of them are summarized here:

12.4.1 Breath figure templated assembly of ordered array of pores in polymer films

- Effect of solvent and polymer

  According to the theoretical framework developed here, under the same conditions different solvents undergo a different extent of evaporative cooling, provide different supersaturation, and the final size of drops and pore is different. The theoretical

predictions about choice of solvent, and effect of air flow conditions requires careful experiments, where the quality of air used should be the same (for it determines the number density of aerosols that can be activated to grow into drops) , the volume of polymer solution and underlying substrate should be the same (for these determine the timescales of evaporation and cooling) and the flow of moist air should be controlled. Similarly, for experiments on the effect of molecular weight, or concentration or architecture of polymers should require controlled conditions. The effect of polymer is expected to be felt to a greater extent in how quickly and efficiently drops are able to assemble together.

- Aspects about nucleation and growth of drops

  The theoretical arguments presented in this thesis imply that the local aerosol concentration affects the number of available growth sites. This prediction can be verified using air flow, where the number distribution of condensation nuclei is known. This can be accomplished by measuring air quality using particle counters typically employed by atmospheric physicists. The size of drops can be manipulated by varying the humidity or velocity of airflow. It would be interesting to use air flow where humidity or air flow is altered during the course of experiment, to influence the size of the drops. An increase in number density of nucleation sites, will lead to a decrease in the mean drop size under the same supply of water vapor.

- Noncoalescence and self-assembly of drops

The dissertation includes approximate computation of forces that lead to the levitation of drops over substrate, where the normal forces exerted were computed using on an inclined bar, rather than a sphere. Further, if the drops levitate over the solution with a deformed meniscus, the shape and size of meniscus must be computed to determine the possibility of interaction between levitated drops, through the interaction of the meniscus perturbed by them. The interaction potentials that were computed for drops did not account for effect of concentration and choice of polymer and solvent. The self-assembly of drops can be used as a model system to study how spherical particles organize into an ordered structure, and it is likely that the close packed arrays of drops will prove to be interesting model system to compare with bubble rafts and colloidal crystals. Dynamic effects representative of materials like defect mobility, slip, avalanches, hexatic phase, yield in polycrystalline materials can be possibly studied using the self-assembled drops.

- Wetting-dewetting-drying behavior of drops

  Since the wetting-dewetting phenomenon reported here have not received any attention before, the list of unsolved problems is very rich. The problems related to definition and evolution of contact angle and contact line for drops on hydrophobic and superhydrophobic surfaces are fundamental to understanding of wetting as well as to the behavior observed here. What are limits of validity of Cassie or Wenzel relations? The evidence presented here suggests that the coalescence of drops that pop out in the ordered and disordered arrays exhibit different steps or stages. What capillary forces exist within the cells, and how do these depend upon the choice of

polymer, solvent and airflow conditions? What causes zipping wetting or unzipping dewetting, and how does that depend upon material or environment as well as the pore dimensions that can be measured for holey films? How does the rate of evaporation of thin sessile drops compare to the rate of evaporation of the same volume of drops immersed in another fluid with only a small cap exposed to the airflow? While preliminary thoughts on these are expressed in this dissertation, the experimental observations reported here require more study.

12.4.2 Colloidal gold nanorods

- Separation of colloidal rods from spheres using electrophoresis

  The dissertation provides hydrodynamic arguments for using the shape dependent sedimentation velocity during centrifugation for the separation of rods and spheres. Since the sedimentation process can be thought of as Brownian motion under influence of an external field, it is likely that electrophoresis can help in separation of colloidal gold nanorods from spheres.

- Using ultramicroscopy for observing nanoparticle growth

  The dissertation provides a survey of the contributions made by the pioneers of colloidal science to the field of colloidal gold particles. Zsigmondy invented ultramicroscope to visualize nanoparticles that lie in a Tyndall cone of light. The same principle can be used to study the kinetics of growth of colloidal nanorods. Further, the technique provides a method to visualize rods in their dispersed state, and characterize them, without the recourse to transmission electron microscopy.

- Pattern formation by drying a drop of colloidal gold nanorods

  The dissertation provides only phenomenological arguments about the patterns that were observed on drying a drop of nanorod dispersion on glass slides or on TEM grids. The quantitative comparisons with phase diagrams for short spherocylinders requires a theory of capillary-driven flow in evaporating drops containing rodlike particles, and experimental and theoretical determination of concentration at which the liquid crystalline domains appear in the drying drops.

12.4.3 Iridescent beetle *Chrysina gloriosa*

- Color of tiles that decorate the beetle exoskeleton

  The dissertation provides only phenomenological arguments about why the tiles have a yellow dot at the center surrounded by green color in bright field and why the yellow dot disappears if the cells are visualized using dark field. While the color is found to depend upon the angle of incident on the cells of the beetle, the characteristic changes can be explained only by carrying out computations that account for the interplay of light with the structure of cholesteric focal conic domains. This requires a better understanding of both the structure and the refractive index of the cholesteric material as well as other layers that constitute the beetle exoskeleton.

- Pattern formation on curved surfaces

  The patterns on the beetle were found to have higher disorder (or larger number of cells with coordination number of five or seven) in the regions of greater curvature,

revealing packing issues on curved surfaces. The various pattern formation mechanisms that create hexagonally symmetric patterns on planar two-dimensional surfaces can likewise be expected to break the symmetry on curved surface, if the six fold triangulations are not energetically most favored everywhere. The packing of water drops as well as gold nanorods can be studied on curved surfaces to see how curvature affects the local positional and orientational order.

12.5 References

1. Doyle, A.C., *The Complete Sherlock Holmes*. 2008, New York: Wordsworth Editions Ltd.

VITA

VIVEK SHARMA

Vivek Sharma was born in Mandi, Himachal Pradesh, in a state in the Himalayas in North India. He obtained his schooling at Shimla, Mount Carmel School, Una and finished Matriculation from St. Mary's Convent School, Kasauli. Thereafter he studied in D. A. V. College, Chandigarh for the next two years. Vivek obtained Bachelor of Technology from Indian Institute of Technology, Delhi, with major in Textile Technology, and focus on polymers and polymeric fibers. He moved to the United States in 2001, and obtained a Master of Science degree in Polymer Science from University of Akron, Ohio, for his research on rheology of polymer solutions. After joining Georgia Institute of Technology, Vivek first imaged and studied chaotic mixing in droplets in the Center for Nonlinear Sciences and School of Physics. He also obtained a Master of Science in Chemical Engineering, with minor in Nonlinear Dynamics and Chaos. Vivek obtained another minor in Physics and worked on his research for Doctorate in Philosophy in Polymers, under supervision of Professor Mohan Srinivasarao. When he is not working on his research, Vivek Sharma writes poetry and fiction, and is published in literary journals and newspapers.